Improvement of the Optical and Mechanical Properties of Silica Nanoparticle Ionic Self-Assembled Multilayer Anti-Reflection Coatings on Glass and Polycarbonate Substrates

Jason Ian Ridley

Dissertation submitted to the faculty of the Virginia Polytechnic Institute and State University in partial fulfillment of the requirements for the degree of

Doctor of Philosophy
In
Physics

James R. Heflin
(Committee Chair)
Alfred L. Ritter
(Committee Co-Chair)
Giti Khodaparast
Victoria Soghomonian

February 5, 2010
Blacksburg, Virginia

Keywords: Ionic Self-Assembled Multilayers (ISAM), Silica Nanoparticles, Diazo-Resin (DAR), Calcination, UV Irradiation, Polycarbonate, Glass Fibers

Improvement of the Optical and Mechanical Properties of Silica Nanoparticle Ionic Self-Assembled Multilayer Anti-Reflection Coatings on Glass and Polycarbonate Substrates

Jason Ian Ridley

Abstract

This thesis presents the characterization of the optical and mechanical properties of silica nanoparticle films fabricated by ionic self-assembly, also known as layer-by-layer (LbL) deposition. Utilizing electrostatic attraction of oppositely-charged materials permits uniform and rapid growth of the constituents onto planar and curved surfaces. In this work, silica nanoparticles are adsorbed onto glass and polycarbonate substrates, as well as micron-scale glass fibers, with the purpose of improving the optical quality of the respective media.

Several methods are presented to improve the adhesion and cohesion of silica nanoparticle films on glass substrates. In the first method, the substrate and nanoparticle surfaces are coated with materials containing sulfonate end groups. Next, a photo-reactive polycation known as diazo-resin (DAR) is used in ISAM deposition with the modified silica nanoparticles. Subsequent exposure to UV converts the ionic bonds between the DAR and sulfonate groups into covalent ones. The second method to improve the mechanical strength is to heat the ISAM silica nanoparticle film at a high enough temperature (500 °C) to remove the polymer and partially fuse the nanoparticles. This technique is known as calcination and is shown to significantly improve the mechanical robustness of the film without compromising the optical properties. The final method involves the deposition of precursor and capping polymer layers around bulk silica nanoparticle films with both bilayer and quadlayer designs. The addition of these polymer layers improves the surface contact between adjacent nanoparticles but reduces the film porosity and consequently the optical transparency. Currently the calcination technique is the only one that significantly improves the film adhesion and cohesion, but

suggestions are offered to potentially improve the performance of films made by the other two methods.

An alternative way to functionalize polycarbonate substrates for silica nanoparticle ISAM deposition is also presented. The molecular structure of polycarbonate at the surface can be modified by exposing it to deep UV (λ = 185, 254 nm). By doing so, the surface becomes populated with carboxylate species, and thus permits ISAM deposition of poly(allylamine hydrochloride) (PAH) and silica nanoparticles. A variety of spectroscopic methods show that the molecular structure is changed by this procedure, and SEM shows that UV treatment improves the uniformity of ISAM films on polycarbonate.

Finally, PAH/silica nanoparticle ISAM films are deposited onto glass fibers. The fibers are used for mechanical reinforcement of polymer composite optical media. The role of the nanoparticle film on the fibers is to reduce light scattering at the interfaces of materials with different thermo-optic coefficients, in other words, transmittance losses associated with changes in temperature. Fiber bundles coated with silica nanoparticles suffer from unacceptable levels of aggregation, and hence do not currently improve the transmittance over the temperature spectrum. Some evidence is presented, however, to suggest that the transparency can be improved if fiber aggregation during ISAM deposition can be avoided.

This thesis is dedicated to my parents, Fred and Sylvia Ridley. Without your guidance and care I could not have made it to this point. I love you both.

Acknowledgements

My utmost thanks and appreciation go to my academic advisors, Dr. Randy Heflin and Dr. Jimmy Ritter. Not only did they gladly offer their expertise whenever needed, but they also fostered an environment where education was the top priority. I am honored to have worked for them and will always appreciate their mentorship.

Special thanks go to Dr. Daniel O.' Brien at the Army Research Laboratory for allowing me the privilege to work with him during the summer of 2008.

I am also grateful to Drs. Giti Khodaparast and Victoria Soghomonian for taking an interest in my research and serving on my PhD. committee.

To my parents, what can I say? I could not be in this position without their constant guidance, encouragement, and love. More importantly, they taught me to appreciate the finer things in life and to value the diversity that it offers. For that I can not thank them enough. My love and thanks go to the rest of my family for constant support.

My sincere appreciation goes to a number of faculty members at Virginia Tech for their cooperation and insight. In particular I would like to thank Drs. Timothy Long, Richard Turner, John Morris, Richey Davis, John Dillard, and David Dillard. Furthermore I would like to thank Dr. Junqi Sun and Dr. Alexander Welle for sharing their expertise with me.

All of my thanks and appreciation go to Christa Thomas for her constant support during my time in graduate school.

Much of what I've learned over the course of my PhD. work was gained through insightful discussions with other graduate students. For this, I wish to thank Vaibhav Jain, Cemil Durak, Aziz Kaya, Will Miles, Adam Larkin, Akhilesh Garg, Anamika Gopal, Reza Montazami, Rebecca Brown, Kriton Papavasiliou, Raquel Mejia-Ariza, and Jessica Lu.

Jonathan Metzman and Shane Seaman ran a number of experiments to continue our research and help me finish. I want to thank and acknowledge them for their efforts.

I am very grateful to Frank Cromer for running XPS analysis on numerous samples and for insightful discussions. Training on SEM was graciously provided by Vaibhav Jain and Steve McCartney. I was greatly assisted by the Physics Department machine shop personnel: Melvin Shaver, Scott Allen, John Miller, and Ron Stables. They were always kind and highly professional, and for that I want to thank each of them.

Having a life outside of the lab was vital to keeping sane, and with the friends I've made I can happily say that sanity was preserved! In no particular order these people are: Cemil Durak, Aziz Kaya, Vaibhav Jain, Georges El-Abboud, Devrim Ozdemir, Sameer Arabasi, Jennifer Steding, Jia Jia Dong, Brian Geist, Xiaohua Xu, Akshay Kokil, Amber Hancock, Vrushali Chavan, Wenwei Zhong, Clifton Cassidy, Gade Kimsawatde, Andy and Karlie Herbert, Andy and Jessey Schaudt, Reza Montazami, Courie Cohen, Emily Anderson, Parthiban Rajasekaran, Michelle Grimm, Sayan Naha, Sarah Boor, Linda Lee Varndell, Jan Petrich, Kriton Papavasiliou, Vicky Haskell, Simoni Triantafyllidou, Krisha Chachra, and Erin Cassidy. I have undoubtedly missed many others and my apologies go to those that have not been named.

Special mention goes to Anamika Gopal and Eveline Richert as they will always have a special place in my heart.

I also want to thank the Physics department faculty at my Alma Mater, Delaware State University. Thanks to Drs. Ehsan Helmy, Patrick Gleeson, Arthur Purdy, Al Khan, Essaid Zerrad, and Gabriel Gwanmesia for laying the foundations of my education. Additional thanks to Drs. Al Khan and Essaid Zerrad for encouraging me to pursue an advanced degree. Special mention goes to Joe Pent for being such a great friend and confidant.

Finally, I want to acknowledge financial support from the Army Research Laboratory under the Cooperative Agreement Number W911NF-06-2-0014 and the Army Materials Center of Excellence (MCOE) Multilayered Technologies for Armored Structures and Composites (MultiTASC) Program. Thanks to Jeff Beeby, Tammy Jo Hiner, and Mary Jane Smith for assistance with fiscal matters.

TABLE OF CONTENTS

List of Figures

CHAPTER ONE

CHAPTER TWO

CHAPTER THREE

CHAPTER FOUR

CHAPTER FIVE

CHAPTER SIX

List of Tables

CHAPTER FOUR

CHAPTER FIVE

CHAPTER ONE

Introduction

This thesis presents work done to improve the mechanical and optical properties of silica nanoparticle anti-reflection (AR) coatings deposited onto glass and polycarbonate substrates by ionic self-assembled multilayer (ISAM) deposition. Three methods are discussed to improve the nanoparticle cohesion and adhesion of the film to glass substrates. In addition, UV irradiation of polycarbonate is presented as a highly simple, alternative way to functionalize its surface for subsequent ISAM deposition of silica nanoparticles (SiO_2 NPs). Finally, micron-scale glass fibers are coated with SiO_2 NPs to form an intermediate refractive index region that can partially mitigate thermo-optic related losses of light.

1.1 Motivation

There is a high demand for optical media in our everyday life. These media vary from windows, displays (e.g., television, computer, cell phone), eyewear, visors, etc. The type of medium may differ depending on its application. Glass is typically used in cases where high transparency in the visible is desirable. If a more robust medium is required, however, one may use a variety of available thermoplastics, such as polycarbonate, poly(methyl methacrylate), etc. In many cases, reflection of light from these surfaces can result in undesirable glare. This glare can be suppressed substantially by coating the surface of the optical medium with a material that has an index of refraction between the indices of refraction of the media on either side of the film. The films are commonly referred to as "anti-reflection" coatings because the phenomenon is caused by destructive interference of light reflected from the interfaces of the optical medium and coating. Additionally, the fraction of light transmitted through the optical medium increases and thus, the benefits of applying an AR coating to a surface are two-fold.

In addition to the multitude of commercial applications, significant attention has been given to developing high quality AR coatings by the military. This is because highly transmittant coatings can improve threat detection, and the reflectance suppression can help avoid detection by the enemy. Coatings are typically applied to many different media, such as

helmet visors, windows on moving and stationary armored structures, displays, etc. In some applications, such as displays, glass would be a suitable material to use. In other cases, however, the military requires optical media with outstanding impact resistance, in which case a thermoplastic is a more appropriate choice. In light of the global presence of our military and the nature of its work, it is common for soldiers and mobile structures to be exposed to a variety of harsh and dynamic climates. Thus, it is important for any AR coating deposited onto an optical medium to not only have excellent optical properties, but to also have outstanding mechanical resistance to those environments. In response to this need, our research group has worked to develop anti-reflection coatings that meet these rigorous demands. More specifically our work is part of a collaborative research initiative with other faculty at Virginia Tech, in conjunction with the U.S. Army Research Laboratory, as part of a Materials Center of Excellence. The overarching goal of our research team is to develop extremely tough, multifunctional thermoplastics. The research is divided into four different platforms, which in general are categorized as: (1) synthesis, (2) fabrication, (3) performance, and (4) surfaces. Our work falls under the "surfaces" category. If we are able to develop durable coatings with high transmittance using ISAM deposition, we will be able to provide the U.S Army with an efficient, cost effective way to coat small or large structures without regard to their complexity.

1.2 Theoretical Principles of Anti-Reflection Coatings

The governing principles for minimal reflectance of light are quite simple. Here I consider linearly polarized light with wavelength "λ" in an external medium, and incident on a substrate coated with a homogeneous thin film with thickness "d" (**Figure 1.1**). Thus, there are two distinct boundaries, or interfaces, that light may encounter: (I) the boundary between the external medium and the film, and (II) the boundary between the film and the substrate. The external medium, film, and substrate have refractive index values of n_0, n_1, and n_S, respectively. Please note the adopted nomenclature that follows is from the 2nd edition of Hecht Optics,[1] which gives a complete formalism for the requirements of zero reflectance of light passing through a single-layer film. Moreover, I will begin the derivation with expressions for the Fresnel transmission and reflection coefficients, "t" and "r", respectively. These are eventually obtained after taking advantage of the condition that the tangential components of the electric (**E**) and

magnetic (**H** = **B**/μ) fields are continuous across the boundaries and describe the transmitted and reflected electric field amplitudes as a function of the indices of refraction of the two media, angle of incidence, and polarization of the incident light.

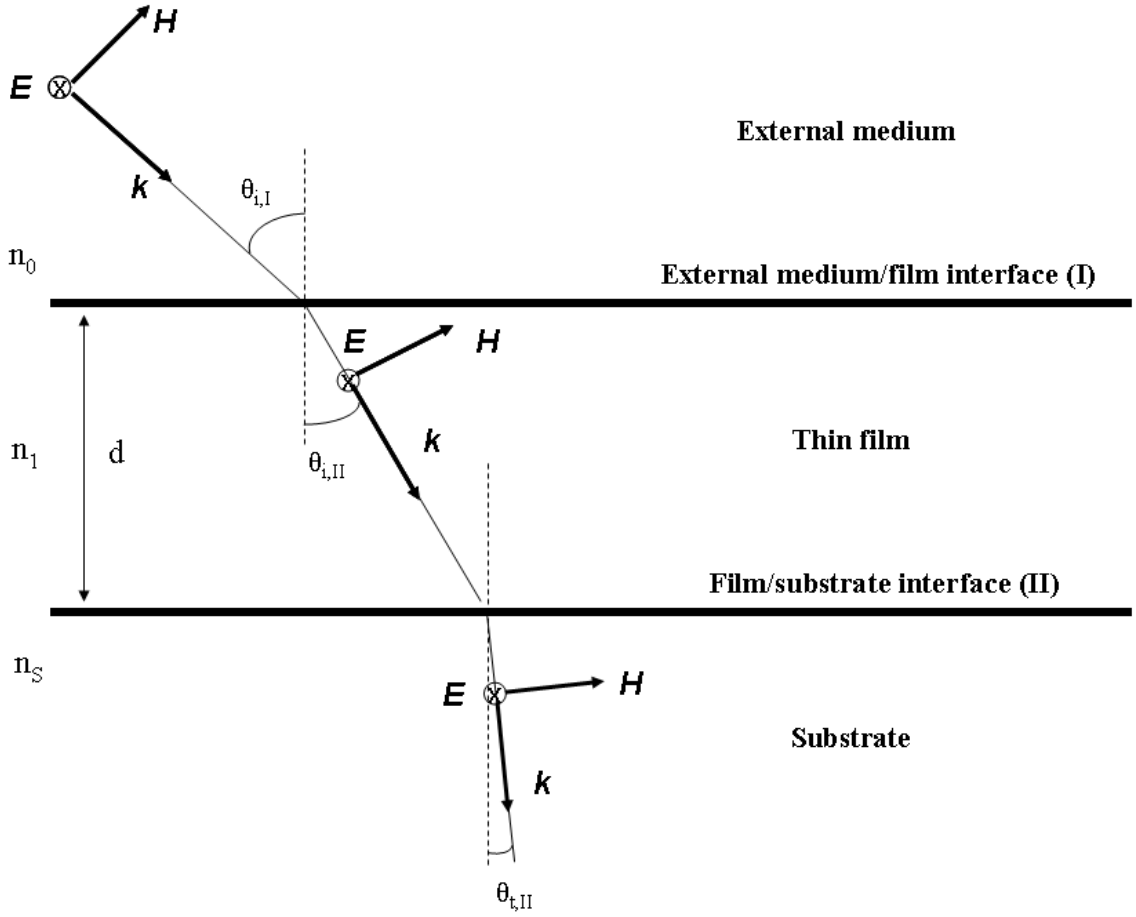

Figure 1.1 Light passing through a homogeneous single-layer AR coating.

The Fresnel equations describe the behavior of light passing between two media with different refractive indices. Separate expressions are given for the amplitude transmission (t) and reflection (r) coefficients if the electric field (**E**) is normal or parallel to the plane of incidence. For now, only consider light passing across a single interface (the external medium/film interface). If **E** is normal to the plane of incidence, the transmission and reflection coefficients are given by:

$$t_{\perp} = \frac{2n_0 \cos\theta_{i,I}}{n_0 \cos\theta_{i,I} + n_1 \cos\theta_{i,II}} \quad \text{(Eq. 1)}$$

$$r_{\perp} = \frac{n_0 \cos\theta_{i,I} - n_1 \cos\theta_{i,II}}{n_0 \cos\theta_{i,I} + n_1 \cos\theta_{i,II}} \quad \text{(Eq. 2)}$$

If **E** is parallel to the plane of incidence, the coefficients are given by:

$$t_{\parallel} = \frac{2n_0 \cos\theta_{i,I}}{n_0 \cos\theta_{i,II} + n_1 \cos\theta_{i,I}} \quad \text{(Eq. 3)}$$

$$r_{\parallel} = \frac{n_1 \cos\theta_{i,I} + n_0 \cos\theta_{i,II}}{n_0 \cos\theta_{i,II} + n_1 \cos\theta_{i,I}} \quad \text{(Eq. 4)}$$

These are the Fresnel equations for light passing across a single optical interface. We, however, are more interested in general expressions for the transmission and reflection coefficients of light passing through a system with two interfaces, that is, the external medium/film and film/substrate interfaces. For the given case the transmission and reflection coefficients are:

$$t = \frac{2\mathrm{Y}_0}{\mathrm{Y}_0 \cos(kh) + (\mathrm{Y}_0\mathrm{Y}_S / \mathrm{Y}_1)[i\sin(kh)] + \mathrm{Y}_1[i\sin(kh)] + \mathrm{Y}_S \cos(kh)} \quad \text{(Eq. 5)}$$

$$r = \frac{\mathrm{Y}_0 \cos(kh) + (\mathrm{Y}_0\mathrm{Y}_S / \mathrm{Y}_1)[i\sin(kh)] - \mathrm{Y}_1[i\sin(kh)] - \mathrm{Y}_S \cos(kh)}{\mathrm{Y}_0 \cos(kh) + (\mathrm{Y}_0\mathrm{Y}_S / \mathrm{Y}_1)[i\sin(kh)] + \mathrm{Y}_1[i\sin(kh)] + \mathrm{Y}_S \cos(kh)} \quad \text{(Eq. 6)}$$

<u>Definitions:</u>

$k = \frac{2\pi}{\lambda} \equiv$ wavenumber

$h \equiv (n_1 d)\cos\theta_{i,II} \equiv$ optical thickness of the film

d ≡ physical thickness of the film

$\mathrm{Y}_0 \equiv \sqrt{\frac{\varepsilon_0}{\mu_0}} n_0 \cos\theta_{i,I}$

$Y_1 \equiv \sqrt{\frac{\varepsilon_0}{\mu_0}} n_1 \cos\theta_{i,II}$ **,** assuming the electric field ***E*** is not in the plane of incidence

$Y_1 \equiv \sqrt{\frac{\varepsilon_0}{\mu_0}} n_1 / \cos\theta_{i,II}$, if the electric field ***E*** is in the plane of incidence

$Y_S \equiv \sqrt{\frac{\varepsilon_0}{\mu_0}} n_S \cos\theta_{t,II}$

$\varepsilon_0 \equiv$ permittivity of free space

$\mu_0 \equiv$ permeability of free space

$n_0 \equiv$ index of refraction of external medium

$n_1 \equiv$ index of refraction of film

$n_S \equiv$ index of refraction of substrate

$\theta_{i,I} \equiv$ angle of incident light at the external medium/film interface#

$\theta_{i,II} \equiv$ angle of incident light at the film/substrate interface#

$\theta_{t,II} \equiv$ angle of transmitted light at the film/substrate interface#

$\theta_{i,I}$, $\theta_{i,II}$, and $\theta_{t,II}$ are defined from the normal to the interfaces

I will only consider the case of normally incident light at the external medium/film interface (i.e., $\theta_{i,I} = \theta_{i,II} = \theta_{t,II} = 0$). As a result the reflection coefficient relation simplifies nicely:

$$r = \frac{n_1(n_0 - n_S)\cos(kh) + (n_0 n_S - n_1^2) i \sin(kh)}{n_1(n_0 + n_S)\cos(kh) + (n_0 n_S + n_1^2) i \sin(kh)} \qquad \text{(Eq. 7)}$$

To obtain the reflectance "R" the reflection coefficient must be multiplied by its complex conjugate r*:

$$r^* = \frac{n_1(n_0 - n_S)\cos(kh) - (n_0 n_S - n_1^2) i \sin(kh)}{n_1(n_0 + n_S)\cos(kh) - (n_0 n_S + n_1^2) i \sin(kh)} \qquad \text{(Eq. 8)}$$

$$R = rr^* = \frac{n_1^2(n_0 - n_S)^2 \cos^2(kh) + (n_0 n_S - n_1^2)^2 \sin^2(kh)}{n_1^2(n_0 + n_S)^2 \cos^2(kh) + (n_0 n_S + n_1^2)^2 \sin^2(kh)} \qquad \text{(Eq. 9)}$$

One criterion to achieve minimal reflectance is that the reflections from the external medium/film (boundary I) and film/substrate (boundary II) interfaces are 180° out of phase at boundary I. This occurs when the optical thickness "h" is equal to λ/4, in which case light reflected from the film/substrate interface travels through the film an optical distance equal to λ/2. Therefore, assuming the optical thickness "h" equals λ/4:

$$kh = \left(\frac{2\pi}{\lambda}\right)\left(\frac{\lambda}{4}\right) = \frac{\pi}{2} \quad \text{(Eq. 10)}$$

Therefore, the reflectance reduces to:

$$R = \frac{(n_0 n_S - n_1^2)^2}{(n_0 n_S + n_1^2)^2} \qquad \text{(Eq. 11)}$$

Finally, the reflectance is zero when the refractive index of the film is:

$$n_1 = \sqrt{n_0 n_S} \qquad \text{(Eq. 12)}$$

Therefore, the two conditions that satisfy zero reflectance of light with wavelength "λ" passing through a single homogeneous layer are:

(1) optical thickness h = λ/4, and

(2) $n_1 = \sqrt{n_0 n_S}$

In summary, the reflectance of light with wavelength "λ" passing through a single layer is dependent on the thickness and refractive index of the coating. The thickness criterion is very simple to satisfy since many film deposition techniques exhibit exceptional control over this parameter. Therefore, the coating thickness only dictates the wavelength at which one wishes to

achieve minimal reflectance. The second criterion, the film index of refraction, can be far more difficult to satisfy. Consider a film deposited on glass ($n_S = 1.5$), and surrounded by air ($n_0 = 1$). In this situation the film index of refraction (n_1) should be around 1.22 to match the wave amplitudes of light reflected from boundaries I and II. There are no reports of a homogeneous material possessing such a low index of refraction. Magnesium fluoride (MgF_2) is a durable material commonly used for AR coatings on glass substrates. However, its refractive index, while quite low for homogeneous materials ($n = 1.38$), is still well above what is desired. Because of this, much attention has been given to develop nanoporous thin films that have a smaller refractive index. In our research we have fabricated AR coatings using silica nanoparticles. These films have a porous structure and low refractive index ($n \approx 1.26$-1.30). The inherent drawback of a film consisting of pores, however, is a general lack of mechanical strength. Thus, the primary thrust of our research is to explore possible solutions to improve the cohesive and adhesive strength of silica nanoparticle AR coatings.

1.3 Outline

Chapter 2 gives an overview of the history of AR coatings and ISAM deposition. The discovery of AR coatings by Lord Rayleigh is mentioned, as well as early developments of the technology for integration in optical systems. Next, common thin film deposition techniques are discussed including physical and chemical vapor deposition, spin coating, and the Langmuir-Blodgett technique. The advantages and disadvantages associated with each method of deposition are described in order to stress the value of fabricating coatings by the ISAM method. Next, early and more recent works utilizing ISAM deposition are discussed, which demonstrate the ability to create ordered, uniform, and versatile films using a broad range of polymeric materials. Finally, ISAM deposition with spherical nanoparticles is presented. Significant attention is given to the adsorption and formation of layered structures with respect to NP size, surface functionality, and charge density. The effect of these parameters on the optical properties of NP films is also discussed in order to stress the advantages of using silica nanoparticles in the fabrication of AR coatings.

Chapter 3 details the experimental methods in this research ranging from substrate preparation to thin film deposition by the ISAM technique and other various protocols. Methods

to characterize the optical and mechanical properties of AR coatings are also discussed including UV/VIS/IR spectroscopy, ellipsometry, AFM, SEM, a surface abrasion test, and a tape peel test.

Chapter 4 contains the bulk work of the thesis, which focuses on improving the mechanical strength of SiO_2 NP films. Three different approaches are considered. In the first approach, colloidal silica nanoparticles are surface-modified by ISAM deposition with poly(allylamine hydrochloride) and poly(styrene sulfonate). Furthermore, the glass substrate is coated with a silane that has thiol end groups that can be converted to sulfonate groups after chemical modifications. The resulting SiO_2 surfaces are completely coated with sulfonate end groups. The modified nanoparticles are deposited along with diazo-resin (DAR), a photoreactive polycation, using the ISAM technique. Subsequent UV irradiation of the films converts the ionic bonds between DAR and the sulfonate groups into covalent ones, thus improving the mechanical strength. In the second approach, SiO_2 NPs are deposited with poly(allylamine hydrochloride), and the resulting films are heated to high enough temperatures to remove the organic material and partially fuse the nanoparticles. The final approach involves the deposition of three polymer layers for every layer of SiO_2 NPs. The improved coverage of polymers on the nanoparticle surface improves the cohesive strength of adjacent nanoparticles, but also compromises the film transparency.

Chapter 5 presents an alternative way to functionalize the surface of polycarbonate (PC) substrates with charged groups to enable ISAM deposition. Deep UV irradiation (λ = 185, 254 nm) initiates molecular reorganization and surface oxidation, and improves the adsorption of silica nanoparticles and poly(allylamine hydrochloride) on PC. Several analytical techniques clearly show that the PC surface is altered by exposure to UV. Optical characterization of ISAM films with alternating layers of poly(allylamine hydrochloride) and SiO_2 NPs on PC is presented and shows that the film uniformity can also be improved. Finally, a report on the (inhomogeneous) adsorption of nanoparticles on untreated PC substrates is presented, along with speculation as to the cause for adsorption in this case.

Chapter 6 details ISAM deposition of poly(allylamine hydrochloride) and SiO_2 NPs onto micron-scale glass fibers for use as reinforcement in polymer composite structures. The alignment of fiber bundles in polymer matrices and their consequent effect on light scattering is discussed, followed by a proposed alignment to improve the reproducibility of transmittance spectra. Next, the transparency of fiber bundles with and without ISAM coatings is compared as

a function of polymer matrix temperature. Finally the cause of increased scatter of coated fiber bundles is identified by SEM.

The thesis ends with a summary of each of the presented topics in this research. Recommendations are given to further improve the optical and mechanical properties of silica nanoparticle films on the various optical media discussed in the thesis.

[1] Eugene Hecht, *Optics*, 2nd ed. (Addison-Wesley Publishing Company, Inc., 1987), pp.373-375.

CHAPTER TWO

Background and Literature Review of Anti-Reflection Coatings and Ionic Self-Assembled Multilayer Deposition

2.1 Anti-Reflection Coatings

Anti-reflective coatings were discovered quite by accident by John William Strutt, more famously known as Lord Rayleigh, in 1886.[1] At the time he was studying the intensity of reflected light from glass surfaces with the intention of experimentally confirming Fresnel's equation of reflection for normally incident light. Rayleigh studied the reflection of light, in contrast to the work by Ogden Nicholas Rood[2] in 1870, who studied the intensity of transmitted light through glass. Rayleigh had two major concerns with Rood's experimental preference; the first being the absorption of light passing through the media, leading to discrepancies between experimental data and theoretical predictions of Fresnel. Secondly, this discrepancy in transmission may be negligible when compared to the value of transmitted light, but becomes magnified nearly tenfold when compared to the intensity of reflected light. For the experiment, Rayleigh used a prism in order to mitigate reflections from the back surface and easily calculate the medium index of refraction. At one point while using an older prism of crown glass, he noticed that the reflected intensity was significantly less compared to recently polished prisms and could not correlate this result with Fresnel's equation. After polishing the surface of the old prism, he reported a marked increase in the reflected intensity. He postulated that a material of intermediate refractive index was on the surface which was suppressing the interfacial reflections. The following is an excerpt from his paper:

"The question as to the cause of the falling off, I am not in a position to answer satisfactorily. Anything like a disintegration of the surface might be expected to reveal itself on close inspection, but nothing of this kind could be detected. A superficial layer of lower index, formed under atmospheric influence, even though no thicker than 1E-5 inch, would explain a diminished reflection. Possibly a combined examination of the lights reflected and transmitted by glass surfaces in various conditions would lead to a better understanding of the matter. If the superficial film act by diffusion or absorption, the transmitted light might be expected to fall off.

On the other hand, the mere interposition of a transparent layer of intermediate index would entail as great an *increase* in the transmitted as falling off in the reflected light. There is evidently room here for much further investigation, but I must content myself with making these suggestions."[1]

Bauer[3] was the first to explain that the anti-reflection phenomenon was a result of destructively interfering waves, but the first practical application of anti-reflection coatings came in 1935[4] when Alexander Smakula, while working for Carl Zeiss AG, found he could improve the transmission of light through binoculars when applying a thin coating to the lens surface.

Vacuum deposition of homogeneous materials was the predominant early deposition technique. Magnesium fluoride (MgF_2) became a standard material to deposit onto glass substrates because of its relatively low index of refraction (n = 1.38) and resistance to abrasion.[5] Other materials such as cerium dioxide (CeO_2), silicon monoxide (SiO), and zinc sulfide (ZnS)[6] were used on substrates possessing high transparency in the infrared. Jacobsson experimented with simultaneous vacuum deposition of two different materials onto a surface to create inhomogeneous layers for control over the index of refraction. He used CeO_2-MgF_2 and ZnS-Na_3AlF_6 blends to suppress reflection in the visible, and Ge-MgF_2 for the infrared.[7] Hass and Ritter[8] wrote an excellent review together outlining suitable materials for various optical applications, all of which were deposited in vacuum.

Over time, a number of novel approaches have been developed to create anti-reflection coatings. Some have inherent advantages and drawbacks, and are taken into consideration depending on the specifications and demands of the AR coating. Before discussing our research group's preferred deposition method (ISAM), I will briefly discuss other commonly used thin film deposition techniques. Furthermore, I will include some interesting research publications that utilize the method to create AR coatings. Finally, I will point out the strengths and weaknesses of each deposition method.

2.1.1 Physical Vapor Deposition (PVD)

Physical vapor deposition is perhaps the most widely known and used technique for controlled deposition on planar substrates. This technique involves the thermal evaporation and subsequent condensation of a material onto a surface. The birth of PVD is generally attributed to

Michael Faraday,[9] who in 1857, observed the formation of a metal film on a target after passing a high current through a metal wire. Integrating this technique into vacuum-controlled systems for significantly improved thin film uniformity was introduced by Nahrwold[10] in 1887. A number of variations of PVD have been developed over the years. They include:

Resistive heating – One of the most conventional PVD techniques. The material of interest for evaporation is loaded into or onto another conducting metal platform (i.e. spiral filament, crucible, etc.) with a higher melting temperature. Various platforms are available in consideration of the various metallic sources and target geometries.

Flash evaporation – The constituent is initially in a crushed or powder state. The powder is then carried along a chute and gradually dropped onto an extremely hot surface, resulting in rapid evaporation of the material. This technique can be extremely useful when deposition of alloyed films is desired.

Arc evaporation – The sample is placed between two electrodes of a conducting material. An arc is generated between the electrodes after creating a sufficiently high potential difference and bringing them close to each other.

Exploding-wire technique – The PVD method used by Faraday in 1857, the exploding-wire technique requires very high current densities to trigger very sudden heating in the wire.

Laser evaporation – By utilizing the high energy output of a pulsed laser and focusing it on the sample, rapid evaporation of material and very fast deposition rates are attainable with this technique. Another advantage of this technique is that the laser may be kept outside of the vacuum chamber.

Electron-bombardment heating – In this highly common technique, a filament is heated to supply electrons for bombardment. The electron beam is created by setting up a potential difference from the filament to the sample. A broad range of energies are possible by tuning the potential. Energy transfer from the energetic electrons to the sample causes it to form into a molten drop, and eventually evaporates onto the target (**Figure 2.1**).

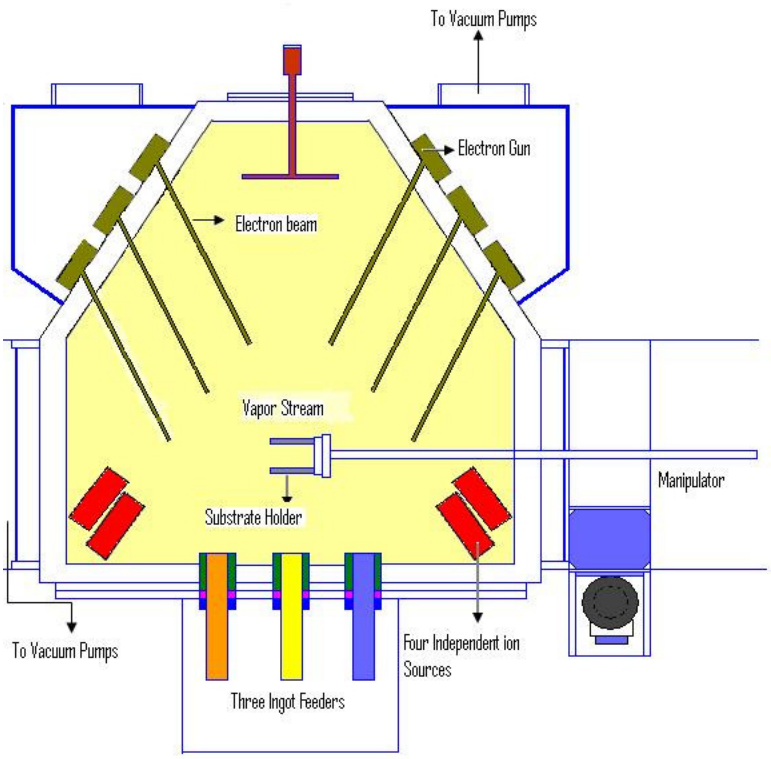

Figure 2.1 Electron beam PVD schematic. Image reproduced from http://en.wikipedia.org/wiki/Electron_beam_physical_vapor_deposition, and released to the public domain by author.

In the early 90s, Bosch provided theoretical[11] and computational[12] analyses regarding the impact of the substrate geometry (spherical and planar) on uniform deposition of materials by PVD. By implementing a more complex system design, including static correcting shutters, he found the thickness uniformity could be improved and double-sided coating of substrates could be executed more efficiently.

Maier-Komor et al.[13] used a complex e-beam PVD technique to deposit alternating layers of ^{6}LiF and ^{62}Ni onto silicon PIN diodes for detection of ultracold neutrons (UCNs). The ^{6}LiF was integrated into the film design in order to convert incident neutrons, but due to its positive optical potential (strongly reflects neutrons) it was assembled alternately with ^{62}Ni (negative optical potential). Balancing the optical potential reduced neutron reflectivity in the conversion layer and improved the UCN detection efficiency to 80%.

Mohite and coworkers[14] used e-beam PVD to deposit silicon oxynitride (SiO_XN_Y) films onto silicon wafers. They discovered that the reflectivity depended sensitively on the substrate

temperature during deposition, and attributed this to the corresponding change in the amount of silicon nitride (Si_3Ni_4) in the resultant films. They also varied the deposition times (0.5-2.5 minutes), which determined the wavelength at which minimal reflectance occurred. They found that the best optical properties could be attained when the substrate was heated to 350 °C, and SiO_XN_Y was evaporated for 1.5 minutes. This yielded minimal reflectance of 1.72% at a wavelength of 548 nm.

More recently, Xi and coworkers[15] used e-beam PVD to deposit SiO_2 and TiO_2 nanorods onto an AlN substrate at various angles to form an omnidirectional graded-index coating that essentially eliminated Fresnel reflection over a broad wavelength range. **Figure 2.2** is a cross-sectional SEM image showing the orientation of the nanorods and the effect that it has on the layer index of refraction. The bottom layer of TiO_2 nanorods has a refractive index that closely matches (n = 2.03) the AlN substrate (n = 2.05), while the topmost layer of silica nanorods (n = 1.05) is nearly the same as air (n = 1). With this configuration the reflectivity was kept below 0.3% for incident angles between 0° and 55° at λ = 632.8 nm.

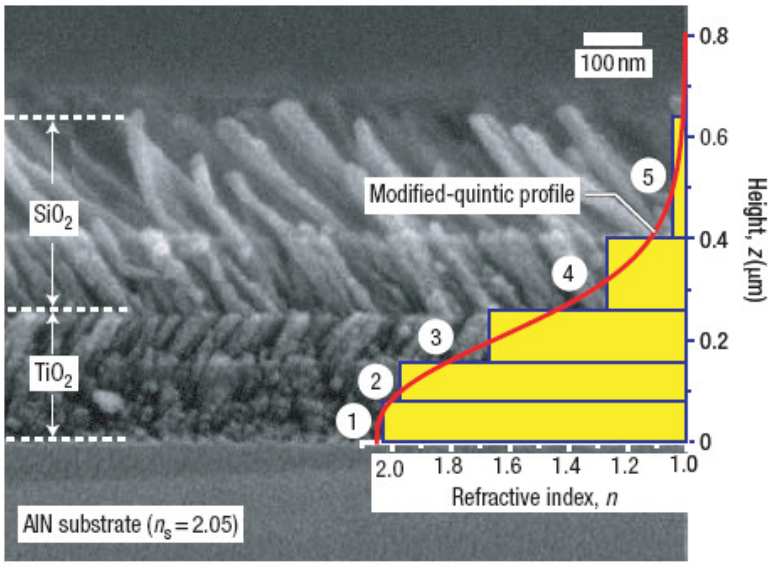

Figure 2.2 Cross-sectional SEM image of a graded-index film consisting of TiO_2 and SiO_2 nanorods with varying orientations with respect to the AlN substrate. The orientation and type of nanorod used in each layer is responsible for creating an index gradient from the substrate (n = 2.05) to air (n = 1). Reprinted with permission from Macmillan Publishers Ltd: [J. Q. Xi, M. F. Schubert, J. K. Kim et al., "Optical thin-film materials with low refractive index for broadband elimination of Fresnel reflection," Nature Photonics **1** (3), 176-179 (2007)].[15]

PVD is an effective deposition technique to produce robust quality coatings. Unfortunately, deposition is performed in vacuum and thus the size of the target surface is limited to the size of the vacuum chamber. Furthermore, significant modifications to the system design are necessary in order to achieve uniform thickness on curved surfaces, and may in fact not be possible in cases where the surface is too complex.

2.1.2 Chemical Methods

Chemical Vapor Deposition (CVD) – Chemical vapor deposition is the process of vaporizing volatile products and allowing them to react with other liquids, gases, or vapors at the substrate to form a thin film. A number of different reactions to deposit thin films can be classified under CVD; they include: pyrolysis, hydrogen reduction, halide disproportionation, transfer reactions, and polymerization. Furthermore, many different forms of CVD can be found in the literature. Among them are atmospheric and low-pressure CVD (APCVD and LPCVD, respectively), ultrahigh vacuum (UHVCVD), aerosol assisted (AACVD), microwave plasma-assisted (MPCVD), plasma-enhanced (PECVD),[16] hot wire (HWCVD), and rapid thermal (RTCVD).

Electrodeposition – In electrodeposition cations from a material are reduced by an electrical current and coated onto a surface. The circuit consists of an anode (source material) and a cathode (surface to be plated). The anode and cathode are immersed in an electrolyte solution, which permits migration of the dissolved anodic material to the cathode. Once at the solution/cathode interface, the metal ions are reduced and thus plate onto the cathode.

In 1972, Lou Hall prepared germanium and silicon AR coatings by CVD.[17] The effect of deposition parameters, such as germane concentration and growth temperature, on the surface topography, grain size, and infrared absorption were reported. He found the best germane and silicon films could be grown at temperature ranges of 325-375 °C and 525-575 °C, and concentration ranges of 1-2% and 1-1.5%, respectively.

Shibata made Si-oxide/Si-oxynitride (SiO_X/SiN_XO_Y) double layer AR coatings on Si solar cells using plasma CVD.[18] As shown in a previous paper,[19] he was able to vary the index of refraction for both SiO_X and SiN_XO_Y layers by changing the silane (N_2 balance) to O_2 and silane (N_2 balance) to silane (H_2 balance) gas mixing ratios during P-CVD, respectively.

Supreme control over the index of refraction made it possible to design an optical system for improved conversion efficiency (from 6.80 % to 10.96 %) of the solar cell.

More recently, Limmanee et al.[20] made hydrogenated amorphous silicon carbon nitride (a-SiCN:H) AR coatings on solar cells using hot-wire CVD, or HWCVD. They used hexamethyldisilazane (HMDS), a non-explosive and inexpensive material, and H_2 as a passivation layer to deposit the coatings onto silicon substrates. They reported on the structural, optical, electrical, and passivating properties of the coatings as a function of the deposition parameters. The prepared solar cells achieved a conversion efficiency of 13.7%.

CVD is a highly versatile way to quickly produce coatings with high purity and performance. Additionally, the film thickness can be tuned by limiting the chemical reaction time. Unfortunately, the process can be quite complex, and chemical reactions typically are facilitated at quite high temperatures. Like PVD, it is difficult to uniformly coat complex surfaces using this technique.

2.1.3 Spin Coating

Spin coating is a commonly used thin film deposition technique due to its relative simplicity and cost effectiveness. It is also an exceptionally quick way to deposit uniform films with fairly precise control over the thickness. To make a film by spin coating, one only needs to dissolve the film constituent (homogeneous or blend materials) in a volatile solvent, and drop cast the solution onto the substrate, which is fixed to a rotating stage (see **Figure 2.3**). The centrifugal force created by rotation spreads the material over the substrate surface. The film is left behind as the solvent rapidly evaporates. Finally, the films are typically heated in a vacuum oven for several hours to remove any remaining solvent. The thickness of the coating is tunable, and is governed by the rotational speed of the stage, the concentration of material in solvent, and the choice of solvent.

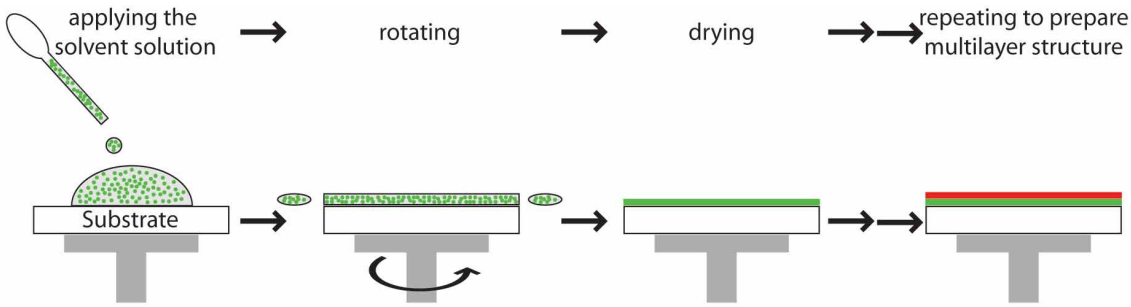

Figure 2.3 Procedure for thin film deposition by spin coating. Image used with permission from Paul Scherrer Institute (PSI) and reproduced from http://materials.web.psi.ch/Research/Thin_Films/Methods/Spin.htm.

Ishihara[21] and coworkers used spin coating to deposit double layers onto glass substrates. The first layer consisted of a highly conductive material such as antimony-doped tin oxides (ATO) or indium-tin oxides (ITO). The second layer consisted of porous silica particles with an approximate core diameter of 30 nm and a 10 nm rigid shell structure. The nanoparticles satisfied the need for a low refractive index layer to achieve minimal reflectance. As a result of the double layer, the film exhibited multifunctional properties. By adjusting the ATO/ITO concentration before spin coating, they were able to control the sheet resistance of the film. Similarly, they were able to control the refractive index of the 2nd layer by changing the load (wt %) of silica particles. As a consequence, they found they could minimize the reflectance and achieve broadband anti-reflective properties by increasing the load of silica particles, though above silica loading of 50% they reported fingerprints on the film were difficult to remove. Therefore, for practical purposes, they recommended silica loading below 50%. They also inspected the cross-section of the films by TEM and reported partial diffusion of the silica layer into the ITO. They hypothesized that this blend layer also provided a graded refractive index that further reduced light scattering.

Broadband reflectance was achieved by Kim[22] by spin coating three layers onto soda-lime glass. The three layers consisted of a bottom layer of ITO, porous silica, and an outermost layer of zinc-embedded silica nanoparticles. Zinc has a strong absorption peak around 250 nm, which decreases gradually into the visible spectrum. Because of this, there were two mechanisms responsible for broadband reflectance: Strong absorption of near visible light due to zinc, and control over the porosity of the outermost layer, which consisted of the zinc-embedded

silica nanoparticles. The second mechanism was important because too much absorption of light by zinc reduced the optical transparency, so this helped to somewhat counteract those transmission losses. They were able to demonstrate this effect by coating an ITO/SiO_2 double layer with a single non-absorbing layer of silica nanoparticles, and varying the refractive index of the outermost layer from 1.25 to 1.50. They found the reflectance significantly decreased at shorter wavelengths (400-600 nm) when the outer layer had a smaller refractive index.

Krogman[23] was able to spin coat colloidal dispersions of silica and ceria onto acrylic substrates. They also demonstrated control over the layer thicknesses and refractive index values by adjusting the concentration of the nanoparticles in each solution. The ceramic nanoparticles were used because of their hardness and abrasion resistance. They used the tumble test, which simulates abrasive wear and measures the increase in haze of the film. Haze is attributed to scattering of light due to scratches on the surface. They found that the abrasive resistance of the spin coated films compared favorably with coatings formed in vacuum-based systems.

Joo[24] and coworkers found an interesting way to create a nanoporous structure for minimal reflection of light. They synthesized a block copolymer consisting of polystyrene-*block*-poly(methyl methacrylate) (PS-*b*-PMMA), which was dissolved in toluene (2 ~ 3 wt %) and spin coated onto glass. By exposing the cast solution to UV (253.7 nm), they were able to cross-link the polystyrene but degrade the PMMA, which was removed by dipping the films in acetic acid. As a result the film became highly porous, and achieved reflectance less than 0.1%.

In 2007, Kim[25] synthesized the copolymer poly(methyl silsesquioxane) (PMSSQ) and mixed it with a photoacid generator (triphenylsulfonium trifluoromethanesulfonate) (PAG). The PMSSQ with 1 wt % of PAG was mixed with a pore-generating polymer, spin coated onto glass, exposed to UV, and finally heated at 420 °C for 1 hour. As a result, an organosilicate matrix with nanopores was realized. By varying the loading of the pore-generating polymer, they were able to tune the porosity, and consequently the refractive index, of the film. This enabled them to adjust the refractive index to 1.23 and achieve exceptionally high transmittance (> 99.8%) over a narrow wavelength range. By depositing a second layer with higher refractive index (1.45), they were able to create a broadband coating with transmittance above 98% over the visible spectrum.

More recently Chen[26] and coworkers prepared two inorganic/organic sols for bilayer deposition. These sols consisted of low (silica nanoparticles) and high (titania nanoparticles)

refractive index materials in order to make broadband coatings. They found after spin coating a bilayer of the high and low refractive index sols that they could reduce the reflection to 1%.

A key advantage of spin-coating is that relatively thick and uniform films can be rapidly deposited onto a substrate. However, the size of the coated surface is limited by the size of the rotating stage; hence spin-coating is not a practical deposition technique for large surfaces. It is also not a suitable method for deposition on curved surfaces.

2.1.4 Langmuir-Blodgett Technique

Langmuir-Blodgett (LB) films[27] are created when a solid surface is dipped into an aqueous solution containing an amphiphilic (hydrophilic head and hydrophobic tail, see **Figure 2.4**) organic material. Surfactants are the most common materials used for this application. As the substrate is removed from the solution a monolayer of surfactant is uniformly attached to the surface. Control of the film thickness is a trivial matter because the thickness of each monolayer is known. To determine the number of dip cycles for a desired film thickness, one only needs to divide the desired thickness by the monolayer thickness.

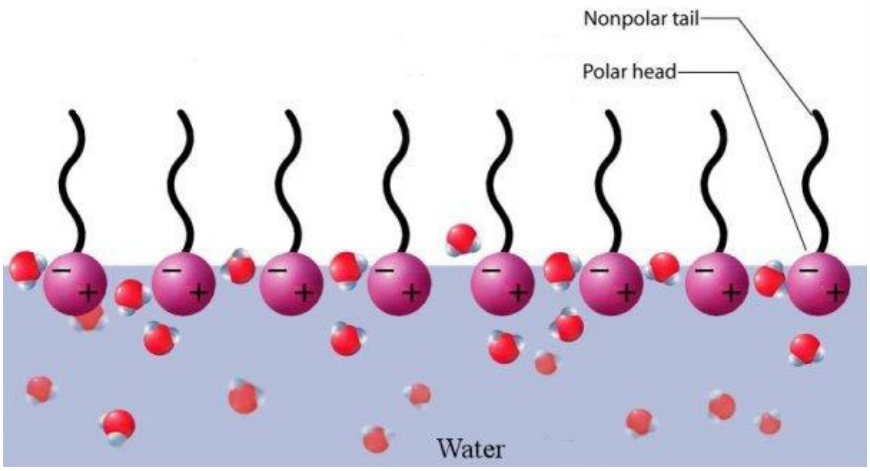

Figure 2.4 Representation of amphiphilic materials used in Langmuir-Blodgett deposition. The polar head of the constituent adsorbs onto the substrate while it is extracted from the aqueous solution. Image reproduced from http://en.wikipedia.org/wiki/Langmuir%E2%80%93Blodgett_film and released to the public domain by author.

In 1985, Buckner[28] used the LB technique to deposit monolayers of stearic acid onto silicon wafers ($n > 3.0$) to reduce reflection and consequently improve device efficiency. The refractive index of the stearic acid films was determined to be between 1.42 and 1.48. While this was not the ideal refractive index, a dramatic reduction in reflection was realized as the film provided an effective refractive index gradient from air to the substrate. Reflection was reduced to 5% by covering the silicon wafers with the stearic acid monolayers.

Deak[29] synthesized and modified the surface of silica nanoparticles using the Stöber method[30] for LB deposition onto glass. The synthesized nanoparticles were either 92 or 107 nm in diameter. Furthermore, they were initially hydrophilic, but could be made hydrophobic by silylating with trimethylsilyl-N,N-dimethylcarbamate (TDC). They explored the optical characteristics (refractive index, transmittance) of mono and multilayer films created with these nanoparticles. They found that the particle diameter and wettability had a significant influence on the transmission spectrum. They later[31] made complex LB films with varying silica nanoparticle sizes (20, 25, 50, and 80 nm respectively) in an effort to mitigate short wavelength light scattering. They accomplished this goal by constructing a film with a nanoparticle size gradient: with larger nanoparticles on the substrate (80 nm), smaller particles at the surface (20 nm), and intermediate particles in between (50 and 25 nm).

Nagy[32] and coworkers made multifunctional LB films by depositing SiO_2 and ZnO nanoparticles. The silica nanoparticles were prepared using the aforementioned Stöber method, while the ZnO nanoparticles were synthesized according to the methods of Meulenkamp,[33] and Seelig et al.[34] Naturally, the silica particles gave rise to anti-reflective properties, and the ZnO particles enhanced the photocatalytic activity of the film. In particular, this work highlighted one of the advantages of LB deposition, which is the ability to impart multi-functionality in films with thicknesses on the nanoscale.

Unlike the previously discussed techniques, LB films with highly ordered structure can be uniformly adsorbed onto large and complex surfaces, and can also be made at ambient temperature and pressure conditions. The films can be built up in a layer-by-layer fashion with distinct monolayers having relatively constant thickness. The monolayer buildup however is typically at the nanometer to sub-nanometer scale, and thus film fabrication can be very time consuming if thicker films are desired. Furthermore, LB films are composed of amphiphilic

molecules, and thus are limited to a small range of materials. Without access to a broad range of materials, it can be difficult to make LB films for a given application in which the properties and hence performance are competitive with films made using other techniques.

2.2 Ionic Self-Assembled Multilayer (ISAM) Deposition

Our research group does extensive research with ionic self-assembled multilayer (ISAM) deposition of thin films. In ISAM [also known as layer-by-layer (LbL) self-assembly] deposition, a charged substrate is dipped into positively and negatively charged aqueous solutions for rapid buildup of a multilayered structure. Adsorption is governed by the electrostatic attraction of oppositely charged constituents. **Figure 2.5** illustrates how ISAM deposition is achieved (please note in the figure that the surface is positively charged, however our surfaces are negatively charged using our cleaning method). Initially, the surface of a glass substrate is oxidized by any number of methods, including plasma etching, piranha, or RCA[35] cleaning. As a result the glass surface becomes functionalized with hydroxyl groups (OH^-), and is ready for ISAM deposition. The substrate is immersed in a positively charged solution, which may consist of polymers, colloids, etc. Electrostatic attraction drives the materials with positive charge toward the substrate until the charge on the surface is either saturated or screened by the deposited material. This is the first monolayer to be adsorbed onto the substrate. It is desirable to keep only the particles that have a strong electrostatic interaction with the surface, in other words, the particles closest to the surface. There may be additional particles on the monolayer that are partially screened from the negatively-charged surface, and thus would inevitably form a weak link in the multilayered structure. To prevent accumulation of these unwanted particles the substrate is subjected to a rinsing step with deionized water. The positively charged constituent typically has a uniform charge distribution consisting of a specific functional group. Since one side of the polymer/colloid/etc. making up the monolayer is attached to the substrate, the other side has available positive charge. As a result, the charge of the new surface is reversed from negative to positive. At this point, the substrate is immersed into the negatively charged solution. The constituents of this solution are adsorbed onto the positively charged monolayer. Adsorption is complete once the charge on the monolayer is quenched. Once again the weakly interacting particles are rinsed away with deionized water. The resulting deposition of two

monolayers is referred to as a bilayer. After one bilayer is completed, the procedure may be repeated as many times as needed. It is typical practice to construct ISAM films with just two oppositely charged constituents, though it is possible to include as many materials as desired. Herein lays one of the key advantages of ISAM deposition, because the technique can easily incorporate species with a vast array of properties to create a multi-functional structure. Furthermore, the effect of these properties can be tuned by adjusting either the film density or thickness. A number of factors govern the density and thickness of ISAM layers, including the pH and concentration of the aqueous solutions, the size of the ionic constituents, and the length of time the substrate is immersed in the solutions. Low cost ISAM films can be easily deposited at room temperature and ambient pressure conditions onto large and complex surfaces with excellent uniformity, unlike many of the techniques discussed above.

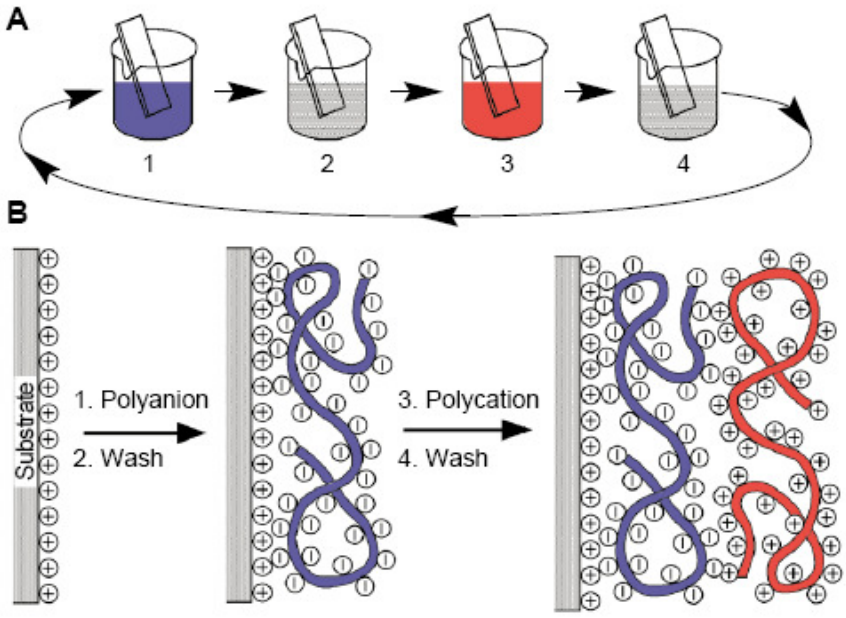

Figure 2.5 Schematic of the film deposition process using slides and beakers (**A**). Steps 1 and 3 represent the adsorption of a polyanion and polycation, respectively, and steps 2 and 4 are washing steps. (**B**) Simplest molecular picture of the first two adsorption steps, depicting film deposition starting with a positively charged substrate. From: [G. Decher, "Fuzzy nanoassemblies: Toward layered polymeric multicomposites," Science **277** (5330), 1232-1237 (1997)].[41] Reprinted with permission from AAAS.

The birth of ISAM deposition is generally credited to R. K. Iler. In 1966,[36] he deposited colloidal silica particles (15-100 nm in size) onto glass surfaces and studied the optical interference effects in order to assess the film thickness. Furthermore, he was able to correlate the estimated film thickness with the average particle size and extend the principle to polyions much smaller in size. Regardless of his intention, it is considered to be the first published work on AR coatings deposited by the ISAM technique.

For some reason, ISAM deposition was largely disregarded by the scientific community after Iler's work until the early nineties. It was at this point when other ISAM pioneers, such as Gero Decher and Yuri Lvov, began their work on ultrathin organic films. In 1992, Decher[37] reported on the buildup of polyelectrolyte films using ISAM deposition. In his study, he used polystyrene sulfonate sodium salt (PSS, polyanion), polyvinylsulfate potassium salt (polyanion), poly-4-vinylbenzyl-(*N*-*N*-diethyl-*N*-methyl-)-ammonium iodide (polycation), and polyallylamine hydrochloride (PAH, polycation). He deposited alternating layers of PSS and poly-4-vinylbenzyl-(*N*-*N*-diethyl-*N*-methyl-)-ammonium iodide and monitored the optical absorbance of the phenyl chromophores at 225 nm. The absorbance increased linearly with the number of deposited layers and showed that ordered assembly of polyelectrolytes was achievable using ISAM deposition. Decher also followed the buildup of polymer layers consisting of PAH and PSS using small angle X-ray scattering (SAXS). The pattern of the Kiesseg fringes changed with the number of PAH/PSS bilayers. The distance between neighboring fringes permitted calculation of the film thickness. The absorbance was also measured for the PAH/PSS films and was plotted in conjunction with the calculated film thickness from SAXS. Both methods confirmed uniform adsorption of the polyelectrolytes up to 39 bilayers, or 43.5 nm as calculated by SAXS. Later,[38] he showed that multilayered films possessed an organized structure using two methods. The first was to create repeat units of $[ABCB]_n$, where A, B, and C were PSS, poly-(1-(4-(3-carboxy-4-hydroxyphenylazo)-benzenesulphonamido)-1,2-ethanediyl) sodium salt (PAZO), and PAH respectively, and "n" refers to the total number of repeat units. Hence the film was comprised of consecutively adsorbed layers of $[PSS/PAH/PAZO/PAH]_n$. These "superlattice" structures gave rise to Bragg peaks in X-ray reflectivity. The spacing of the repeat units was determined to be 9.34 nm. The second method was to dry the film after given deposition intervals of $[AB]_n$ films. Typically, films are kept wet during the ISAM process, but if it is dried the polymers at the surface are forced to reorganize to preserve electroneutrality.

This reorganization reduced the surface roughness, which if done at regular adsorption intervals can drastically alter the composition of the ISAM film. Lvov also constructed ordered superlattice films[39] by combining the LB and ISAM techniques. The glass substrates were first coated with an ISAM precursor layer consisting of poly(vinyl sulfate) (PVS) and PAH to better anchor the film to the surface. The assembly and structural behavior of PVS/PAH layers had been addressed[40] prior to this work. Next, a bilayer of the amphiphile dimethyldioctadecylammonium bromide (DODAB), which was complexed with PVS, was deposited onto the precursor film using the LB method and followed by PVS/PAH ISAM layers. The number of PVS/PAH bilayers between DODAB complex was varied from 0-3 to compare the order of the superlattice structure, which was achieved by measuring small-angle X-ray reflectivity (SAXR) of the films. The superlattice correlation was diminished with added PVS/PAH interlayers, and was attributed to interpenetration of adjacent polymer layers. The potential benefits of creating nanoarchitectures with interpenetrating polymers were later discussed in detail by Decher.[41] The order of the films, however, was improved by heating the films between 70 and 80 °C. Heating above 80 °C resulted in a loss of order and was associated with a phase transition in DODAB (85 °C in bulk). Similar experiments utilizing SAXR were conducted to study the molecular order of polyelectrolytes with DNA[42] and the Carnation Mottle virus.[43] The DNA/polyelectrolyte films possessed higher order than the ones with the virus, but this is because the virus is spherical and rigid. Despite the fact that the DNA is rigid in comparison to the polymer it is assembled with, its shape allowed it to easily blend into an ordered structure. Regardless, ISAM deposition of both the DNA and virus with oppositely-charged polymers was possible.

The works of Decher and Lvov did much to spark and cultivate a general interest in LbL assembly. They were also able to confirm through their various experiments that ISAM could be utilized to include a broad class of materials for ordered deposition at the nanoscale. Around this time much was not understood regarding the control of polymer deposition using the ISAM technique. In 1997 Tsukruk et al.[44] reported on the formation of the first monolayer and bilayer of PSS and PAH onto a charged substrate as a function of dipping time in the aqueous solutions. In their experiments they did not adjust the pH values of PSS or PAH. They discovered for shorter dipping times (< 5 minutes) that the first adsorbed layer of PSS onto the oppositely-charged SAM aggregated into islands located at regions of high charge concentration, such as

holes, scratches, edges, etc. The PSS chains were tethered to these points and were not given sufficient time to equilibrate. As a result the islands of coiled PSS were as thick as 4 nm. In contrast, longer dipping times (> 10 minutes) allowed the chains to spread over the surface, increasing the island diameter to 50 nm, and decreasing their thickness to 1-1.5 nm. The surface became a smooth monolayer as a result of the increased dipping time. Subsequent deposition of PAH onto the smooth PSS monolayer exhibited similar behavior. Yoo[45] examined the effect of the aqueous polymer solution pH on the thickness of PAH/PAA [poly(acrylic acid)] layers. PAH and PAA were selected because they are weak polyelectrolytes, meaning that their linear charge density can be varied by simple adjustments of the solution pH. In this particular study the different pH conditions for both PAH and PAA were 2.5, 3.5, and 4.5; with nine permutations in all. Yoo found that the pH conditions significantly affected the total film thickness. The thickest films had PAH/PAA pH conditions of 4.5/2.5. Furthermore, the thickness of the adsorbed layer did not depend on the thickness or level of interpenetration of the previously adsorbed layer. Yoo also found that the surface wettability could be tuned not only by pH adjustment of the aqueous solutions, but also by the choice of polymer on the outermost layer of the film. The range of measured contact angles varied from essentially zero to as high as 50° by changing these parameters. A far more comprehensive investigation[46] of the pH dependence of these polymers on film morphology and thickness was carried out by Shiratori. This pH range was expanded to include all permutations of 2.5, 3.5, 4.5, 5.5, 6.5, 7.5, 8.5, and 9 for each polymer (**Figure 2.6, left**). Shiratori plotted the measured thickness of each PAH and PAA monolayer when their pH conditions were the same (i.e., the diagonal of the 2X2 matrix in parameter space, **Figure 2.6, right**). The dependence of PAH/PAA adsorption on pH was dramatically different and as a result was divided into four regions. As noted by the authors, PAA is 20-30 % ionized at a pH of 2.5, and fully ionized at a pH of 6.5; PAH is fully ionized over most of this range until the pH is increased above 7. In region I (pH = 2.5-4.5), the thicknesses of the PAH and PAA layers are dependent on the degree of ionization of the PAA chains. As a result, the thickness of the PAA layer decreases as the degree of ionization increases. The amount of PAH increases to compensate for the increased charge of the underlying PAA layer and as a consequence the thickness of the PAH layer increases. In region III (pH = 6-7.5) both PAH and PAA are fully ionized and thus adsorb as very thin, strongly bound layers. The thickness profile of PAH and PAA layers in regions II (pH = 4.5-6) and IV (pH = 7.5-9) has very abrupt features. A common

explanation can be made to explain the observed phenomenon. In region II, the PAH chains are fully ionized and adsorb with PAA chains that are almost completely ionized. In region IV, the reverse is true for PAA and PAH. The adsorption of fully ionized chains with others that are almost completely charged yields unusually thick layers, as shown in the plot. As a result a sharp transition in layer thickness is observed from region II to III and from III to IV.

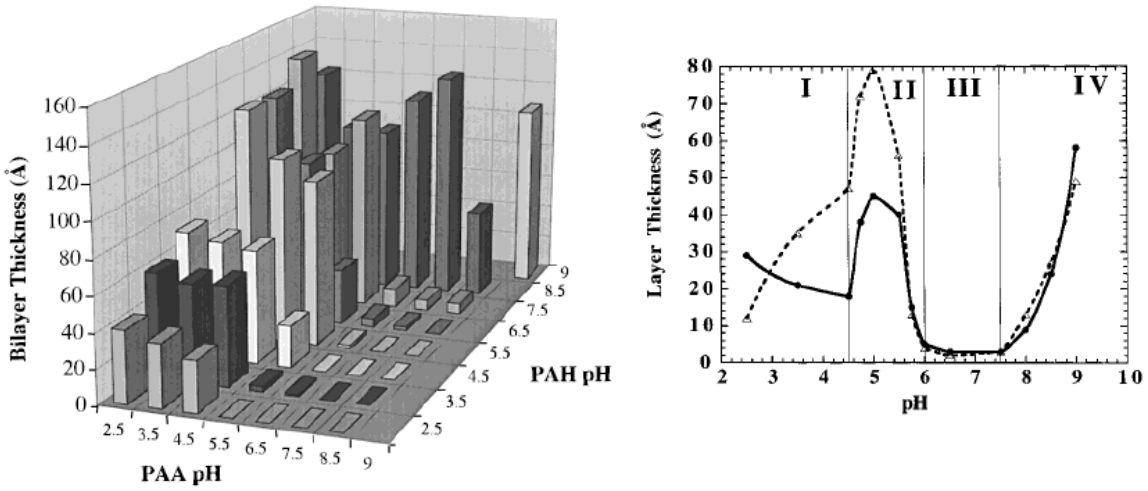

Figure 2.6 PAH/PAA bilayer thickness (in angstroms) as a function of the ionic solution pH values (left), and the monolayer thicknesses of PAH and PAA with respect to the solution pH (right). The solid line represents the PAA layer thickness, and the dashed line is the PAH layer thickness. Reprinted with permission from: [S. S. Shiratori and M. F. Rubner, "pH-dependent thickness behavior of sequentially adsorbed layers of weak polyelectrolytes," Macromolecules **33** (11), 4213-4219 (2000)].[46] Copyright 2000 American Chemical Society.

Dubas[47] looked at a number of factors that were presumed to affect film growth, such as salt type and concentration, solvent quantity, deposition time, and polymer concentration. Alternating ISAM layers were made from PSS and poly(diallyldimethylammonium chloride) (PDADMAC). He discovered that each of the above factors affected multilayer growth, but the most critical factor was the salt concentration, which had an almost linear correlation with the film thickness. Apparently, the presence of salt counterions enabled significant charge reversal at the surface which occurred due to multilayer bulk compensation. The polymer molecular weight was also found to influence film thickness.[48]

ISAM polymer films have also been designed to function as anti-reflection coatings. Hiller et al.[49] made PAH/PAA (pH = 8.5/3.5) coatings and exposed them to an acidic water solution (pH = 1.8). This imparted to the polymer film a tunable porosity, as it reversibly swelled and de-swelled with subsequent immersion and re-immersion into the acidic solution. This control made it possible to adjust the coating index of refraction such that transmittance as high as 99.99% could be attained. When the desired refractive index was found, the film could be stabilized against pH-induced morphological changes by thermal cross-linking. Fujita and Shiratori essentially repeated this work,[50] but showed that the thermal treatment made these coatings waterproof. Later they also demonstrated that the swelling by acidic treatment could be used to drastically reduce deposition times of PAH/PAA films.[51]

The research conducted by the Heflin group at Virginia Tech clearly demonstrates the versatility of ISAM deposition in thin film fabrication. Ionic species have been deposited onto long period gratings (LPGs) with precise control over the film thickness and index of refraction as a means to fine tune the grating properties.[52] The deposited film provided a functional surface to demonstrate biotin-streptavidin binding,[53] making the LPGs an attractive option for use as a highly sensitive biosensor. Layer-by-layer self-assembly has also been used to create electrochromic devices with high contrast and very fast switching speeds. Among the materials used in ISAM deposition for their electrochromic properties were Ruthenium Purple[54] and viologen-bridged polysilesquioxane nanoparticles.[55] In a separate paper[56] single-wall carbon nanotubes (SWCNT) were used as the device electrode. Layer-by-layer of PAH and poly[2-(3-thienyl) ethoxy-4-butylsulfonate] (PTEBS) onto the SWCNT electrode reduced the surface roughness, decreased the impedance, and lastly increased the efficiency of ion transport. In other research ISAM films consisting of PAH and poly[1-4-(3-carboxy-4-hydroxyphenylazo) benzenesulfonamido]-1,2-ethanediyl, sodium salt] (PCBS) were patterned using two different techniques: (1) nanoimprint lithography (NIL), and (2) a combination of electron beam lithography and reactive ion etching.[57] NIL of the PAH/PCBS films produced periodic 2-D structures consisting of holes as well as Bragg gratings. Holes were patterned using the e-beam lithography and reactive ion etching technique. Second harmonic generation (SHG) analysis showed that the nanoimprinting processes did not adversely affect the nonlinear optical (NLO) properties of the film, meaning that the materials are well-suited for nanoimprinting of nonlinear optical photonic structures. Heflin has also used ISAM deposition to develop high quality NLO

films. In 1999, he showed that the absorbance and second harmonic intensity of ISAM films consisting of Poly S-119 (polymeric dye) and PCBS demonstrated linear and quadratic dependences on the number of bilayers, respectively.[58] These films also possessed excellent thermal stability, as their second-order susceptibility $\chi^{(2)}$ decreased by 25% when they were heated to 150 °C. Remarkably, the $\chi^{(2)}$ returned to its initial value when the film was cooled back to room temperature. Lastly the coatings demonstrated excellent temporal stability as the measured $\chi^{(2)}$ did not decrease over a period of more than one year. Unfortunately, the polar ordering of these films was not optimal, so Heflin and coworkers later[59] used a hybrid covalent/ISAM assembly technique to address this problem. They used PAH and Procion Brown MX-GRN for the hybrid assembly process. PAH was adsorbed electrostatically to the film, while polar ordering was achieved by covalent adsorption of the dichlorotriazine end of Procion Brown (PB) with the amine groups of PAH. The sulfonate groups located at the opposite end of PB were a suitable partner for electrostatic interaction with the amine groups of the next adsorbed PAH layer. The higher ordering of these films significantly improved their NLO properties. As a result, the film's electro-optic coefficient was 50% of the value for lithium niobate films. Similarly to the Poly S-119/PCBS films, the PAH/PB films demonstrated excellent thermal and temporal stability. More recently,[60] very thick ISAM films (600 bilayers, 740 nm thickness) consisting of PAH and PCBS were made. The goal of the study was to determine the effect of processing conditions, such as deposition and rinsing times, and solution pH values, on the long range polar ordering of these films. The authors found that adjustment of the pH conditions led to a trade-off between the thickness per bilayer and homogeneity of the film.

2.3 ISAM Films Incorporating Spherical Nanoparticles

The first reported use of nanoparticles in ISAM films was by Iler,[36] as his pioneering work included colloidal silica. The rebirth of ISAM deposition in the early 90s saw much attention directed toward the assembly of organic materials, but soon afterward the benefits of fabricating polyelectrolyte/nanoparticle films was realized. Nicholas Kotov verified through spectroscopy, TEM, AFM, and X-ray diffraction that ordered nanostructured films could be assembled containing a polyelectrolyte and various charged semiconducting nanoparticles.[61]

Lvov, who had previously demonstrated ordered assembly of polyelectrolytes with proteins (spherical particles),[62] began to characterize the adsorption of silica nanoparticles with polymers. In 1997 he used Quartz Crystal Microbalance (QCM) to follow the assembly of silica nanoparticles with PDDA as a function of SiO_2 size, concentration in solution, and ionic strength.[63] He reported stepwise growth in all cases, but found that the adsorption could be improved using higher concentrations of silica nanoparticles and ionic strength. Additionally, he commented on the pairing tendencies of polyions with charged nanoparticles. For the given case, PDDA has a much higher charge density than a silica nanoparticle. To illustrate this, Lvov created PDDA/SiO_2 NP complexes in bulk solution to determine the mixing ratio that yielded maximum flocculation, which was presumed to be the point of neutrality. This ratio was determined to be SiO_2 NP/PDDA = 64 (g/g). For the multilayer films of PDDA/SiO_2 NPs, however, the mass ratio of SiO_2 to PDDA varied anywhere between 13 and 31 (depending on the ionic strength of solution). This was significantly smaller than the mass ratio of the complex solution, meaning that excess charge was present on PDDA. This was inevitably balanced by Cl^- counterions, but the fixed charge distribution on the silica nanoparticles means that long distance ion pairs were formed with the polycation (**Figure 2.7**). Contact ion pairs were formed at the top and bottom surfaces of the nanoparticle, but the discrepancy in charge density between the nanoparticles and polymer chains, coupled with the fixed charge distribution on the nanoparticles ensured some fraction of charge pairs were not in direct contact. Contrast this to ISAM films containing only polymers, where the charge pairs are almost exclusively in contact with each other.

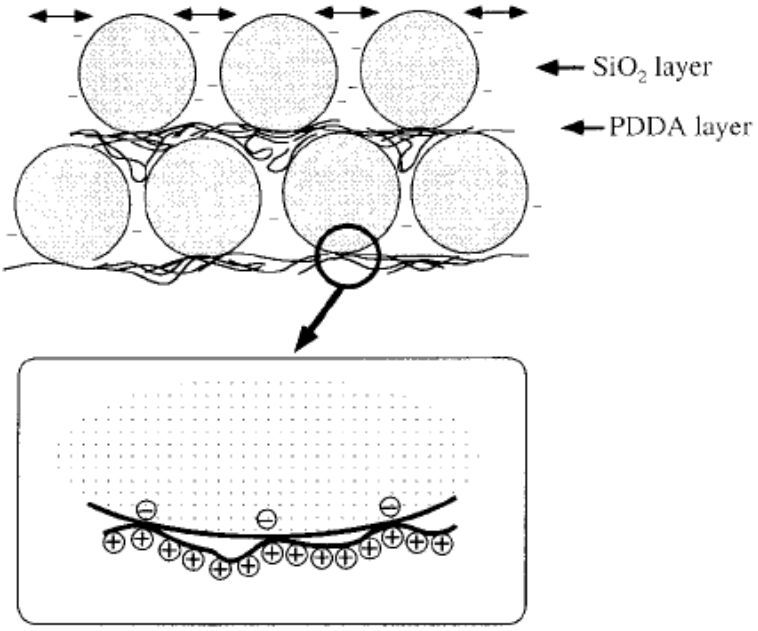

Figure 2.7 Illustration of contact and long distance ion pairs between PDDA and negatively charged silica nanoparticles. The charge is evenly spread over the silica nanoparticles and as a result the charge at locations not in contact with PDDA will form long distance pairs. Reprinted with permission from: [Y. Lvov, K. Ariga, M. Onda et al., "Alternate assembly of ordered multilayers of SiO2 and other nanoparticles and polyions," Langmuir **13** (23), 6195-6203 (1997)].[60] Copyright 1997 American Chemical Society.

Lvov also showed that silica nanoparticle monolayers could be rapidly adsorbed in LbL assembly.[64] In the experiment, 45 nm SiO_2 NPs were deposited along with PDDA on electrodes of a QCM resonator. The films were dried between PDDA and silica nanoparticle adsorption steps. When doing so, the rate of adsorption increased to the point that uniform monolayers of PDDA and SiO_2 NPs could be deposited within 20 and 2 seconds, respectively. Conformational changes in adsorbed PDDA were responsible for the relatively longer dipping times. The silica nanoparticles were well-packed as evidenced by ellipsometric data, which also revealed the volume composition of the film to be 60% SiO_2 + 10% PDDA + 30% void. This was in good agreement with the theoretical dense-packing coefficient for spheres (0.63). The excellent order and surface coverage afforded by silica nanoparticles deposited using the ISAM method made it possible to make AR coatings with just a monolayer.[65] Hayes[66] followed the adsorption of silica nanoparticles onto silicon wafers modified with an aminopropylsilane, as a function of the

particle size and electrolyte concentration. The adsorption was monitored by optical reflectometry, and streaming potential was used to measure the ionic strength at the silicon surface. He found that the initial rate of particle adsorption was smaller for larger particles, while surface coverage could be improved with higher polyelectrolyte concentrations. All observations he made regarding adsorbed silica on silicon surfaces treated with aminopropylsilane were consistent with surfaces coated with polycations.[67] Ostrander et al. commented on two different modes of film growth for yttrium iron garnet (YIG) nanoparticles assembled with PDDA.[68] The first mode was described as the "adsorption of densely packed adsorption layers (normal growth mode)", and the second was "in-plane growth of isolated particle domains (lateral expansion mode)". They determined that the mode of growth was governed not by the substrate, but by particle/particle and particle/polyelectrolyte interactions. Furthermore, they found they could switch between growth modes. The YIG nanoparticles typically formed large domains and expanded laterally. When they were coated with 3-aminopropyl trimethoxysilane however they followed the normal growth mode.

A number of studies have been conducted on the effect of nanoparticle size on multilayer formation and the resulting optical properties of those films. Bogdanovic et al.[69] explored the formation of ISAM films containing 4.6, 4.9, and 12 nm silica nanoparticles by means of *in situ* ellipsometry. The nanoparticles were assembled with a copolymer of acrylamide (AM) and (3-methacrylamide) propyl trimethylammonium chloride (MAPTAC). Regular adsorption of AM-MAPTAC/SiO_2 NPs was observed for each case, but the buildup was much more rapid for the larger nanoparticle films. As a consequence, the films containing larger nanoparticles were bulkier with a comparatively rougher surface. Furthermore, they found that using smaller nanoparticles enabled them to form dense silica layers as evidenced by the relatively larger surface coverage after one deposited bilayer. Since the smaller nanoparticles form dense layers, however, the refractive index of the resultant film was higher, and had a corresponding value above 1.39 for the 4.6 nm NPs. In comparison, the refractive index of films containing 12 nm NPs was never greater than 1.36. Ahn et al.[70] studied the effect of particle size on monolayer formation using polystyrene (PS) nanoparticles. Particle diameters included 0.14, 0.2, 0.5, 1, 2, 3, 4, 5, 8, and 10 microns. They observed a different trend then Bogdanovic however, as the surface coverage was improved with larger particles. This is because they were using micron-sized particles, while the particles used by Bogdanovic were far smaller. The large particles

were rearranged into 2-D structures by virtue of strong lateral capillary forces that overcame the electrostatic repulsion of neighboring particles. They reported that the capillary force did not play a role in particle rearrangement for the smallest particles (140 nm). Since Bogdanovic used particles more than an order of magnitude smaller, it is reasonable to assume the lateral capillary forces played no role in monolayer formation. Ahn also showed through measurements of total and specular transmittance that three different optical phenomena occurred as a function of the particle size: (1) anti-reflection when the particle diameter ($D_{particle}$) was around a quarter of the wavelength of incident light ($D_{particle} \sim \lambda_{vis}/4$), (2) diffraction when $D_{particle}$ was equivalent to the wavelength of the incident beam ($D_{particle} \sim \lambda_{vis}$), and (3) diffusive scattering when $D_{particle}$ was larger than the wavelength of incident light ($D_{particle} > \lambda_{vis}$). Finally, Yancey et al.[71] reported on the influence of silica nanoparticle diameter (15, 45, and 85 nm) on Rayleigh scattering in AR coatings. In this work, they postulated that the scattering could be attributed to surface roughness or inhomogeneities in the bulk film. They discovered that the Rayleigh scattering was independent of the film thickness, and as a result they concluded it was primarily a surface effect. Like Bogdanovic they also found that films consisting of smaller nanoparticles (15 nm diameter) were too densely packed, and thus could not achieve optimal AR properties. The 45 and 85 nm particles on the other hand provided a fairly porous structure, but suffered from some surface scattering associated with increased roughness. They determined that films incorporating 45 nm particles were a good compromise to balance surface scattering with porosity.

The Rubner group at MIT was able to demonstrate the multi-functionality of silica nanoparticle films with superhydrophilic and superhydrophobic surfaces. Cebeci[72] made PAH/SiO_2 NP films and evaluated the hydrophilicity as a function of the nanoparticle size, silica and polymer concentrations and pH values in solution, and the number of assembled bilayers. Silica nanoparticles with diameters of 7, 12, and 22 nm were used for the comparison. Cebeci found that the superhydrophilic behavior was observed only after 8 bilayers, and so it was not possible to create high quality coatings using the larger nanoparticles. As a result, the 7 nm particles were used for the remainder of the study. Stable transparent PAH/SiO_2 NP films with superhydrophilicity were made with PAH and nanoparticle pH ranges of 4-9 and 7.5-9, respectively. Films with more than 14 bilayers exhibited the best hydrophilicity, as it took approximately 0.16 seconds to completely wet (i.e., contact angle < 5 degrees) the surface with a drop of water. Superhydrophobicity was also achieved using silica nanoparticles[73] by mimicking

the self-cleaning properties of the lotus plant. This was achieved by controlling the placement and level of aggregation of differently sized nanoparticles throughout the film. In total, the film contained three distinct ISAM regions. The first was an adhesive layer of polymers [PAH and poly(sodium 4-styrenesulfonate)] deposited onto glass. Secondly, PAH was alternately deposited with a blend solution of silica nanoparticles with different sizes (50 and 20 nm). Next, layers of PAH and 20 nm NPs were deposited to create a smoother surface on top of the larger aggregates. Finally, the film was capped with trichloro(1H,1H,2H,2H-perfluorooctyl) silane by CVD. They reported advancing contact angles as large as 160°, and a maximum transmittance of 94.6%.

Daeyeon Lee published several papers involving ISAM deposition of positively and negatively charged colloids. In 2006 he made films containing positively charged titania (7 nm diameter) and negatively charged silica nanoparticles (7 and 22 nm).[74] A primary reason to include TiO_2 NPs in ISAM deposition is that it has a relatively high index of refraction, making it suitable to create broadband AR coatings. The transmittance of 5 and 6 bilayer TiO_2/SiO_2 NP films was measured to be greater than 97% from 500-800 nm. Next, Lee looked at the influence of solution pH conditions of TiO_2 and SiO_2 on multilayer formation and properties.[75] He found that the film thickness per deposited bilayer depended sensitively on the pH conditions (**Figure 2.8**). The leftmost image in **Figure 2.8** is a plot of the film thickness versus the number of deposited bilayers for samples made from a TiO_2 solution with fixed pH (3), and SiO_2 solutions with varying pH (2, 3, 4, and 5 respectively). The plot shows a dramatic improvement in adsorption when the pH values of both colloids are at 3. A matrix of pH values ranging from 2-5 for SiO_2 and 2-4 for TiO_2 were tested in order to determine optimal assembly parameters. This is illustrated in **Figure 2.8 (right)**, which shows the bilayer thickness for all permutations of pH. Maximum adsorption occurs when the pH values of TiO_2 and SiO_2 are kept at 4 and 3, respectively. In the same year, Lee reported on the multilayer growth of ISAM films consisting entirely of silica nanoparticles.[76] Negatively charged SiO_2 nanoparticles of different sizes (8.6, 15.4, and 24.2 nm diameter) were deposited with aminopropyl-functionalized SiO_2 (16.2 nm). The ζ-potential for each of the negatively charged nanoparticles depended on the pH of the solution over a pH range of 2-7.5. The ζ-potential of the AP-SiO_2 NPs on the other hand remained fairly constant over a pH range of 2-6.5. Therefore, Lee was able to find the optimal adsorption with respect to the normalized ζ-potential (**Figure 2.9**). In the plot, the average

bilayer thickness "h" and ζ-potential "z" were normalized against the maximum layer thickness of each system "h_0" and the ζ-potential of the AP-SiO_2 NPs "z_0", respectively. The curves corresponding to the different particle sizes matched up remarkably well, and indicate that maximum adsorption occurred when the ζ-potential for each of the negatively charged particles was around $-0.6z_0$. Lee also found that the film porosity was not significantly affected by the difference in particle sizes.

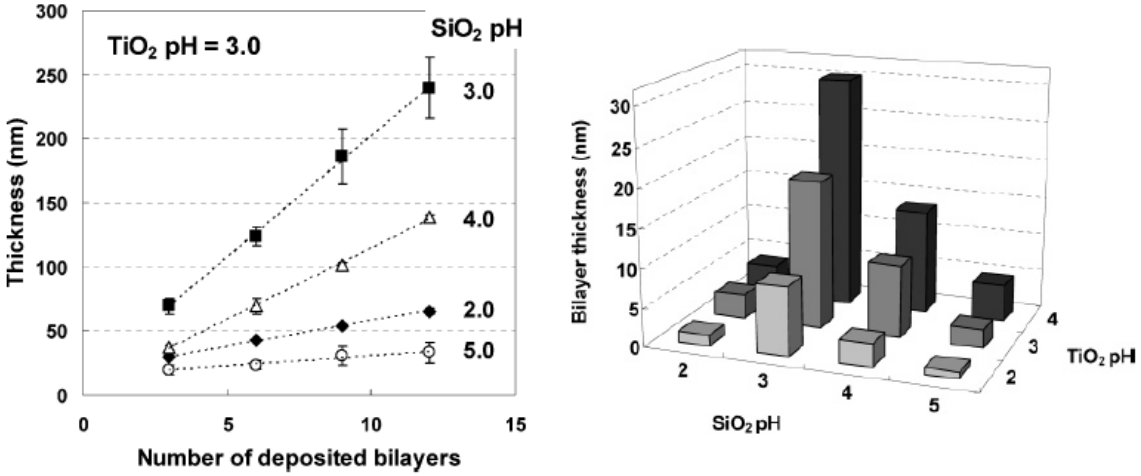

Figure 2.8 Increase in layer thickness (nm) of TiO_2/SiO_2 NP films as a function of the number of deposited bilayers while the TiO_2 solution pH was fixed at 3, and the SiO_2 solution pH varied (left). A complete matrix of TiO_2/SiO_2 solution pH values (right) was explored for their effect on the bilayer thickness (nm). Reprinted with permission from: [D. Lee, D. Omolade, R. E. Cohen et al., "pH-Dependent structure and properties of TiO2/SiO2 nanoparticle multilayer thin films," Chemistry of Materials **19** (6), 1427-1433 (2007)].[72] Copyright 2007 American Chemical Society.

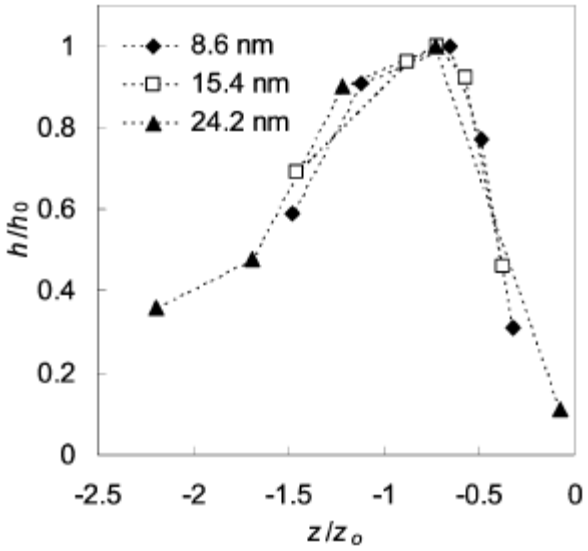

Figure 2.9 Normalized average bilayer thickness as a function of normalized ζ-potential for each multilayer system. The average bilayer thickness (h) and ζ-potential of the negatively charged particles (z) were normalized to the maximum bilayer thickness of each system (h_0) and the ζ-potential of the positively charged silica nanoparticles (z_0; determined in the pH range between 2 and 6), respectively. Reprinted with permission from: [D. Lee, Z. Gemici, M. F. Rubner et al., "Multilayers of oppositely charged SiO2 nanoparticles: Effect of surface charge on multilayer assembly," Langmuir **23** (17), 8833-8837 (2007)].[73] Copyright 2007 American Chemical Society.

Spherical nanoparticles can also be directly surface-functionalized by ISAM deposition of polyelectrolytes and smaller nanoparticles by simply mixing them in the colloidal suspension, as demonstrated by Sukhorukov,[77] Caruso,[78] and Radzuik.[79] In general, their work illuminated one of the potential benefits of incorporating ISAM deposition onto nanoparticle surfaces, namely creating hollow microcapsules provided assembly was performed on soluble cores. They found the molecular weight of the polyelectrolytes could be adjusted to design a capsule with a permeable (low molecular weight) or nonpermeable (high molecular weight) membrane. This level of control made macromolecular loading into the shell for drug delivery a definite possibility. Additionally, they showed that insoluble NPs could be stabilized in solution and their surface properties changed by simple addition of polymers with different functional groups. Further details concerning these published articles and their relevance to the presented research are contained in **Chapter 4**.

[1] Lord Rayleigh, "On the intensity of light reflected from certain surfaces at nearly perpendicular incidence," Proceedings of the Royal Society of London (41), 275-294 (1886).

[2] Ogden Nicholas Rood, American Journal of Science **49** (1870).

[3] G. Bauer, "Optical absorption constants of alkali halide crystals in the region of the ultra-violet characteristic frequencies," Annalen der Physik **19** (4), 434-464 (1934).

[4] http://www.companyseven.com/zeiss/history.html

[5] L. Holland and E. W. Van Dam, "Wear Resistance of Magnesium Fluoride Films on Glass," journal of the Optical Society of America **46** (10), 773-777 (1956).

[6] J. T. Cox, "Antireflection coatings for Germanium and Silicon in the Infrared," Journal of the Optical Society of America **48** (10), 677-680 (1958); W. A. Farber, "Improvement in infrared detector performance through use of antireflection film," Journal of the Optical Society of America **51** (1), 115 (1961).

[7] Roland Jacobsson, "Evaporated inhomogeneous thin films," Appl. Optics **5** (1), 29-34 (1966).

[8] G. Hass, E. Ritter, "Optical film materials and their applications," Journal of Vacuum Science & Technology **4** (2), 71-79 (1967).

[9] Michael Faraday, "The Bakerian Lecture: Experimental Relations of Gold (and Other Metals) to Light," Phil. Trans. Roy. Soc. **147**, 145-181 (1857).

[10] R. Nahrwold, Wied. Ann. **31**, 546 (1887).

[11] S. Bosch, "Geometrical limiting performances of a thermal evaporation PVD unit for lens coating," Proceedings of SPIE-The International Society for Optical Engineering, v 1270, 292-298 (1990).

[12] S. Bosch, "Computer-aided procedure for optimization of layer thickness uniformity in thermal evaporation physical vapor deposition chambers for lens coating," Journal of Vacuum Science & Technology A (Vacuum, Surfaces, and Films) **10** (1), 98-104 (1992).

[13] P. Maier-Komor, I. Altarev, A. Bergmaier et al., "Development of antireflection coatings with a ^{6}LiF/^{62}Ni multilayer converter for ultracold neutron detectors," Nuclear Instruments and Methods in Physics Research A 480, 104-108 (2002).

[14] K. C. Mohite, Y. B. Khollam, A. B. Mandale et al., "Characterization of silicon oxynitride thin films deposited by electron beam physical vapor deposition technique," Mater. Lett. **57** (26-27), 4170-4175 (2003).

[15] J. Q. Xi, M. F. Schubert, J. K. Kim et al., "Optical thin-film materials with low refractive index for broadband elimination of Fresnel reflection," Nature Photonics **1** (3), 176-179 (2007).

[16] L. Martinu and D. Poitras, "Plasma deposition of optical films and coatings: A review," Journal of Vacuum Science & Technology A (Vacuum, Surfaces, and Films) **18** (6), 2619-2645 (2000).

[17] L. H. Hall, "Preparation and properties of antireflection coatings by chemical vapor deposition," Journal of Applied Physics **43** (11), 4615-4621 (1972).

[18] N. Shibata, "Plasma-chemical vapor-deposited silicon oxide/silicon oxynitride double-layer antireflective coating for solar cells," Japanese Journal of Applied Physics, Part 1 **30** (5), 997-1001 (1991).

[19] N. Shibata, "Improvement of solar-cell performance using plasma-deposited silicon-nitride films with variable refractive-indexes," Japanese Journal of Applied Physics Part 1 **27** (4), 480-484 (1988).

[20] A. Limmanee, M. Otsubo, T. Sato et al., "Preparation of hydrogenated amorphous silicon carbon nitride films by hot-wire chemical vapor deposition using hexamethyldisilazane for silicon solar cell applications," Japanese Journal of Applied Physics, Part 1 **46** (1), 56-59 (2007).

[21] Y. Ishihara, T. Hirai, C. Sakurai et al., "Applications of the particle ordering technique for conductive antireflection films," presented at the 2nd International Symposium on Transparent Oxide Thin Films for Electronics and Optics (TOEO-2), Tokyo, Japan, (2001).

[22] S. W. Kim, D. S. Bae, and H. Shin, "Zinc-embedded silica nanoparticle layer in a multilayer coating on a glass substrate achieves broadband antireflection and high transparency," Journal of Applied Physics **96** (11), 6766-6771 (2004).

[23] K. C. Krogman, T. Druffel, and M. K. Sunkara, "Anti-reflective optical coatings incorporating nanoparticles," Nanotechnology **16** S338-S343 (2005).

[24] W. Joo, M. S. Park, and J. K. Kim, "Block copolymer film with sponge-like nanoporous strucutre for antireflection coating," Langmuir **22** (19), 7960-7963 (2006).

[25] S. Kim, J. Cho, and K. Char, "Thermally stable antireflective coatings based on nanoporous organosilicate thin films," Langmuir **23** (12), 6737-6743 (2007).

[26] C. C. Chen, D. J. Lin, T. M. Don et al., "Preparation of organic-inorganic nano-composites for antireflection coatings," Journal of Non-Crystalline Solids **354** (32), 3828-3835 (2008).

[27] Katharine B. Blodgett, "Monomolecular films of fatty acids on glass," Journal of the American Chemical Society **56** (2), 495-495 (1934); Katharine B. Blodgett and Irving Langmuir, "Built-up films of barium stearate and their optical properties," Physical Review **51** (11), 964 (1937).

[28] S. L. Buckner and V. K. Agarwal, "Organic films as anti-reflective coatings on solar cells," Solar Energy Materials **12** (2), 131-136 (1985).

[29] A. Deak, I. Szekely, E. Kalman et al., "Nanostructured silica Langmuir-Blodgett films with antireflective properties prepared on glass substrates," Thin Solid Films **484** (1-2), 310-317 (2005).

[30] W. Stober, A. Fink, and E. Bohn, "Controlled growth of monodisperse silica spheres in the micron size range," Journal of Colloid and Interface Science **26** (1), 62-69 (1968).

[31] A. Deak, B. Bancsi, A. L. Toth et al., "Complex Langmuir-Blodgett films from silica nanoparticles: An optical spectroscopy study," Colloids and Surfaces a-Physicochemical and Engineering Aspects **278** (1-3), 10-16 (2006).

[32] L. N. Nagy, N. Abraham, O. Sepsi et al., "Complex Langmuir-Blodgett Films of SiO2 and ZnO Nanoparticles with Advantageous Optical and Photocatalytical Properties," Langmuir **24** (21), 12575-12580 (2008).

[33] E. A. Meulenkamp, "Size dependence of the dissolution of ZnO nanoparticles," Journal of Physical Chemistry B **102** (40), 7764-7769 (1998).

[34] E. W. Seelig, B. Tang, A. Yamilov et al., "Self-assembled 3D photonic crystals from ZnO colloidal spheres," Materials Chemistry and Physics **80** (1), 257-263 (2003).

[35] W. Kern and D. A. Puotinen, "Cleaning solutions based on hydrogen for use in silicon semiconductor technology," RCA Review **31** 187-206 (1970).

[36] R. K. Iler, "Multilayers of colloid particles," Journal of Colloid and Interface Science **21** (6), 25 (1966).

[37] G. Decher, J. D. Hong, and J. Schmitt, "Buildup of ultrathin multilayer films by a self-assembly process: III. Consecutively alternating adsorption of anionic and cationic polyelectrolytes on charged surfaces," Thin Solid Films, 210/211 831-835 (1992).

[38] G. Decher, Y. Lvov, and J. Schmitt, "Proof of multilayer structural organization in self-assembled polycation polyanion molecular films," Thin Solid Films **244** (1-2), 772-777 (1994).

[39] Y. Lvov, F. Essler, and G. Decher, "Combination of polycation polyanion self-assembly and Langmuir-Blodgett transfer for the construction of superlattice films," Journal of Physical Chemistry **97** (51), 13773-13777 (1993).

[40] Y. Lvov, G. Decher, and H. Mohwald, "Assembly, structural characterization, and thermal-behavior of layer-by-layer deposited ultrathin films of poly(vinyl sulfate) and poly(allylamine)," Langmuir **9** (2), 481-486 (1993).

[41] G. Decher, "Fuzzy nanoassemblies: Toward layered polymeric multicomposites," Science **277** (5330), 1232-1237 (1997).

[42] Y. Lvov, G. Decher, and G. Sukhorukov, "Assembly of thin-films by means of successive deposition of alternate layers of DNA and poly(allylamine)," Macromolecules **26** (20), 5396-5399 (1993).

[43] Y. Lvov, H. Haas, G. Decher et al., "Successive deposition of alternate layers of polyelectrolytes and a charged virus," Langmuir **10** (11), 4232-4236 (1994).

[44] V. V. Tsukruk, V. N. Bliznyuk, D. Visser et al., "Electrostatic deposition of polyionic monolayers on charged surfaces," Macromolecules **30** (21), 6615-6625 (1997).

[45] Dongsik Yoo, Seimei S. Shiratori, and Michael F. Rubner, "Controlling Bilayer Composition and Surface Wettability of Sequentially Adsorbed Multilayers of Weak Polyelectrolytes," Macromolecules **31** (13), 4309-4318 (1998).

[46] S. S. Shiratori and M. F. Rubner, "pH-dependent thickness behavior of sequentially adsorbed layers of weak polyelectrolytes," Macromolecules **33** (11), 4213-4219 (2000).

[47] S. T. Dubas and J. B. Schlenoff, "Factors controlling the growth of polyelectrolyte multilayers," Macromolecules **32** (24), 8153-8160 (1999).

[48] Z. J. Sui, D. Salloum, and J. B. Schlenoff, "Effect of molecular weight on the construction of polyelectrolyte multilayers: Stripping versus sticking," Langmuir **19** (6), 2491-2495 (2003).

[49] J. Hiller, J. D. Mendelsohn, and M. F. Rubner, "Reversibly erasable nanoporous anti-reflection coatings from polyelectrolyte multilayers," Nature Materials **1** (1), 59-63 (2002).

[50] S. Fujita and S. Shiratori, "Waterproof anti reflection films fabricated by layer-by-layer adsorption process," Japanese Journal of Applied Physics Part 1 **43** (4B), 2346-2351 (2004).

[51] Shiro Fujita and Seimei Shiratori, "The optical properties of ultra-thin films fabricated by layer-by-layer adsorption process depending on dipping time," Thin Solid Films **499** (1-2), 54-60 (2006).

[52] Z. Y. Wang, J. R. Heflin, R. H. Stolen et al., "Highly sensitive optical response of optical fiber long period gratings to nanometer-thick ionic self-assembled multilayers," Appl. Phys. Lett. **86** (22) (2005).

[53] Z. Y. Wang, J. R. Heflin, K. Van Cott et al., "Biosensors employing ionic self-assembled multilayers adsorbed on long-period fiber gratings," Sensors and Actuators B-Chemical **139** (2), 618-623 (2009).

[54] V. Jain, R. Sahoo, J. R. Jinschek et al., "High contrast solid state electrochromic devices based on Ruthenium Purple nanocomposites fabricated by layer-by-layer assembly," Chemical Communications (31), 3663-3665 (2008).

[55] V. Jain, M. Khiterer, R. Montazami et al., "High-Contrast Solid-State Electrochromic Devices of Viologen-Bridged Polysilsesquioxane Nanoparticles Fabricated by Layer-by-Layer Assembly," Acs Applied Materials & Interfaces **1** (1), 83-89 (2009).

[56] V. Jain, H. M. Yochum, R. Montazami et al., "Modification of single-walled carbon nanotube electrodes by layer-by-layer assembly for electrochromic devices," Journal of Applied Physics **103** (7) (2008).

[57] A. Kroetch, S. C. Buswell, S. Evoy et al., "Fabrication of nonlinear optical devices in ionically self-assembled monolayers," Journal of Micro-Nanolithography Mems and Moems **8** (1) (2009).

[58] J. R. Heflin, C. Figura, D. Marciu et al., "Thickness dependence of second-harmonic generation in thin films fabricated from ionically self-assembled monolayers," Appl. Phys. Lett. **74** (4), 495-497 (1999).

[59] J. R. Heflin, M. T. Guzy, P. J. Neyman et al., "Efficient, thermally stable, second order nonlinear optical response in organic hybrid covalent/ionic self-assembled films," Langmuir **22** (13), 5723-5727 (2006).

[60] A. Garg, R. M. Davis, C. Durak et al., "Polar orientation of a pendant anionic chromophore in thick layer-by-layer self-assembled polymeric films," Journal of Applied Physics **104** (5) (2008).

[61] N. A. Kotov, I. Dekany, and J. H. Fendler, "Layer-by-layer self-assembly of polyelectrolyte-semiconductor nanoparticle composite films," Journal of Physical Chemistry **99** (35), 13065-13069 (1995).

[62] Y. Lvov, K. Ariga, I. Ichinose et al., "Molecular film assembly via layer-by-layer adsorption of oppositely charged macromolecules (linear polymer, protein and clay) and concanavalin A and glycogen," Thin Solid Films **285**, 797-801 (1996).

[63] Y. Lvov, K. Ariga, M. Onda et al., "Alternate assembly of ordered multilayers of SiO_2 and other nanoparticles and polyions," Langmuir **13** (23), 6195-6203 (1997).

[64] Y. M. Lvov, J. F. Rusling, D. L. Thomsen et al., "High-speed multilayer film assembly by alternate adsorption of silica nanoparticles and linear polycation," Chemical Communications (11), 1229-1230 (1998).

[65] H. Hattori, "Anti-reflection surface with particle coating deposited by electrostatic attraction," Advanced Materials **13** (1), 51-54 (2001).

[66] R. A. Hayes, M. R. Bohmer, and L. G. J. Fokkink, "A study of silica nanoparticle adsorption using optical reflectometry and streaming potential techniques," Langmuir **15** (8), 2865-2870 (1999).

[67] M. R. Bohmer, "Effects of polymers on particle adsorption on macroscopic surfaces studied by optical reflectometry," Journal of Colloid and Interface Science **197** (2), 251-256 (1998).

[68] J. W. Ostrander, A. A. Mamedov, and N. A. Kotov, "Two modes of linear layer-by-layer growth of nanoparticle-polylectrolyte multilayers and different interactions in the layer-by-layer deposition," Journal of the American Chemical Society **123** (6), 1101-1110 (2001).

[69] G. Bogdanovic, T. Sennerfors, B. Zhmud et al., "Formation and structure of polyelectrolyte and nanoparticle multilayers: Effect of particle characteristics," Journal of Colloid and Interface Science **255** (1), 44-51 (2002).

[70] J. S. Ahn, P. T. Hammond, M. F. Rubner et al., "Self-assembled particle monolayers on polyelectrolyte multilayers: particle size effects on formation, structure, and optical properties," Colloids and Surfaces a-Physicochemical and Engineering Aspects **259** (1-3), 45-53 (2005).

[71] S. E. Yancey, W. Zhong, J. R. Heflin et al., "The influence of void space on antireflection coatings of silica nanoparticle self-assembled films," Journal of Applied Physics **99** (3) (2006).

[72] F. C. Cebeci, Z. Z. Wu, L. Zhai et al., "Nanoporosity-driven superhydrophilicity: A means to create multifunctional antifogging coatings," Langmuir **22**, 2856-2862 (2006).

[73] J. Bravo, L. Zhai, Z. Z. Wu et al., "Transparent superhydrophobic films based on silica nanoparticles," Langmuir **23** (13), 7293-7298 (2007).

[74] D. Lee, M. F. Rubner, and R. E. Cohen, "All-nanoparticle thin-film coatings," Nano Letters **6** (10), 2305-2312 (2006).

[75] D. Lee, D. Omolade, R. E. Cohen et al., "pH-Dependent structure and properties of TiO_2/SiO_2 nanoparticle multilayer thin films," Chemistry of Materials **19** (6), 1427-1433 (2007).

[76] D. Lee, Z. Gemici, M. F. Rubner et al., "Multilayers of oppositely charged SiO_2 nanoparticles: Effect of surface charge on multilayer assembly," Langmuir **23** (17), 8833-8837 (2007).

[77] G. B. Sukhorukov, E. Donath, H. Lichtenfeld et al., "Layer-by-layer self assembly of polyelectrolytes on colloidal particles," Colloids and Surfaces a-Physicochemical and Engineering Aspects **137** (1-3), 253-266 (1998); G. B. Sukhorukov, E. Donath, S. Davis et al., "Stepwise polyelectrolyte assembly on particle surfaces: a novel approach to colloid design," Polymers for Advanced Technologies **9** (10-11), 759-767 (1998).

[78] F. Caruso, H. Lichtenfeld, M. Giersig et al., "Electrostatic self-assembly of silica nanoparticle - Polyelectrolyte multilayers on polystyrene latex particles," Journal of the American Chemical Society **120** (33), 8523-8524 (1998).

[79] D. Radziuk, D. G. Shchukin, A. Skirtach et al., "Synthesis of silver nanoparticles for remote opening of polyelectrolyte microcapsules," Langmuir **23** (8), 4612-4617 (2007); D. Radziuk, A. Skirtach, G. Sukhorukov et al., "Stabilization of silver nanoparticles by polyelectrolytes and poly(ethylene glycol)," Macromolecular Rapid Communications **28** (7), 848-855 (2007).

CHAPTER THREE
Experimental Details

This chapter provides information regarding instrumentation, materials, and protocols used in all experiments presented in this thesis. **Section 3.1** contains the experimental information related to the work described in **Chapters 4** and **5** of the thesis, while **Section 3.2** provides similar information for **Chapter 6**.

3.1 AR Coatings Incorporating Silica Nanoparticles

3.1.1 Equipment

Spectroscopic Methods

Transmittance data for λ = 300-1100 nm was acquired using a Perkin Elmer Lambda 25 UV/VIS spectrophotometer. Reflectivity data was gathered using a Filmetrics F-20 thin-film measurement system (λ = 300-850 nm). The Filmetrics instrument was also used to acquire transmittance spectra when extinction coefficient (1-T-R) calculations were needed. The film surface composition was analyzed by X-ray photoelectron spectroscopy (XPS) using a Perkin Elmer Physical Electronics 5400 instrument with a Mg X-ray source ($h\nu$ = 1253.6 eV). Surfaces were swept 10 times at a 45° angle of incidence with energies ranging from 0 to 1100 eV. Spectroscopic ellipsometry was performed using a J.A. Woollam VB-2000 ellipsometer at wavelengths ranging from 400-1000 nm at angles of 54, 56, and 58°. Infrared studies (4000-450 cm^{-1}) on polycarbonate substrates were conducted using Perkin-Elmer Spectrum One FT-IR Spectrometer. Sixteen total scans were run at a resolution of 4.00 cm^{-1}.

UV Irradiation of Samples

DAR/SiO_2 NP films on glass substrates were cross-linked using a Kinsten KVB-30 exposure unit, which had six 20 W UV fluorescent bulbs. Polycarbonate substrates were

oxidized with a UV exposure unit from Atlantic Ultraviolet (Cat. No. G12T6VH). The unit contained two 10 W lamps that emitted wavelengths of 185 and 254 nm.

Imaging Techniques

The surface of the DAR/SiO_2 NP films was imaged by atomic force microscopy (AFM) using a Veeco Metrology Multimode AFM instrument in tapping mode with a tip from Nanosensors™ with a force constant of k = 42 N/m. Film surfaces were also imaged with a LEO 1550 field-emission scanning electron microscope (FESEM) unit at an accelerating voltage of 5 kV.

Other Equipment

An automated dipper from nanoStrata, Inc. was used to deposit multilayer thin films. Tape peel tests on all films were carried out on an Instrumentors, Inc. slip/peel tester Mod 3M90. Dynamic Light Scattering (DLS) size and zeta potential measurements of colloidal silica were performed with a Zetasizer nanoZS (Malvern Instruments) operating at a fixed angle of 173° and 633 nm wavelength. Quartz Crystal Microbalance (QCM) was carried out using a Q-Sense E4 from qsense. Ionic species were adsorbed onto Au crystals (Cat. No. QSX 301).

3.1.2 Materials

Snowtex® colloidal silica nanoparticles (ST-20L) were purchased from Nissan Chemical. The particles had an average particle size of 45 nm and a stable pH range from 9.5 to 11. The concentration of the silica nanoparticles in solution was 45 mg/mL (3.76 M). 4-diazodiphenylamine/formaldehyde condensate hydrogen sulfate (DAR) was generously provided by Secant Chemicals Inc. DAR aqueous solutions (52.6 mg/mL) were prepared under dark-room conditions and at 40 °C. Poly(allylamine hydrochloride) (M_w = 15000, 56000), 30 wt. % poly(methacrylic acid, sodium salt) (M_w = 9500), 20 wt. % poly(diallyldimethyl ammonium chloride) (M_w = 400000-500000), and 3-mercaptopropyl trimethoxysilane were purchased from Sigma-Aldrich. Poly(styrene sulfonic acid), sodium salt (M_w = 70000) was purchased from Polysciences, Inc. Deionized water (Milli-Q, 18 MΩ) was used to prepare ionic solutions

containing the above polymers. Makrolon® GP bisphenol A polycarbonate sheets were purchased from Sheffield Plastics, Inc.

3.1.3 Protocols

Substrate Preparation

The manner in which substrates were pretreated for ISAM deposition depended on the type of substrate, the materials to be used, and the desired functionality.

Glass substrates with alternating layers of PAH and SiO_2 NPs were first cleaned with acetone and then cleaned according to the RCA method.[1]

The procedure to prepare glass substrates containing sulfonate groups, however, was more involved. I followed a similar protocol to that reported by Wu and coworkers.[2] First, the substrates were cleaned with acetone and then by piranha etching. In piranha etching, substrates are immersed in a mixture of H_2SO_4 and 30% H_2O_2 (7/3 by volume) heated to 90 °C for 30 minutes. After this, the substrates were rinsed thoroughly with deionized water and dried with N_2 gas. Next, the substrates were dipped in a solution containing 7mM 3-mercaptopropyl trimethoxysilane (MPTS) in MeOH for approximately 18 hours. After this, the silylated substrates were rinsed with MeOH and dried with N_2 gas. Then they were dipped in a solution containing CH_3COOH and 30% H_2O_2 (5/1 by volume) for 50 minutes and heated at 70 °C. Finally, the substrate was rinsed with deionized water and dried with N_2. Immersion in the acetic acid bath converted the thiol group of MPTS into a sulfonate group.

Au crystals for QCM experiments were used multiple times, so a highly effective cleaning method was needed to remove the previously adsorbed film before the next film could be deposited. As noted in **Chapter 4**, the following procedure was adopted midway through the experimental set. First, the crystals were sonicated for 5 minutes in a 1:1 mixture of toluene:H_2O. Next, they were placed in a Bioforce Nanosciences UV ozone cleaner for 10 minutes. After this, the crystals were immersed in a solution containing H_2O:NH_3:H_2O_2 (5:1:1) heated between 60-75 °C for 20 minutes. Next, they were dried with N_2 gas and placed back in the UV ozone cleaner for another 10 minutes. This procedure was repeated immediately after the QCM experiment was completed; hence, the crystals were cleaned in this manner before and after each experiment.

The polycarbonate substrates had a masking adhesive protecting the surface from scratches, dust, etc. Residual adhesive remained on the surface after removing the masking layer, and thus the surface required cleaning. The substrates were gently cleaned with isopropanol using a microfiber cloth. Wiping the surface with standard laboratory tissues left scratches on the polycarbonate, so it was important to use the microfiber cloth. After this, the PC substrates were rinsed with deionized water and dried with N_2 gas. Just before ISAM deposition the substrates were placed under the UV (λ = 185, 254 nm) exposure unit. The substrates were flipped over midway through exposure so that both sides had the similar dosages to UV.

ISAM Hand-Dipped

In my Master's project the DAR/SiO_2 NP ISAM films were hand-dipped and done so under dark-room conditions. The glass substrates were dipped in the ionic solutions for 3 minutes and then rinsed under running deionized water for 30-40 seconds. After the last adsorption and rinse step the film was dried with N_2 gas.

ISAM Auto-Dipper

The nanoStrata unit (**Figure 3.1**) contained a platform that could hold up to 8 beakers (**Figure 3.1B**). Two of the beakers facing opposite of each other were reserved for the ionic solutions, while the rest contained deionized water for rinsing steps; meaning an ionic adsorption step was followed by three rinse steps. After a rinse step, the contaminated water was removed from the beaker and replaced with fresh deionized water. The platform was raised by a pressurized gas cylinder and mechanically rotated to the next beaker location when lowered. Substrates were secured to a small inverted stage placed above the platform containing the beakers. The stage was connected to a small motor, which made it possible to rotate the samples for the rinsing steps in water. A turn dial on unit controlled the rotational speed of the stage. There was nothing on the dial indicating how fast or slow the stage was rotating, but I positioned the dial so that the corresponding speed was at a minimum.

A.

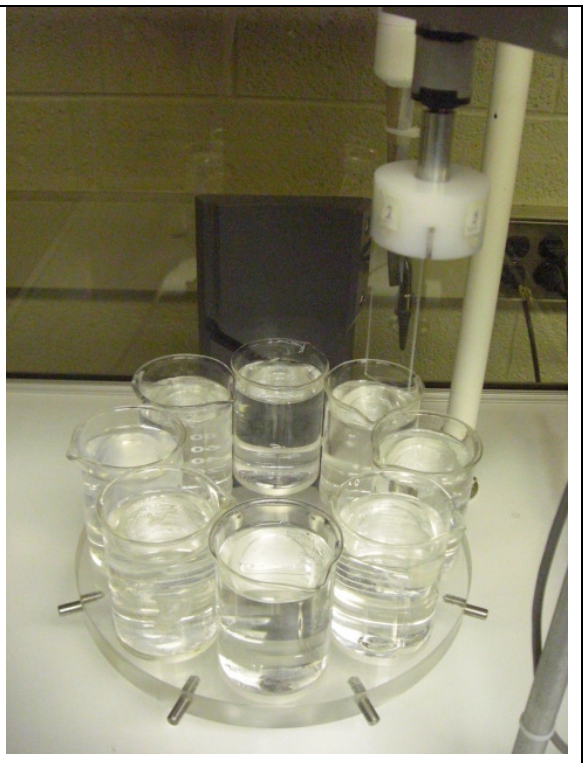

B.

Figure 3.1 (**A**) Outside view of the auto-dipper unit, (**B**) inverted sample stage and beaker platform.

In some experiments, the dipping times and rinsing conditions were varied. This also depended on the polymer used in ISAM deposition. For DAR/SiO_2 NP films, the substrate was dipped in the ionic solutions for 3 minutes each. After immersion in DAR, the samples were rinsed for a total of 3 minutes. After the SiO_2 adsorption step, the sample was rinsed for just 1 minute. After the desired number of layers was deposited, the sample was dried with N_2 gas. The deposition of DAR/SiO_2 NPs in the auto-dipper was carried out in dark-room conditions. The protocol was different, however, for PAH/SiO_2 NP films. Each time, the sample was dipped in the ionic solution for 3 minutes and followed by 1 minute of rinsing.

Tape Peel tests

The instrument was reconfigured as seen in **Figure 3.2** to carry out 90° tape peels in accordance with military spec. MIL-M-13508C, Sec. 4.4.6. The substrate was secured to a metal plate positioned normal to the main platform. Scotch® Magic Tape (2 cm width) was applied to

the film surface by rolling a metal cylinder weighing 88.8 grams back and forth along the length of the tape four times. The other end of the tape was wrapped around a metal hook that was connected to a force sensor. When the peel test was initiated the platform holding the sample was moved at a constant rate (14.5 inches/minute, referred to as the "platen speed") away from the platform on which the hook and force sensor rested. An average force value was acquired over a 5 second duration. The sensor was calibrated in such a way that readings of "0" and "100" on the display corresponded to forces of 0 and 9.8 N, respectively.

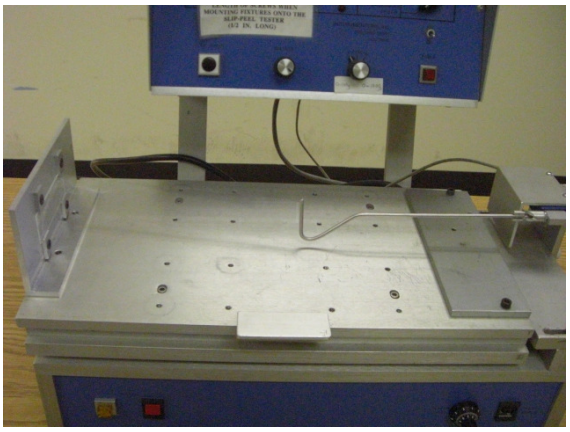

A.

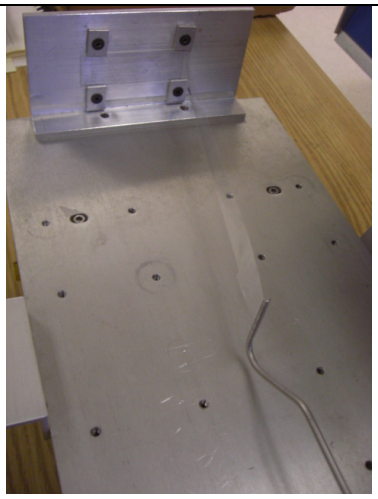

B.

Figure 3.2 (**A**) Tape peel tester reconfigured for 90° tests, (**B**) closer inspection showing how the tape connects the sample on the vertical platform with the hook attached to the force sensor.

Ellipsometry

In ellipsometry, light with *s*- and *p*-polarization (r_s and r_p, respectively) reflected from a sample can be measured to determine a number of properties about the film. The ratio of the polarized light can be used in the following relation:

$$\frac{r_p}{r_s} = \tan(\Psi)e^{i\Delta}$$

where the parameters tan(Ψ) and Δ are the reflected amplitude ratio and phase shift, respectively. It is possible to determine optical constants, such as the film refractive index and thickness, by using an iterative modeling process. By varying the optical constants, corresponding theoretical curves can be generated plotting Ψ and Δ versus wavelength. These curves are matched against the measured spectra of Ψ and Δ, and the fit of the curves is quantified by determination of the mean-squared error (MSE). The fit is highly dependent on the type of model chosen for data analysis. The Maxwell-Garnett effective medium approximation (EMA) was used to model the presented data in this research. Under the EMA approximation, it is assumed that the layer of interest is a mixture of two or three materials. Adjusting the volume fraction of each material in the modeling process determines the effective index of refraction of the layer. This was ideal for modeling SiO_2 NP films since the film consisted of silica and void. In addition to the EMA layer, the films were also modeled with a top layer of surface roughness. This layer was treated as an EMA layer with a fixed silica/void volume ratio equal to 1.

X-ray photoelectron spectroscopy

Atomic composition percentages obtained from XPS analysis are reported in various parts of this thesis. The atomic composition percentage is a useful way to estimate the relative amount of an element at the topmost layer of a surface. An electron emitted from the surface and collected by the detector has a specific kinetic energy which in turn makes it possible to calculate its binding energy. Thus, a spectrum of binding energies can be generated with peaks corresponding to electron configurations for various elements. The amount of a given element on a surface is related to the total area of the peaks associated with that element. To determine the atomic composition, the total intensity of an XPS signal is divided by a relative sensitivity factor and normalized over all of the detected elements.

Calcination of PAH/SiO_2 NP films

After PAH/SiO_2 NP films were made by ISAM deposition, they were calcined in order to remove the organic material and fuse the nanoparticles. The sample was placed in an oven at room temperature. Next, the oven temperature was ramped at 5 °C/minute until it reached the desired value (~ 500 °C) and then was kept constant for 4 hours. Finally, the system was slowly cooled back to room temperature and the calcined samples were removed.

3.2 Silica Nanoparticles on Glass Fibers

3.2.1 Equipment

Transmittance spectra were acquired using a Perkin Elmer Lambda 950 UV/VIS spectrometer (λ = 175-3300 nm). A Digitrol II heat source from Glas-Col was used to heat the glass fiber bundle/polymer matrix system. The temperature of the system was recorded with a Fluke 54II thermometer. Images of the coated fibers were acquired with a LEO 1550 field-emission scanning electron microscope (FESEM) unit at an accelerating voltage of 5 kV.

3.2.2 Materials

Snowtex® colloidal silica nanoparticles (ST-20L) were purchased from Nissan Chemical. The particles had an average particle size of 45 nm and a stable pH range from 9.5 to 11. The concentration of the silica nanoparticles in solution was 45 mg/mL (3.76 M). Poly(allylamine hydrochloride) (M_w = 56000) was purchased from Sigma-Aldrich. Deionized water (Milli-Q, 18 MΩ) was used to prepare ionic solutions containing PAH and silica nanoparticles. Astroquartz® II fibers with 9 μm diameter were obtained from JPS Composite Materials.

3.2.3 Protocols

Glass Fiber Preparation

Fiber bundles first were cut to size and taped at one end to keep the bundle together. Then the glass fibers were dipped in acetone for nearly 1 minute. Next, they were thoroughly rinsed with deionized water and dried with N_2 gas. Finally the fiber surface was functionalized using the RCA method.[1]

ISAM Deposition of PAH/SiO_2 on Glass Fibers

First, aqueous solutions of silica nanoparticles (3.76 M) and PAH (10 mM) were prepared. The solutions were sonicated during ISAM deposition in order to reduce fiber aggregation. Next, the fiber bundle was immersed in the PAH solution for 3 minutes. In the rinse step, the bundle was repeatedly dipped and raised from a beaker containing deionized water 15 times. After this, the fiber bundle was immersed in the SiO_2 solution under sonication for 3 minutes and rinsed again. This was repeated until 25 bilayers were deposited on the fibers.

[1] W. Kern and D. A. Puotinen, "Cleaning solutions based on hydrogen for use in silicon semiconductor technology," RCA Review **31**, 187-206 (1970).

[2] C. G. Wu, L. F. Tzeng, Y. T. Kuo et al., "Enhancement of the photocatalytic activity of TiO_2 film via surface modification of the substrate," Applied Catalysis a-General **226** (1-2), 199-211 (2002).

CHAPTER FOUR

Methods to Improve Cohesion and Adhesion of ISAM Silica Nanoparticle Films

In this chapter I will describe three approaches I developed in attempts to improve the cohesion and adhesion of AR coatings consisting of silica nanoparticles. The first approach was a continuation of my Master's degree project. The idea was to build the film through the standard ISAM technique and then to convert the ionic bonds into covalent ones. In order to facilitate this it required the incorporation of a photo-reactive polymer, which in this case was diazo-resin (DAR). The second approach involved heating of the ISAM film in a process referred to as calcination, which burned away the polymer, but more importantly fused the silica nanoparticles together. This gave the films exceptional cohesive strength, which were able to survive moderate tape peel and abrasion tests. The optical transparency was not compromised as a result of the thermal treatment. The final approach was to completely preserve the ionic nature of the coating, but to instead partially fill the interstitial voids with polymer. As a result of this approach, I was able to improve the adhesion and cohesion, but saw a reduction in the optical clarity of the films. The nanoparticle adsorption depended sensitively on the pH conditions of poly(allylamine hydrochloride) (PAH) and poly(methacrylic acid) (PMA).

4.1 Introduction and Review

The deposition of ISAM films containing negatively-charged silica nanoparticles onto glass substrates can dramatically improve the substrate's optical transmittance by forming an excellent AR coating. This is because the nanoparticles are arranged in such a way that interstitial voids are present throughout the film. The corresponding amount of void fraction in the film, which is controlled by the nanoparticle size, dispersion, and number of deposited bilayers, is tied to the effective refractive index of the coating, which can vary between 1.26 and 1.30, which is close to the ideal value of 1.22 for an AR coating on glass. When the nanoparticles are well-dispersed they form a random closed-packed structure (RCP). The theoretical void fraction of an RCP structure is 36%, which according to the Effective Medium

Approximation (EMA) corresponds to a refractive index of 1.32. If the nanoparticles are more dispersed they pack in such a way that the film has a larger void fraction and thus a smaller refractive index. This assumes that the size of the aggregate nanoparticles is sufficiently small so as not to scatter visible light, particularly at shorter wavelengths.

While the geometry of the spherical nanoparticles improves the optical transmission, it also reduces the cohesive strength of the ISAM film. This is because the polycation strongly interacts only at the contact points between nanoparticles. Away from these contact points the electrostatic interaction between the polycation and neighboring nanoparticles is considerably weaker, particularly when compared to the interaction of all-polymer ISAM films, which can be considered as long intertwined chains containing oppositely-charged functional groups. As a result the silica nanoparticle ISAM films do not adhere strongly to the substrate and are not suitable for applications that would require them to be cleaned or wiped.

There are two approaches I have considered to improve the cohesive strength of silica nanoparticle films. The first approach is to strengthen the existing bonds that join the nanoparticles, while the second approach would be to partially fill the interstitial voids with charged polymers thus increasing the total contact area. The preferred method would clearly be the first approach because it may not necessarily compromise the AR properties of the film by changing the net refractive index, while the second method is certain to do so at least a little. Three methods are presented in this chapter; two of them fall under the first approach, and the third under the second approach. They are listed below, along with previous research that guided the work:

1. UV Cross-Linking of Diazo-Resin Polycation with Modified Silica Nanoparticles Bearing Sulfonate End Groups: The weak ionic bonds between the nanoparticles are converted into stronger covalent ones in this method. This is accomplished by using a photo-sensitive polycation known as diazo-resin (DAR) during the ISAM deposition with silica nanoparticles followed by cross-linking the film by exposure to UV. The synthesis of DAR was described in 1998 by Shuguang Cao and coworkers.[1] Weixiao Cao[2] improved the stability of polyelectrolyte complexes (PECs) by mixing DAR with various anionic solutions and irradiating them with UV. The incorporation of DAR into ISAM films however was first introduced by Sun. In 1998 Sun[3] made an organic thin film that was stable in a ternary solvent by making ISAM films consisting

of diazo-resin and poly(styrene sulfonate) (PSS), and later converting the ionic bonds between adjacent polymers to covalent by UV irradiation. This was demonstrated by dipping films with and without UV exposure into a ternary solvent (H_2O:DMF:$ZnCl_2$, 3:5:2 w/w/w). Within 5 minutes nearly 30% of the films without UV irradiation were dissolved. In contrast no detectable change could be found in the coatings with UV exposure after 30 minutes of solvent immersion. Later this approach was used for ISAM films containing porphyrins,[4] which are a promising class of conjugated materials with potential applications in the fields of photovoltaics, electrochromics, and nonlinear optics. ISAM deposition involved DAR and the porphyrin tetrasodium 5,10,15,20-tetraphenyl-21H,23H-porphine-P,P',P",P'"-tetrasulfonic acid ($tpps_4$). Electrostatic attraction between the diazonium and sulfonate groups of the ISAM constituents facilitated rapid and uniform deposition of the thin film. This ionic bond was converted to covalent by subsequent UV irradiation. In a manner similar to the DAR/PSS films, Sun tested the stability of cross-linked DAR/$tpps_4$ films by immersion in the H_2O:DMF:$ZnCl_2$ ternary solvent. He again found that the cross-linked films were more stable in solvent than their ionically-bonded counterparts. Furthermore using polarized UV/VIS spectroscopy he found that UV irradiation did not appreciably affect the orientation of $tpps_4$. Sun continued to demonstrate the effect of UV cross-linking on the stability of ISAM films containing DAR with other polyanions, including poly(aniline-co-*N*-propanesulfonic acid aniline) (PAPSAH),[5] poly(acrylic acid) (PAA),[6] sodium (phthalocyaninetetrasulfonato) copper (CuTsPc), 2-(4-Sulfo-1-naphthylazo)-1,8-dihydroxy-3,6-naphthalene disulfonic acid (SNAN), and Bathophenanthrolinedisulfonic acid disodium salt trihydrate (BST).[7]

Section 4.2 covers my research related to DAR/SiO_2 NP films. First the efforts to optimize the optical and mechanical properties of ISAM films containing DAR and unmodified silica nanoparticles are discussed. Next I will discuss how the solvent test verified that the DAR/SiO_2 NP films were not cross-linked after UV irradiation. Finally the proposed solution is presented, which requires that the substrate and silica nanoparticles be covered with molecules containing sulfonate groups. Subsequent solvent tests indicate that the DAR/modified SiO_2 NP films are more stable than ones in which the nanoparticles are not coated with sulfonates. Due to the coating process however, the sulfonate-containing nanoparticles are larger and more dispersed in size. Thus the new coatings, while more stable, also scatter too much light. A

number of possible solutions to this latter problem are addressed in the **Summary and Future Studies** chapter.

2. Thermal Fusing of PAH/SiO_2 NP Films:

The second approach is much simpler than the one above and highly effective. Fusing the nanoparticles is possible by heating PAH/SiO_2 NP films near the annealing temperature of glass. If heated at an appropriate temperature for a particular length of time, the nanoparticles will partially fuse while the film still retains its nanoporosity. In this way the optical properties are not compromised, yet the mechanical strength is significantly improved.

This work follows and looks to expand upon the progress made by the Rubner/Cohen groups at MIT, however the general method, referred to as calcination, was a generally accepted practice on non-ISAM particulate films many years earlier.[8] In 2006, Lee, Rubner, Cohen and collaborators[9] constructed anti-reflection coatings consisting of alternating layers of silica and titania nanoparticles. Next they heated the films at 550 °C for 3 hours, and showed that the durability was greatly enhanced by the procedure. Cebeci[10] also used the calcination procedure to improve the mechanical strength of PAH/SiO_2 NP films. He heated the samples to 500 °C for 4 hours to burn away the polymer and fuse the nanoparticles. In both papers the authors report very high transmittance of the calcined films. The SiO_2/TiO_2 NP films made by Lee had a transmittance greater than 97 % (max. T > 99 %) over most of the visible spectrum, while the PAH/SiO_2 films made by Cebeci had a maximum transmittance of 99.8%. Similarly we report very high transmittance in our PAH/SiO_2 NP films (**Section 4.3**) with significantly improved mechanical strength by calcination. I address subsequent extension of the research in the **Summary and Future Studies** chapter, which will focus on the correlation between calcination temperature/time, and how they affect the film thickness and void fraction.

3. Addition of Polymer Interlayers During ISAM Deposition of PAH/SiO_2 NP Films: The final method to improve film cohesion is to partially fill the interstitial voids with charged polymers. This would effectively increase surface area of contact and electrostatic interaction between adjacent nanoparticles. This is achieved by constructing films with quadlayers as opposed to bilayers. The quadlayers consist of PAH/SiO_2 NPs/PAH/PMA. To my knowledge there is no

mention in the literature of incorporating polymer interlayers to improve the cohesion of ISAM AR coatings. In addition to the interlayers, PAH/PMA polymer layers were deposited onto the substrate to improve the adhesion of the nanoparticles with the glass. Finally a capping layer of PAH/PMA was deposited onto the film to increase the degree of infiltration of polymers in the nanoparticle network. The nanoparticle adsorption was strongly affected by the pH conditions of the interlayer polymers PAH and PMA. Therefore as part of the study films were made with varying pH conditions of the interlayer constituents. To increase the sensitivity of the study I used Quartz Crystal Microbalance (QCM) to monitor the nanoparticle adsorption with respect to interlayer polymer pH settings. In the end I found using tape peel and abrasion tests that the mechanical strength was improved when incorporating the quadlayer system, as well as bottom and capping polymer layers. As a consequence, however, the optical transparency and homogeneity were slightly diminished. It was expected that the transparency could be compromised using this technique but not the uniformity. Thus future studies will focus on ways to improve the uniformity of the quarter layer films.

4.2 UV Cross-Linking of Diazo-Resin Polycation with Modified Silica Nanoparticles Bearing Sulfonate End Groups

As I mentioned above, this research was a continuation of my Master's work, and was the most thoroughly studied approach of the three that I discuss in this chapter. The recent findings of this work suggest that covalent bonds can be successfully incorporated throughout the ISAM network, but only if the diazo-resin (DAR) is ionically attached to a sulfonate end group. Hence the reader will see how I modified both the substrate and silica nanoparticles in order to put this functional group on the respective surfaces. However a significant amount of work and characterization on DAR/unmodified silica nanoparticles was done before this was realized. For the sake of completeness I first will briefly cover the work described in my Master's project report, as well as my PhD. work leading up to the discovery that cross-linking between DAR/unmodified silica nanoparticles does not occur. Following this I will discuss the current approach used to successfully cross-link the ISAM films (**Section 4.2.2**).

4.2.1 Discussion of Master's Research and Eventual Discovery of Failed Cross-Linking in DAR/SiO_2 NP ISAM Films

The guiding principle of my Master's work was to improve the strength of the ionic bonds "gluing" the silica nanoparticles together. This route was preferred instead of filling the interstitial voids with additional ionic species because there is, in principle, no tradeoff in transmittance. One way to improve the strength of the ionic bonds between nanoparticles is to convert them into covalent ones. Hence our motivation was to find a polymer that could partner with the silica nanoparticles via ISAM deposition and undergo this conversion. From the early works of Sun[3-7] with diazo-resin (DAR) (**Figure 4.1**), which demonstrated successful UV cross-linking of the polycation with various polyanions, we deduced it would be a suitable polymer for this task.

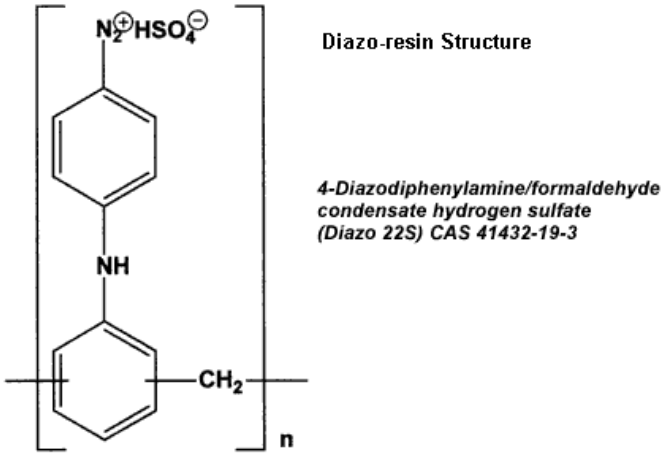

Figure 4.1 Molecular structure of diazo-resin (DAR). Image reproduced from http://www.secantchemicals.com/products/03.html with permission from Secant Chemicals Inc.

As I will show later, however, DAR can ionically attach to silica nanoparticles to create highly uniform films, but they cannot UV cross-link with the nanoparticle surface. The initial (and incorrect) proposed UV reaction between DAR/SiO_2 NPs can be seen below in **Figure 4.2**. On the left of the figure is the correct ionic interaction between the diazonium groups ($R\text{-}N_2^+$) of DAR and the hydroxyl groups (OH^-) on the surface of the nanoparticle. It was assumed

(incorrectly) after UV irradiation (λ = 365 nm) that water and nitrogen gas would be released, and an oxygen atom would covalently link the benzene ring of DAR and the nanoparticle.

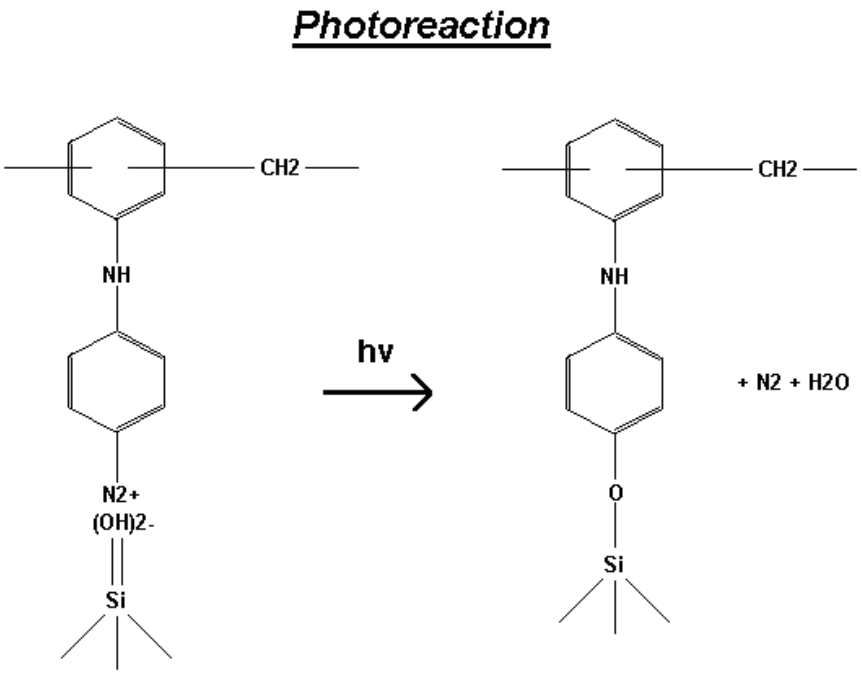

Figure 4.2 Ionic-to-covalent conversion between DAR and silica nanoparticles. This reaction was later determined to be incorrect by a solvent test.

The study was based on a statistical analysis of the mechanical and optical properties of DAR/SiO_2 NP ISAM films. The critical considerations of the statistical study were to determine appropriate quantitative representations (called "response variables") of the mechanical and optical properties, and identify processing conditions (factors) that could potentially affect the response variables. I decided to implement two response variables in the study, one to quantify the optical performance, and one for the mechanical stability. The optical response variable was called "Peak-to-Valley", which was simply the difference between the maximum and minimum of the reflection spectra in the visible (**Figure 4.3**). The reason this was selected as a response variable was because uniform coatings are less likely to scatter light, and thus will have well-defined constructive and destructive interference fringes, i.e. resulting in a larger "Peak-to-Valley". To quantify the mechanical stability I configured a very rough 180° tape peel test by fixing the sample onto a ramp (**Figure 4.4**), and used the weight of a cart with a given load to pull the tape from the sample. For the tests I used ¾" Scotch™ Multitask tape. The angle of

inclination of the ramp with the floor "θ" was increased until the tape pulled away from the sample. Knowing the angle θ and the mass of the cart + load I was able to calculate the applied force (mgsinθ) along the direction of the ramp, where "m" is the mass of the cart +load. The response variable was given the name "Shear".

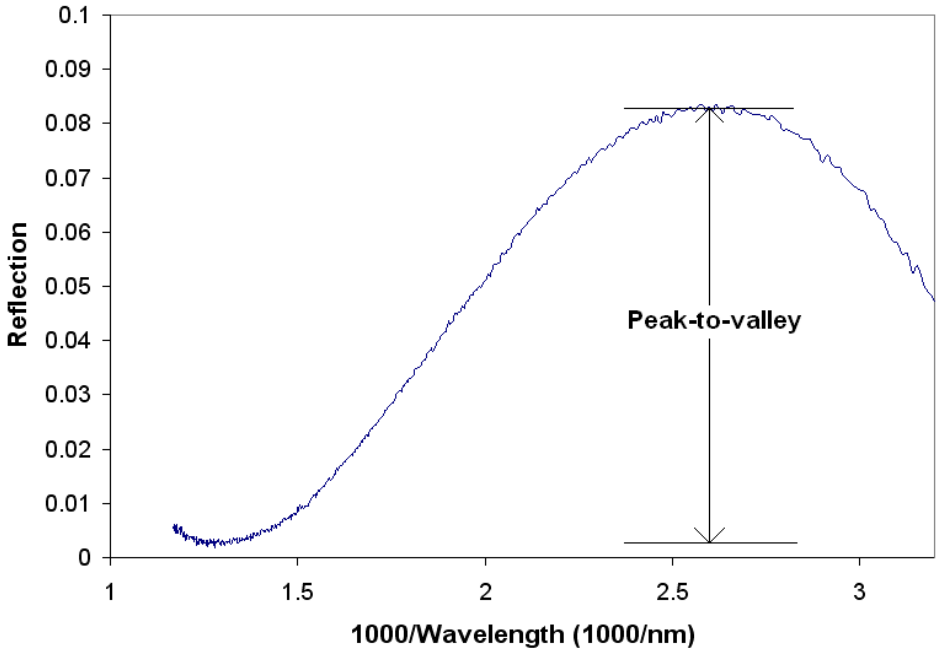

Figure 4.3 Example of "Peak-to-Valley" measurement for reflection spectrum of a DAR/SiO_2 NP coating.

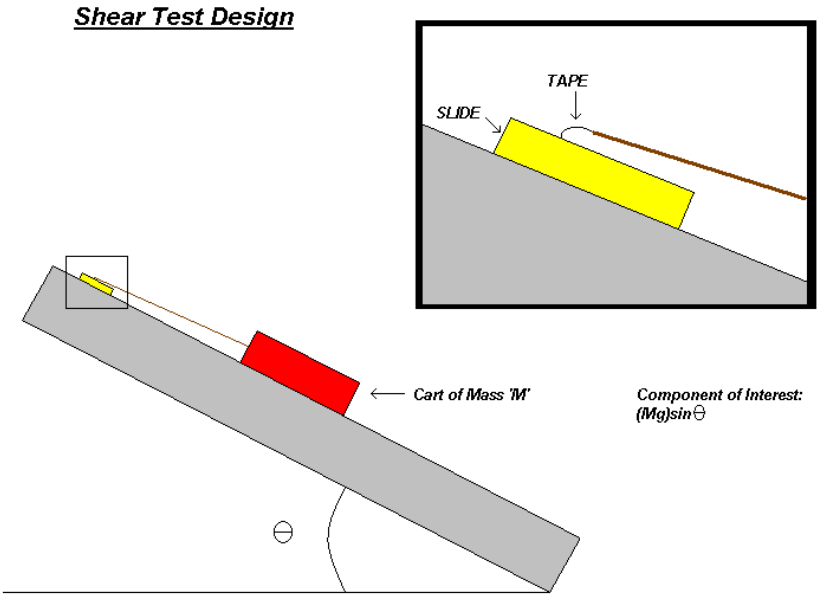

Figure 4.4 Response variable "Shear" used to quantify the mechanical strength of DAR/SiO_2 NP films during my Master's work.

A number of factors were considered in the study to see if they had an impact on the aforementioned response variables. Those factors are listed below, along with the motivation for their inclusion in the study:

$ZnCl_2$ Concentration: The presence of $ZnCl_2$ in the diazo-resin structure was said to provide stability to the compound. This made it an important factor to study regarding the adhesive properties of the AR films.

Number of Bilayers: Changing the number of bilayers could affect the optical properties of the film due to light scattering through a thicker medium. It also was strongly suspected that it could affect the adhesive properties when coupled with the UV exposure time. The UV light is absorbed as it passes through a film so there could be less cross-linking at the bottom of the film than at the top.

UV Exposure Time: The length of time that the AR coating was exposed to UV, which directly affects the degree of cross-linking in the film.

pH-Silica Solution: Changing the pH of the silica solution affects the strength of interactions between the polycation and anion layers. This was considered to be one of the most important factors in the study.

Molarity-SiO_2 in Silica Solution: The nanoparticle concentration in solution could influence the packing of SiO_2 particles that form the anion layer and the electrostatic interactions with the subsequent polycation layer.

Factorial Design was the statistical utility of choice for the study. The premise of this utility is that experiments are generated based on processing factors that may statistically affect the response variables. Each factor is varied over two levels, referred to as "high" and "low". A full factorial experiment covers all possible permutations of the factors included in the design. Therefore the total number of experiments in a full factorial is 2^n, where "n" represents the number of factors in the design. For example a full factorial design with three factors would require $2^3 = 8$ total experiments. An added benefit of factorial design is that it can uncover interaction terms which occur when the response to changing one factor depends on the settings of another factor. A full factorial can be quite cumbersome when increasing the number of factors coupled with experiments that consume a significant amount of time. Hence it is possible to reduce the total number of experiments by using half or quarter factorial designs. This can save a lot of time, but it also reduces the statistical power of the experimental design. I had a total of five factors under consideration, and chose not to conduct a full factorial (32 experiments). Instead I augmented a quarter factorial, which has the equivalent statistical power of a half factorial (17 total experiments). A half factorial containing five factors typically would require 16 experiments, but the additional experiment was necessary to compensate for the lost degree of freedom from augmentation of the quarter factorial. Listed below in **Table 4.1** are the factors chosen for the study, along with their respective levels and a brief description.

Factor	Factor Levels	Description
$ZnCl_2$ concentration	0, 2 %	Wt % of $ZnCl_2$ in DAR
Number of bilayers	5, 10	Number of DAR/SiO_2 NP layers
UV exposure time	3, 10 minutes	Length of time the coatings were irradiated by UV
pH-silica solution	Acidic (~ 3.0) Basic (~ 10.7)	pH level of silica nanoparticle solution
Molarity-SiO_2 in silica solution	0.3, 3.0 M	Concentration of silica nanoparticles in solution

Table 4.1 Factors chosen for the experimental design, with their levels and description

Design-Expert® was the software I used to design and run the statistical analyses for the study. **Table 4.2** has been included to summarize the results of the factorial experiment. In the table are listed the response variables, the factors (also known as "main effects" that significantly affect the response, and the factors involved in second order interactions. A dramatic conclusion that could be drawn from the results was that the pH of the nanoparticle solution had a profound effect on both the optical (**Figure 4.5A**) and mechanical properties (**Figure 4.5B)**. This was evident even by visual inspection of the films. The silica solutions with a basic pH consistently produced higher quality films with respect to both response variables. Higher Shear values were generally recorded for samples with longer periods of UV irradiation; however the difference in Shear between "high" (10 minutes) and "low" (3 minutes) was not statistically significant. Lastly the factors "$ZnCl_2$ concentration" and "Molarity-SiO_2" (**Figure 4.6**) were involved in second order interactions. Films consisting of 5 bilayers had larger Peak-to-Valley and Shear values when a 3.0 M SiO_2 aqueous solution was used. The Shear for 10 bilayer coatings, however, was better when the 0.3 M SiO_2 solution was used, but no appreciable difference was observed in the Peak-to-Valley. I could not incorporate the factor "$ZnCl_2$ concentration" in future studies because the manufacturer of DAR discontinued the brand with 2 % $ZnCl_2$. From that point on I strictly used the DAR brand that contained no $ZnCl_2$. This concluded the work in my Master's research. What follows is my PhD. research.

Response Variable	High Variability	Variability from Second Order Effects
Shear	Silica Sol. pH UV Exp. Time (moderate variability)	$ZnCl_2$ concentration Molarity-SiO_2
Peak-to-Valley	Silica Sol. pH	$ZnCl_2$ concentration Molarity-SiO_2

Table 4.2 List of factors that affected the response variables, and factors involved in second order effects.

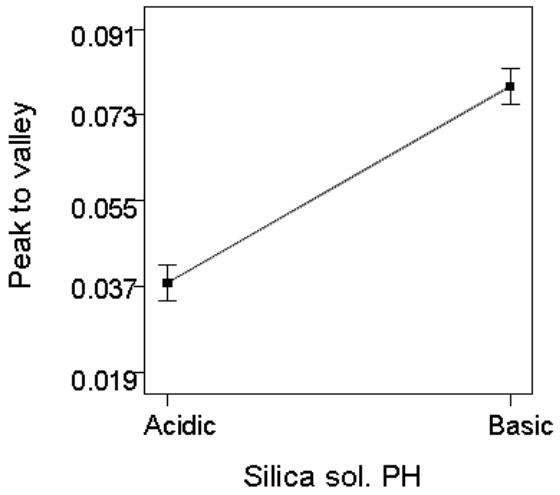

A.

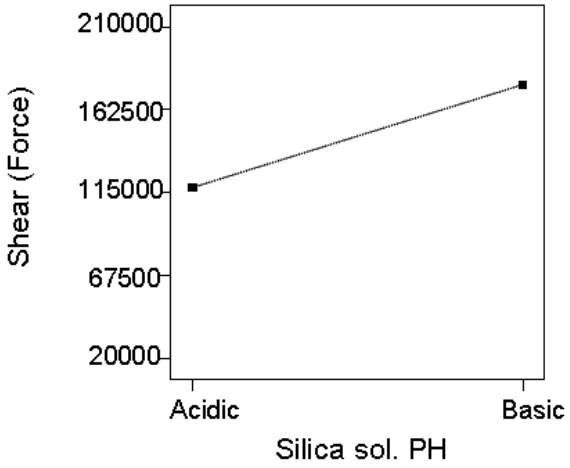

B.

Figure 4.5 The effect of the silica solution pH on the (**A**) optical and (**B**) mechanical properties of DAR/SiO_2 NP films.

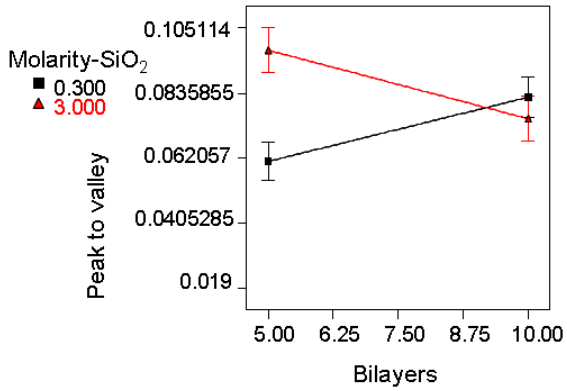

A.

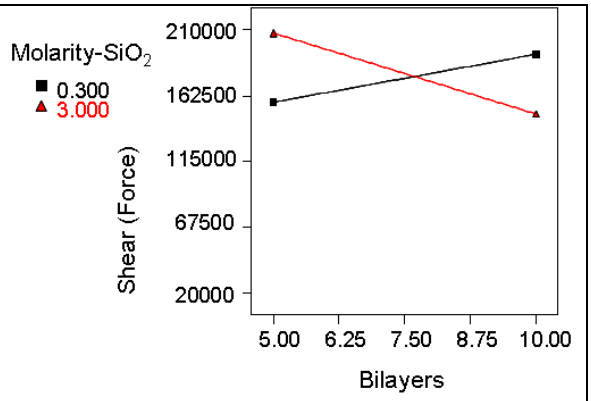

B.

Figure 4.6 Interaction plot involving the factors "molarity-SiO_2" and "number of bilayers" and their effect on the (**A**) optical and (**B**) mechanical properties of DAR/SiO_2 NP films.

Once these critical factors were identified, the plan was to incorporate them in a follow-up statistical experimental design known as "Response Surface Experiments". To reiterate, the goal of Factorial Design is to identify the factors that significantly affect the response variables. Once those factors have been determined, Response Surface Experiments are used to find the factor settings that optimize the response. Typically the response variables used in the Factorial Design are also used in Response Surface Experiments. At this time however it was realized that the Peak-to-Valley response variable was an unreliable choice to quantify the uniformity of the coatings. The reason for this was because the first order maximum/minimum was measured only for the 5-bilayer coatings. Since the first order interference fringe of the 10-bilayer coatings was somewhere in the near IR and beyond the measuring range of the instrument, the second order maximum/minimum was measured and represented the Peak-to-Valley for the thicker coatings. This naturally was an unfair comparison since the second order interference peaks are typically smaller in amplitude compared to the first order peaks. Because of this Peak-to-Valley was deemed unsuitable as an optical response variable. In place of Peak-to-Valley, I chose to quantify the homogeneity of the coating by measuring the relative amount of diffuse scattering by optical spectroscopy. Rayleigh scattering occurs when light is scattered by particles that are much smaller than the wavelength of the light. If light is subjected to Rayleigh scattering by a non-absorbing medium (**Figure 4.7**), there will be a linear correlation between the extinction

coefficient (1-T-R) and $1/\lambda^4$, where T and R refer to the transmission and reflection coefficients, respectively, and λ is the wavelength of light. The relative amount of Rayleigh scattering in the films was quantified by how large or small this slope was. A larger relative slope implies that more diffuse light scattering occurs as it passes through the film. The slope was calculated in the 450-850 nm wavelength range in order to avoid strong absorption of glass and diazo-resin at shorter wavelengths. Finally another optical response variable was added, but given less priority. The variable was the optical thickness/bilayer, and it was incorporated into the design as a way to monitor film growth. The optical thickness of the film can be estimated by using the quarter wavelength equation. If one were to identify the wavelength at which the 1st order minimum occurs, the equation is simply:

$$OT = \lambda/4 \text{ (for } 1^{st} \text{ order minimum)},$$

where OT is the optical thickness (film index of refraction*physical thickness). If only the 1st order maximum can be seen in the measured spectral range, then the equation becomes:

$$OT = \lambda/2 \text{ (for } 1^{st} \text{ order maximum)}$$

If the 1st order fringes cannot be seen in the measured spectral range, then the optical thickness can be calculated by identifying the nth order minimum and maximum, and plugging them into the following equation:

$$OT = (\lambda_{n,min} - \lambda_{n,max})/2,$$

where $\lambda_{n,min}$ and $\lambda_{n,max}$ are the wavelengths corresponding to the nth order minimum and maximum, respectively.

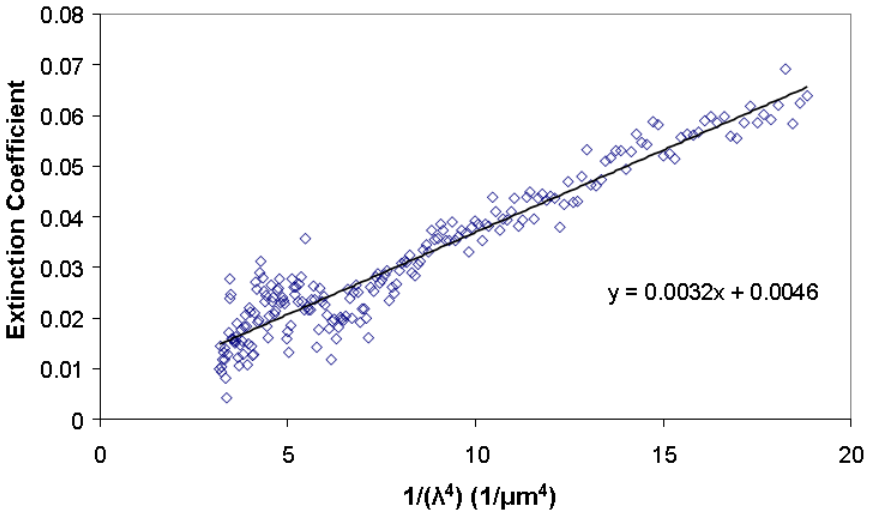

Figure 4.7 Evidence of Rayleigh scattering in a DAR/SiO_2 NP film, as a linear correlation exists between the extinction coefficient (1-T-R) and $1/\lambda^4$.

For the Response Surface Experiments, the mechanical strength was again quantified by a tape peel test. This time however I was able to procure a Tape Peel Tester, a far superior alternative to the previous tape peel design (**Figure 4.4**). The instrument was originally configured to perform 180° tests, but it was modified in order to conduct 90° tests (**Figure 4.8**) in accordance with military specifications. For more information about the peel tests, see **Chapter 3**.

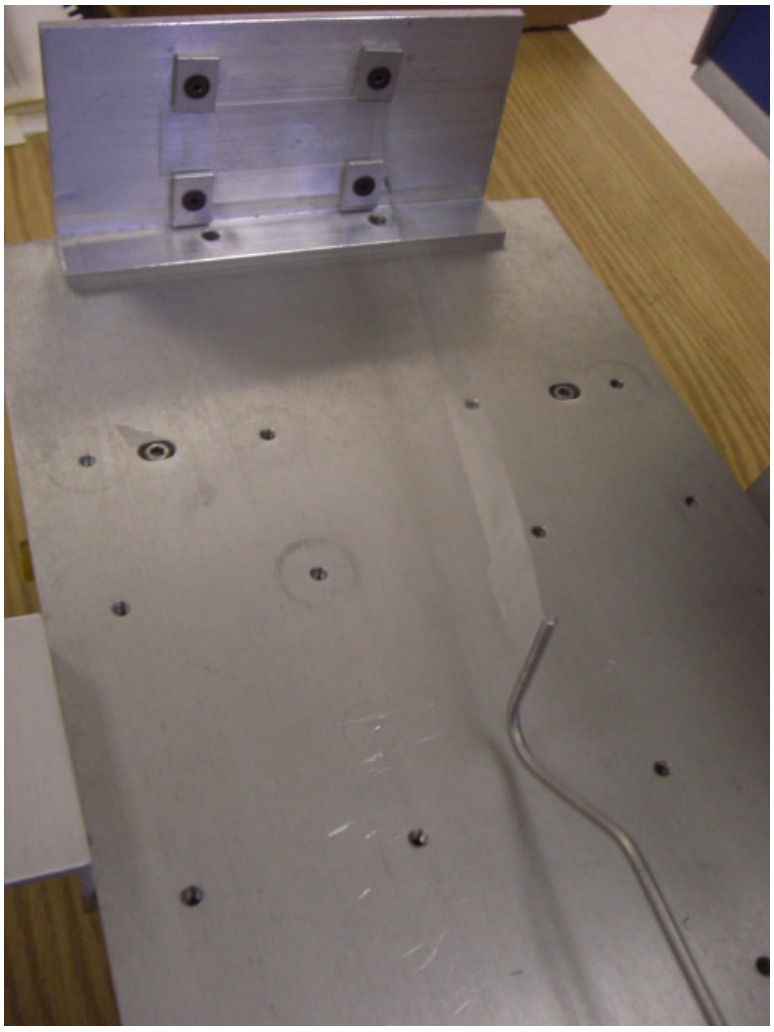

Figure 4.8 Configuration of 90° tape peel tester. The glass substrate is held in place against a metal plate (top). A piece of cellophane tape joins the substrate and a hook (bottom) attached to a force sensor. In order to collect measurements, the stage holding the substrate moves away from the platform with the hook and force sensor at a constant velocity.

The type of Response Surface Experiment used for the study is known as a Central Composite Design (CCD) (**Figure 4.9**). A CCD consists of three different sets of runs: factor levels, center points, and axial points. The factor levels are the same as those in factorial design and are off-axis in parameter space. The center points are typically replicated a number of times in order to improve the statistical power of the experiment. Finally the axial points are on-axis factor levels that are outside of the "high" and "low" points defined by said factor levels. With

this set of points defining the parameter space, it is possible to construct models of the response variable up to second order (quadratic).

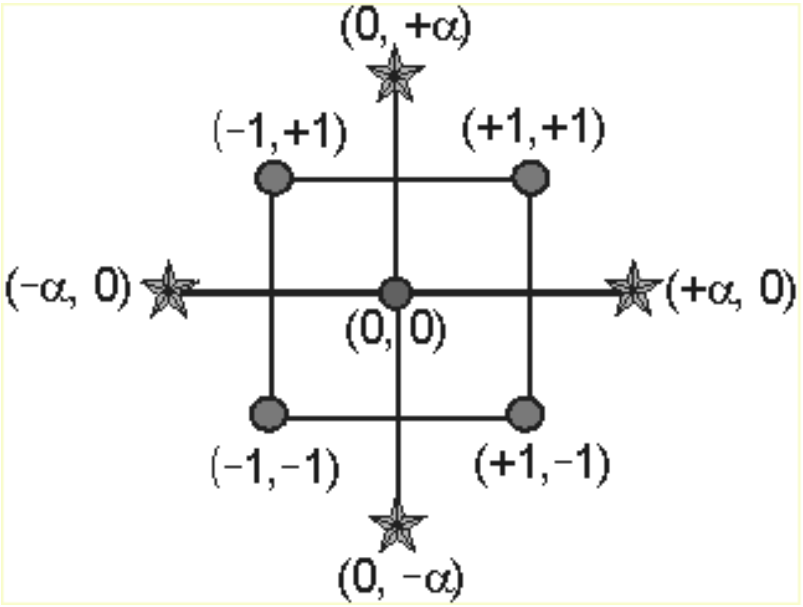

Figure 4.9 Two dimensional Central Composite Design (CCD).

The CCD consisted of three numerical factors (**Table 4.3**), namely the "pH of silica nanoparticle solution", "molarity of SiO_2 in solution", and "UV exposure time". These factors varied over five levels according to the experimental design. The "number of bilayers" was treated as a categorical factor because I witnessed differing tape peel failure mechanisms for 5- and 10-bilayer coatings in the factorial design. Tape peel tests on 5-bilayer coatings resulted in a complete removal of the film from the substrate, while tests on 10-bilayer coatings only partially removed the film (cohesive failure). Therefore 5 bilayers was treated as "low" and 10 as "high". When a categorical factor is incorporated into a design, all of the design points corresponding to the numerical factor are repeated for both high and low levels of the categorical factor. The center point can be replicated as many times as desired, but I chose to replicate this set of conditions 6 times. Hence a typical 3-factor CCD with 6 center point replicates requires a total of 20 experiments, but since a categorical factor was added to the design the total number was doubled to 40. The number of center point runs was also doubled from 6 to 12. The resulting response surface model indicated, however, that the processing conditions required to optimize the coating's mechanical strength lay outside of the tested CCD parameter space. Furthermore,

questions arose regarding the interpretation of the observed tape peel failure modes and the corresponding Shear values produced by the tape peel tester. The ambiguous results of the tape peel data meant that this particular test was best suited to supplement other tests of mechanical strength as opposed to being the primary response variable.

Factors	Factor Levels
pH of silica nanoparticle solution	8.5, 9.11, 10, 10.89, 11.5
Molarity of SiO_2 in solution	0.3, 0.85, 1.65, 2.45, 3.0 moles/liter
UV exposure time	3, 4.42, 6.5, 8.58, 10 minutes
Number of bilayers	5, 10

Table 4.3 Factors included in the CCD and their respective levels. The "number of bilayers" was treated as a categorical factor, and thus was only varied over two levels.

The DAR/SiO_2 NP films possessed excellent optical properties. Transmittance (**Figure 4.10**) and reflectance (**Figure 4.11**) measurements were taken in the UV-VIS regions for coatings consisting of 2, 4, 6, 8, and 10 bilayers. The measured R and T values have been plotted versus $1/\lambda$ (μm^{-1}). The transmittance peak and reflectance minima shifts clearly indicate an increase in film thickness with the number of deposited bilayers. The coatings have very high transmittance (~99%) and very low reflectance (<0.3%), owing to the void interstices present in the nanoparticle network.

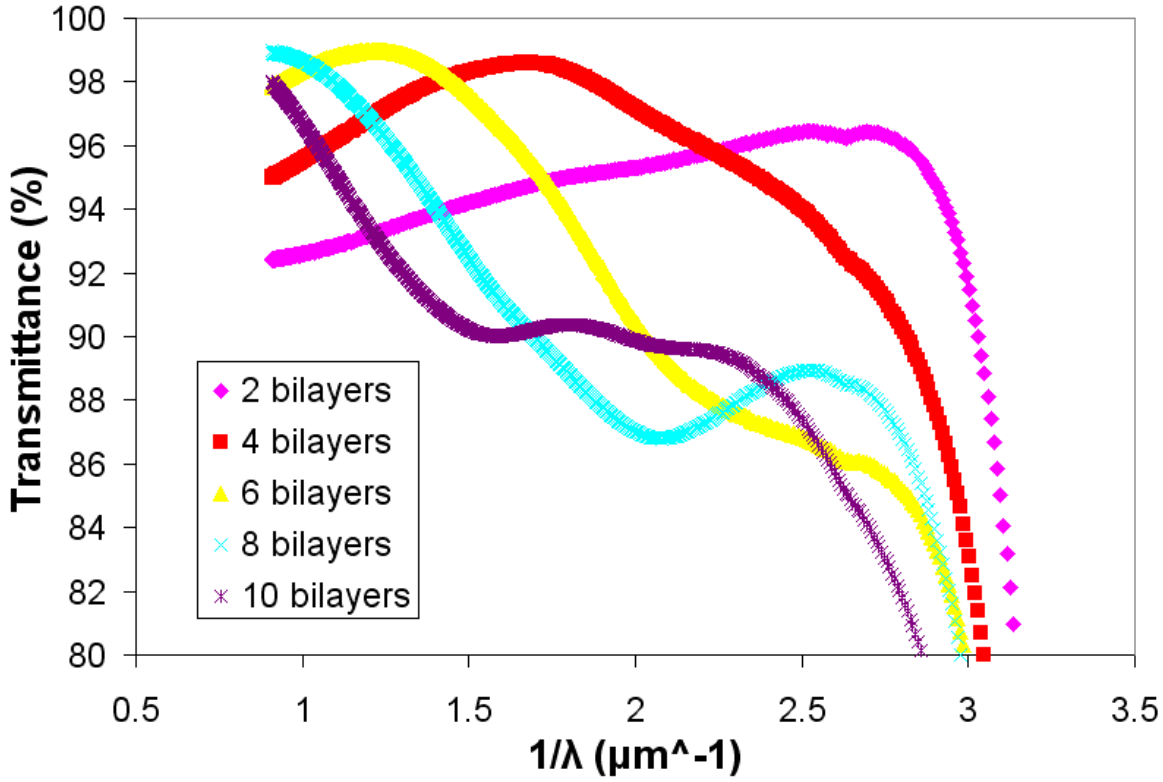

Figure 4.10 Plot of transmittance versus 1/λ as a function of the number of deposited bilayers.

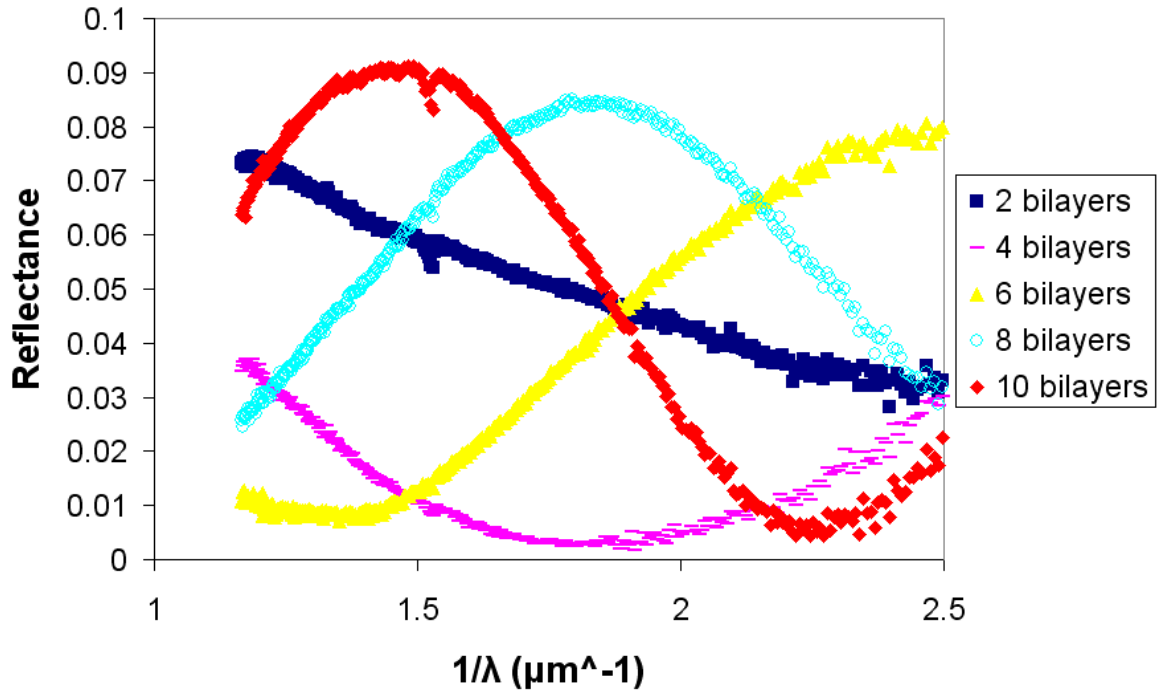

Figure 4.11 Plot of reflectance versus 1/λ as a function of the number of deposited bilayers.

Ellipsometry measurements

Ellipsometric measurements were performed on 2-, 4-, 6-, 8-, and 10-bilayer DAR/SiO_2 NP films in order to better estimate their thickness and porosity. Several models were implemented to determine which best matched the measured values of ψ and Δ with respect to wavelength. The tested models were: a single layer of surface roughness consisting of 50% silica and 50% void (SR), a single Effective Medium Approximation layer consisting of varying amounts of silica and void (EMA), and finally a single EMA layer with an added layer of surface roughness on top (EMA+SR). The models were fit to the data acquired for each film, and the thicknesses determined according to each model (**Figure 4.12**). For each of the models studied, I found relative agreement with respect to film thickness as a function of the number of bilayers. In order to determine the optimal model for the DAR coatings, the resulting mean-squared error (MSE) for each fit was plotted versus the number of bilayers (**Figure 4.13**). It can be argued that all of the models sufficiently described the composition of the 2 and 4 bilayer coatings given their relatively low MSE values. The MSE of the SR model however, sharply increased for coatings exceeding four bilayers, and thus did not accurately describe the film composition above that limit. The MSE of the EMA layer slowly increased up to eight bilayers, and sharply increased at ten. The MSE of the EMA+SR model however, remained fairly small regardless of film thickness, and therefore best described the film composition.

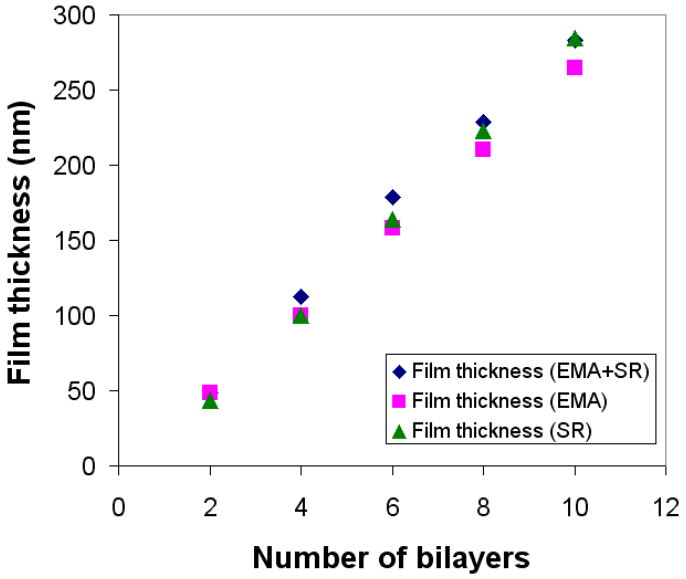

Figure 4.12 Thickness comparison of different models that were fit to experimental data for 2-, 4-, 6-, 8-, and 10-bilayer DAR coatings. The models of interest were: (▲) single layer of surface roughness, (■) a single EMA layer consisting of silica and void, and (♦) an EMA layer followed by a layer of surface roughness.

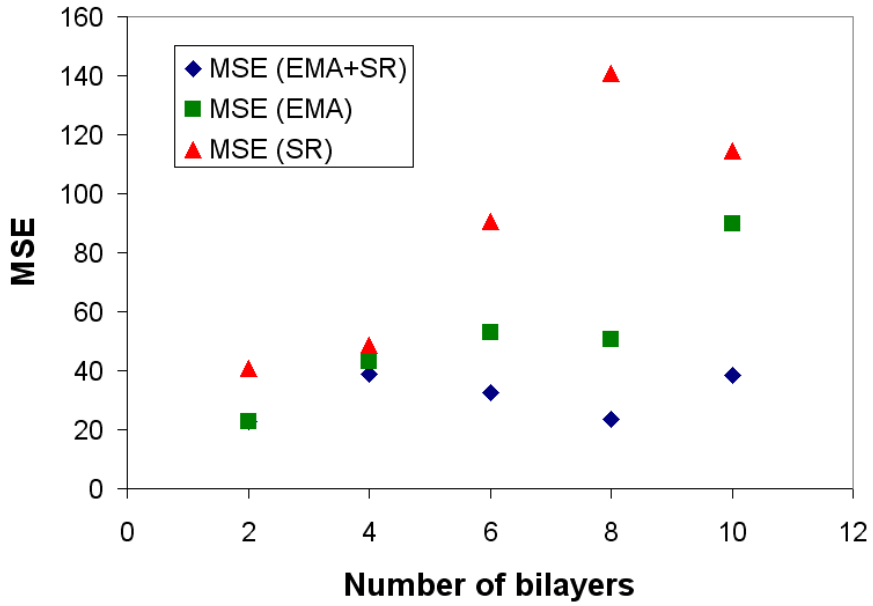

Figure 4.13 MSE values of (▲) a single layer of surface roughness, (■) a single EMA layer of silica and void, and (♦) a composite layer of EMA and surface roughness, plotted with respect to the number of deposited bilayers.

Using the composite EMA+SR model, the void fraction was determined as a function of the number of bilayers (**Figure 4.14**). As the first layer of nanoparticles is deposited onto the substrate, it is simultaneously attracted to the positively charged monolayer of diazo-resin already on the surface and repelled by neighboring nanoparticles. If the repulsion is not strong enough to overcome the attractive forces, the nanoparticles tend form tiny aggregate islands. This results in poor nanoparticle coverage on the surface. The large void fraction for two bilayers in **Figure 4.14** confirms this well-documented behavior.[11,12] The void regions of the substrate are eventually filled in as additional nanoparticles are adsorbed. This typically happens after four or five bilayers have been deposited, and the film begins to resemble a completely homogenous layer of silica with interstitial voids. This explains why the MSE of the SR model dramatically increases above four bilayers because a pure layer of surface roughness can not sufficiently describe such a structure. With continued deposition of silica nanoparticles, the structure more closely resembles a random closed-packed (RCP) configuration, which has a theoretical void fraction of 36%. The inability, however, of the nanoparticles to completely conform to an RCP structure leads to a higher void fraction, and reduces the reflectance. A plot of the coating refractive index (λ = 400 nm) versus the number of bilayers can be seen in **Figure 4.15**. I found that the refractive index increased dramatically from two to four bilayers, which was a result of the increasing surface coverage of nanoparticles on the substrate. From four to ten bilayers, a gradual increase in the refractive index was observed, which corresponds to the decrease in void fraction seen in **Figure 4.14**. The refractive index is still considerably less than the theoretical prediction of 1.32 for an RCP structure even after ten deposited bilayers.

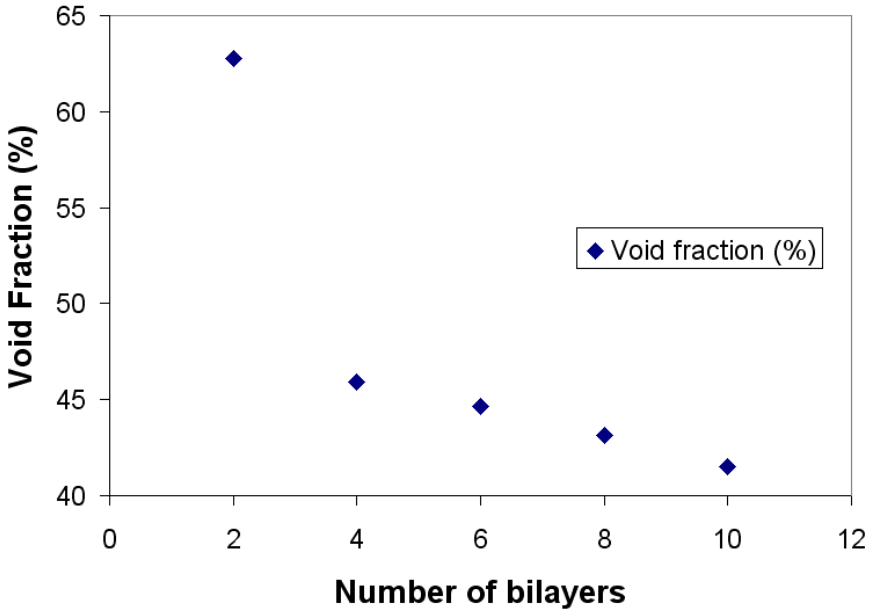

Figure 4.14 Void fraction versus the number of bilayers as determined by ellipsometry using the EMA approximation. As the film thickness increases, the void fraction approaches the theoretical value for an RCP structure.

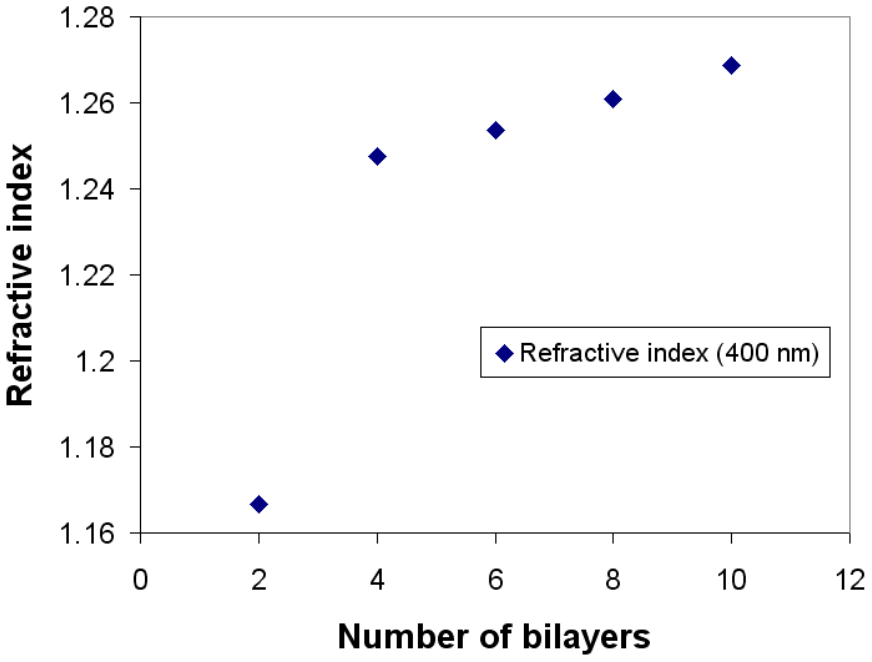

Figure 4.15 Refractive index (λ = 400 nm) as a function of the number of bilayers.

I wanted to compare film thicknesses determined by ellipsometry and hand calculation. Film thickness by "hand calculation" was determined by dividing the optical thickness by the film refractive index at λ = 400 nm (obtained by ellipsometry). The results are shown in **Figure 4.16**, where the thickness is plotted versus the number of bilayers, and in **Table 4.4**. The reported ellipsometric thickness measurements include both the EMA silica/void layer plus the layer of surface roughness. Clearly, the growth of DAR/SiO_2 NP films is linearly dependent on the number of deposited bilayers. The agreement between both thickness calculations is quite good, with the thickness/bilayer values within 4% of each other. Thus the DAR/SiO_2 NP films demonstrate linear growth, and can yield clean spectral data that permit consistent, accurate calculations of thickness by simple or rigorous means.

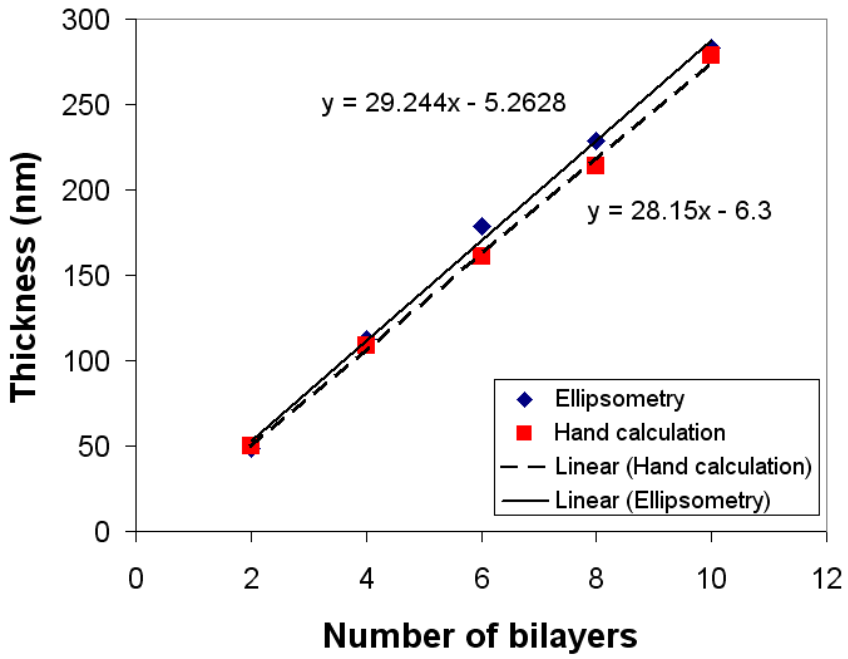

Figure 4.16 Film thickness versus the number of bilayers as determined by ellipsometry (solid line) and hand calculation (dashed line). Uniform growth per bilayer is observed regardless of which method was used to calculate the thickness.

Number of bilayers	Thickness determined by calculation (nm)	Thickness determined by ellipsometry (nm)
2	50	49
4	109	112
6	161	179
8	214	229
10	279	283

Table 4.4 Comparison of film thickness as determined by ellipsometry and hand calculation.

Finally the values of the surface roughness layer from the EMA+SR model were plotted versus the number of bilayers (**Figure 4.17 A.**). From the figure it can be seen that the surface roughness steadily increased with increasing film thickness. This can be cause for concern since the mechanical stability of a film can be compromised with a sufficiently large increase in surface roughness.[13] The reported roughness of 0 nm at two bilayers under the EMA+SR model is not likely however, since the composition of aggregate nanoparticle islands constitutes a purely rough surface. It is plausible however to use the SR model in this case since it more accurately describes a rough surface, and has a fairly comparable MSE value to the EMA+SR model. The Rayleigh scattering slope (see **Figure 4.7**) was measured for each of these films and plotted against the corresponding number of bilayers (**Figure 4.17 B.**). The Rayleigh scattering slope, like the surface roughness, increased linearly with the number of deposited bilayers. Finally, the Rayleigh scattering slope was plotted against the surface roughness (**Figure 4.17 C.**). The linear fit of the data indicates that the increased roughness associated with increasing film thickness is responsible for the increase in Rayleigh scattering of light incident on the film. In short, the scattering of light is due to the irregular surface created by the nanoparticles and not by the bulk film. Yancey and coworkers[14] reported a similar phenomenon with ISAM films containing 45 nm silica nanoparticles and PAH. While they reported an initial increase in the Rayleigh slope with the film thickness, they found that the slope leveled off above thicknesses of 150 nm. Furthermore, they attributed light scattering to the surface properties of the film but did not provide surface roughness data to correlate with the Rayleigh scattering slope. In contrast to their results, the Rayleigh slope of DAR/SiO_2 NP films does not level off even at thicknesses approaching 300 nm. This could be explained by the fact that different polymers were used in the respective experiments. In Yancey's work, aqueous PAH solutions with pH values of 7 and 9 were used to make the films. In comparison, the DAR solutions had a pH value less than 1.

The high acidity of this solution would reduce the surface charge on the nanoparticles during the polycation immersion steps. This, in turn, could have promoted nanoparticle reorganization and aggregation at the surface each time the substrate was dipped in DAR. Such a scenario, while purely speculative at this point, could explain why the Rayleigh slope of DAR/SiO_2 NP films continued to increase rather than level off.

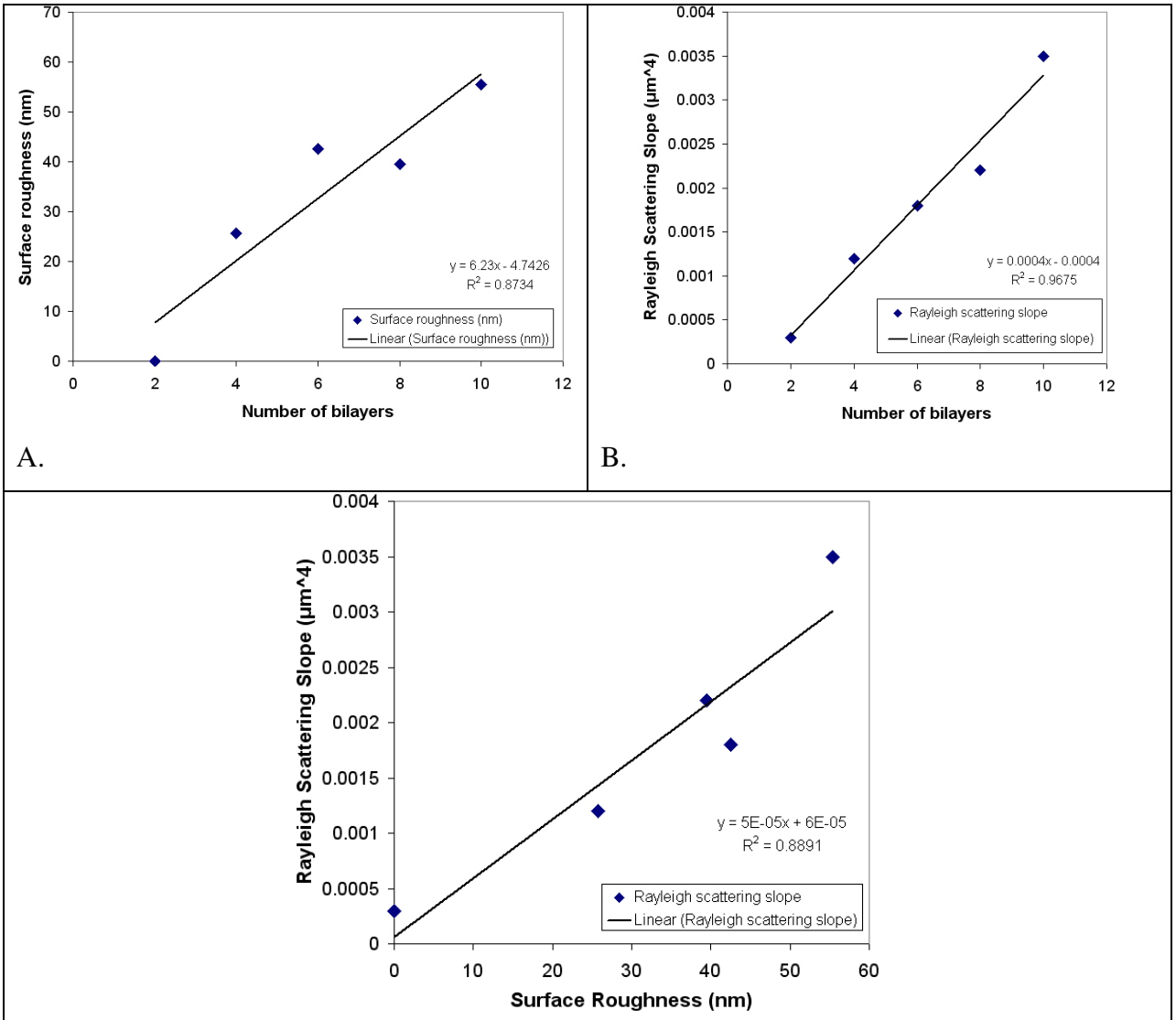

Figure 4.17 Surface roughness as determined by ellipsometry versus the number of bilayers (A), the Rayleigh scattering slope versus the number of bilayers (B), and finally the Rayleigh scattering slope plotted against the surface roughness (C).

Atomic force microscopy

Atomic force microscopy images were taken on a 5-bilayer DAR/SiO_2 NP film in order to better understand its packing structure and to determine the surface roughness. The image shown (**Figure 4.18**) was taken over a 4 μm^2 surface and revealed that the nanoparticles were not completely dispersed. Not surprisingly, the formation of the film appears to take place through the attraction of larger clusters of silica nanoparticles with one another. The result is a nano-scaled surface that is dominated by nanoparticle mountains and valleys, with an RMS surface roughness of 22.5 nm.

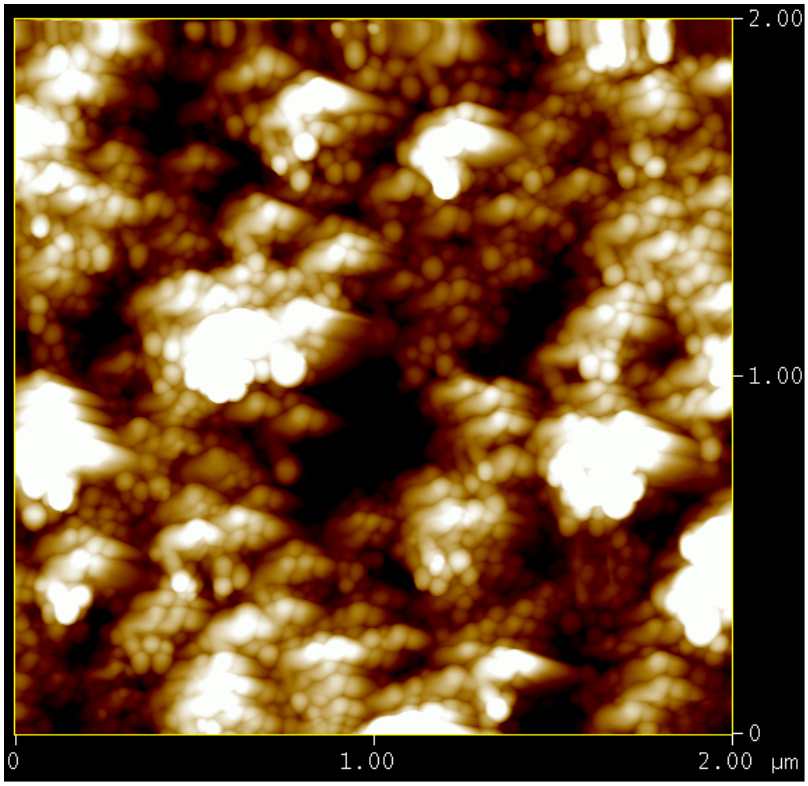

Figure 4.18 AFM image of a DAR/SiO_2 NP AR coating.

Therefore a number of forces were at work with competing influences over the optical and mechanical properties. The lack of a completely dispersed nanoparticle structure increased the porosity of the film, which decreased the refractive index and resulted in very high transmission with low reflectivity. On the other hand, a well-dispersed colloidal suspension will keep nanoparticle aggregation to a minimum, and improve the overall cohesion. Furthermore,

one would observe minimal surface roughness, which would improve surface adhesion and reduce surface scatter of light at shorter wavelengths in the visible. The degree of film porosity, however, will ultimately determine its optical performance.

Failed Cross-Linking of DAR/SiO_2 NP Films

To recap the goal of the response surface experiment was to optimize the AR coating performance by finding appropriate parameter settings that maximize the experimental response variables. After acquiring the relevant data necessary for the response variables, Design Expert® identified the factor settings that improved both the optical and mechanical properties. The films were highly uniform, and thus the optical properties were acceptable. The mechanical strength by contrast, was marginally better. The premise of exposing the DAR/SiO_2 NP films to UV was to initiate cross-linking between the ISAM constituents. The solvent test conducted by Sun[3] was an effective method to determine if the bonds were converted from ionic to covalent, so the DAR/SiO_2 NP films were put through a similar test. As described by Sun, the ternary solvent consisted of a mixture of H_2O:dimethylformamide (DMF):$ZnCl_2$ (3:5:2 by weight). Five-bilayer DAR/SiO_2 NP films with (10 minutes) and without UV irradiation were dipped in the solvent for 30 minutes and then thoroughly rinsed with deionized water. Unfortunately, neither film survived immersion in the solvent. On the other hand this helped explain why the mechanical stability wasn't dramatically better after the optimization experiments. The fact that the UV-exposed films were dissolved in solvent clearly indicated that UV cross-linking did not occur. Furthermore, it showed that the reaction scheme in **Figure 4.2** was incorrect. Of particular interest is the fact that Sun linked a progressive decrease in absorbance at 380 nm with increased UV exposure, to the successful decomposition of the diazonium group. I attempted to make a similar comparison and measured the absorbance of 5- (**Figure 4.19**) and 10- (**Figure 4.20**) bilayer DAR/SiO_2 NP films at 380 nm as a function of UV irradiation. In both 5- and 10-bilayer cases the absorption peak completely disappeared within 1 minute of UV irradiation. Therefore while degradation of the peak is indicative of structural decomposition of diazo-resin, it does not necessarily imply that cross-linking has occurred. The diazo-resin apparently cannot cross-link with the surface hydroxyl groups of the silica nanoparticles but requires sulfonate groups instead.

Thus, an alternative approach needed to be developed to successfully cross-link the DAR/SiO_2 NP network. That approach is discussed in the following section (**Section 4.2.2**).

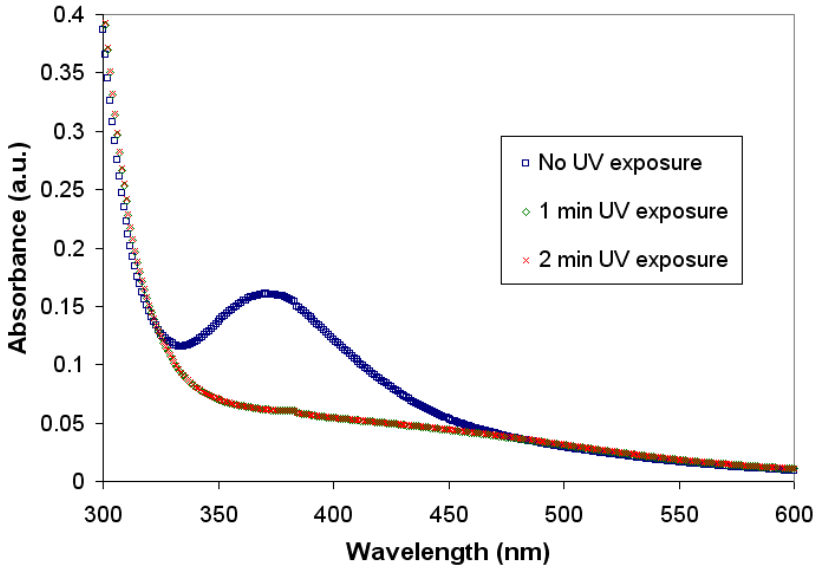

Figure 4.19 Absorption spectra for a 5-bilayer DAR/SiO_2 NP coating as a function of UV exposure time. Complete degradation of the absorption peak at 380 nm occurs within 1 minute of exposure.

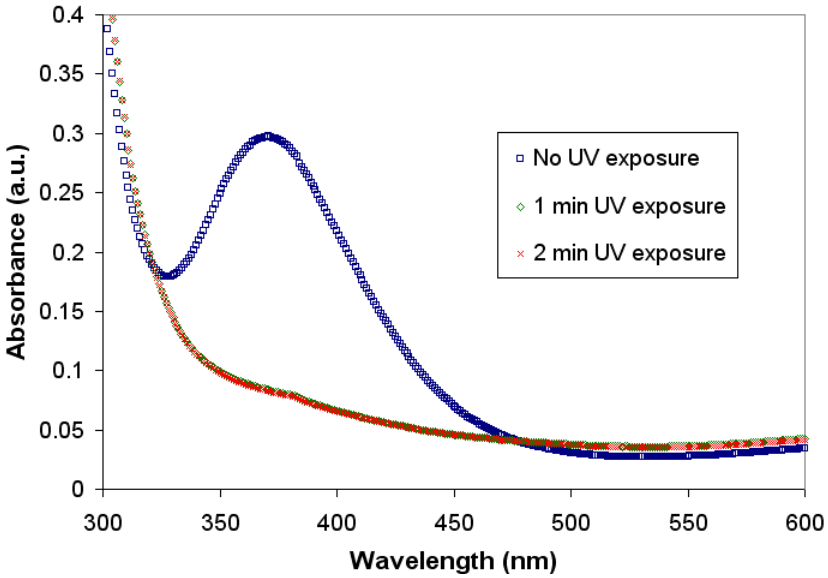

Figure 4.20 Absorption spectra for a 10-bilayer DAR/SiO_2 NP coating as a function of UV exposure time. Complete degradation of the absorption peak at 380 nm occurs within 1 minute of exposure.

4.2.2 Alternative Method to Cross-Link Diazo-Resin and Silica Nanoparticle ISAM Films

By immersing the DAR/SiO_2 NP films into a ternary solvent, I discovered that the UV treatment did not cross-link the ISAM network. As a result, a different approach was needed. A common theme in most of Sun's work was that diazo-resin was successfully cross-linked with various polyanions containing sulfonate and carboxyl groups. A particular work in which Sun collaborated with Fu[15] showed that diazo-resin could be cross-linked with Au nanoparticles. In order to accomplish this 3-mercapto-1-propanesulfonic acid sodium salt was mixed with the gold nanoparticles. Naturally the thiol preferentially bonded to the gold surface, and left an exposed sulfonate group which also stabilized the colloidal suspension. They also put sulfonate groups on the glass substrate surface by silylating it with 3-mercaptopropyl trimethoxysilane (MPTS). This idea was also used by Wu[16] and coworkers around the same time to improve the photocatalytic activity of TiO_2 films. The terminal –SH functional groups were later oxidized to sulfonic acid by immersion in a 30 % H_2O_2/HOAc (1:5 v/v) mixture for 30 minutes. Films comprised of DAR/Au nanoparticles were then exposed to the ternary solvent for 90 minutes. The films not irradiated by UV were mostly dissolved, while 80% remained of the films with UV treatment. This means that the UV irradiation cross-linked most of the film (**Figure 4.21**). The results of this published work served as the catalyst and motivation for my approach to improve the mechanical strength of the DAR/SiO_2 NP films because it demonstrated successful cross-linking of the polycation to sulfonate-bearing nanoparticles. As a result, I decided to coat both the glass surface and silica nanoparticles with material such that their surface contained sulfonate groups. Next I will discuss the process of silylating glass with MPTS and subsequent stability tests of a DAR monolayer cross-linked onto the silane layer.

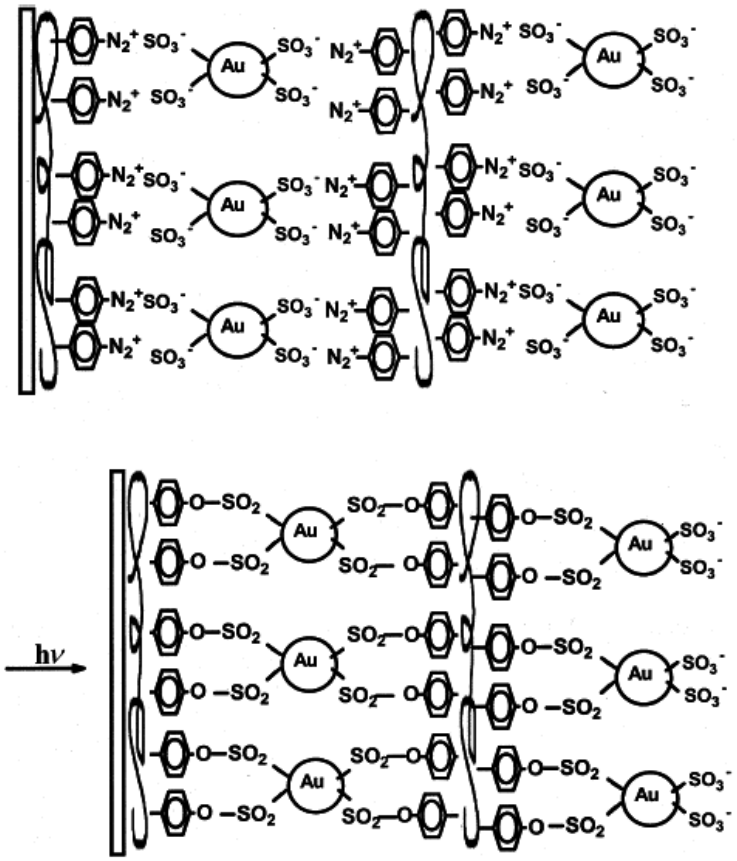

Figure 4.21 UV cross-linking of diazo-resin and sulfonate-bearing Au nanoparticles. [Y. Fu, H. Xu, S. L. Bai et al., "Fabrication of a stable polyelectrolyte/Au nanoparticles multilayer film," Macromolecular Rapid Communications **23** (4), 256-259 (2002)].[15] Copyright Wiley-VCH Verlag GmbH & Co. KGaA. Reproduced with permission.

Preparation and Deposition of the Silane Monolayer and Stability Test of Adsorbed DAR

The procedure for silylating glass substrates was fairly similar to the one used by Wu.[16] Seven mM of 3-mercaptopropyl trimethoxysilane (**Figure 4.22**) in methanol was prepared. Piranha-etched glass substrates were immersed and kept in the silane for approximately 18 hours. After this the substrates were rinsed with methanol, dried with N_2 gas, and dipped in a H_2O_2/CH_3COOH (1:5 v/v) bath heated to 70 °C for approximately 50 minutes. This bath converted the thiol group into a sulfonic acid.

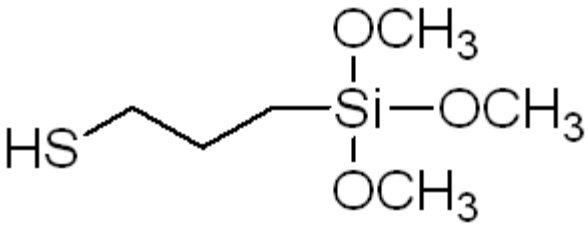

(3-Mercaptopropyl)trimethoxysilane [MPTS]

Figure 4.22 Molecular structure of MPTS. The thiol group (SH) is later oxidized to a sulfonic acid. Permission granted by Sigma Aldrich for use and reproduced from: http://www.sigmaaldrich.com/catalog/ProductDetail.do?lang=en&N4=175617|ALDRICH&N5=SEARCH_CONCAT_PNO|BRAND_KEY&F=SPEC.

A solvent test was conducted in order to determine if the silane layer could form a stable bridge between the substrate surface and the DAR/SiO_2 NP film. Three different sample types were prepared on glass substrates for the study: 1) self-assembled monolayer of MPTS, 2) a monolayer of DAR on the silane without UV irradiation, and 3) a monolayer of DAR on the silane with UV irradiation. For each sample type two samples were prepared: 1) a control which was not immersed in the ternary solvent, and 2) a sample that was dipped in the solvent for 30 minutes and thoroughly rinsed with deionized water. After this, the atomic composition (a.c.) of the samples was determined by XPS analysis. By comparing the atomic composition of the samples dipped in solvent with their control counterparts, I could determine if UV cross-linking stabilized the DAR monolayer. The molecular structure of DMF, one of the solvent constituents, can be seen below in **Figure 4.23**. This is important to note because not all of the solvent could be removed from the samples, and hence some residual carbon, nitrogen and oxygen had to be accounted for in the analysis of the atomic composition.

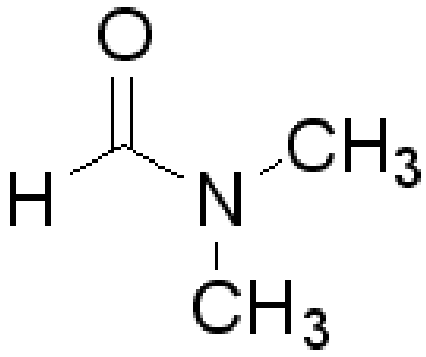

Dimethylformamide

Figure 4.23 Molecular structure of DMF, which is one of the constituents of the ternary solvent. Permission granted from Sigma Aldrich for reuse and reproduced from: http://www.sigmaaldrich.com/catalog/ProductDetail.do?lang=en&N4=D4254|SIGMA&N5=SEARCH_CONCAT_PNO|BRAND_KEY&F=RP#.

Analysis by XPS focused on the C1s, O1s, S2p, and N1s orbitals. Plots of the atomic composition versus the sample type for each of the orbitals can be seen in **Figures 4.24** (C1s), **4.25** (O1s), **4.26** (S2p), and **4.27** (N1s). The type of sample in each plot from left to right is: 1) monolayer of silane, 2) monolayer of silane in solvent, 3) DAR on silane no UV, 4) DAR on silane no UV in solvent, 5) DAR on silane with UV, and 6) DAR on silane with UV in solvent. The best way to analyze the plots below is to address each sample type separately:

MPTS monolayer on glass: The prediction before viewing the analysis results was that the silane layer would remain stable if dipped in the solvent because the molecule was covalently attached to the glass substrate. XPS did in fact confirm this prediction with relatively little change in the amount of carbon (**Figure 4.24**), oxygen (**4.25**), sulfur (**4.26**), and nitrogen (**4.27**). The small changes observed most likely can be attributed to detection of residual solvent on the sample surface. The most glaring evidence to support this assumption is the fact that the silane sample contains no nitrogen atoms, but traces of the element were detected on the sample dipped in the solvent. The molecular structure of DMF contains a nitrogen atom as shown in **Figure 4.23** thus suggesting that a small amount of solvent is still on the sample. The change in atomic composition however was quite small, and it is clear that the silane monolayer was relatively unaffected by the solvent.

DAR monolayer on MPTS without UV irradiation: The carbon a.c. of the control sample was 31.5%, while the relative amount was significantly less for the sample dipped in the solvent (15.9%). An interesting point to note is that the carbon a.c. of the solvent-dipped monolayer of DAR without UV is much closer to the a.c. of the silane layer. This means that the solvent dissolved an appreciable amount of DAR to reveal the underlying MPTS atomic structure. This approach can also be applied to the O1s orbital (**Figure 4.25**). The initial oxygen a.c. of the DAR monolayer without UV was 43.5%, but was 55.8% when dipped in the solvent. Once again the a.c. approached the value for the silane monolayer in solvent (58.1%), but was significantly different than its control (43.5%). This phenomenon can also be seen in the S2p and N1s orbitals. Since DAR contains nitrogen, it initially had a non-zero (2.1%) atomic composition. After being dipped in the solvent however the final quantity (1%) was nearly the same as the corresponding silane sample. In short, the surface properties of the DAR monolayer without UV after it had been subjected to the solvent test closely resembled the MPTS layer.

DAR monolayer on MPTS with UV irradiation: While the surface properties of the DAR monolayer without UV changed significantly and closely resembled the a.c. of the silane layer, the a.c. of the DAR monolayer with UV changed very little after immersion in the ternary solvent. It is difficult to determine if the changes in a.c. represent changes in the molecular structure, random error, or if they were due to residual solvent on the sample. Regardless the key point is that the a.c. did not undergo significant change, and thus I was able to conclude that the DAR monolayer successfully cross-linked with the sulfonate-bearing silane.

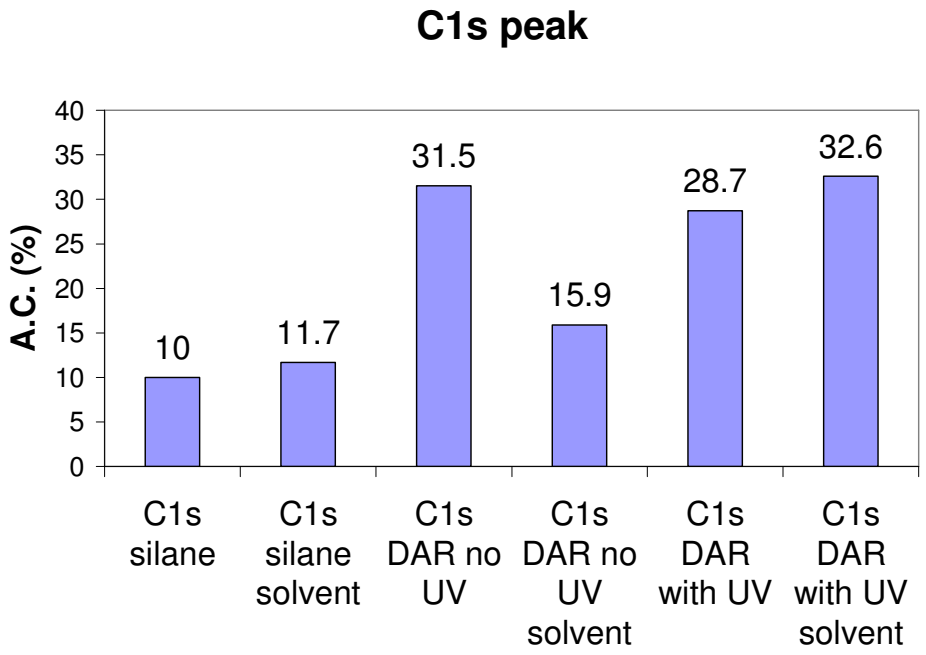

Figure 4.24 Atomic composition of the C1s orbital for each sample type dipped in solvent and control.

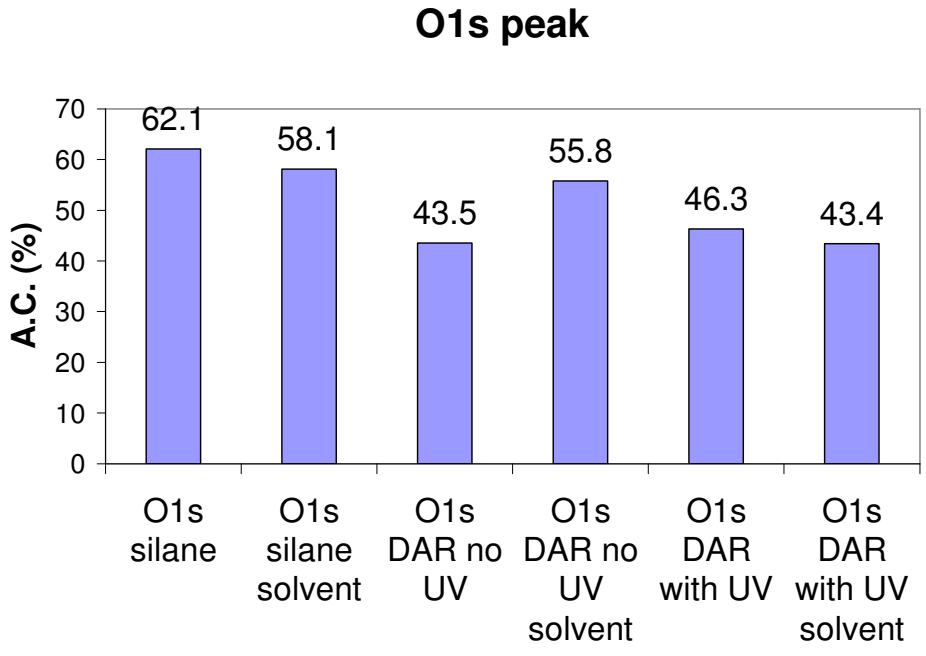

Figure 4.25 Atomic composition of the O1s orbital for each sample type dipped in solvent and control.

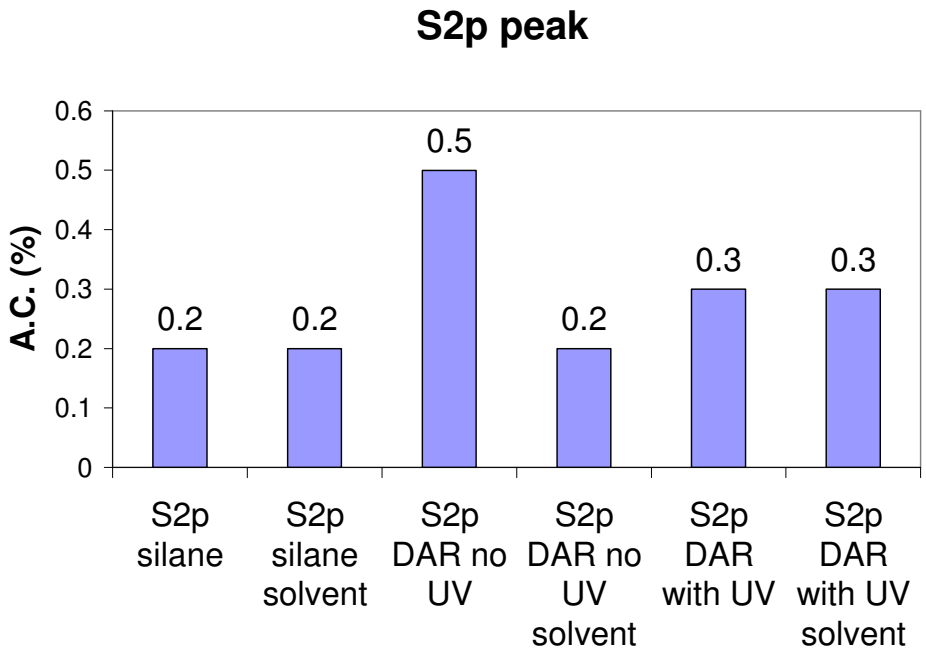

Figure 4.26 Atomic composition of the S2p orbital for each sample type dipped in solvent and control.

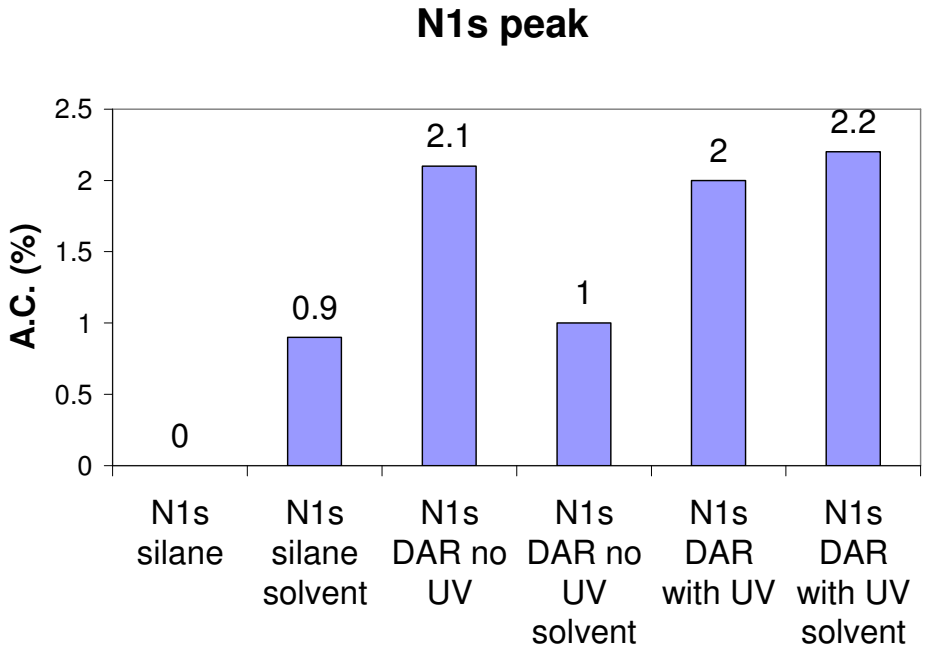

Figure 4.27 Atomic composition of the N1s orbital for each sample type dipped in solvent and control.

To summarize, the stability of UV-exposed DAR attached to MPTS was tested by solvent immersion. For comparison, samples containing an MPTS monolayer, and DAR without UV on MPTS were also dipped in the solvent. The composition of the samples was analyzed by XPS, which showed that the MPTS and DAR monolayer with UV remained intact, while the DAR layer without UV was mostly dissolved. As a result I was able to identify an approach to create a stable covalent bridge from the glass substrate to the film. The next step was to change the functional end groups of the silica nanoparticles from hydroxyl to sulfonate. By doing so it is possible to UV cross-link the entire ISAM film.

ISAM Deposition of PAH and PSS on Silica Nanoparticles for Modified Surface Functionality

With a stable bridge formed between the sulfonate-covered substrate and the first ISAM layer of DAR, the next step was to coat the silica nanoparticles with a molecule containing sulfonates. The initial plan was to silylate the colloidal silica with MPTS, which in theory should work because the surface functionality (hydroxyl groups) of the nanoparticles is the same as piranha-etched glass substrates. The problem with this approach however, is that silylation onto glass must be mediated in methanol. This would require evaporation of water from the colloidal mix, and re-suspension of the nanoparticles in methanol. After silylation the nanoparticles would need to be rinsed and re-dispersed into a heated H_2O_2/CH_3COOH bath. After sufficient rinsing the nanoparticles could then be re-suspended in deionized water. In short, the procedure would require a number of complex steps to remove and introduce the nanoparticles from one medium to another, and would result in significant nanoparticle aggregation.

A novel approach to coat spherical particles was introduced by Sukhorukov and coworkers.[17] They described ISAM assembly of polyelectrolytes onto micron-sized latex particles. The polymers used in the study were poly(allylamine hydrochloride) (PAH), poly(styrene sulfonate) (PSS), and poly(diallyldimethyl ammonium chloride) (PDADMAC). The deposition of polyelectrolytes was accomplished in two ways: 1) adsorption onto the microparticles by adding supersaturated concentrations of the ionic polymer and removing the excess by three centrifugation rinse steps, or by 2) adsorption without centrifugation, but at polyelectrolyte concentrations just below ζ-potential saturation. Particle dispersion was

maintained by adsorbing polyelectrolytes in colloidal suspensions with low concentration, and sonication after each adsorption step. As a result they were able to form a stable particle suspension with positive or negative charge. Thus, I attempted to coat the silica nanoparticles with a bilayer of PAH and PSS (**Figure 4.28**), meaning that the outermost layer would consist of sulfonate end groups. These modified nanoparticles could then be deposited onto glass with DAR and subsequently exposed to UV to convert the ionic bonds into covalent ones. Using this approach ionic bonds would only exist at the nanoparticle surface; that is, between the nanoparticle surface and the polyelectrolyte layers on its surface. The assumption was, however, that the polycation would have a sufficiently strong electrostatic interaction with the nanoparticle because it would, if fully charged, lay relatively flat along the nanoparticle surface. The next adsorbed polymer layer (polyanion) would also strongly interact with its oppositely-charged counterpart. Hence, the strength of the interaction of the polymers adsorbed onto the nanoparticles is akin to all-polymer films on glass, which typically possess excellent mechanical strength.

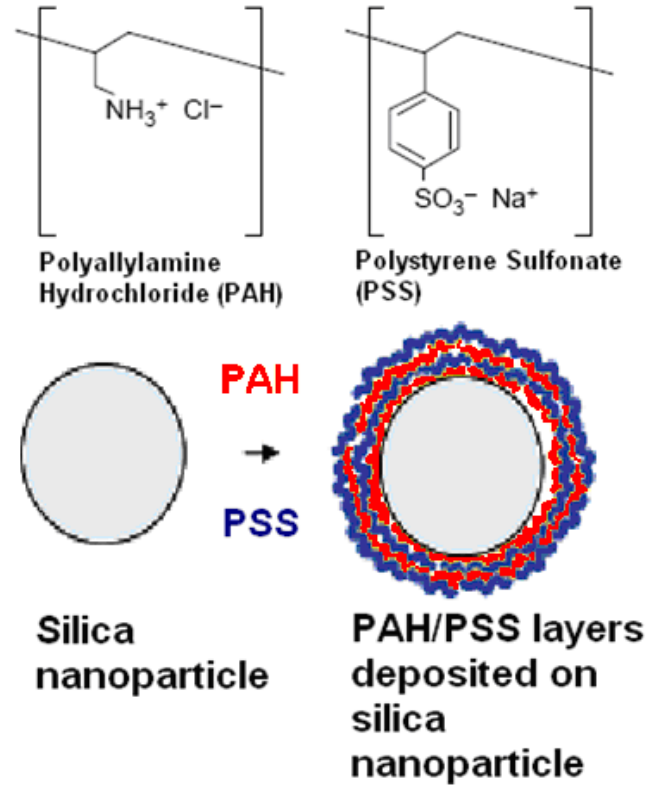

Figure 4.28 ISAM deposition of PAH and PSS onto silica nanoparticles. PAH and PSS images are from: [G. Decher, "Fuzzy nanoassemblies: Toward layered polymeric multicomposites," Science **277** (5330), 1232-1237 (1997)]. Reprinted with permission from AAAS. Image of ISAM deposition on silica nanoparticle is adapted with permission from: [D. Radziuk, D. G. Shchukin, A. Skirtach et al., "Synthesis of silver nanoparticles for remote opening of polyelectrolyte microcapsules," Langmuir **23** (8), 4612-4617 (2007)].[17] Copyright 2007 American Chemical Society.

I decided to determine the ζ-potential saturation point for the respective polyelectrolytes as they were added to the silica nanoparticles. First, I reduced the silica nanoparticle concentration from 3.76 to 0.376 M to minimize unwanted aggregation resulting from polymer addition to the colloidal suspension. The polymers were mixed overnight with the solution in order to completely dissolve in solution and adsorb onto the nanoparticles. Various amounts of PAH were added to the silica nanoparticle solution to determine the concentration at which the ζ-potential became saturated. **Figure 4.29** is a plot of the ζ-potential versus the PAH concentration. Without any polymer added to the solution, the nanoparticles were highly stable

(**Figure 4.30A left**), with a ζ-potential of -46 mV. After adding 1 mM of PAH (**Figure 4.30A right**), the ζ-potential increased to nearly -20 mV. This solution was only partially stable. As some of the particles were neutralized, aggregation occurred, and the aggregates settled to the bottom. The generally accepted stability range for colloids is above ± 20 mV, with highly stable solutions possessing a ζ-potential above ± 40 mV. Concentrations of 2 and 3 mM PAH (**Figure 4.30B**) effectively destabilized a significant fraction of the nanoparticles, though an appreciable amount of colloid remained in suspension. Consequently, the ζ-potential could not be accurately determined for these samples. Complete phase separation of PAH-coated silica occurred when the concentration was increased to 4 and 5 mM (**Figure 4.30C**). The silica nanoparticles became positively charged and stable when 6 and 7 mM of PAH were added (**Figure 4.30D**). There was minimal aggregation in the case of 6 mM PAH, but none was observed with the 7mM sample. Furthermore, the ζ-potential was in the highly stable range, with a value above + 50 mV. It is also clear from **Figure 4.29** that the potential begins to saturate around 7 mM. Hence, this was determined to be the ideal PAH concentration needed for optimal NP surface coverage.

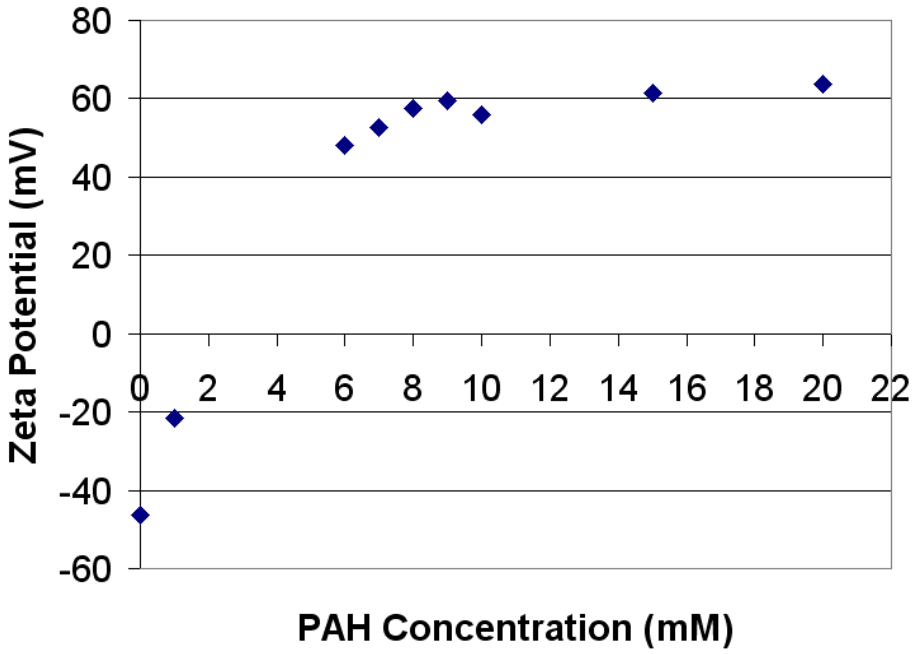

Figure 4.29 ζ-potential versus the concentration of PAH in 0.376 M silica nanoparticle solution. The initially negatively charged nanoparticles become a positively stable colloid when adding more than 6 mM of PAH.

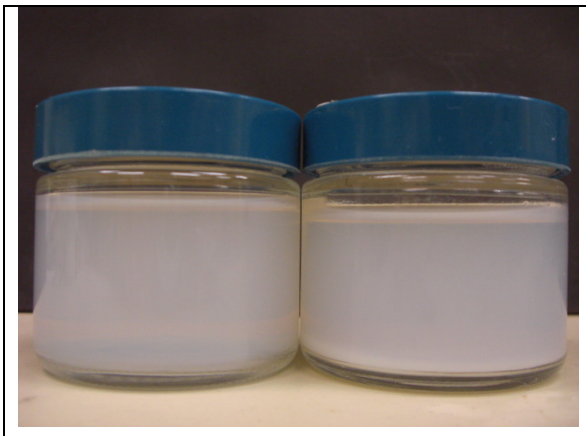

A.

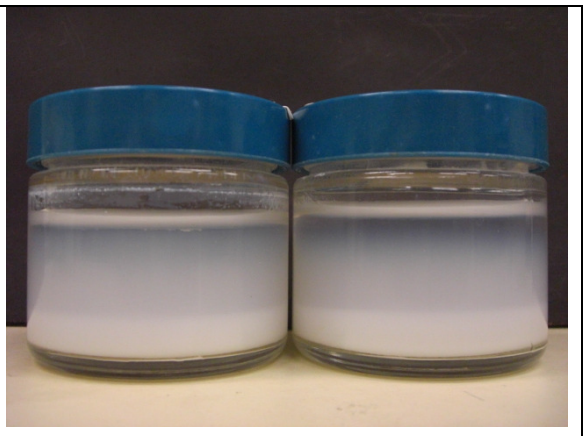

B.

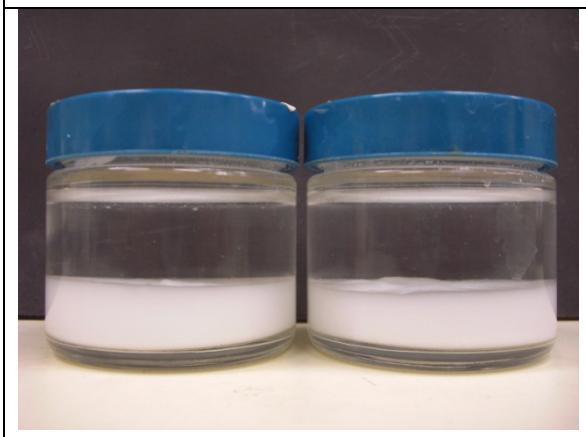

C.

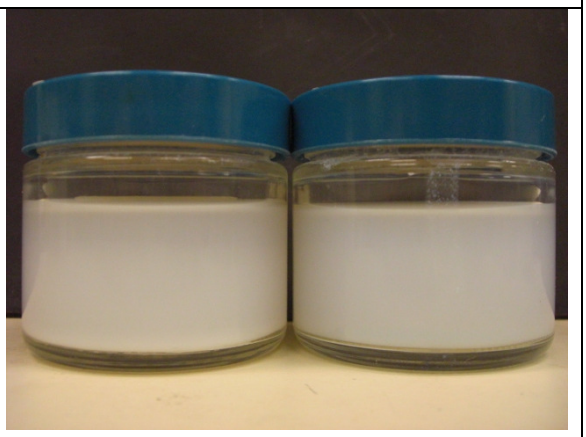

D.

Figure 4.30 Images of PAH-coated silica nanoparticle solutions to illustrate the effect of the polymer on colloidal stability. **A)** no PAH and 1mM PAH, **B)** 2 and 3 mM PAH, **C)** 4 and 5 mM PAH, and **D)** 6 and 7 mM PAH in 0.376 M silica nanoparticle solution.

Next, the ideal PSS concentration was determined using the same method. **Figure 4.31** is a plot of the ζ-potential versus the PSS concentration in the 0.376 M silica nanoparticle solution. All of the samples were coated with 7 mM of PAH, and sonicated for 80 minutes before the PSS was added. The ζ-potential of the PAH-coated nanoparticles after adding 1 mM of PSS decreased to around + 41 mV. The particles once again became unstable when 2-4 mM of PSS was added to the solution, but were stable (< -40 mV) at concentrations of 5 mM and above. From the plot, I incorrectly deduced that the ζ-potential saturation point occurred at a PSS concentration of 10 mM. I later discovered that this solution was supersaturated, but will comment on that in a moment. For now, it will suffice to say that the appropriate PSS concentration is 5 mM.

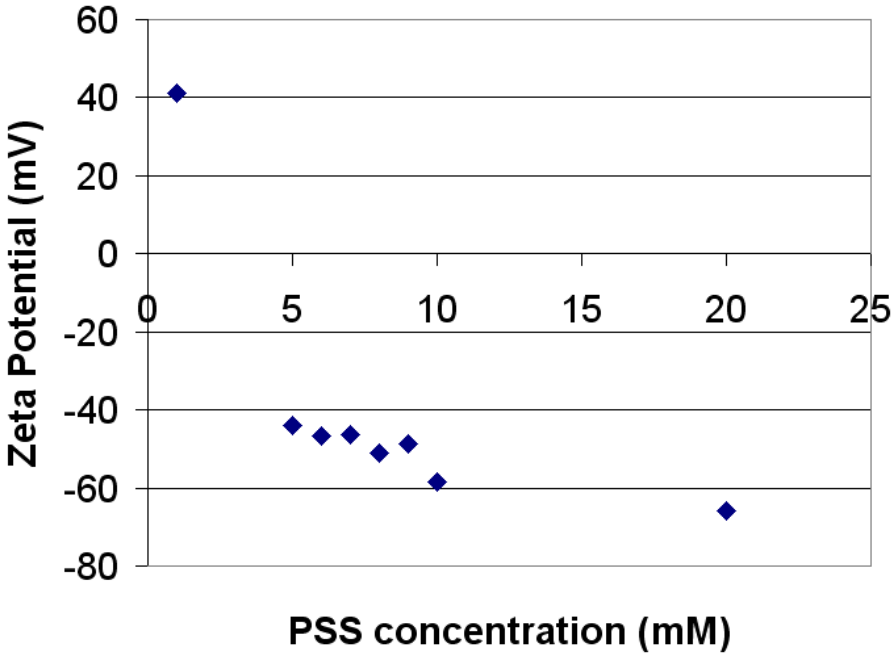

Figure 4.31 ζ-potential versus the concentration of PSS added to the 0.376 M silica nanoparticle solution previously coated with 7 mM of PAH.

It was necessary to monitor the nanoparticle aggregation of the colloidal suspension because the inability to maintain a fairly dispersed solution could significantly affect the optical clarity of the films. Dynamic Light Scattering (DLS) methods enabled the average particle size to be measured for the coated nanoparticles. In **Figure 4.32**, one can see the distribution of particle sizes for samples with and without sonication. Without adding polymer to the colloid, the average particle size was 64.6 nm (**Figure 4.32A**). When 7 mM of PAH was added to the solution, significant aggregation occurred and the average size increased to around 525 nm (**Figure 4.32B**). A wide range of particle sizes were present in this solution as evidenced by the three well-defined peaks at 291, 1220, and 5010 nm respectively. After 80 minutes of sonication the nanoparticles became dispersed as the particle size decreased to 95 nm (**Figure 4.32C**). Finally, after adsorption of the PSS layer and sonication the modified nanoparticles had an average size of 156 nm (**Figure 4.32D**).

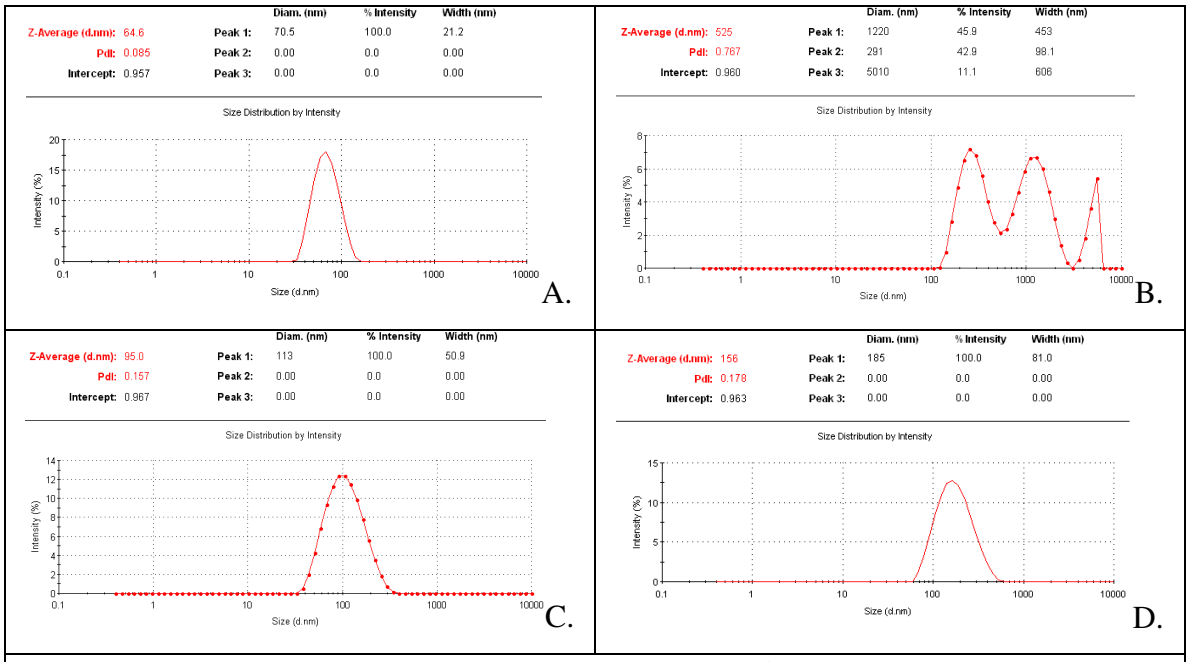

Figure 4.32 Particle size measurements by DLS of: **A)** silica nanoparticle solution without polymer, **B)** 7 mM PAH in solution without sonication, **C)** 7 mM PAH in solution with 80 minutes of sonication, and **D)** 7 mM PAH/10 mM PSS in solution with 80 minutes of sonication.

Next, ISAM films consisting of DAR and the PAH/PSS-coated silica nanoparticles were fabricated on sulfonate-bearing glass substrates. The films were put through 5 and 10 adsorption cycles, but upon inspection it appeared as if nothing was present on the substrates. Additional DAR/modified SiO_2 NP films were made consisting of 5, 10, 15, and 20 bilayers. SEM images (**Figure 4.33**) of these specimens were taken to determine the degree of nanoparticle adsorption as a function of the number of adsorption cycles. Each row in the figure corresponds to a fixed number of bilayers (i.e. **A** and **B** = 5-bilayer sample, **C** and **D** = 10-bilayer sample, etc.). All images in the left column were taken at a magnification of 50 kX, and 200 kX for the right column. One can clearly see that the nanoparticles did not adsorb onto the surface after 5 cycles (**A** and **B**). After 10 cycles however (**C** and **D**) aggregate nanoparticles attached to the surface. The coverage improved only moderately after 15 (**E** and **F**) and 20 (**G** and **H**) cycles, still leaving a majority of the substrate surface open. Furthermore, the nanoparticles that attached to the surface were not well-dispersed, but this was expected given the above DLS measurements.

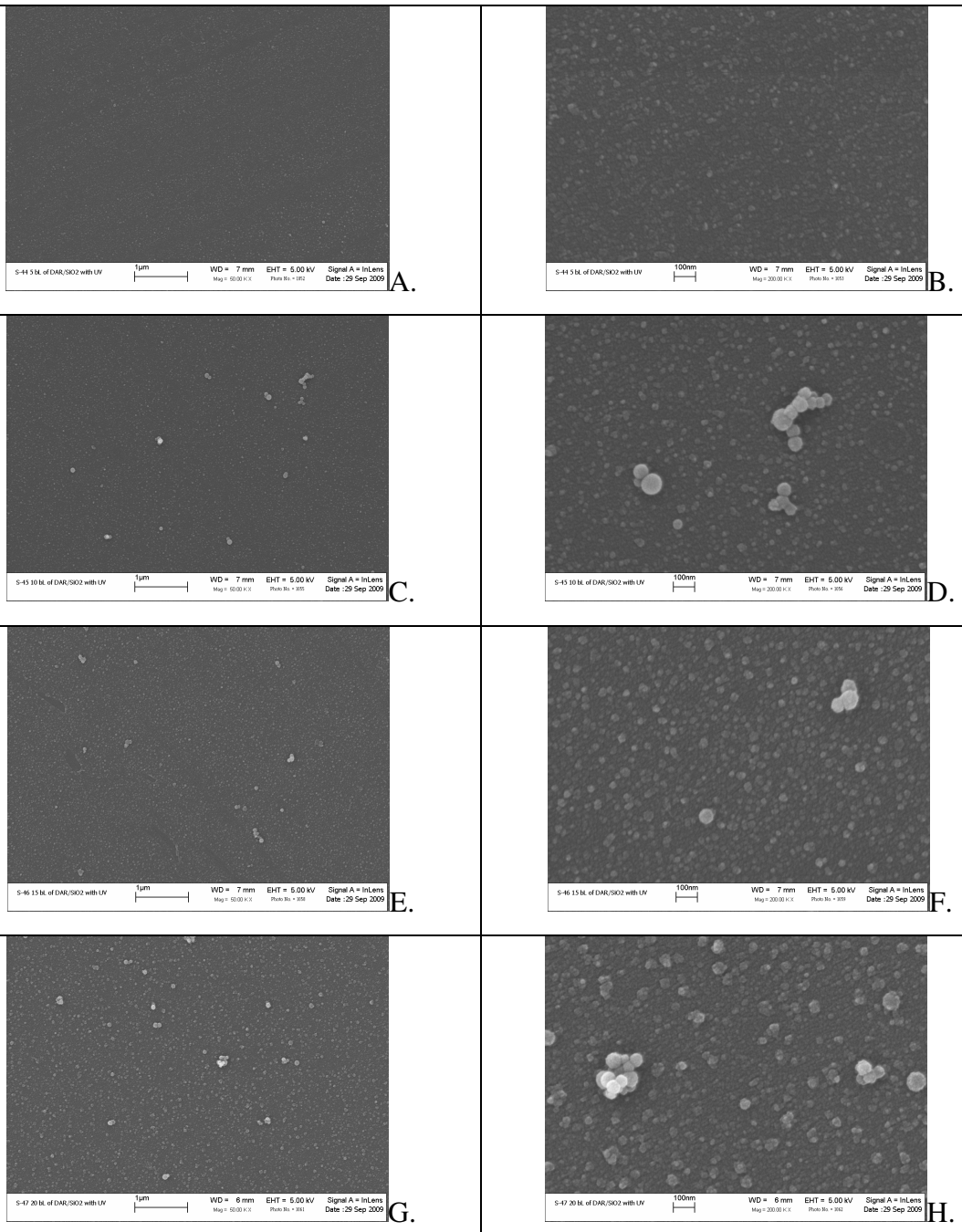

Figure 4.33 SEM images ISAM films containing DAR and silica nanoparticles (NP) coated with a bilayer of PAH/PSS. **A)** 5 bl DAR/NP 50 kX magnification, **B)** 5 bl DAR/NP 200 kX mag., **C)** 10 bl DAR/NP 50 kX mag., **D)** 10 bl DAR/NP 200 kX mag., **E)** 15 bl DAR/NP 50 kX mag., **F)** 15 bl DAR/NP 200 kX mag., **G)** 20 bl DAR/NP 50 kX mag., **H)** 20 bl DAR/NP 200 kX. The scale bars for images magnified by 50 and 200 kX represent 1 μm and 100 nm, respectively.

One additional feature of the images was the smaller globules observed on the substrate surface. It is difficult to say what they were; perhaps they are the MPTS molecules, or maybe even excess PAH/PSS floating in the modified nanoparticle solution. In fact the latter scenario became a possible explanation for the lack of nanoparticle adsorption. If too much PSS had been added to the PAH-coated nanoparticles, then the excess would first couple to any free PAH in solution, while the remaining would have nowhere to attach. It would remain suspended in solution along with the PAH/PSS-coated nanoparticles. Now, consider for a moment this solution with excess PSS being used to coat a substrate via ISAM deposition. After the substrate is covered with a uniform layer of DAR, it is dipped into this solution. Both the excess PSS and the modified nanoparticles are attracted to the positively charged surface. It is quite reasonable to expect the smaller PSS molecules to rapidly adsorb onto the surface in contrast to the larger nanoparticles, which by comparison will diffuse slowly towards the surface. This is exacerbated by the fact that they are, on average, even larger in size because of aggregation during the PAH/PSS coating. By the time the massive nanoparticles have reached the substrate, the charged DAR layer has been quenched by the excess PSS, which now repels the nanoparticles from the surface. In this competitive process, the likelihood of a nanoparticle winning the race against a smaller PSS molecule is very small, though still possible as evidenced by the SEM images above.

After consulting the plot of the ζ-potential versus PSS concentration (**Figure 4.31**), it appeared that the potential became saturated at 5 mM, and not 10 mM as previously thought. I could not choose a smaller concentration than 5 mM because the nanoparticle suspension was no longer stable in that range. As a result, I made new PAH/PSS-coated silica nanoparticles with PAH and PSS concentrations of 7 and 5 mM, respectively. I made 5- and 10-bilayer coatings using DAR and these nanoparticles. It turns out that the reason for poor nanoparticle adsorption mentioned above was due to excess PSS, because these new films had improved nanoparticle coverage. The problem however with these films was that they scattered a significant amount of light. This is due to the nanoparticle aggregation during the PAH/PSS ISAM process. DLS measurements on nanoparticles coated with a bilayer of 7 mM PAH/5 mM PSS revealed an average particle size around 196 nm (**Figure 4.34**). Furthermore, the plot showed that the degree of aggregation varied, and consequently the nanoparticle sizes covered a wide range.

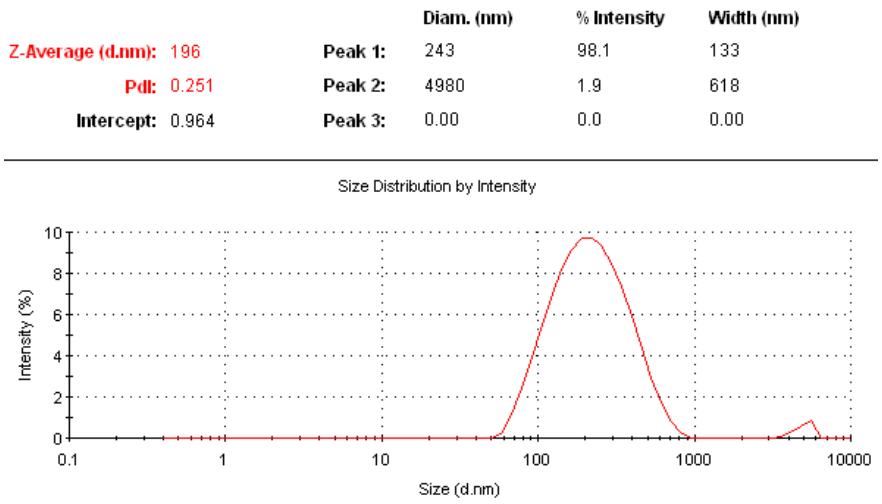

Figure 4.34 DLS measurements of a 0.376 M silica nanoparticle solution coated with a bilayer of 7 mM PAH/5 mM PSS.

The coatings were subjected to a solvent test in order to assess the effect of the UV treatment on the film stability. **Figure 4.35** is a plot of the transmission spectra of 5- and 10-bilayer coatings before and after UV treatment, as well as UV irradiated samples subjected to 30 minutes of solvent immersion. The first striking feature of the spectra is the high degree of scattering, particularly at short wavelengths. Clearly the aggregation that occurred during nanoparticle coating severely impacted the optical transparency. This however can be remedied by a number of possible steps, which are discussed in the "**Summary and Future Studies**" chapter. The absorption peak at 380 nm disappears with UV irradiation, which has been shown by others. What is interesting, however, is the emergence of an absorption peak around 650 nm. It is unclear what molecular change corresponds to this peak, but I wanted to verify that this change was related to DAR. As a control I deposited two sets of 5-, 6-, 7-, and 8-bilayer DAR/PSS polymer films (**Figure 4.36**). In one case the set of films were not irradiated by UV, while the other set was irradiated for 15 minutes. The absorbance was plotted versus the wavelength for the 8 samples. One can clearly see the lack of an absorbance peak around 650 nm for all of the samples without UV. By comparison the UV-irradiated samples had the absorbance peak at 650 nm, which appeared to increase with the number of deposited DAR/PSS layers. Additionally this peak was not present after UV irradiation of films consisting of diazo-resin and the unmodified silica nanoparticles. This means that the peak can be attributed to the molecular reorganization between the diazonium and sulfonate groups, though the specific origin

is uncertain at this time. Returning to the analysis of **Figure 4.35**, it appeared that the solvent removed some of the film. This was because the films initially had a dark green-brown tint, but the intensity of this color was lessened after being dipped in the solvent. Furthermore, the intensity of the absorbance peak at 650 nm decreased, though it is still uncertain whether this peak can be used to assess film thickness after UV irradiation. If one looks at the transmission spectrum of the 5-bilayer sample after UV irradiation and solvent immersion, the peak at 650 nm has nearly disappeared, though clearly the film is still on the substrate because incident light is still heavily scattered throughout the UV/VIS/IR. One very important observation concerning the color of the films should be addressed. The DAR and unmodified silica nanoparticle films, regardless of UV exposure, possessed the dark green-brown tint alluded to earlier. This tint can be attributed to the diazo-resin. The tint is also present on DAR/PSS polymer films *without* UV irradiation. After exposure to UV, however, this color disappeared completely. Also noteworthy is the fact that these DAR/PSS coatings were stable in solvent after UV treatment. Therefore it may be reasonable to assume that when DAR has been successfully cross-linked with the sulfonate end groups, the color also disappears. Consequently, this tint could be used to indicate if UV cross-linking is successful. This has strong implications because the DAR/modified SiO_2 NP films had the dark green-brown tint even after UV irradiation. Under the above assumption, this means that many of the ionic bonds between DAR and sulfonate were not converted to covalent ones, which would explain why part of the film was dissolved by the solvent. Furthermore, a mild abrasion test using a cheesecloth completely removed the film from the substrate. This is expected, however, since the film was not successfully cross-linked by the UV treatment. It is speculated that the large nanoparticle aggregates (~ 196 nm on average) are scattering the UV light intended to cross-link the film. This is supported by the poor transmittance at shorter wavelengths seen in **Figure 4.35**. Additionally, it is even less likely that sufficient cross-linking between DAR and the sulfonates from the MPTS occurred because of heavy scattering. Hence, the adhesion of the film to the substrate would be very poor, which also may explain why the mild abrasion test could remove the film from the substrate.

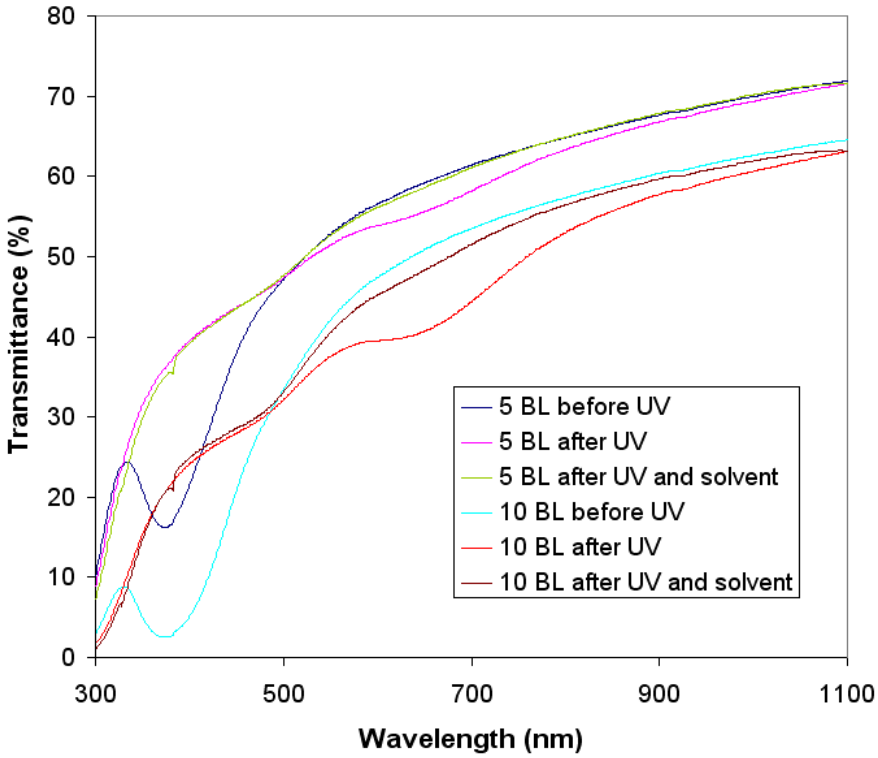

Figure 4.35 Transmittance spectra of DAR/modified SiO_2 NP films consisting of 5 and 10 bilayers. The spectrum was acquired before and after UV irradiation, as well as after the UV-treated sample was dipped in a ternary solvent.

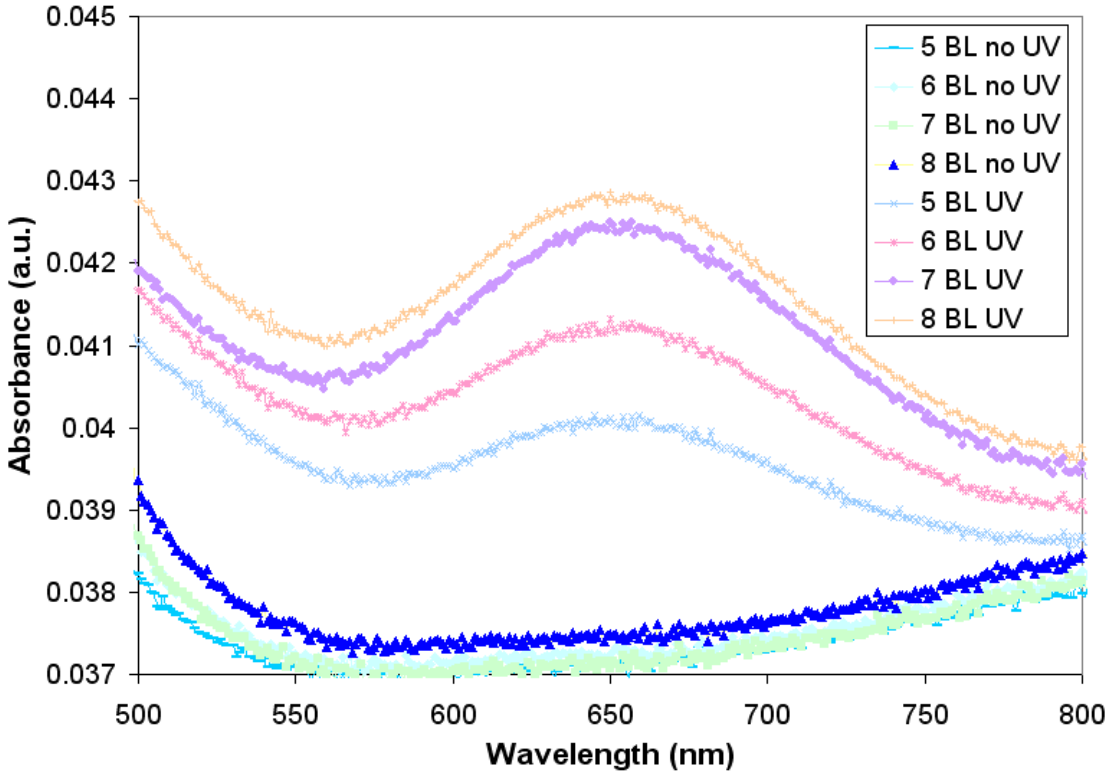

Figure 4.36 Absorbance spectra of DAR/PSS films on MPTS-coated glass substrates consisting of 5, 6, 7, and 8 bilayers. The emergence of a peak at 650 nm after UV irradiation can be attributed to molecular restructuring of the diazonium and sulfonate groups of the ISAM constituents.

I took SEM images (**Figures 4.37-48**) of DAR/modified SiO_2 NPs consisting of 1, 2, 3, and 4 bilayers in order to support the assumption that UV light used to convert the ionic bonds in the film is scattered by large aggregate nanoparticle domains. The first three images correspond to a single bilayer of DAR and modified silica nanoparticles at magnifications of 10 kX (**4.37**), 50 kX (**4.38**), and 200 kX (**4.39**), respectively. At a magnification of 10 kX one can clearly see a surface with fairly high nanoparticle adsorption, but populated with a number of irregular micron-scale domains of aggregate nanoparticles. The comparative size of these domains with the individual nanoparticles can be better seen at a magnification of 50 kX (**4.38**). In addition to the very large aggregate particles, one can see that the remaining nanoparticles on the surface were not well-dispersed. At 200 kX magnification (**4.39**) the aggregation of the nanoparticles away from the micron-scale domains can be seen in greater detail. Very few nanoparticles on the surface were not coupled to others; in fact the aggregation was quite severe excluding the

larger domains. These nano-scale domains also contributed to the scattering of light seen in **Figure 4.35**. Clearly, the ISAM deposition of PAH and PSS on the nanoparticles adversely affected their dispersion and consequently the optical transparency of ISAM films made using said nanoparticles. Note that the extraordinary degree of aggregation was present on just a single bilayer of DAR/modified SiO_2 NPs, and that the problem became exacerbated at 2, 3, and 4 bilayers.

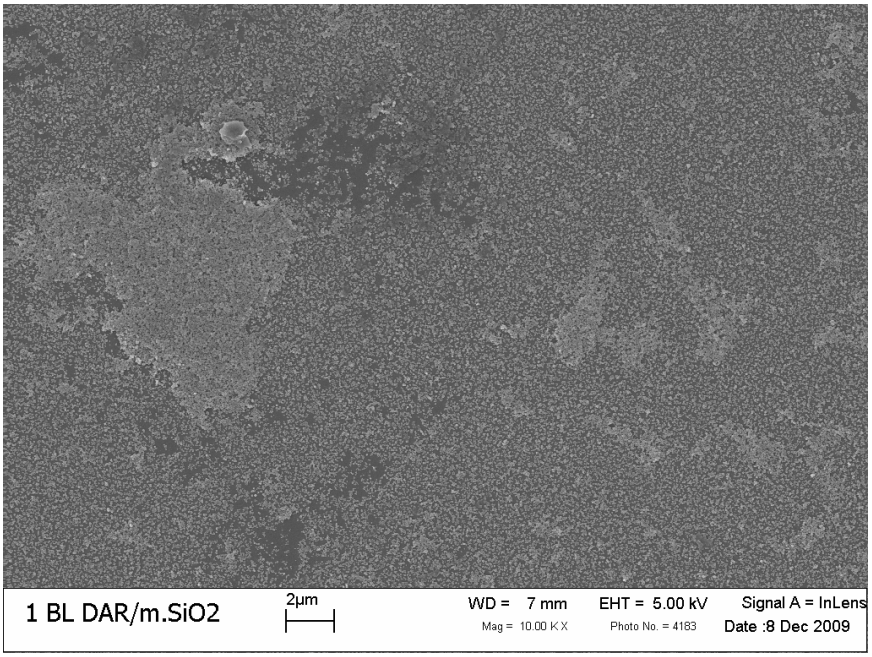

Figure 4.37 One bilayer of DAR/modified SiO_2 NPs taken at a magnification of 10 kX. The scale bar represents 2 µm.

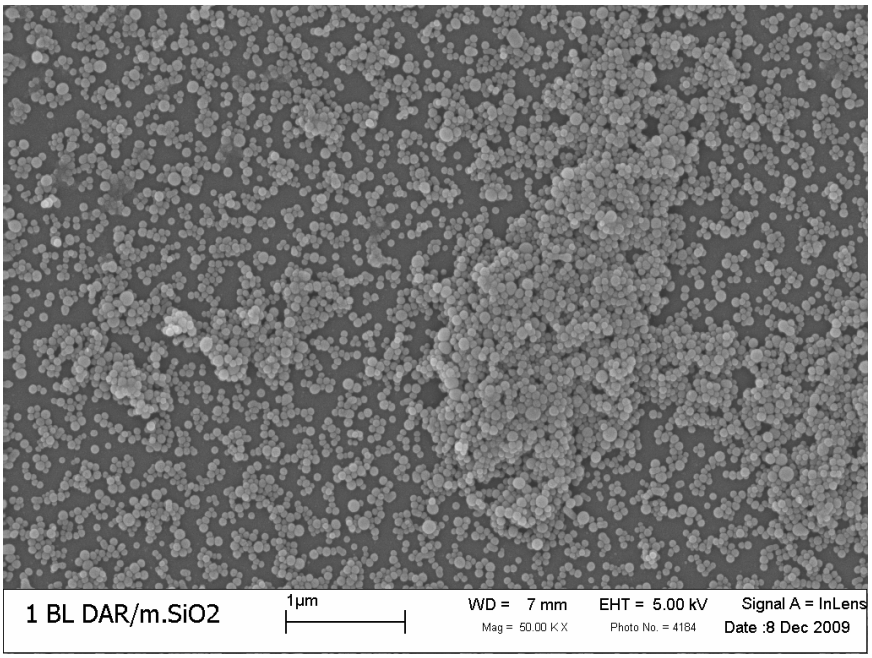

Figure 4.38 One bilayer of DAR/modified SiO_2 NPs taken at a magnification of 50 kX. The scale bar represents 1 µm.

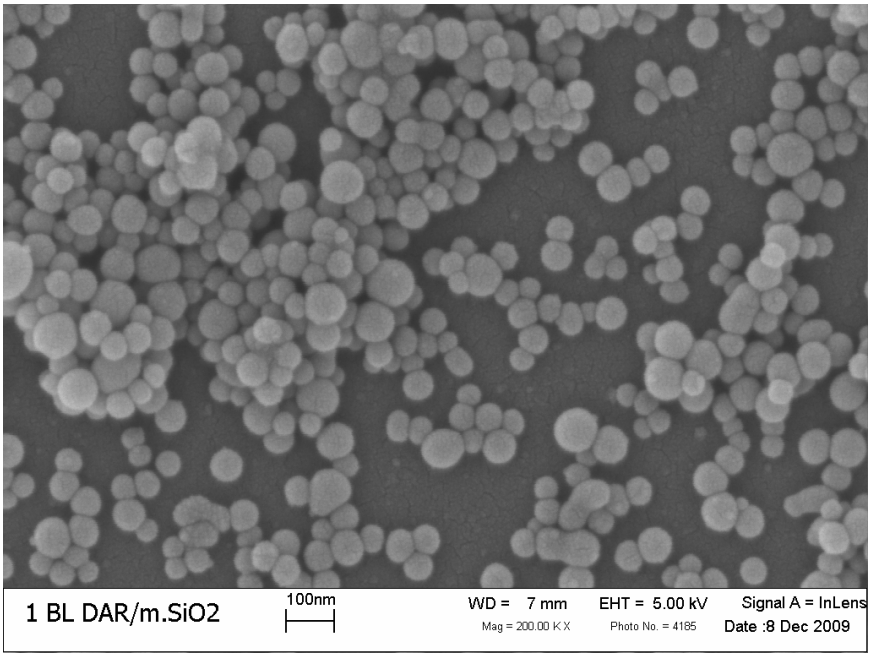

Figure 4.39 One bilayer of DAR/modified SiO_2 NPs taken at a magnification of 200 kX. The scale bar represents 100 nm.

The images corresponding to two bilayers of DAR and the modified silica nanoparticles are below in **Figures 4.40** (mag.: 10 kX), **4.41** (50 kX), and **4.42** (200 kX). The large domains were observed on this sample as well (**4.40**), although it is not as easy to see them because most of the surface was covered by the second layer of nanoparticles. One of these domains can be more clearly seen at a magnification of 50 kX (**4.41**) in the bottom left corner of the image. The size of the domain was on the order of 1-2 microns across. Finally at a magnification of 200 kX (**4.42**) one can see that there were still regions on the glass surface that were not coated with nanoparticles, however the micro and nano-scale domains effectively formed a relatively thick layer with irregular topographical features. The regions on the glass that are uncoated remained that way because the incident nanoparticles were too large to diffuse to the substrate.

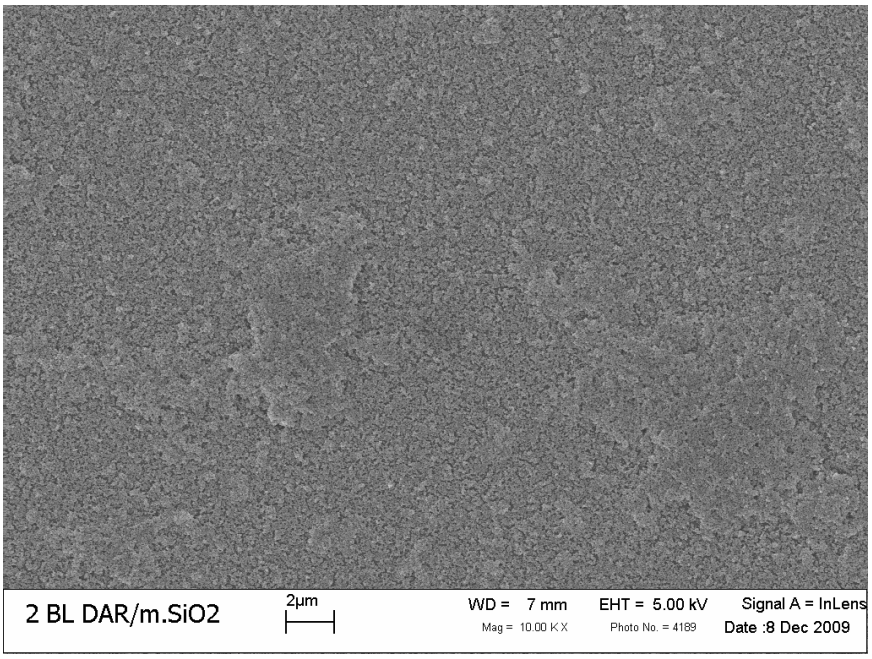

Figure 4.40 Two bilayers of DAR/modified SiO_2 NPs taken at a magnification of 10 kX. The scale bar represents 2 µm.

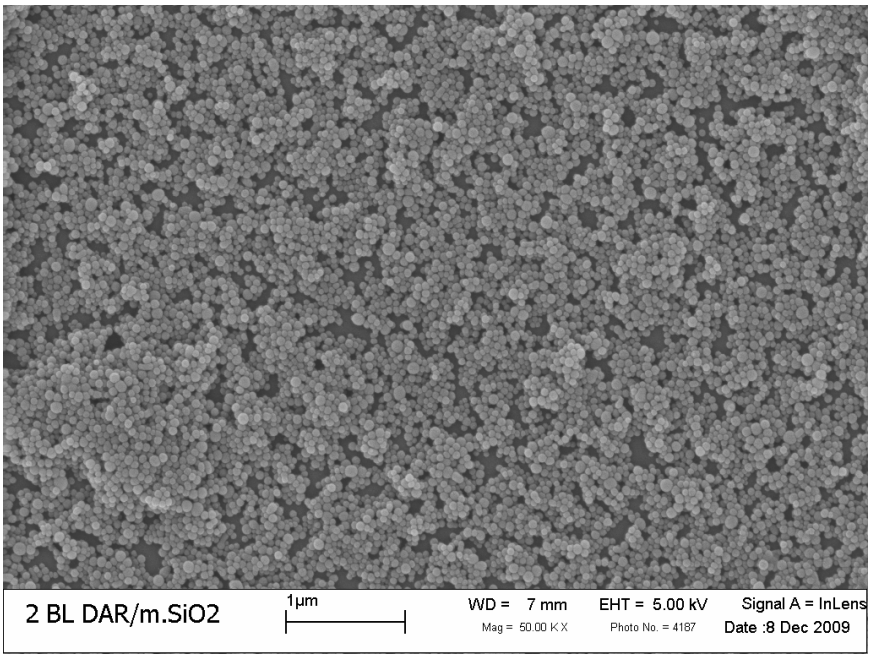

Figure 4.41 Two bilayers of DAR/modified SiO_2 NPs taken at a magnification of 50 kX. The scale bar represents 1 µm.

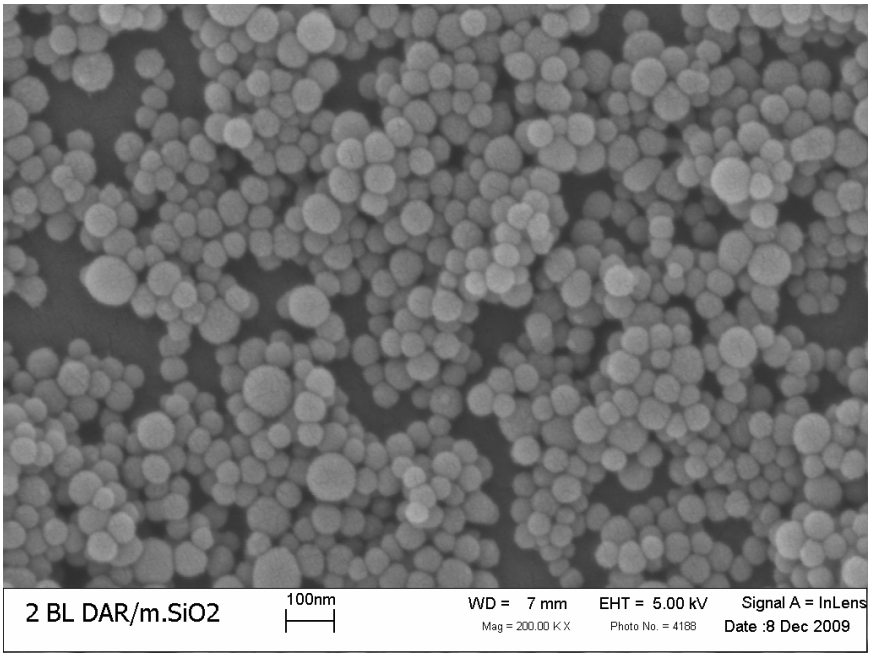

Figure 4.42 Two bilayers of DAR/modified SiO_2 NPs taken at a magnification of 200 kX. The scale bar represents 100 nm.

SEM images of three DAR/modified SiO_2 NP bilayers are shown in **Figures 4.43** (mag.: 10 kX), **4.44** (50 kX), and **4.45** (200 kX). A glaring problem with a film with charged mounds on the surface is that the mounds also grow with the film. As a result the surface became very rough and consisted of mounds and valleys. This phenomenon is quite apparent at a magnification of 50 kX (**4.44**). This resulted in unwanted surface scattering and prevented sufficient cross-linking of DAR with the substrate and modified silica nanoparticles to occur.

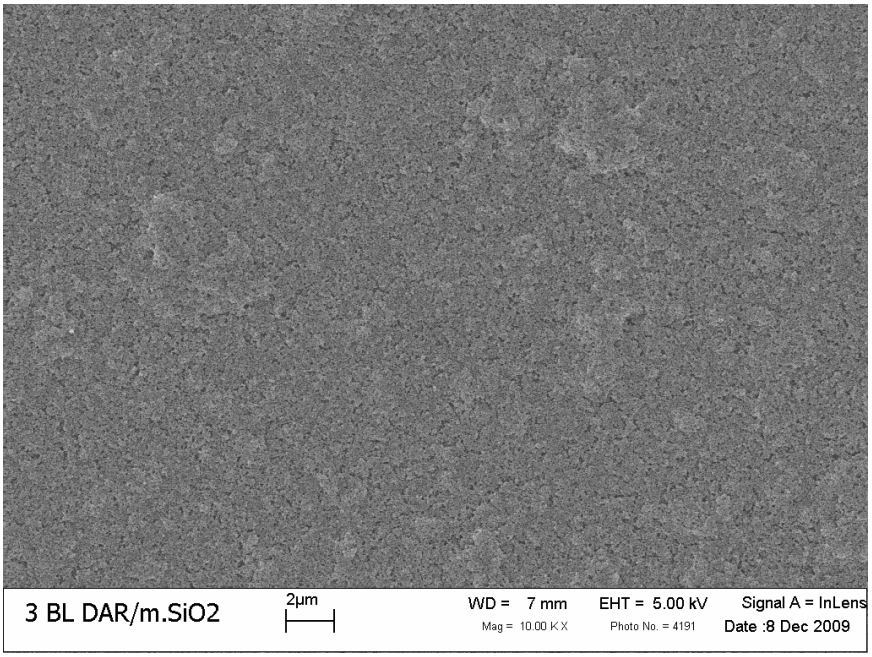

Figure 4.43 Three bilayers of DAR/modified SiO_2 NPs taken at a magnification of 10 kX. The scale bar represents 2 µm.

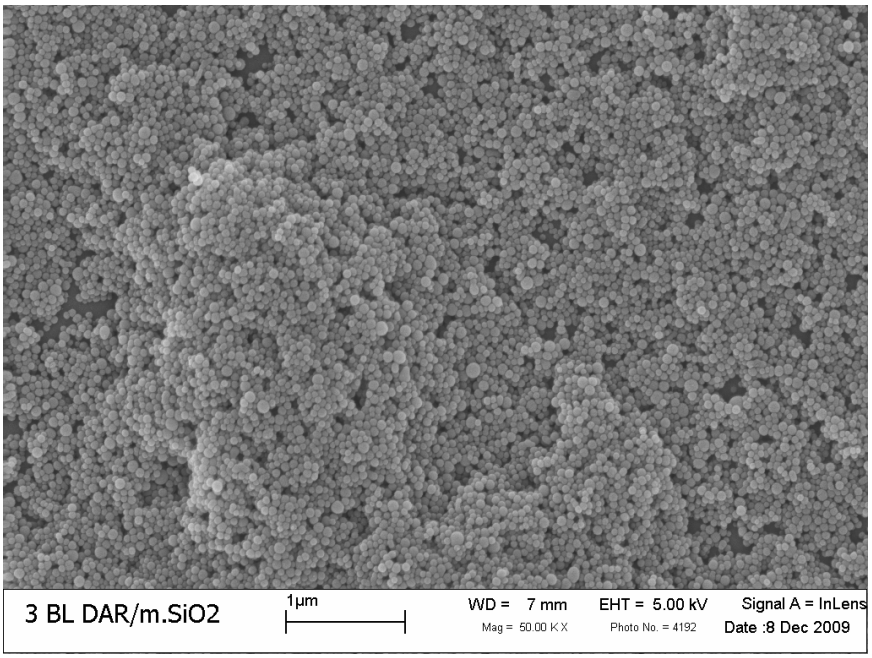

Figure 4.44 Three bilayers of DAR/modified SiO_2 NPs taken at a magnification of 50 kX. The scale bar represents 1 µm.

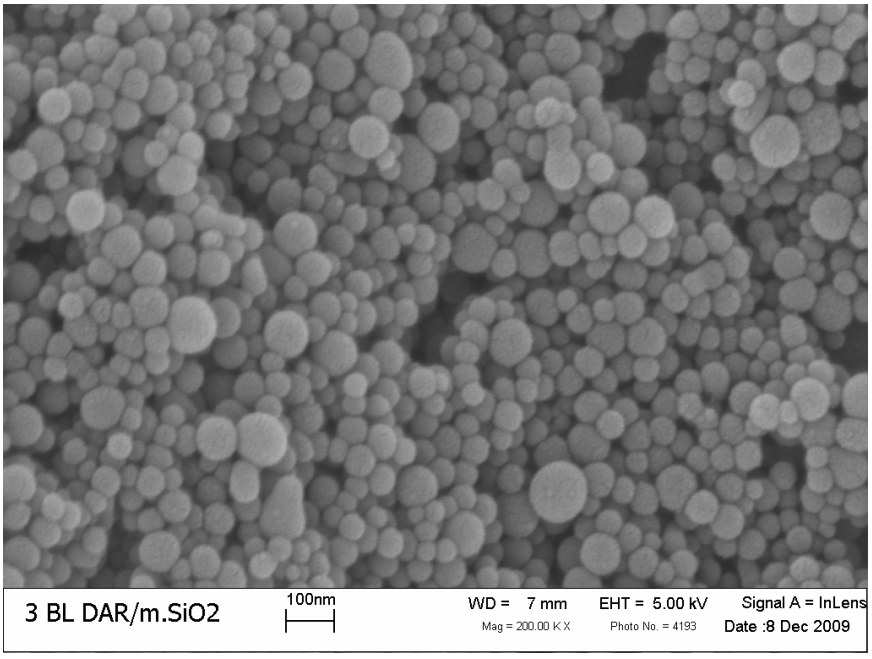

Figure 4.45 Three bilayers of DAR/modified SiO_2 NPs taken at a magnification of 200 kX. The scale bar represents 100 nm.

SEM images of the 4 bilayer samples are shown in **Figures 4.46** (10 kX), **4.47** (50 kX), and **4.48** (200 kX). The presence of the nanoparticle mounds was even more obvious in this sample (**4.46**), resulting in a highly irregular topography. It is difficult to accurately determine the height of the mounds, but by comparing them with the 1 micron scale bar in **4.47** and the 100 nanometer scale bar in **4.48** it appears as if their height may be on the order of microns. In conclusion, the SEM images acquired indicate that light most likely was scattered both at the surface by micron-scale nanoparticle mounds, and by nano-scale aggregates averaging nearly 200 nm in diameter (**Figure 4.34**). As a result it is likely that the aggregates compromised UV cross-linking throughout the film and particularly at the film/substrate interface.

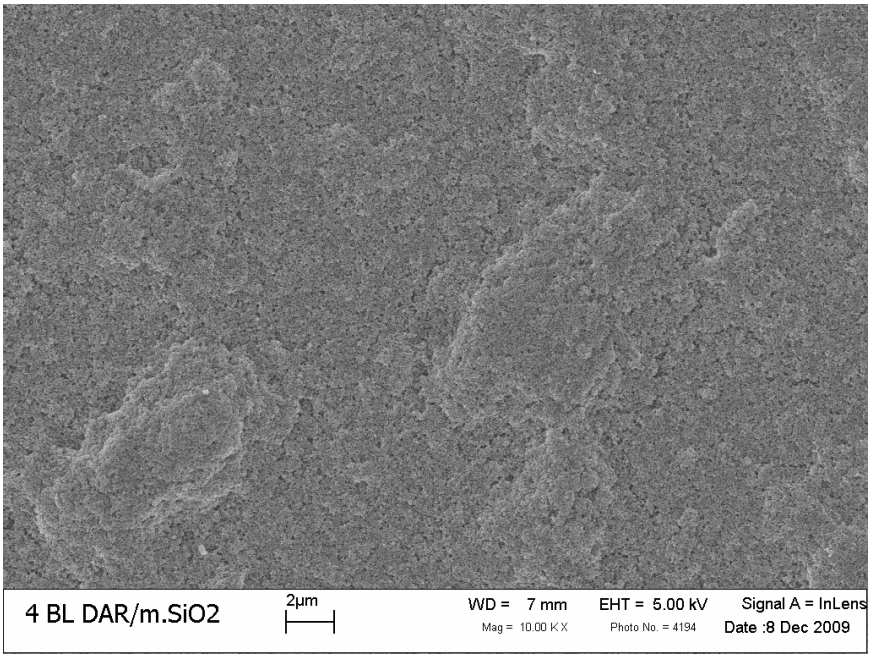

Figure 4.46 Four bilayers of DAR/modified SiO_2 NPs taken at a magnification of 10 kX. The scale bar represents 2 µm.

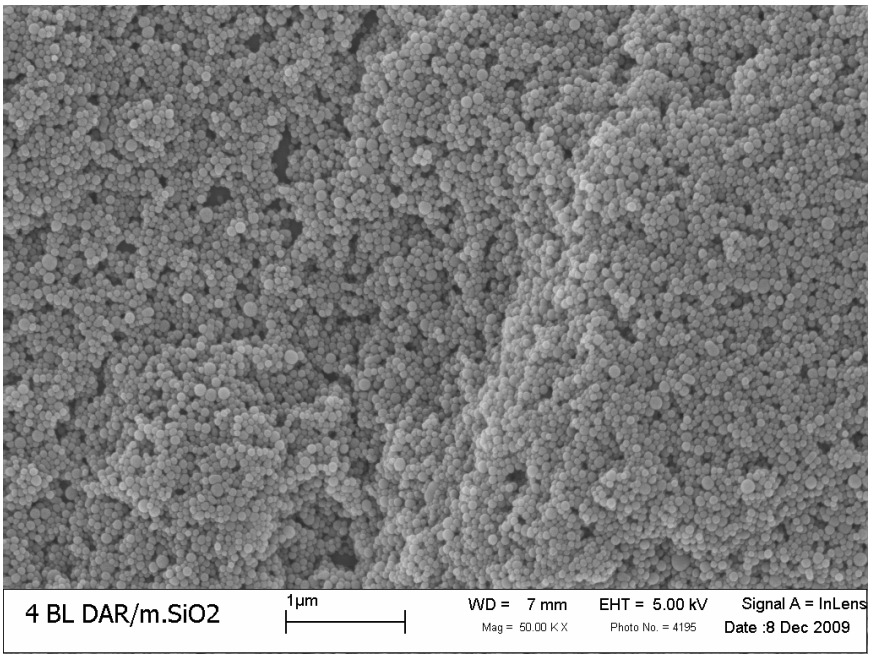

Figure 4.47 Four bilayers of DAR/modified SiO_2 NPs taken at a magnification of 50 kX. The scale bar represents 1 µm.

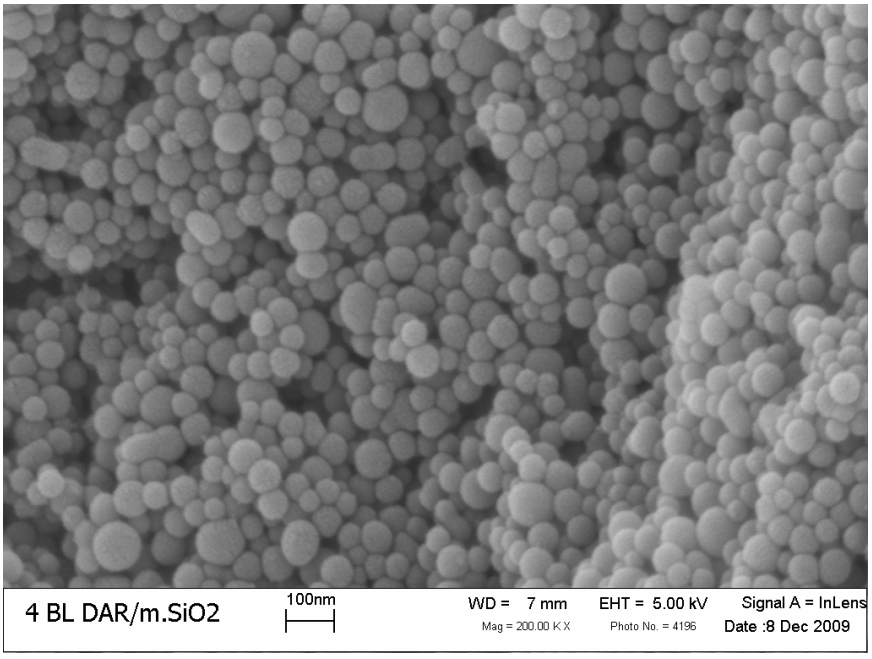

Figure 4.48 Four bilayers of DAR/modified SiO_2 NPs taken at a magnification of 200 kX. The scale bar represents 100 nm.

4.3 Thermal Fusing of PAH/SiO_2 NP Films

A more simplistic approach to improve the strength of the inter-nanoparticle bonds is by calcination, which can be accomplished by heating for short periods of time near the glass melting temperature (1650 ± 75 °C), or for longer periods of time near the annealing temperature (500-560 °C). If calcined at appropriate time and temperature conditions, the nanoparticles will partially fuse and form highly stable siloxane bonds. Furthermore, the calcination temperature typically is high enough to burn away the polymer that initially joins the nanoparticles during ISAM deposition. Consequently, the void fraction of the film is modified by two competing factors: 1) polymer removal (increase in void fraction), and 2) nanoparticle fusion (decrease in void fraction). As a result, the optical transparency is not compromised, coupled with significant gains in terms of the cohesive strength.

The eventual goal of this project is to better understand how the calcination time and temperature affect the void fraction, so that we can have optimal control over the optical properties of the film. Additionally, it will be of interest to see how the calcination parameters affect the film thickness, which directly affects the void fraction. Before these properties could be thoroughly studied, we wanted to see how well the technique improved the cohesive strength. The easiest way to gauge this was to use similar time and temperature settings described by Lee[9] and Cebeci.[10] Before the results of the research are discussed, it should be noted that the majority of the work on calcination was done by Jonathan Metzman, who had recently joined our research group and was continuing my work. He fabricated and calcined the films and then measured the spectra of the samples, while I assisted him with SEM imaging, and offered instruction and guidance throughout. As mentioned above, the calcination process partially fuses neighboring nanoparticles together. This can be seen in **Figure 4.49** below. On the left (**A**) one can see a typical PAH/SiO_2 NP film consisting of 4 bilayers. In this sample, the nanoparticles are neatly and uniformly arranged. The sample on the right (**B**) is a 10-bilayer PAH/SiO_2 NP film that was heated at 500 °C for 4 hours. One can clearly see the nanoparticles have been partially fused, but sufficient void space exists to preserve the excellent optical clarity.

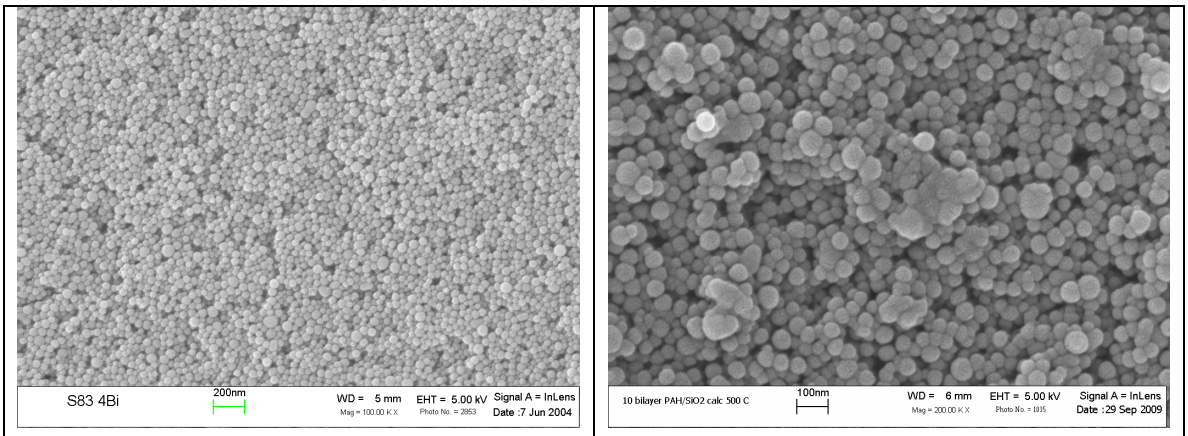

A. B.

Figure 4.49 SEM micrographs of a A) Four-bilayer PAH/SiO_2 NP film without thermal treatment at a magnification of 100 kX (scale bar = 200 nm), B) ten-bilayer PAH/SiO_2 NP film that has been heated at 500 °C for 4 hours (magnification = 200 kX, scale bar = 100 nm).

Since the nanoparticles are partially fused throughout the film, it is logical to conclude that the film thickness decreases somewhat. Evidence of this can be seen in **Figures 4.50 & 4.51**. **Figure 4.50** shows plots of the transmittance spectra of 5- and 10-bilayer coatings with and without thermal treatment. The 1st order maximum and 2nd order minimum of the 5- and 10-bilayer films, respectively, are located in a narrow wavelength range (700-760 nm). The calcination apparently did little to change the thickness of the 5-bilayer coatings as their transmission peaks are at nearly the same wavelength. A change in the thickness is observed for the 10-bilayer films, as the 2nd order minima of the calcined sample is located at a smaller wavelength (697 nm) than the untreated one (747 nm). Using rough calculations this corresponds to an 8-10 nm change in thickness. The corresponding reflection spectra of these samples are shown below in **Figure 4.51**. Similar conclusions can be drawn from the plot. The reflection spectra of the 5-bilayer samples essentially overlap and imply that the thickness is unchanged by the thermal treatment. The spectra corresponding to the 10-bilayer samples, on the other hand do not overlap. The 2nd order minimum of the calcined sample occurs at a smaller wavelength compared with the untreated one. Another significant observation to make from both figures is that the optical transmittance and reflectance of the calcined samples are not compromised by the procedure. The only consequence is the aforementioned spectral shift of

minima/maxima to smaller wavelengths as a result of the decrease in film thickness. Hence, calcination for this time/temperature condition does not adversely affect the optics, yet significantly improves the film strength, which will be shown next.

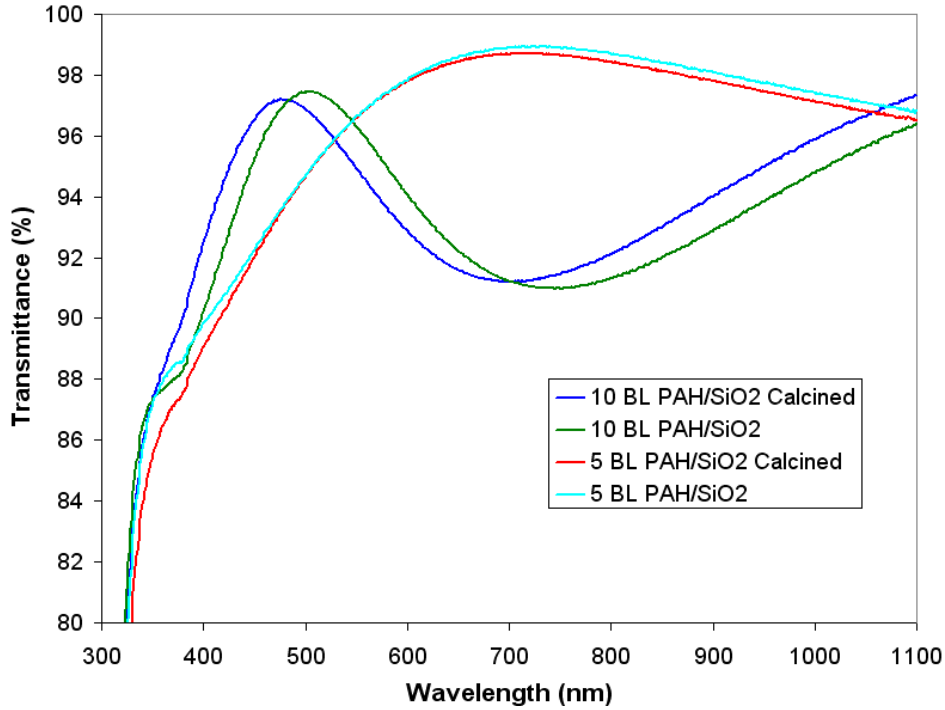

Figure 4.50 Transmittance spectra for 5- and 10-bilayer PAH/SiO_2 NP films with and without calcination.

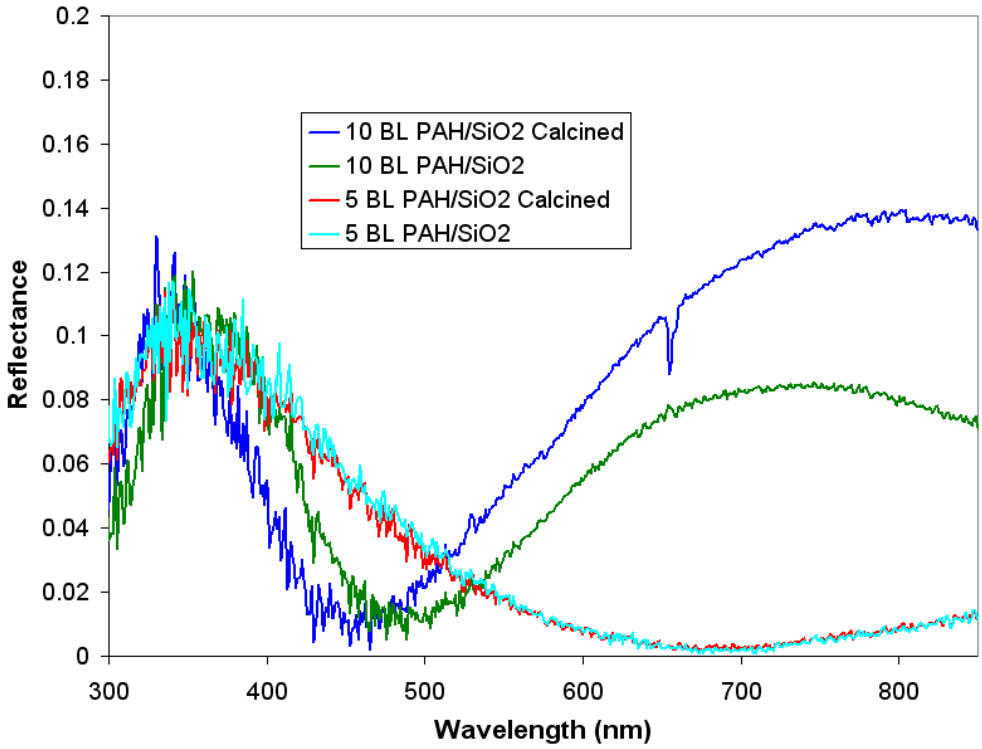

Figure 4.51 Reflectance spectra for 5- and 10-bilayer PAH/SiO_2 NP films with and without calcination.

Calcined PAH/SiO_2 NP samples (5 and 10 bilayers) were subjected to a tape peel test. As a control, films without thermal treatment were also tested. The results of the tape peel test on the untreated samples were similar to what has been observed over numerous trials on 5- and 10-bilayer coatings. Peels on the 5-bilayer sample removed the entire film from the substrate, which is considered as a failure between the substrate and the first nanoparticle layer. A fairly uniform layer of nanoparticles was removed from the 10-bilayer sample, which is referred to as cohesive failure. It is suspected that this occurs because the tape penetrates the coating to some extent, and may come in contact with the substrate on thinner films (5 bilayers). On thicker films, however, (10 bilayers) the tape penetrates to some depth a given distance away from the substrate; although it is still possible that the tape is in partial contact with the substrate. This could explain why a layer of nanoparticles remain after peel tests on the 10-bilayer coatings. The failure mechanism of the calcined samples was considerably different than the ones without thermal treatment. For both 5- and 10-bilayer samples, the adhesive on the tape was pulled from the plastic backing, and remained on the coating surface. Essentially the calcined films removed

the adhesive from the tape, while remaining firmly adhered to the substrate. SEM micrographs were taken for the samples. **Figure 4.52** is an image of the 5-bilayer film heated at 500 °C for 4 hours. The magnification of the image is 10 kX. The lower right portion of the image corresponds to the region of the film that was not part of the tape peel test. The remaining upper portion of the image is the region that had the tape removed from the surface. The large irregular bodies in this region are residual adhesive from the tape. In addition to the large particles, a uniform layer of the adhesive rests on top of the nanoparticles. This is more obvious when the magnification is increased to 50 kX (**Figure 4.53**). At the border between the tested/untested domains the residual adhesive layer becomes thin to the point that it is somewhat transparent. In this transparent region underlying nanoparticles can be seen, making it clear that the film is completely intact despite the peel test, and that the adhesive was pulled from the tape and left behind, as was observed by visual inspection.

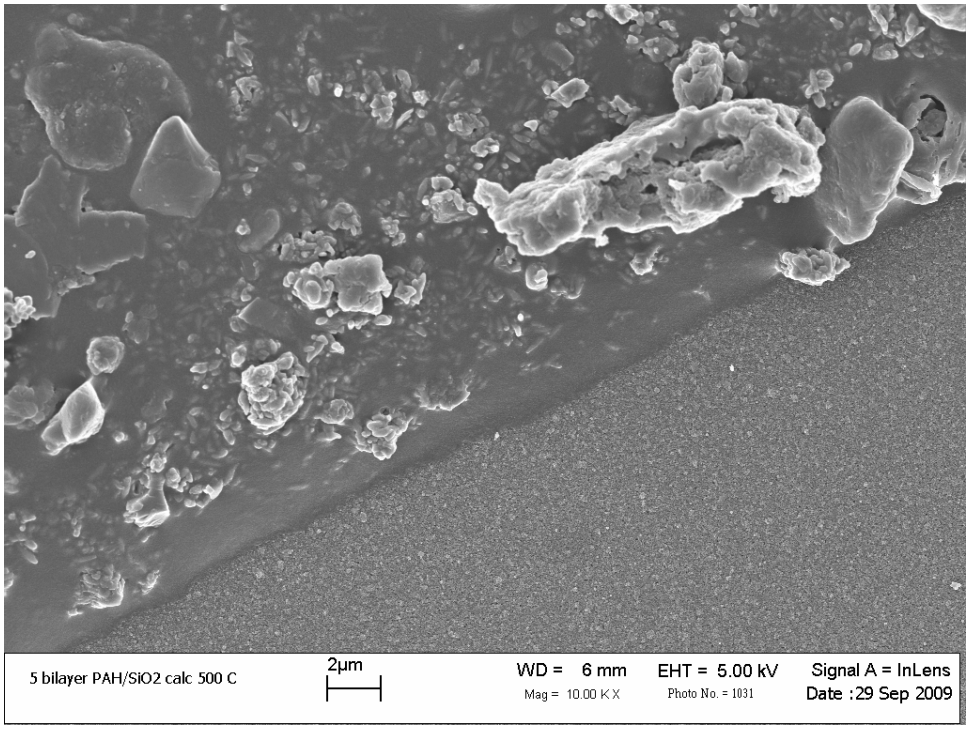

Figure 4.52 SEM image of a 5-bilayer PAH/SiO_2 NP film subjected to calcination and a subsequent tape peel test. Image magnification: 10 kX (scale bar = 2 µm).

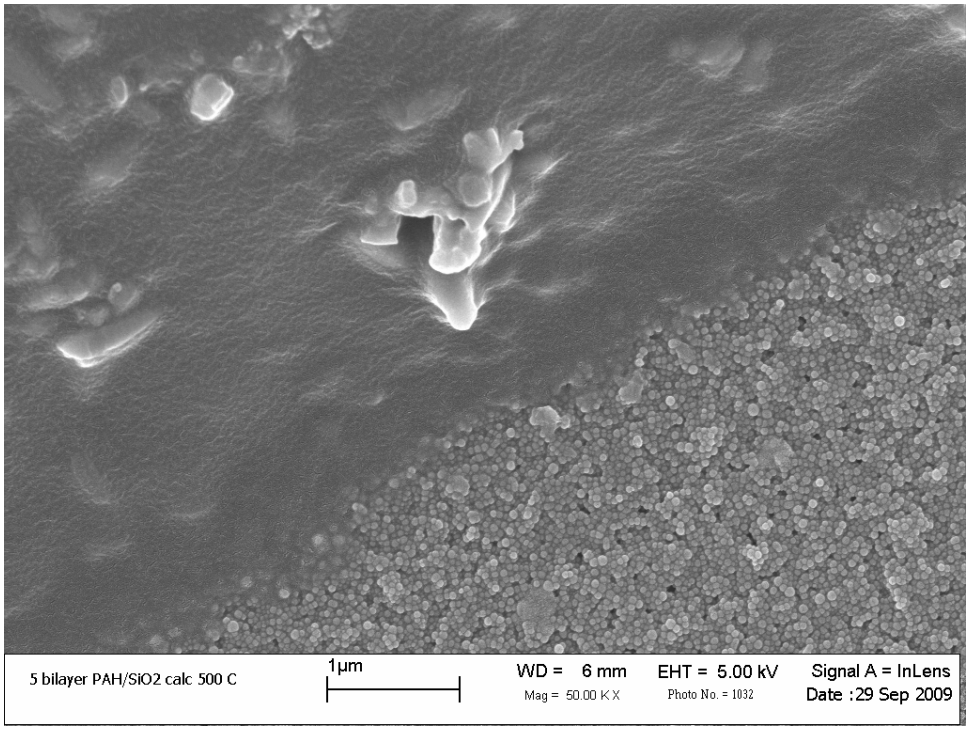

Figure 4.53 SEM image of a 5-bilayer PAH/SiO_2 NP film subjected to calcination and a subsequent tape peel test. Image magnification: 50 kX (scale bar = 1 µm).

As stated above, the failure mechanism on the calcined 10-bilayer sample was similar. Confirmation by SEM can be seen in **Figure 4.54**, which was taken at a magnification of 10 kX. Once again, some larger particles were left behind, as well as traces of adhesive. This time, however, there was less adhesive compared to the 5-bilayer coating. A closer look at the border of the peel and untested regions can be seen in **Figure 4.55**.

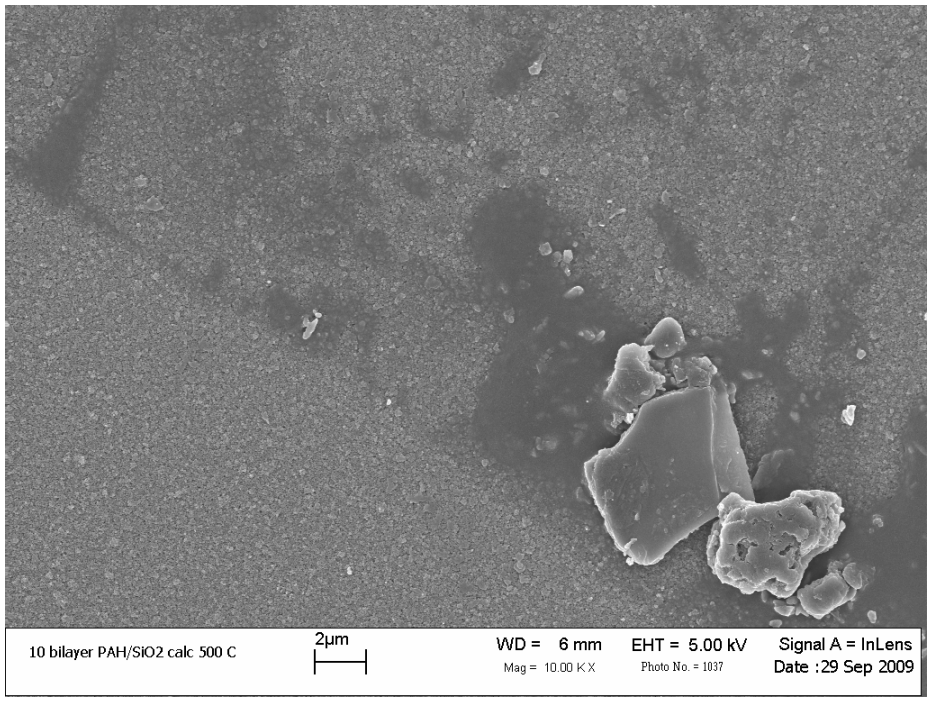

Figure 4.54 SEM image of a 10-bilayer PAH/SiO_2 NP film subjected to calcination and a subsequent tape peel test. Image magnification: 10 kX (scale bar = 2 µm).

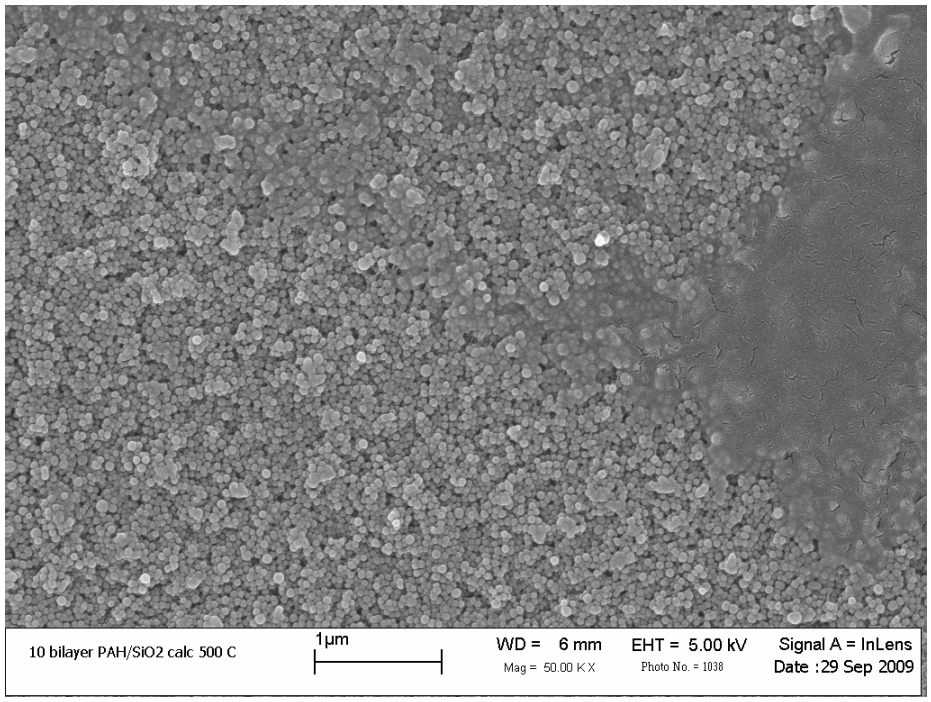

Figure 4.55 SEM image of a 10-bilayer PAH/SiO_2 NP film subjected to calcination and a subsequent tape peel test. Image magnification: 50 kX (scale bar = 1 µm).

While the tape peel test can be a useful tool, it is best to incorporate additional tests to have a comprehensive assessment of the film strength. To complement the tape peel test, I conducted a mild abrasion test on both calcined and uncalcined PAH/SiO_2 NP coatings. The test was performed by rubbing the surface of the coatings with a cheesecloth with sufficient pressure. This back-and-forth motion was repeated for roughly 5 seconds. The untreated films were easily removed from the substrate after being subjected to this procedure. The calcined samples on the other hand were not visibly affected by the abrasion test. Quantitative methods are preferred in order to assess the abrasive resistance of the calcined films. One method in particular is the haze test[18] which monitors the decrease in transmission attributed to increased scattering from abrasion. This along with other methods to evaluate the film's cohesive strength will be discussed in the "**Summary and Future Studies**" chapter. For the time being the tape peel and abrasion tests show that films subjected to calcination have vastly superior mechanical strength compared to films with no thermal treatment.

4.4 Addition of Polymer Interlayers During ISAM Deposition of PAH/SiO_2 NP Films

The final approach I investigated to improve the mechanical strength of silica nanoparticle films is to partially fill the interstitial voids and dramatically increase the cross-link density. As mentioned previously, the cohesive strength is predominantly governed by the interaction of the polycation chains in contact with adjacent nanoparticles. Naturally, there will be polymers in contact with a nanoparticle that exert an electrostatic force on neighboring ones, but the interaction is much weaker due to the $1/r^2$ dependence of charged materials. Therefore, it is ideal to increase the total surface area of direct contact between adjacent nanoparticles. This can be accomplished by increasing the amount of polymer in the corresponding void regions of the film. As a consequence, there is potentially a trade-off between the cohesive strength of the film and the optical transparency.

Since the films were made by the ISAM deposition technique, two oppositely-charged polymers, poly(allylamine hydrochloride) (PAH) and poly(methacrylic acid) (PMA) (**Figure 4.56**), were used to fill the interstitial void space. Two approaches were used to fill the void space and are discussed below. The first involves the deposition of PAH/PMA precursor and capping layers that surround the PAH/SiO_2 NP network. In the second approach, quadlayer

stacks consisting of [PAH/SiO_2 NPs/PAH/PMA]$_n$ were deposited, where "n" refers to the total number of sequential adsorption cycles. Precursor and capping layers were also deposited on top of this film to improve the polymer infiltration in the nanoparticle network.

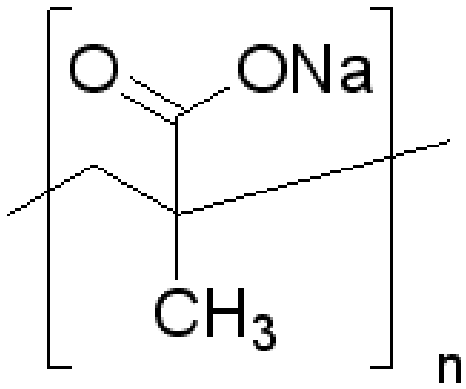

Figure 4.56 Molecular structure of poly(methacrylic acid) (PMA). Permission granted from Sigma Aldrich for reuse and reproduced from: http://www.sigmaaldrich.com/catalog/ProductDetail.do?lang=en&N4=02351|FLUKA&N5=SEARCH_CONCAT_PNO|BRAND_KEY&F=SPEC.

4.4.1 PAH/PMA Capping and Precursor Layers in PAH/SiO_2 NP Films

The premise of depositing a polymer capping layer on top of silica nanoparticle films was the strong likelihood that the much smaller polymers could diffuse throughout the nanoparticle structure, and settle into the various interstitial voids. While this could potentially address the lack of nanoparticle cohesion, the adhesion of the first layer to the substrate would still be poor. To address this, a precursor film[10,12,19,20] consisting of [PAH/PMA]$_5$ was deposited onto the substrate before ISAM assembly of the nanoparticle coating. In essence, the film comprised three layers: [PAH/PMA]$_5$ precursor, [PAH/SiO_2 NP]$_n$ bulk film, and the [PAH/PMA]$_5$ capping layer. The pH conditions of PAH and PMA were different for the precursor and capping layers because the requirements for the respective layers were different. The function of the precursor film was to essentially provide a malleable ionic bed for the nanoparticles to settle into. Diffusion of the nanoparticles into the precursor layer was desired because this would improve the adhesion to the substrate. These criteria required that the precursor film be as thick as

possible with fewer bilayers to minimize deposition time. As a result, the pH values of PAH and PMA in the precursor film were adjusted to 9 and 5, respectively. At these values much of the charge on the polymers was neutralized, and thus the polymers have a tethered configuration, in other words, anchored to a few points, but with a free-floating chain. The criteria for the capping layer were very different. The polymers needed to have a higher charge density in order to strongly link the nanoparticles. Furthermore, it was necessary for them to occupy as little space as possible to prevent excessive interstitial filling. Following these criteria, I adjusted the pH values of both PAH and PMA to 7. The pH conditions of the solutions comprising the bulk film (PAH/SiO_2 NPs) were adjusted to their typical levels (7/9, respectively). **Figure 4.57** is a detailed illustration of the multi-layered structure. The three distinct layers are clearly indicated along with the pH conditions of the aqueous polymer and inorganic solutions used to build them.

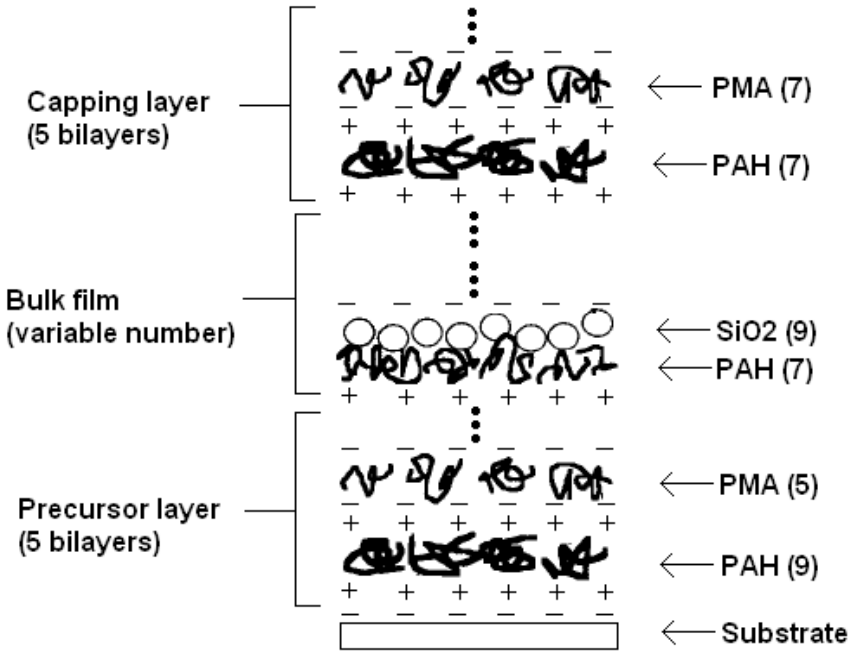

Figure 4.57 Illustration of the silica nanoparticle film with precursor and capping polymer layers. The number of bilayers for the precursor and capping layers was fixed at 5, while the number of bilayers for the bulk film was typically varied between 5 and 10. The pH conditions of the respective polymer and nanoparticle solutions (right of the film) are listed in parentheses. Image is adapted with permission from: [Y. Lvov, K. Ariga, M. Onda et al., "Alternate assembly of ordered multilayers of SiO2 and other nanoparticles and polyions," Langmuir **13** (23), 6195-6203 (1997)]. Copyright 1997 American Chemical Society.

I first wanted to determine if the precursor and capping layers improved the film adhesion without severely compromising the optical clarity. Films were constructed according to three categories: control (silica nanoparticle bulk film only), precursor + bulk, and bulk + cap. Five and 10 bilayers of the PAH/SiO_2 NP stratum were made for each category. The samples are listed below in **Table 4.5**, along with a description of the film layers and the pH conditions of the solutions used to make them. In order to differentiate between the layer types, the description of the precursor layer was written in red text, while the description of the capping layer was written in blue text. The control samples were "F-72" and "F-73" and corresponded to 5 and 10 bilayers of PAH/SiO_2 NPs, respectively. "F-74" and "F-75" were the 5- and 10-bilayer counterparts of the control, but with a capping layer that was constructed using PAH and PMA solutions both with a pH equal to 7. "F-80" and "F-81" were similar to the control specimens, but with a precursor layer consisting of 5 bilayers of PAH/PMA (pH = 9/5). Finally "F-82" and "F-83" were similar to "F-74" and "F-75" because the bulk films had a capping layer, but this time the pH values of the PAH and PMA solutions used to make the capping layer were 9 and 5, respectively.

Sample Name	Sample Description
F-72	5 bilayers of PAH/SiO_2 NPs
F-73	10 bilayers of PAH/SiO_2 NPs
F-74	5 bilayers of PAH/SiO_2 NPs + 5 bilayers of PAH/PMA (pH = 7/7)
F-75	10 bilayers of PAH/SiO_2 NPs + 5 bilayers of PAH/PMA (pH = 7/7)
F-80	5 bilayers of PAH/PMA (pH = 9/5) + 5 bilayers of PAH/SiO_2 NPs
F-81	5 bilayers of PAH/PMA (pH = 9/5) + 10 bilayers of PAH/SiO_2 NPs
F-82	5 bilayers of PAH/SiO_2 NPs + 5 bilayers of PAH/PMA (pH = 9/5)
F-83	10 bilayers of PAH/SiO_2 NPs + 5 bilayers of PAH/PMA (pH = 9/5)

Table 4.5 Description of the sample composition consisting of the bulk film with precursor (red text) or capping (blue text) layers.

The transmittance (**Figure 4.58**) and reflectance were measured for each of the samples, and the corresponding slope of extinction coefficient (1-T-R) versus $1/\lambda^4$ was calculated (**Table 4.6**). The reader should be reminded that the smaller the value of the "extinction coefficient

slope", the less light is scattered as it passes through the film. Both 5- and 10-bilayer control films (F-72, 73) had a slope equaling 0.0007. By comparison the two samples with the bulk film on top of a precursor layer (F-80, 81) had a slope of 0.0006, which was smaller than the control samples. This is not surprising because the refractive index of the precursor layer is probably somewhere between that of the bulk film ($n \approx 1.26$) and the glass substrate ($n = 1.5$). This creates a graded index for light traveling from air to the substrate, which could reduce not only reflection at the interfaces, but diffuse scattering as well. In general, the films with bulk and capping layers (F-74, 75, 82, 83) exhibited higher slopes than the control specimens. The lone exception was F-82, which was the 5-bilayer PAH/SiO_2 NP film with 5 bilayers of PAH/PMA (pH = 9/5) on top. Using a similar argument to the one above, it is likely that the extinction coefficient slope is larger for these samples because light incident on the film first encounters the capping layer. Therefore, reflection and diffuse scattering at this interface would be higher compared to an interface consisting of air/silica nanoparticles. The plot in **Figure 4.58** shows that the film that does not contain a precursor or capping layer (control sample) has the highest transmittance. This is the expected result because homogeneous polymer layers would likely scatter incident light. The sample with the precursor layer (PAH/PMA pH = 9/5) has an appreciably smaller transmittance than the control sample. In fact, the transmittance peak can not be seen in the plot, meaning that the nanoparticles did not adsorb as well to the polymer layer as they did to the glass surface. The samples with capping layers had interesting transmittance spectra. The transmission peak of the sample with PAH/PMA pH = 7/7 occurs at a larger wavelength than the control, although the peak is not as high. The sample with the PAH/PMA pH = 9/5 capping layer has a transmission peak that occurs at nearly the same wavelength as the PAH/PMA pH = 7/7 sample, but the peak is not as high. This may imply that a higher degree of polymer infiltration into the nanoparticle structure occurs using these pH conditions (9/5), although this is merely speculative.

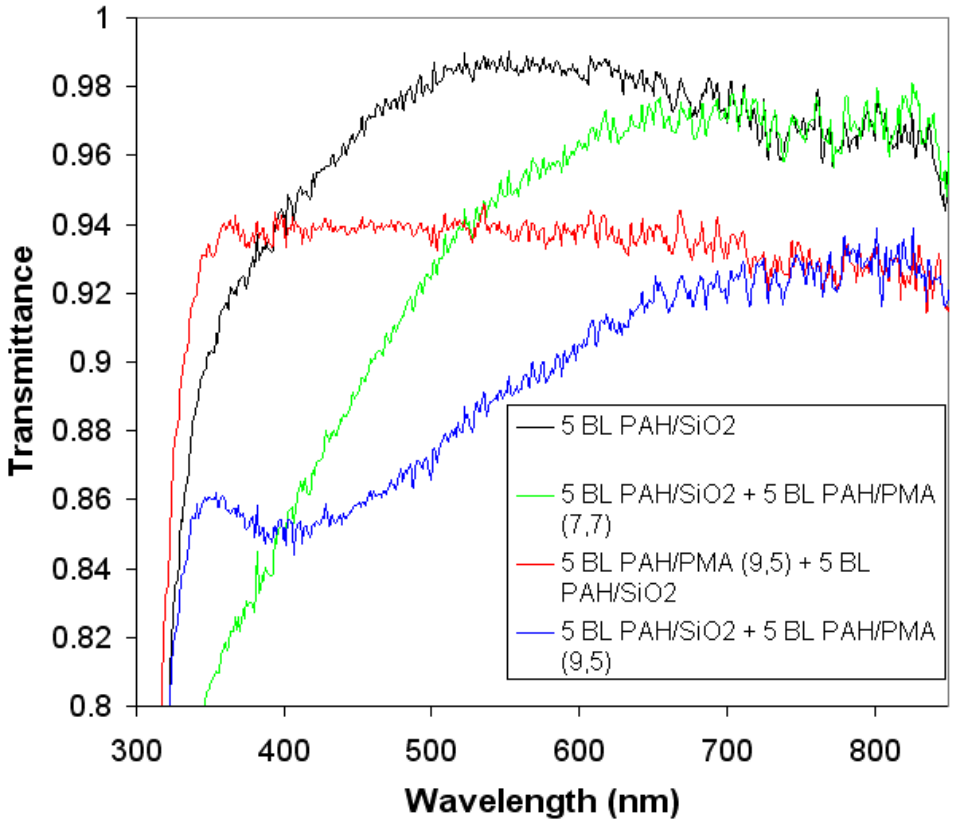

Figure 4.58 Transmittance spectra comparing the effect of precursor and capping polymer layers on 5 BL PAH/SiO_2 NP films. The optical quality is affected by the pH conditions of the polymer solutions used to make both precursor and capping layers.

The adhesive strength was quantified by the tape peel test and is also shown in **Table 4.6**. First, consider the measurements for the control samples. The reading for the 5-bilayer sample (F-72) is approximately three times higher than the 10-bilayer one. As mentioned in **Section 4.2**, this difference can be attributed to two different failure mechanisms. Five-bilayer films subjected to the tape peel test were typically removed completely from the substrate. The predominant failure mechanism for the 10-bilayer films however was cohesive, meaning that a layer of nanoparticles were removed with the tape, but a layer was also left behind on the substrate. The implication is that the tape was in partial contact with the substrate when it adhered to a 5-bilayer sample, but to an even lesser degree for a 10 bilayer one. Naturally, it would be more difficult to remove the tape from the substrate even if the contact is somewhat limited, than it would be to separate a layer of nanoparticles (cohesive failure). Next, consider the readings for F-74 and F-75, the 5 and 10 bilayer PAH/SiO_2 NP films with the PAH/PMA (pH

= 7/7) capping layer. The readings are fairly similar between F-72 (5 bilayer control) and F-74 (5 bilayer control + cap), though it is slightly greater for F-74. This is expected since the tape peel test most likely measured the strength of the interaction between the substrate and the first nanoparticle layer. A considerable difference, however, can be seen when comparing the readings for the 10-bilayer samples (F-73 and F-75). The measurement is nearly three times greater for the capped film. Recall that the tape peel test on 10-bilayer samples measured the cohesive strength, and one of the premises of the capping layer is that the polymers will infiltrate the nanoparticle network. Thus it appears as if the premise is correct to some degree. It may also be that little infiltration occurs, but the tape removed just the capping layer, and so the reading is a measure of the interaction between the topmost nanoparticle layer and the thin polymer film. Furthermore, it appears as if the pH conditions are an important consideration with respect to the capping layer. Notice that the readings for the samples with a PAH/PMA capping layer (pH = 9/5) are near or below that of the control. This suggests that it is better to use highly charged polymers for the capping layer that can diffuse into the bulk and bind nanoparticles. Lastly, consider the readings of the samples with a PAH/PMA (pH = 9/5) precursor layer (F-80, 81). In both cases, the readings are significantly greater than the control, with the 5-bilayer counterpart being nearly twice as high and the 10-bilayer one more than three times higher. This means that the tape was in contact with the precursor film in both cases, but more so with the 5-bilayer coating. These measurements clearly indicate that the precursor and capping layers individually improve the mechanical strength of the film. Therefore, the next step was to fabricate silica nanoparticle films including both layers.

Sample Name	Tape Peel Instrument Reading*	Extinction Coefficient Slope
F-72	47.1	0.0007
F-73	15.6	0.0007
F-74	59.1	0.0013
F-75	43.8	0.0019
F-80	81.8	0.0006
F-81	49.9	0.0006
F-82	38.6	0.0006
F-83	14.3	0.0017

Table 4.6 List of samples with their corresponding tape peel measurements and calculated extinction coefficients. *Tape peel instrument was calibrated such that a reading of "100" corresponded to 9.8 N of force. The width of the tape being pulled from the samples was 1.27 cm.

Silica nanoparticle films with both precursor and capping layers were made to determine how well they improved the film adhesion and cohesion. **Table 4.7** below gives a description of the sample composition. Two control samples were made and consisted of 5- (F-152) and 10- (F-153) bilayers of PAH/SiO_2 NPs. Next 5- (F-154) and 10- (F-155) bilayer films with precursor and capping layers were fabricated using the pH conditions of PAH and PMA that best improved the mechanical strength from the previous study. The pH values of solutions containing PAH and PMA used to make the precursor film were 9 and 5 respectively, and 7 for each constituent in the capping layer.

Sample Name	Sample Description
F-152	5 bilayers of PAH/SiO_2 NPs
F-153	10 bilayers of PAH/SiO_2 NPs
F-154	5 bilayers of PAH/PMA (9/5) + 5 bilayers of PAH/SiO_2 NPs + 5 bilayers of PAH/PMA (7/7)
F-155	5 bilayers of PAH/PMA (9/5) + 10 bilayers of PAH/SiO_2 NPs + 5 bilayers of PAH/PMA (7/7)

Table 4.7 Description of the sample composition consisting of the bulk film with precursor (red text) and capping (blue text) layers.

These samples were subjected to the tape peel test (**Table 4.8**). The numerical readings for the control samples were fairly similar to what was seen in **Table 4.6**. The data for the composite films (F-154, 155) are significantly higher than their counterparts, but it is necessary to discuss the failure of these two peels. The reading corresponding to the 5-bilayer composite film was 117.8, but during the test the adhesive was torn from the tape backing and remained on the film. Therefore, the result more accurately represents the adhesive strength of the tape, and not the film. This means that the adhesive strength of the film is greater than the tape. The reading for the 10-bilayer film (F-155) was 53.3, but an odd phenomenon occurred during the test. As the tape was removed, alternating bands of residual adhesive and film were left on the surface. In other words a pattern of thin rectangular regions of residual adhesive were left behind and stretched across the width of the substrate. The space between each of these bands of adhesive appeared to be untouched by the tape. It seems as if the tape was not in sufficient contact with the film at these untouched regions, although the tape was applied uniformly to the surface (discussed in **Experimental Details** chapter). Naturally, if the tape is not properly bonded to the untouched regions, then the reading for sample F-155 does not accurately represent the cohesive strength of the film, and would lead one to believe that the number should be higher than what is reported. New 5- and 10-bilayer composite films were made so that an abrasion test could be conducted on them. They were gently wiped with a Kimwipe®, and while they were clearly more resistant to abrasion than the control films, they were still removed from the substrate. As a result, I tried a different approach by implementing quadlayers in the construction of the bulk film. This is discussed in the next section.

Sample Name	Tape Peel Instrument Reading (same calibration described in Table 4.6)
F-152	35.8
F-153	17.8
F-154	117.8*
F-155	53.3#

Table 4.8 List of samples with their corresponding tape peel measurements. *Adhesive from the tape was left behind on the film. #Alternating bands of residual adhesive and film remained after tape peel. These phenomena are explained in greater detail above.

4.4.2 Polymer Interlayers with PAH and Silica Nanoparticles

Since the PAH/SiO_2 NP films with a precursor and capping layer were not strong enough to survive the abrasion test, it was assumed that diffusion of polymers from the capping layer into the nanoparticle matrix was limited. In order to guarantee that the nanoparticle interstitial void space was partially filled with polymers throughout the entire film, I made coatings in which the bulk region consisted of PAH/SiO_2 NP/PAH/PMA quadlayers (**Figure 4.59**). The precursor and capping layers were incorporated into the design since they improved the general adhesion and cohesion. The pH conditions of the PAH/PMA solutions were kept at 9/5 for the precursor film, and 7/7 for the cap. Furthermore, the pH values of the PAH/SiO_2 NP solutions were fixed at 7/9. The interlayer pH conditions of PAH and PMA, were varied in order to determine their effect on the film uniformity and cohesive strength.

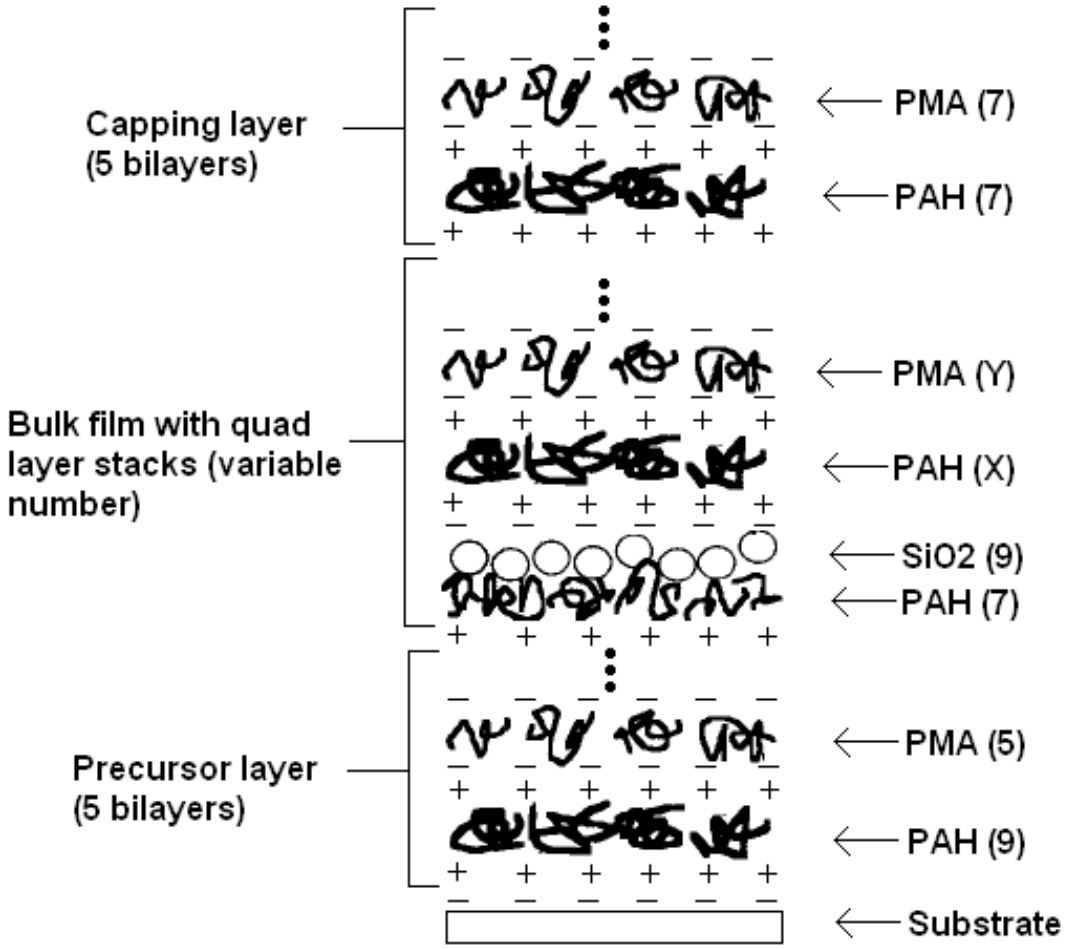

Figure 4.59 Multilayer design with polymer precursor and capping layers that also incorporates polymer interlayers in the bulk region to improve nanoparticle cohesion. The pH conditions of the various ISAM constituents on the right of the image are denoted in parentheses. The PAH and PMA pH values for the interlayers were varied throughout the study, and hence are denoted by "X" and "Y", respectively. Image is adapted with permission from: [Y. Lvov, K. Ariga, M. Onda et al., "Alternate assembly of ordered multilayers of SiO2 and other nanoparticles and polyions," Langmuir **13** (23), 6195-6203 (1997)]. Copyright 1997 American Chemical Society.

Five different samples were fabricated with varying PAH and PMA interlayer pH conditions in order to determine how they affected the optical properties of the multilayer system. A description of each sample is listed below in **Table 4.9**. The specimen F-253 was the control, and comprised precursor and capping layers, with $[PAH/SiO_2\ NP]_5$ bilayers in between. The bulk film of the four remaining samples had quadlayer stacks of [PAH/SiO_2

NPs/PAH/PMA]$_5$. The PAH/SiO_2 NP component of the quadlayer had fixed pH values of 7/9, while the PAH/PMA monolayers were changed according to the sample specifications.

Sample Name	Sample Description
F-253	5 bilayers of PAH/PMA (9/5) + 5 bilayers of PAH/SiO_2 NPs + 5 bilayers of PAH/PMA (7/7)
F-254	5 bilayers of PAH/PMA (9/5) + 5 quadlayers of PAH/SiO_2 NPs/PAH/PMA (7/9/6.5/6.5) + 5 bilayers of PAH/PMA (7/7)
F-255	5 bilayers of PAH/PMA (9/5) + 5 quadlayers of PAH/SiO_2 NPs/PAH/PMA (7/9/9/3) + 5 bilayers of PAH/PMA (7/7)
F-256	5 bilayers of PAH/PMA (9/5) + 5 quadlayers of PAH/SiO_2 NPs/PAH/PMA (7/9/7/7) + 5 bilayers of PAH/PMA (7/7)
F-257	5 bilayers of PAH/PMA (9/5) + 5 quadlayers of PAH/SiO_2 NPs/PAH/PMA (7/9/8/5) + 5 bilayers of PAH/PMA (7/7)

Table 4.9 Description of sample composition for quadlayer films surrounded by polymer precursor and capping layers.

Transmittance spectra (**Figures 4.60** and **4.61**) were acquired for the samples to compare their optical transparency as a function of the interlayer pH conditions. **Figure 4.60** includes spectra of all the samples. There is a large discrepancy between the transmission profile of the sample with interlayer PAH/PMA pH values of 9/3 and the rest of the samples. As a result, the finer details of the other spectra can not be clearly seen, and thus I include **Figure 4.61**. As expected, the peak transmittance of the control sample was higher (~ 98.5%) than the samples with quadlayer stacks. This implies that the PAH/PMA interlayers partially filled the interstitial voids. Of the samples with the quadlayer design, only two of them had a peak transmittance above 94%, those being when the PAH/PMA interlayer pH values were 7/7 (F-255) and 6.5/6.5 (F-254). Also of particular interest is the fact that the transmittance peaks were located at a different wavelength for each sample. Recall that the location of the 1st order peak along with the film index of refraction can allow one to estimate the physical thickness of the film. The transmittance peak for F-253 was located at 620 nm and at 556, none, 544, and 467 nm for F-254 – F-257, respectively. Assuming that the refractive index of the quadlayer films is reasonably

similar, one can compare their thicknesses. The samples with PAH/PMA values hovering around 7/7 appear to produce thicker, optically clear films. The worst sample had PAH/PMA interlayer pH conditions of 9/3. The spectrum indicates that the film scattered a significant amount of light. This means that the attraction of silica nanoparticles to the surface was weakened or hindered by the interlayer polymer solution pH values. It is typical for desorption to occur during the rinse cycle when the interaction between the top-most layer of nanoparticles and the underlying polymer surface is weak. As a result, an irregular surface can be formed that makes light more susceptible to scattering.

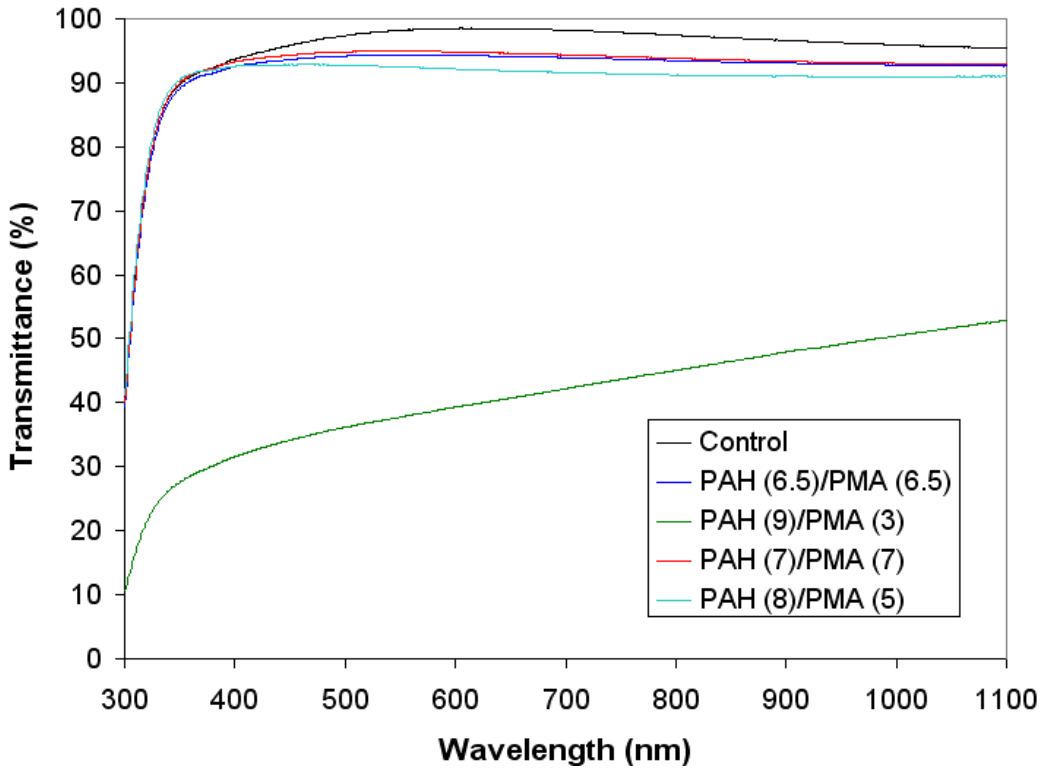

Figure 4.60 Transmittance spectra of samples with varying interlayer pH conditions. The effect of partial interstitial filling by PAH and PMA polymers can be observed by the decrease in transmittance compared to the control sample.

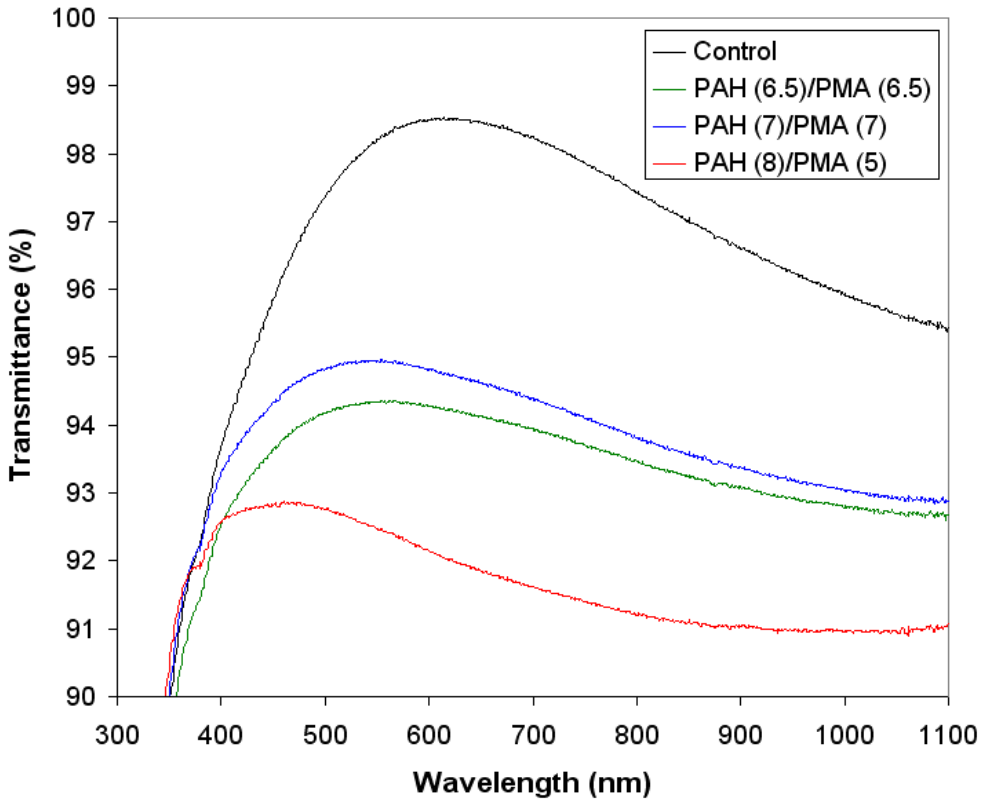

Figure 4.61 Zoom in of **Figure 4.60**, including all spectra with the exception of the sample with interlayer pH conditions of 9/3 for PAH/PMA. Using this scale it is easier to identify the peak transmittance and location for the given spectra.

4.4.3 Quartz Crystal Microbalance (QCM-D) Study on the Effect of Polymer Interlayer pH Conditions on Nanoparticle Adsorption

Quartz Crystal Microbalance is a highly effective technique for determining the areal mass density of thin ISAM films deposited onto a piezoelectric crystal with a known resonant frequency. The crystals are typically coated with gold electrodes to take advantage of their piezoelectric property. When material is adsorbed onto the crystal surface, it can be considered as an extension of the substrate and as a result will resonate at the same frequency as the crystal. Naturally, the frequency of the composite structure will decrease as more and more material is adsorbed. Sauerbrey[21] was the first to correctly determine the correlation between the changing frequency and mass of a rigid film on a crystal and produced his famous equation in 1959:

$$\Delta f = \left[\frac{-2 f_0^2}{A(\rho_q \mu_q)^{1/2}} \right] \Delta m \ldots\ldots \text{(Sauerbrey equation), where:}$$

f_0 = resonant frequency (Hz)

A = Piezoelectrically active crystal area (cm^2)

ρ_q = Density of quartz (2.648 g/cm^3)

μ_q = Sheer modulus of quartz (2.947×10^{11} $g/cm \cdot s^2$)

The above equation is valid for a crystal oscillating in air. If QCM-D is performed in liquid[22], the change in frequency is represented by:

$$\Delta f = -f_0^{3/2} \left(\frac{\eta_l \rho_l}{\pi \rho_q \mu_q} \right)^{1/2}, \text{ where:}$$

η_l = viscosity of the liquid

ρ_l = density of the liquid

Furthermore, the frequency shift in viscoelastic films cannot be accurately determined using the Sauerbrey equation. One of the challenges associated with QCM-D is determining whether the thin film on the crystal is rigid or viscoelastic. Lvov[19,23] used QCM to study the adsorption of negatively charged silica nanoparticles with poly(diallyldimethylammonium chloride) (PDDA), and used the Sauerbrey model to correlate film growth with the shift in frequency. He also used QCM to compare the adsorption time of coatings dried in between immersion steps, with films that were continuously immersed in ionic solutions and rinse cycles. His decision to treat the film/crystal as a rigid system may have seemed reasonable since the nanoparticles themselves are rigid, and as a result of their relatively larger size shifted the resonant frequency far more (1200 ± 60 Hz) than PDDA (100 ± 10 Hz). On the other hand, it is now a common practice amongst QCM-D users to monitor the energy dissipation[24] (D) in order to categorize a film as being either rigid (D = 0) or viscoelastic (D > 0).

The overarching goal of this particular study was to monitor the adsorption kinetics of the $[PAH/SiO_2\ NP/PAH/PMA]_n$ quadlayer stacks as a function of the PAH/PMA pH conditions. Furthermore, an in-depth look at the adsorption kinetics by QCM-D could complement the gathered transmittance data seen in **Figure 4.60**. I should mention that the majority of the QCM work was performed by Shane Seaman, an undergraduate that I was supervising at the time. Jonathan Metzman and I also assisted with the work, but my primary role was to plan and direct the research, and advise the students when necessary. The set of interlayer pH conditions selected for the study are listed below in **Table 4.10.** All permutations of PAH/PMA interlayers with pH values of 5 and 9 were considered, including a center point of 7/7. The center point was intentionally added because the transmittance data shown above (**Figure 4.60**) indicated that nanoparticle adsorption was relatively good under these conditions. For each sample, a precursor film with four PAH/PMA (pH = 9/5) bilayers was deposited onto the quartz resonator. Next four adsorption cycles of the sample were deposited on top of the precursor layer. Since we had limited time and knowledge of QCM modeling we decided to simply monitor the frequency shift during the silica nanoparticle adsorption step as a means of quantitatively assessing the overall adsorption of the films. Based on dissipation data (not shown), it is likely that the films should be treated as a viscoelastic system. We also chose not to consider the frequency shift of the first deposited silica nanoparticle layer because its adsorption is partially governed by the underlying precursor film.

One final note of importance is the cleaning regimen for the quartz substrates. This is also covered in the "**Experimental Details**" chapter, but a couple of samples were treated differently, which may have affected the data. Before they were used in an experiment the quartz crystals were ozone-cleaned, and then RCA-cleaned. The only difference was that instead of immersion in an acid bath, the crystals were ozone-cleaned a second time. Since the crystals are expensive, they are typically used many times until they are deemed unusable, which is usually after they have been used 20-30 times. The cleaning procedure above is generally considered robust enough to remove films from previous experiments. In fact, we RCA-cleaned our samples immediately AFTER the experiment was finished, only to RCA-clean them once more before reuse. We found after our experiments, however, that some residual material was left behind on the resonator. We continued to follow the recommended cleaning procedures, but at times we had data that was unusable. This was the case for a couple of samples, including

PAH/PMA pH conditions of 5/9 and 7/7. Hence they were not included in this analysis. Fortunately we intended to make two samples with interlayer pH conditions of 7/7, so one data set was acceptable. At some point, I conferred with a colleague with QCM experience, and he suggested that I sonicate the quartz crystals in a 1:1 mixture of toluene:water for 5 minutes and then perform RCA cleaning. This appeared to help remove the material from the resonator. Only two permutations in the experimental design remained at this point (PAH/PMA pH = 5/5, and 9/5), so they were adsorbed onto "clean" surfaces. The control sample was the first one we made, so it also was deposited onto a clean surface. There is, however, some uncertainty as to how clean the remaining samples were, so caution is advised when reviewing the reported data. For the time being, it is my recommendation that the quartz crystals should always be RCA-cleaned and sonicated in the toluene:water mixture for 5 minutes in order to guarantee that the surface is free of residual material.

Sample PAH/PMA Interlayer pH Conditions	**Number of samples**
Control (no PAH/PMA interlayers)	1
PAH/PMA pH = 5/5	1
PAH/PMA pH = 9/9	1
PAH/PMA pH = 5/9	1
PAH/PMA pH = 9/5	1
PAH/PMA pH = 7/7	2

Table 4.10 Original experimental design with various PAH/PMA interlayer pH conditions. The adsorption of these films was compared with a film containing no interlayers (control).

The QCM data are presented below for the following PAH/PMA pH conditions: control (no interlayers) (**Figure 4.62**), 5/5 (**Figure 4.63**), 7/7 (**Figure 4.64**), 9/9 (**Figure 4.65**), and 9/5 (**Figure 4.66**). The figures are plots of the frequency shift (Hz) versus time (seconds). The QCM instrument can monitor the frequency shift of the 1^{st}, 3^{rd}, 5^{th}, 7^{th}, 9^{th}, 11^{th}, and 13^{th} harmonic frequencies. In a well-behaved system under equilibrium, the harmonic frequencies may separate with added mass, but they should follow a common trend. To prevent unnecessary cluttering in the figures, I have only plotted the 3^{rd}, 5^{th}, and 7^{th} harmonic frequencies. In the

early stages of each experiment, the quartz resonator is loaded with the PAH/PMA precursor film. This can be seen in approximately the first hour of the QCM plot by small changes in the frequency. After one hour, a significantly larger frequency shift is observed and is attributed to the deposition of the first nanoparticle layer. This frequency shift was the smallest when compared to the other silica adsorption steps for all of the samples, except for the one with PAH/PMA pH values of 9/5. This implies that the pH conditions of the precursor film (PAH/PMA = 9/5) impaired the adsorption of the first layer of nanoparticles. It should be no surprise therefore that the only sample in which nanoparticles did not readily deposit was the one with PAH/PMA interlayer pH values of 9/5 (**Figure 4.66**). The nanoparticle adsorption steps, although fairly evident by the comparatively large frequency shift, are indicated in the figures by "SiO_2".

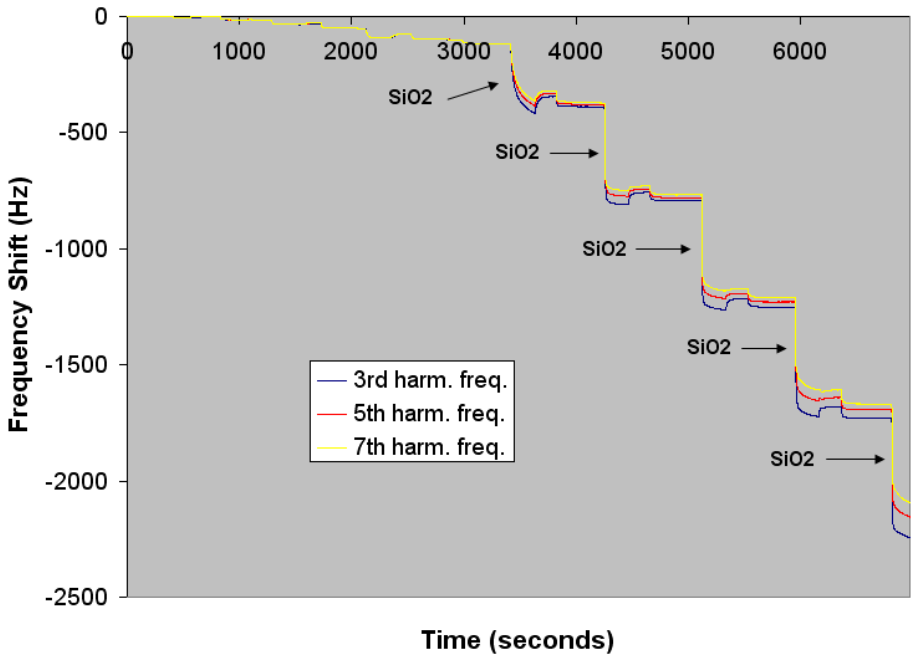

Figure 4.62 Frequency change of a quartz crystal as a function of time for a composite coating with 4 PAH/PMA (pH = 9/5) bilayers, and followed by 4 PAH/SiO_2 NP (pH = 7/9) bilayers.

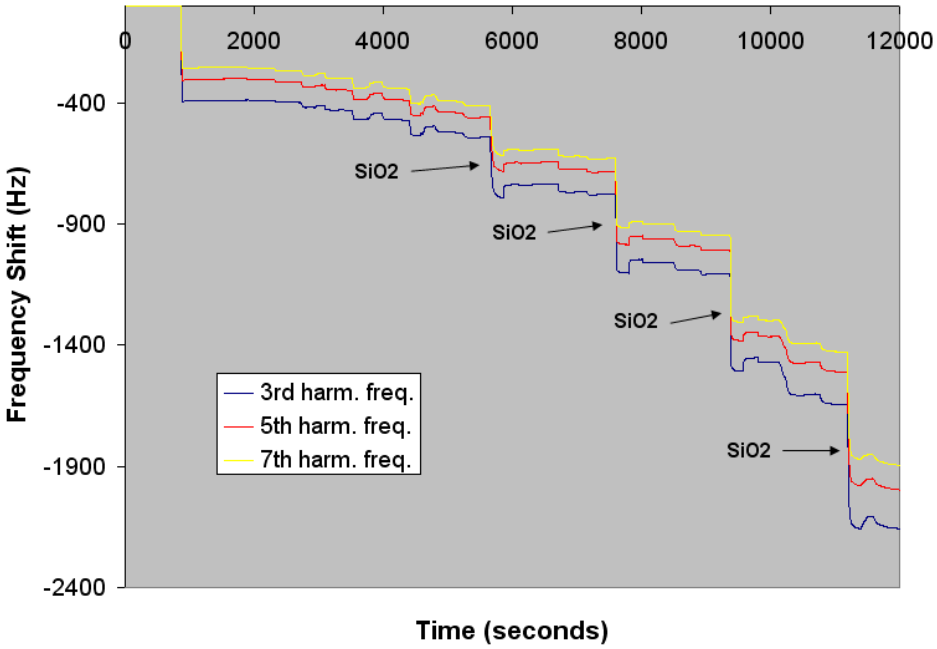

Figure 4.63 Frequency change of a quartz crystal as a function of time for a composite coating with 4 PAH/PMA (pH = 9/5) bilayers, and followed by 4 PAH/SiO_2 NP/PAH/PMA (pH = 7/9/5/5) quadlayers.

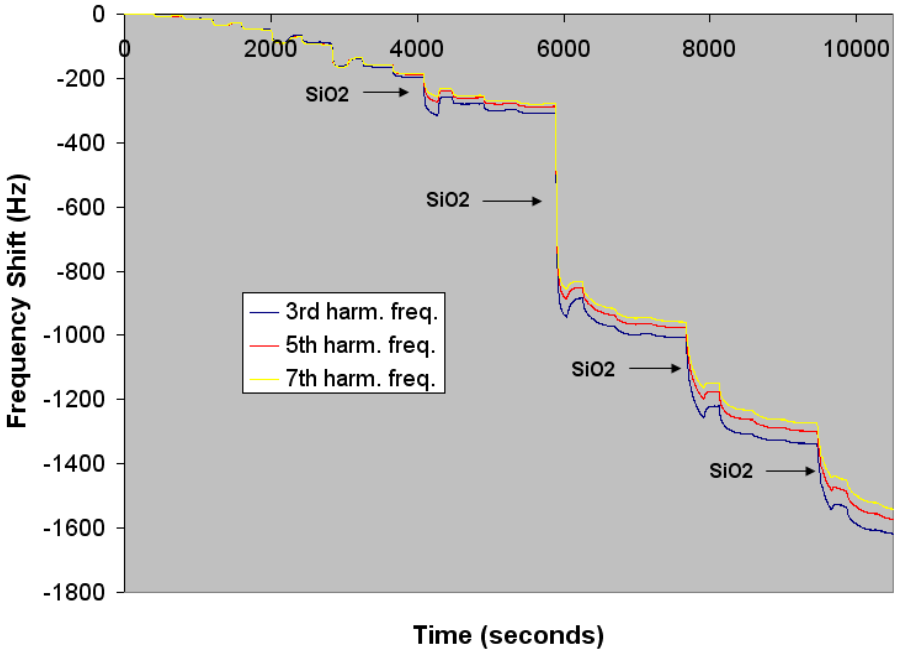

Figure 4.64 Frequency change of a quartz crystal as a function of time for a composite coating with 4 PAH/PMA (pH = 9/5) bilayers, and followed by 4 PAH/SiO_2 NP/PAH/PMA (pH = 7/9/7/7) quadlayers.

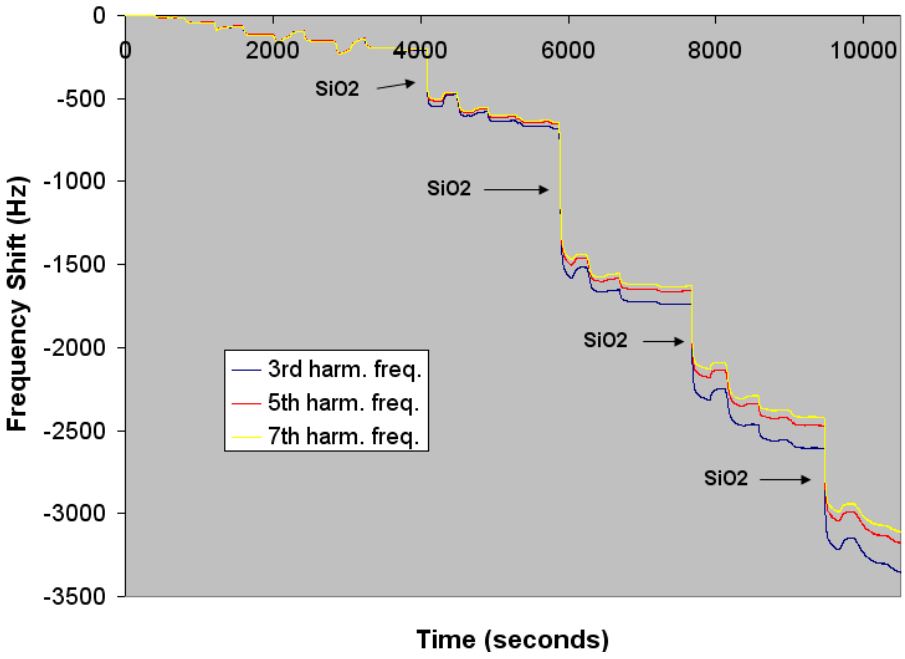

Figure 4.65 Frequency change of a quartz crystal as a function of time for a composite coating with 4 PAH/PMA (pH = 9/5) bilayers, and followed by 4 PAH/SiO_2 NP/PAH/PMA (pH = 7/9/9/9) quadlayers.

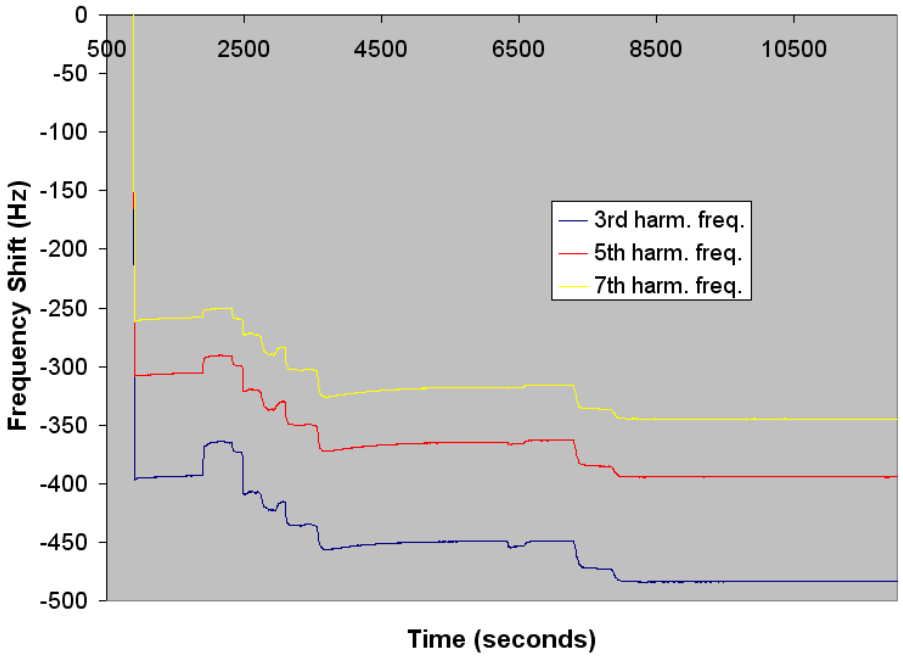

Figure 4.66 Frequency change of a quartz crystal as a function of time for a composite coating with 4 PAH/PMA (pH = 9/5) bilayers, and followed by 4 PAH/SiO_2 NP/PAH/PMA (pH = 7/9/9/5) quadlayers.

The frequency shifts of the 3rd, 5th, and 7th harmonic frequencies for the 2nd, 3rd, and 4th nanoparticle adsorption steps of each sample are listed below in **Table 4.11**. The changes corresponding to the 3rd, 5th, and 7th harmonic frequencies are remarkably close for each nanoparticle adsorption step. Had the films fit the Sauerbrey model, then direct correlations could have been made between changing frequency and mass, which could have yielded an estimation of the increase in thickness per nanoparticle adsorption cycle. With that knowledge, it would have been much easier to determine the interlayer pH conditions that optimize nanoparticle adsorption. As stated above the films are viscoelastic, so more sophisticated and time-consuming modeling will be necessary to properly correlate changes in frequency with thickness. Furthermore, the fact that residual material (viscoelastic) may have been present on some surfaces could potentially bias some of the data below. Now that an effective cleaning procedure in place for the crystal surfaces, this problem can be eliminated. For now, however, a direct comparison of the frequency shifts at each adsorption step between the samples is not advisable. The goal of the QCM study was to complement and expand on the spectroscopic results. In the QCM experiments, we found that a film with PAH/PMA interlayer pH values of 9/5 did not adsorb much material. In the spectroscopic study I made a film with similar interlayer pH conditions (PAH/PMA = 9/3), and the resulting spectrum indicates that it has inferior nanoparticle adsorption and poor uniformity. **Figure 4.61** also indicates that the film with interlayer pH values of 7/7 produce thicker, more homogeneous films. While this cannot be confirmed by the present QCM data, one can merely note that progressive deposition of this film was realized. Therefore, some parallels can be made between the spectroscopic and QCM studies, even if they are extremely limited. One additional point worth noting is that QCM involves dynamic adsorption of ionic species (flow rate = 0.3 mL/min), while deposition of films in the auto-dipper was done under static condition (i.e., flow rate = 0 mL/min). Regardless, there is potential to make direct correlations in the future between both studies if the films are modeled as viscoelastic media and common interlayer pH conditions are used for the specimens deposited both on glass for transmittance data and the quartz resonators for QCM.

Sample	Harmonic Frequency	Δf: 2nd SiO_2 layer (Hz)	Δf: 3rd SiO_2 layer (Hz)	Δf: 4th SiO_2 layer (Hz)
Control (no PAH/PMA interlayers)	3rd	-365	-425	-429
	5th	-361	-415	-413
	7th	-358	-403	-403
PAH/PMA interlayer pH: 5/5	3rd	-286	-367	-518
	5th	-289	-363	-492
	7th	-272	-361	-473
PAH/PMA interlayer pH: 7/7	3rd	-575	-211	-200
	5th	-567	-210	-193
	7th	-557	-188	-171
PAH/PMA interlayer pH: 9/9	3rd	-835	-512	-547
	5th	-809	-476	-526
	7th	-798	-462	-526
PAH/PMA interlayer pH: 9/5	3rd	~ 0	~ 0	~ 0
	5th	~ 0	~ 0	~ 0
	7th	~ 0	~ 0	~ 0

Table 4.11 Samples with varying PAH/PMA interlayer pH values, and the corresponding frequency shifts of the 3rd, 5th, and 7th harmonics for the 2nd, 3rd, and 4th adsorption steps of silica nanoparticles.

In comparison to the PAH/SiO_2 NP films with precursor/capping layers, the composite films with PAH/PMA interlayers are not as optically transparent. This is primarily due to the interstitial filling of PAH and PMA polymers in the nanoparticle network. On a positive note, the partial filling appeared to marginally improve the film cohesion. Several samples were rubbed with a cheesecloth, and they were more resistant to the abrasion compared to the films with precursor/capping layers. Their mechanical strength, however, is not on the level of the calcined samples since they were still removed from the substrate.

4.5 Summary

The focus of this chapter was the exploration of different methods to improve the cohesion of silica nanoparticle films and the adhesion of the film to the substrate. Three different techniques were presented. The first method involved the use of a photo-reactive polymer called diazo-resin in ISAM deposition with silica nanoparticles. Provided sulfonate groups populated the substrate and nanoparticle surfaces, it was possible to convert the ionic bonds between diazo-resin and these surfaces into covalent ones. Different approaches were used to coat the substrate and nanoparticles with sulfonate groups. For the substrate, this was a relatively straightforward process as it was silylated with MPTS and dipped in an acid bath to convert the thiol into a sulfonate. ISAM assembly of a PAH/PSS bilayer was performed on colloidal silica nanoparticles in order to give them the necessary sulfonate end groups. UV/VIS spectroscopy and SEM imaging indicates that the nanoparticle aggregation sustained during PAH/PSS deposition caused unwanted light scattering, and possibly shielded the bulk film from the UV irradiation necessary for cross-linking. The second method involved thermal fusing of silica nanoparticles with each other and the glass substrate, a process known as calcination. The mechanical strength of these coatings was significantly improved without compromising the optical transparency. In the final method, precursor and capping polymer layers consisting of PAH and PMA were incorporated into PAH/SiO_2 NP films in order to improve the adhesion to the substrate and nanoparticle cohesion, respectively. To further improve the cohesion PAH/PMA interlayers were deposited between the PAH/SiO_2 NP layers. This was countered by a moderate decrease in the optical transparency. The effect of the interlayer polymer pH values on the silica nanoparticle adsorption was studied by optical spectroscopy and QCM-D.

[1] S. G. Cao, C. Zhao, and W. X. Cao, "Synthesis of diazoresin and its photocrosslinking reaction," Polymer International **45** (2), 142-146 (1998).

[2] W. X. Cao, S. J. Ye, S. G. Cao et al., "Novel polyelectrolyte complexes based on diazo-resins," Macromolecular Rapid Communications **18** (11), 983-989 (1997).

[3] J. Q. Sun, T. Wu, Y. P. Sun et al., "Fabrication of a covalently attached multilayer via photolysis of layer-by-layer self-assembled films containing diazo-resins," Chemical Communications (17), 1853-1854 (1998).

[4] J. Q. Sun, Z. Q. Wang, Y. P. Sun et al., "Covalently attached multilayer assemblies of diazo-resins and porphyrins," Chemical Communications (8), 693-694 (1999).

[5] J. Q. Sun, C. B. Long, F. Liu et al., "Covalently attached multilayer assemblies containing photoreactive diazo-resins and conducting polyaniline," Colloids and Surfaces a-Physicochemical and Engineering Aspects **169** (1-3), 209-217 (2000).

[6] J. Q. Sun, T. Wu, F. Liu et al., "Covalently attached multilayer assemblies by sequential adsorption of polycationic diazo-resins and polyanionic poly(acrylic acid)," Langmuir **16** (10), 4620-4624 (2000).

[7] J. Q. Sun, T. Wu, B. Zou et al., "Stable entrapment of small molecules bearing sulfonate groups in multilayer assemblies," Langmuir **17** (13), 4035-4041 (2001).

[8] K. K. Unger, *Porous Silica: Its Properties and Use as Support in Column Liquid Chromatography*. (Elsevier, Amsterdam, NY, 1979), pp.pp xi, 336.

[9] D. Lee, M. F. Rubner, and R. E. Cohen, "All-nanoparticle thin-film coatings," Nano Letters **6** (10), 2305-2312 (2006).

[10] F. C. Cebeci, Z. Z. Wu, L. Zhai et al., "Nanoporosity-driven superhydrophilicity: A means to create multifunctional antifogging coatings," Langmuir **22**, 2856-2862 (2006).

[11] J. W. Ostrander, A. A. Mamedov, and N. A. Kotov, "Two modes of linear layer-by-layer growth of nanoparticle-polylectrolyte multilayers and different interactions in the layer-by-layer deposition," Journal of the American Chemical Society **123** (6), 1101-1110 (2001); J. Jeon, V. Panchagnula, J. Pan et al., "Molecular dynamics simulations of mutilayer films of polyelectrolytes and nanoparticles," Langmuir **22** (10), 4629-4637 (2006).

[12] D. Lee, Z. Gemici, M. F. Rubner et al., "Multilayers of oppositely charged SiO_2 nanoparticles: Effect of surface charge on multilayer assembly," Langmuir **23** (17), 8833-8837 (2007).

[13] Y. I. Rabinovich, J. J. Adler, A. Ata et al., "Adhesion between nanoscale rough surfaces - I. Role of asperity geometry," Journal of Colloid and Interface Science **232** (1), 10-16 (2000); Y. I. Rabinovich, J. J. Adler, A. Ata et al., "Adhesion between nanoscale rough surfaces - II. Measurement and comparison with theory," Journal of Colloid and Interface Science **232** (1), 17-24 (2000); F. W. DelRio, M. L. Dunn, B. L. Boyce et al., "The effect of nanoparticles on rough surface adhesion," Journal of Applied Physics **99** (10) (2006).

[14] S. E. Yancey, W. Zhong, J. R. Heflin et al., "The influence of void space on antireflection coatings of silica nanoparticle self-assembled films," Journal of Applied Physics **99** (3) (2006).

[15] Y. Fu, H. Xu, S. L. Bai et al., "Fabrication of a stable polyelectrolyte/Au nanoparticles multilayer film," Macromolecular Rapid Communications **23** (4), 256-259 (2002).

[16] C. G. Wu, L. F. Tzeng, Y. T. Kuo et al., "Enhancement of the photocatalytic activity of TiO_2 film via surface modification of the substrate," Applied Catalysis a-General **226** (1-2), 199-211 (2002).

[17] G. B. Sukhorukov, E. Donath, H. Lichtenfeld et al., "Layer-by-layer self assembly of polyelectrolytes on colloidal particles," Colloids and Surfaces a-Physicochemical and Engineering Aspects **137** (1-3), 253-266 (1998); G. B. Sukhorukov, E. Donath, S. Davis et al., "Stepwise polyelectrolyte assembly on particle surfaces: a novel approach to colloid design," Polymers for Advanced Technologies **9** (10-11), 759-767 (1998); D. Radziuk, D. G. Shchukin, A. Skirtach et al., "Synthesis of silver nanoparticles for remote opening of polyelectrolyte microcapsules," Langmuir **23** (8), 4612-4617 (2007); D. Radziuk, A. Skirtach, G. Sukhorukov et al., "Stabilization of silver nanoparticles by polyelectrolytes and poly(ethylene glycol)," Macromolecular Rapid Communications **28** (7), 848-855 (2007).

[18] J. Sun, H. Mukamal, Z. Q. Liu et al., "Analysis of the Taber test in characterization of automotive side windows," Tribology Letters **13** (1), 49-54 (2002).

[19] Y. Lvov, K. Ariga, M. Onda et al., "Alternate assembly of ordered multilayers of SiO_2 and other nanoparticles and polyions," Langmuir **13** (23), 6195-6203 (1997).

[20] Frank Caruso, Dirk G. Kurth, Dirk Volkmer et al., "Ultrathin molybdenum polyoxometalate-polyelectrolyte multilayer films," Langmuir **14** (13), 3462-3465 (1998); Izumi Ichinose, Hideo Tagawa, Suguru Mizuki et al., "Formation process of ultrathin multilayer films of molybdenum oxide by alternate adsorption of octamolybdate and linear polycations," Langmuir **14** (1), 187-192 (1998); D. Lee, D. Omolade, R. E. Cohen et al., "pH-Dependent structure and properties of TiO_2/SiO_2 nanoparticle multilayer thin films," Chemistry of Materials **19** (6), 1427-1433 (2007).

[21] G. Sauerbrey, "Use of crystal oscillators for weighing thin films and for microweighing," Zeitschrift fuer Physik (155), 206-222 (1959).

[22] K. K. Kanazawa and J. G. Gordon, "Frequency of a quartz microbalance in contact with liquid," Analytical Chemistry **57** (8), 1770-1771 (1985).

[23] Y. M. Lvov, J. F. Rusling, D. L. Thomsen et al., "High-speed multilayer film assembly by alternate adsorption of silica nanoparticles and linear polycation," Chemical Communications (11), 1229-1230 (1998).

[24] M. V. Voinova, M. Jonson, and B. Kasemo, "On dissipation of quartz crystal microbalance as a mechanical spectroscopy tool," Spectroscopy-an International Journal **18** (4), 537-544 (2004).

CHAPTER FIVE

Improved Adsorption of Silica Nanoparticle Films on Polycarbonate by Deep UV Irradiation

This chapter shows the progress made to improve adsorption and uniformity of silica nanoparticle films on Makrolon® polycarbonate by UV treatment. First a brief review of ways to functionalize polycarbonate for ISAM deposition is given. Next, proof of surface functionalization and molecular reorganization will be presented, followed by the impact of UV irradiation on the transmittance and reflectance of the films, as well as the adsorption characteristics of the nanoparticles in the first several assembly cycles.

5.1 Introduction and Review

Thin film deposition onto thermoplastics has become increasingly important due to their combination of impact resistance and optical clarity. In order to promote thin film growth by electrostatic methods, the surface must be chemically modified so that charged groups are uniformly spread over the area of the substrate. The conventional methods used to oxidize glass surfaces (piranha, RCA[1]) cannot be used on polycarbonate (PC) as they are too severe and would dissolve the substrate. Hence, alternative methods are necessary to functionalize the surface of polycarbonate.

The most widespread method currently used to pre-treat polycarbonate is plasma etching. A number of interesting studies have been conducted to understand the effect of plasma treatment on the surface properties of polycarbonate. Vallon[2] studied the surface modification of PC surfaces exposed to Ar, NH_3, and N_2 plasmas. Furthermore, he deposited a silica layer onto the various treated PC surfaces using a microwave plasma reactor to determine which plasma treatment optimized the surface adhesion. More recently Chen[3] compared the surface adhesion of silicon nitride (SiN_x) films deposited by PECVD onto PC surfaces treated by Ar, N_2, and O_2 plasmas. In general, they found that Ar and N_2 plasma sources were most effective at improving adhesion of the silica layer to the polycarbonate surface. In 1996 Vallon[4] also showed that the Ar source plasma initiated Photo-Fries rearrangements of the polycarbonate surface, resulting in

backbone scission and a dense, cross-linked structure. Acidic charged groups were also discovered on the PC surface. Zajíčková[5] also argued in favor of a cross-linked surface as a result of the Ar plasma and showed by XPS that the PC structure was changed, as evidenced by decreased energy peaks associated with the carbonate and hydrocarbon groups. Dahl[6] similarly showed how N_2 plasma created a graded interphase near the PC surface. The formation of highly stable C–N, C=N, and O–C≡N groups, all verified by XPS, were responsible for the improved adhesion of silica onto PC.

It is important to note that UV photons are emitted from plasma sources,[7] and are responsible for the chain scission and photo-Fries processes in polycarbonate. Rivaton[8] conducted a thorough study on the effects of UV treatment on the surface chemistry of polycarbonate. He determined that different photochemical processes occur in polycarbonate as a result of exposure to long and short UV (λ = 365 and 254 nm, respectively). He attributed chain scission and radical formation with secondary photoreactions of photo-Fries products with exposure to short wavelength UV (254 nm). Long wavelength UV (365 nm), according to his study, was responsible for surface oxidation. This was confirmed using IR spectroscopy by the formation of functional groups in the hydroxyl (3600 – 3100 cm^{-1}) and carbonyl (1750 – 1550 cm^{-1}) ranges. In 1995 he conducted a follow-up study[9] to identify the photochemical mechanisms of the scission process and photo-oxidation products.

Geretovszky[10] and coworkers studied the effects of deep UV irradiation (λ = 172 nm) on polycarbonate. They used attenuated total reflectance infrared spectroscopy (ATR-IR), UV/VIS spectroscopy, and XPS to monitor the change in the PC molecular structure, and identify the photoproducts formed after UV treatment. When looking at the IR spectrum of polycarbonate, two pronounced absorption peaks are present at 1767 and 1505 cm^{-1}. These are attributed to the carbonyl stretching (C=O) of the carbonate group and structural vibration of the aromatic C–C groups, respectively. After deep UV treatment of PC, the IR spectrum was measured. They discovered that the absorption intensity at both peaks progressively decreased with continued UV exposure. The decrease in absorption of the carbonyl group (1767 cm^{-1}) made it clear that the polymer chains were breaking at the carbonate group, while the corresponding decrease at 1505 cm^{-1} implied that a ring opening mechanism was occurring. They attributed this to a photo-oxidative process as described by Rivaton.[9] The photo-Fries products (**Figure 5.1**)

phenylsalicylate and dihydroxybenzophenone are formed competitively by radical formation and recombination during backbone scission.

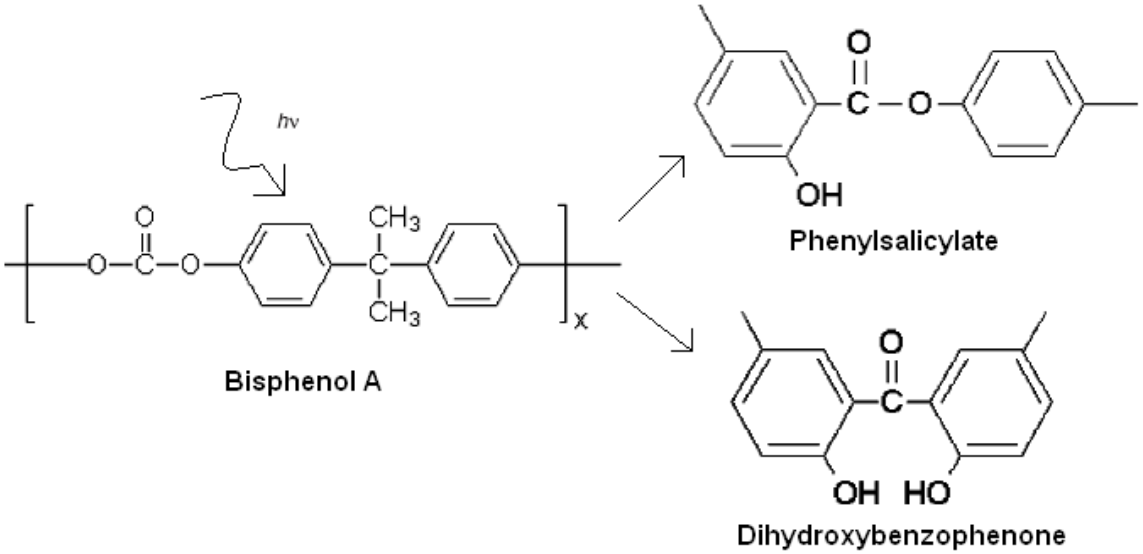

Figure 5.1 Polycarbonate molecular structure and competitive photoproducts formed as a result of deep UV irradiation (λ = 172 nm). Reprinted from: [Z. Geretovszky, B. Hopp, I. Bertoti et al., "Photodegradation of polycarbonate under narrow band irradiation at 172 nm", Appl. Surf. Sci. **186**, 85-90][11] with permission from Elsevier.

In 2002 Welle and Gottwald[11] exposed polycarbonate to a UV source emitting λ = 185 and 253 nm. They showed through dye binding experiments that UV caused carboxylic groups to form on the PC surface. This fact served as motivation for our research since it involves ISAM deposition onto charged substrates. Anti-reflection coatings have been deposited onto *plasma*-treated PC by a number of different methods, including: plasma polymerization,[12] sol-gel,[13] and ISAM deposition.[14] The ISAM process was performed using silica nanoparticles, and resulted in very high transmittance (~ 99 %). Plasma treatment, however, is less than ideal since it is a vacuum-dependent process, and the substrate size is limited to the size of the vacuum chamber. Since deep UV irradiation has been shown to successfully impart charged carboxylic species on the polycarbonate surface, I explored the possibility of fabricating uniform, highly transmittant PAH/SiO_2 NP ISAM films on PC substrates utilizing this UV treatment.

5.2 Early Attempts

The goals of the study were to repeat some of the experiments performed by Geretovszky[10] in order to confirm that polycarbonate undergoes molecular reorganization and photo-oxidation, and to determine if UV irradiation of PC improves the adsorption of ISAM constituents onto the substrate surface. Makrolon® GP Bisphenol A Polycarbonate sheets (Bayer) were shipped from Sheffield Plastics, and came in 2 X 2' sheets with a thickness of 1/16". These large sheets were machined down to 1 X 3" substrates to match the size of a standard microscope glass slide. The sheets were initially covered by a plastic masking adhesive (**Figure 5.2**) that protected the polycarbonate from dust and potential scratches.

Figure 5.2 Makrolon® GP Bisphenol A polycarbonate substrate cut to 1 X 3". The plastic masking has yet to be removed from the sample.

This plastic masking had to be removed before exposing the polycarbonate to UV. After this, the PC was irradiated to deep UV (λ = 185, 254 nm) for equal lengths of time on each side. The experiments from the work of Geretovszky to be repeated, along with the motivation for each experiment, are listed below:

UV/VIS spectroscopy: Absorbance spectra of polycarbonate in the UV/VIS region revealed new bands around 317 and 380 nm. These bands were attributed to the formation of the photoproducts phenylsalicylate and dihydroxybenzophenone, respectively.

FTIR spectroscopy: By monitoring the change in the absorption peaks at 1767 and 1505 cm^{-1}, the degree of chain scission and aromatic ring opening (respectively) near the surface could be monitored.

XPS: This was an effective way to monitor the carbon-to-oxygen ratio of the polycarbonate surface and how it changed as a function of UV irradiation.

The UV/VIS and FTIR experiments yielded inconclusive, if not ambiguous, results. According to FTIR, it was unclear if the UV irradiation initiated the proposed structural modifications, as the peak intensities (in transmission) at 1767 and 1505 cm^{-1} did not progressively increase with continued UV exposure. Only after XPS analysis was it clear that something was wrong. The C1s and O1s orbital profiles of the polycarbonate can be seen in **Figure 5.3**. Three samples with different UV irradiation times (0, 30, and 60 minutes) were used. The glaring problem can be seen in the C1s orbital (**5.3A**). The typical polycarbonate profile includes an intense and broad hydrocarbon peak centered around 285 eV, and a smaller peak around 290-291 eV, which is attributed to the carbonate group. The hydrocarbon peak is present in **5.3A**, but the carbonate peak is not distinguishable from the noise in the data. This indicated that some material with a different molecular structure was being probed rather than the polycarbonate. This led me to the conclusion that residual adhesive from the plastic masking was still on the polycarbonate surface; hence I had been analyzing the properties of the adhesive instead of the polycarbonate.

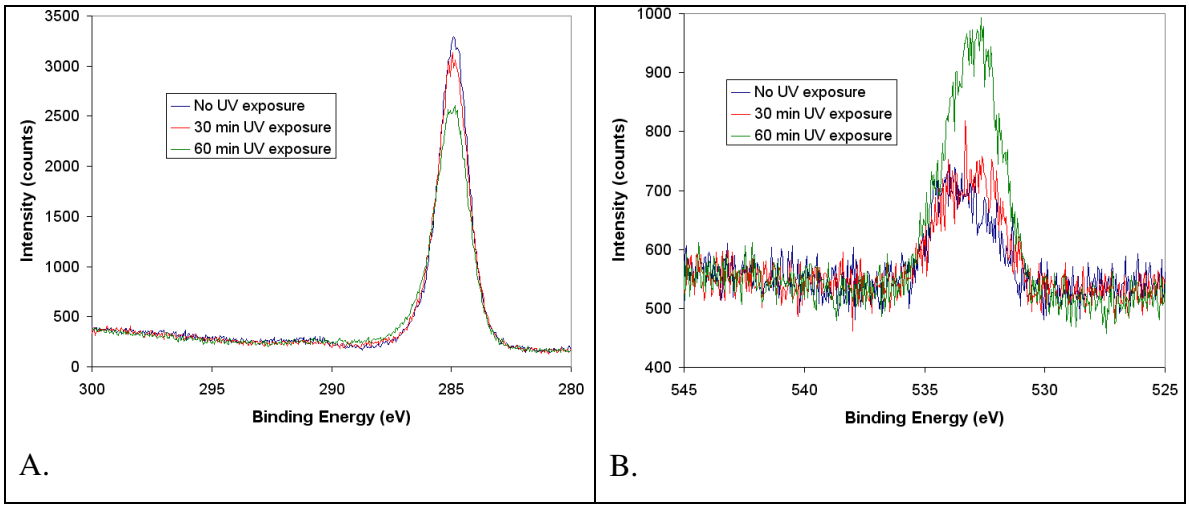

Figure 5.3 XPS profiles of the **A)** C1s and **B)** O1s orbitals of polycarbonate samples with residual adhesive from the plastic masking.

In response to this discovery, I contacted the polycarbonate supplier (Sheffield Plastics) and requested a proper surface cleaning protocol to remove the adhesive. They recommended the following procedure:

Adhesive Removal Protocol (from Sheffield Plastics)

1. Remove plastic masking
2. Using a soft cloth clean surface with isopropanol
3. Rinse with deionized water
4. Wash with concentrated soap (e.g. Palmolive, Joy, etc.)
5. Thoroughly rinse again with deionized water
6. Dry substrate with nitrogen gas

There was a concern that soap residue may be left behind given the above protocol, so I decided to compare the surface and bulk polycarbonate properties by XPS. Two polycarbonate substrates were cut with a razor blade to expose the bulk material. I also included a sample whose surface was cleaned by isopropanol and soap and one cleaned only by isopropanol (suggested by Dr. Harry Gibson, Department of Chemistry, Virginia Tech). A single unit of bisphenol A consists of one double-bonded oxygen and two single-bonded oxygen atoms. Monitoring this 2:1 ratio is easily achieved by XPS in the O1s region. **Table 5.1** shows the O1s

peak area (%) of single and double-bonded oxygen for the aforementioned samples. The single to double-bonded ratios for the bulk are not quite 2:1 (1.75:1 and 1.87:1 for samples 1 and 2, respectively), but this may be due to special additives not disclosed by the manufacturer. Regardless, note that the polycarbonate surface cleaned by both isopropanol ***and*** soap has a single to double-bonded ratio of 1.44, significantly less than the bulk material. Also small traces of sulfur were detected on this sample, evidently from residual soap despite significant rinsing. In contrast, the polycarbonate that was cleaned by isopropanol ***only*** had a single to double-bonded ratio identical to one of the bulk samples. This showed that the best way to clean the substrates was with isopropanol and DI water rinsing.

Sample	**O1s peak area (%)**	
	Single-bonded Oxygen (534 nm)	**Double-bonded Oxygen (532 nm)**
Polycarbonate (bulk) 1	63.7	36.3
Polycarbonate (bulk) 2	65.2	34.8
Polycarbonate-cleaned by isopropanol and soap	59.1	40.9
Polycarbonate-cleaned by isopropanol	63.7	36.3

Table 5.1 Comparison of single and double-bonded oxygen in bulk polycarbonate (PC) with PC surfaces cleaned by different methods.

The carbonate peak (291 eV) in the C1s profile (**Figure 5.4A**) became visible after appropriate cleaning measures were applied. This meant that the isopropanol removed most of the adhesive, and I could accurately study the surface properties of polycarbonate. Analysis of XPS profiles will be discussed in section 5.3. Therefore the final cleaning protocol was as follows:

Adhesive Removal Protocol (modified)

1. Remove plastic masking
2. Using a soft cloth clean surface with isopropanol
3. Rinse with deionized water
4. Dry substrate with nitrogen gas

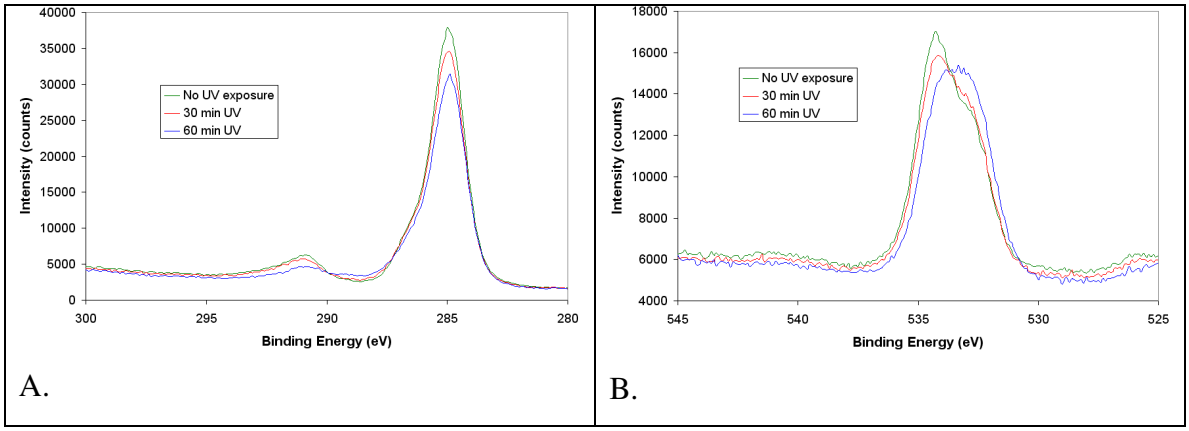

Figure 5.4 XPS profiles of the **A)** C1s and **B)** O1s orbitals of polycarbonate samples cleaned according to the modified protocol.

5.3 Confirmation of Molecular Reorganization and Photo-Oxidation of Polycarbonate by Deep UV

In this section I present results of experiments that show how deep UV affects polycarbonate surface chemistry and oxidation. The experiments include UV/VIS spectroscopy, FTIR spectroscopy, and XPS analysis.

UV/VIS spectroscopy

Five PC substrates were taken and irradiated by UV (λ = 185, 254 nm) on both sides for 0, 5, 10, 20, and 30 minutes, and their absorbance spectra measured in the UV/VIS region. I did this to determine if the photo-products phenylsalicylate (317 nm) and dihydroxybenzophenone (380 nm) were created by photo-Fries rearrangement. The absorbance spectra of these samples can be seen in **Figure 5.5**. The first thing to note in this figure is that the wavelength range does

not include the wavelengths of interest (i.e. 317, 380 nm). This is because our polycarbonate samples were too thick (1/16" or approximately 1.6 mm), resulting in very strong absorbance measurements that became saturated for values below 384 nm. In comparison, the samples used by Geretovszky to measure absorbance were 50 μm thick. From the figure however, it is clear that the overall absorbance increased with the amount of UV exposure. Additionally, the deviation in the data points for various exposures at each wavelength increased at shorter wavelengths approaching 380 nm; largely characteristic of data near a peak. Therefore, while direct evidence in the UV/VIS region could not be measured, some indirect clues exist to support the findings by Geretovszky.

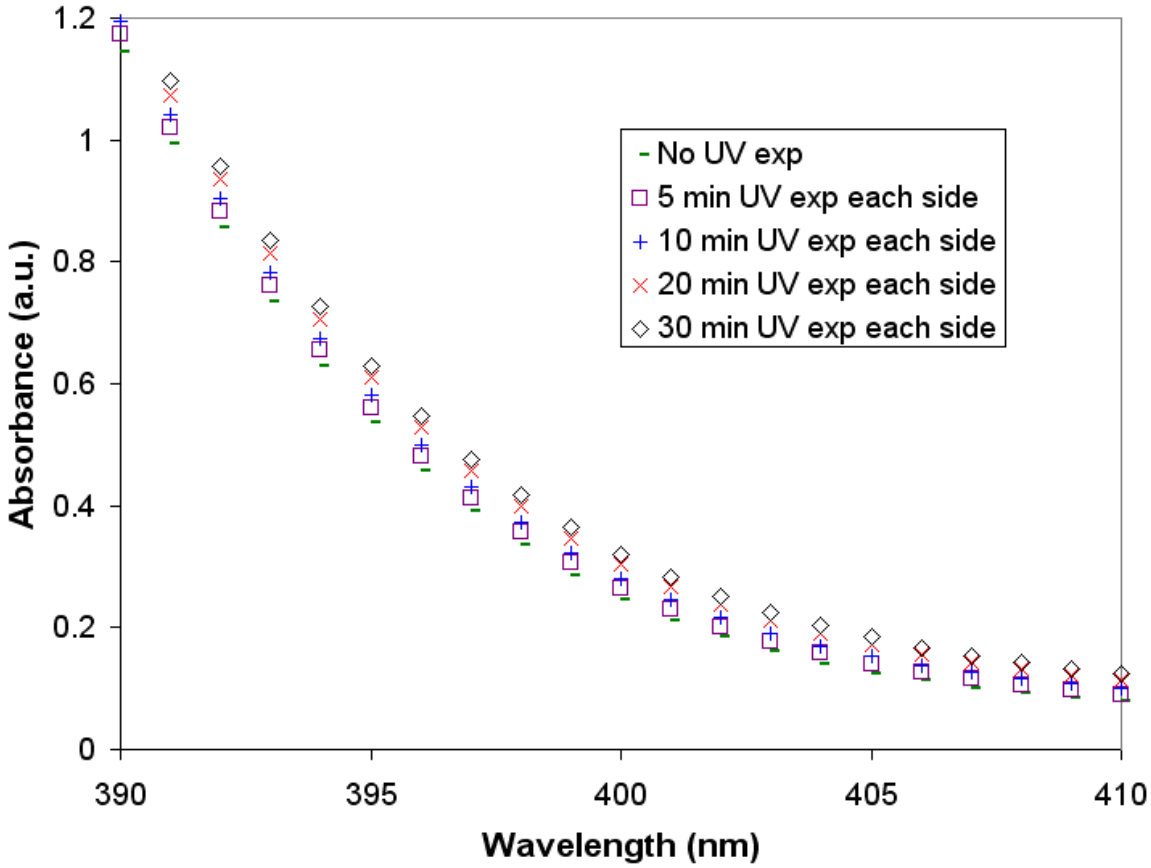

Figure 5.5 Absorbance of UV-irradiated polycarbonate samples as a function of wavelength.

FTIR spectroscopy

Like Geretovszky I used the Attenuated Total Reflectance (ATR) method to measure the IR spectra of our samples. This technique was preferred over the conventional transmission FTIR method because I was only interested in studying the surface properties of PC, and those changes could be drowned out by the spectrum of the bulk material. I measured the spectrum for three polycarbonate samples with different UV exposure times (0, 2, and 4 hours). Long exposure times were chosen to ensure that changes in the spectra could be detected. The transmittance spectra of the polycarbonate samples in the IR are shown in **Figure 5.6**, while **Figure 5.7** specifically targets the absorption peaks around 1768 and 1502 cm^{-1}.

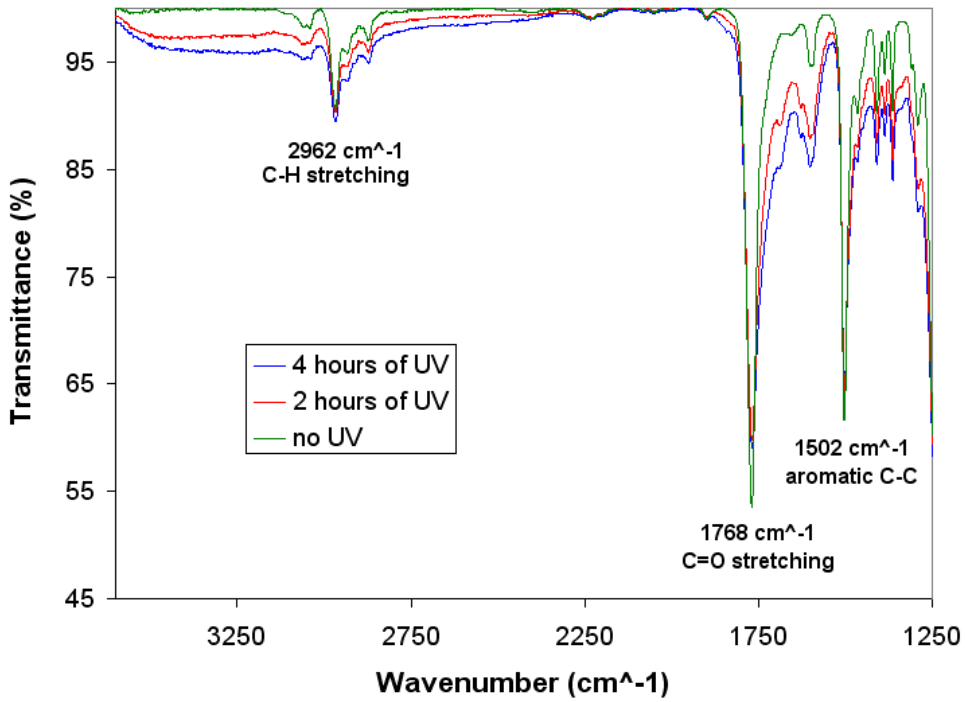

Figure 5.6 IR spectra of polycarbonate samples as a function of UV irradiation.

Three absorption peaks dominate the spectrum in **Figure 5.6**. In transmission these peaks are represented by dips in the intensity. The most energetic mode represents the C–H stretching (2965 cm^{-1}) of the methyl groups in bisphenol A. The next mode is attributed to the C=O stretching (1768 cm^{-1}) of the carbonate group, while the final mode is due to aromatic C–C vibration (1502 cm^{-1}) of the benzene ring. The most notable change in the spectra in **Figure 5.6**

is the broad dip in transmittance with increased UV exposure from approximately 2350 – 3575 cm^{-1}. This results from increasing amounts of hydrogen-bonded carboxylic acids reported by Welle,[11] and additional hydrogen-bonded by-products. The breadth of the dip in transmittance is typical of energy spectra in hydrogen-bonded systems. More importantly, this feature supports the hypothesis that UV irradiation creates charged species on the polycarbonate surface which facilitate ISAM deposition of PAH and silica nanoparticles.

If one looks more closely at the 1450 – 1850 cm^{-1} range (**Figure 5.7**), the changes in the absorption peaks at 1502 and 1768 cm^{-1} become more apparent. The transmission values at 1502 and 1768 cm^{-1} for the untreated polycarbonate are 61.7 and 53.6%, respectively. After two hours of UV irradiation, the transmittance at these peaks increased to 64.3 and 60%. As mentioned previously, these changes in transmittance are directly related to changes in the molecular structure of polycarbonate at the surface. Chain scission of the carbonate group is responsible for the increase in transmittance at 1768 cm^{-1}, while aromatic ring opening is responsible for the increase at 1502 cm^{-1}. As shown by Geretovszky, chain scission leads to the formation of phenylsalicylate and dihydroxybenzophenone by photo-Fries rearrangement and ring opening is achieved by a photo-oxidative route that contributes to the implantation of charged carboxylic groups on the surface. Molecular reorganization of the photo-products appears to be quenched after *at most* two hours of UV, as the peaks undergo little to no change from two to four hours of irradiation. On the other hand the total degree of surface oxidation steadily increases from two to four hours of UV as seen from **Figure 5.6**.

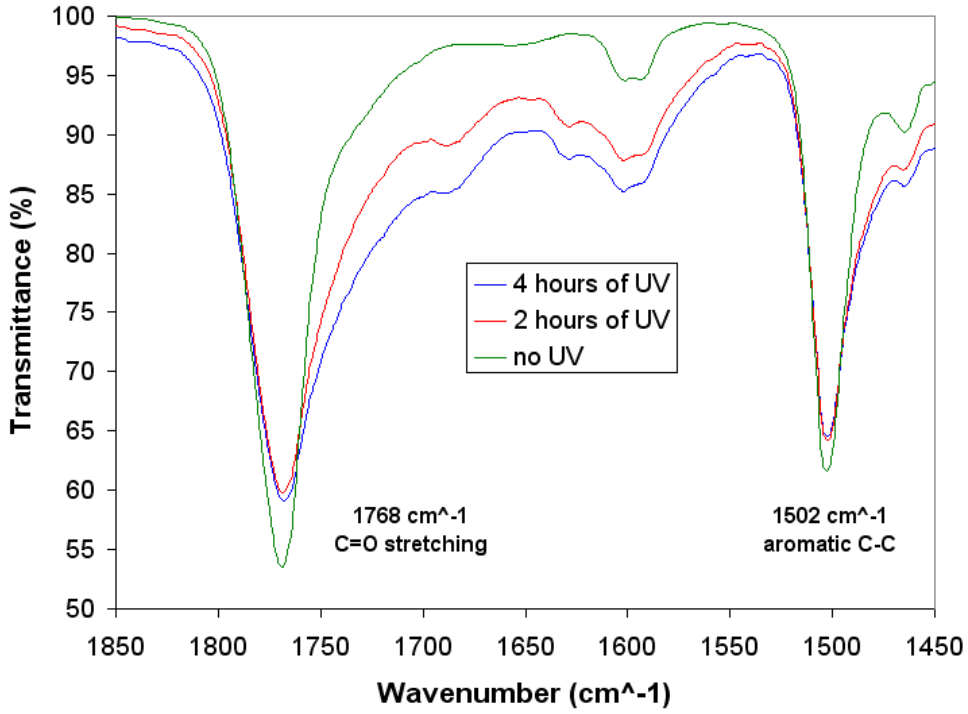

Figure 5.7 IR spectra as a function of UV exposure of polycarbonate focusing specifically on the molecular changes of the carbonate (1768 cm^{-1}) group and benzene ring (1502 cm^{-1}).

XPS analysis

The C1s and O1s orbital profiles of three different polycarbonate samples were measured by X-ray Photoelectron Spectroscopy (XPS). The samples varied according to their exposure to UV (0, 30, and 60 minutes of UV). In a single unit of bisphenol A there are 16 carbon atoms and three oxygen atoms. This means that PC is composed of 84% carbon and 16% oxygen (excluding hydrogen). The elemental composition of our samples is listed below in **Table 5.2**. Without UV irradiation, the carbon-to-oxygen (C/O) ratio was 84.9/15.1, which is very close to the typical composition of PC. The samples with UV irradiation had a smaller C/O ratio, which decreased to 84.3/15.7 for 30 minutes of UV and finally to 82.9/17.1 for one hour. The change in the ratio is not overwhelming, but at the same time is not negligible. The increased presence of oxygen with UV irradiation indicates that oxidation occurs and supports the claim that oxidized species populate the polycarbonate surface as a result of the treatment.

Sample	A.C. (%) Carbon	A.C. (%) Oxygen
No UV exposure	84.9	15.1
30 minutes UV exposure	84.3	15.7
60 minutes UV exposure	82.9	17.1

Table 5.2 Atomic composition of carbon and oxygen at the surface of polycarbonate as a function of UV irradiation.

A second look at the C1s and O1s profiles previously shown in **Figures 5.4A** and **B** provides additional information regarding the structural modification of bisphenol A due to UV. The C1s orbital (**Figure 5.8**) has several peaks of interest. The broad hydrocarbon peak (centered around 285 eV) is typically modeled as a superposition of two or three smaller peaks (in our case two), each associated with different molecular interactions in the benzene ring. The carbonate peak (290.8 eV) is clearly visible after implementing cleaning protocols to remove sufficient amounts of residual adhesive (described in section 5.2). From the figure, it is clear that polycarbonate samples with increased UV exposure have fewer energetic electrons ejected from the benzene ring. This is consistent with the ring opening mechanism proposed by Geretovszky, and the IR data that shows an increase in transmittance at 1502 cm^{-1} (**Figure 5.7**) with UV irradiation. A similar conclusion can be derived from the steady decrease in intensity of the carbonate group (290.8 eV) with an increase in UV exposure. This further supports the claim that chain scission occurs and is consistent with the increase in transmittance at 1768 cm^{-1} from IR spectroscopy. A final observation can be made from the C1s profile, which is the subtle increase in electron intensity spanning the energy range from 287.5 to 289.8 eV. The molecular compositions covering these energies range from hydrocarbon C–O bonds to the more energetic carboxylic acids. The general increase of this spectrum of energies supports the idea that UV irradiation is responsible for the presence of functional carboxylate species on the surface of polycarbonate. The above observations are further supported by inspection of the O1s energy profile (**Figure 5.9**). Typical polycarbonate has three oxygen atoms (all are a part of the carbonate group); two that are single-bonded to carbon (534.3 eV), and one double-bonded to carbon (532.7 eV). Therefore, the single-to-double bonded oxygen ratio is 2:1. The peak areas of the single and double bonded oxygen of the untreated sample were 63.7 and 36.3%, respectively; yielding a ratio of 1.75 (**Table 5.3**). This ratio undergoes dramatic change as the

sample is treated with deep UV, and drops to 1.42 for 30 minutes and finally to 1.04 for 60 minutes. Therefore, after an hour of exposure an equal number of single and double-bonded oxygen atoms are present on the surface. This is an interesting observation, particularly since carboxylate groups also have a 1:1 ratio of single-to-double bonded oxygen.

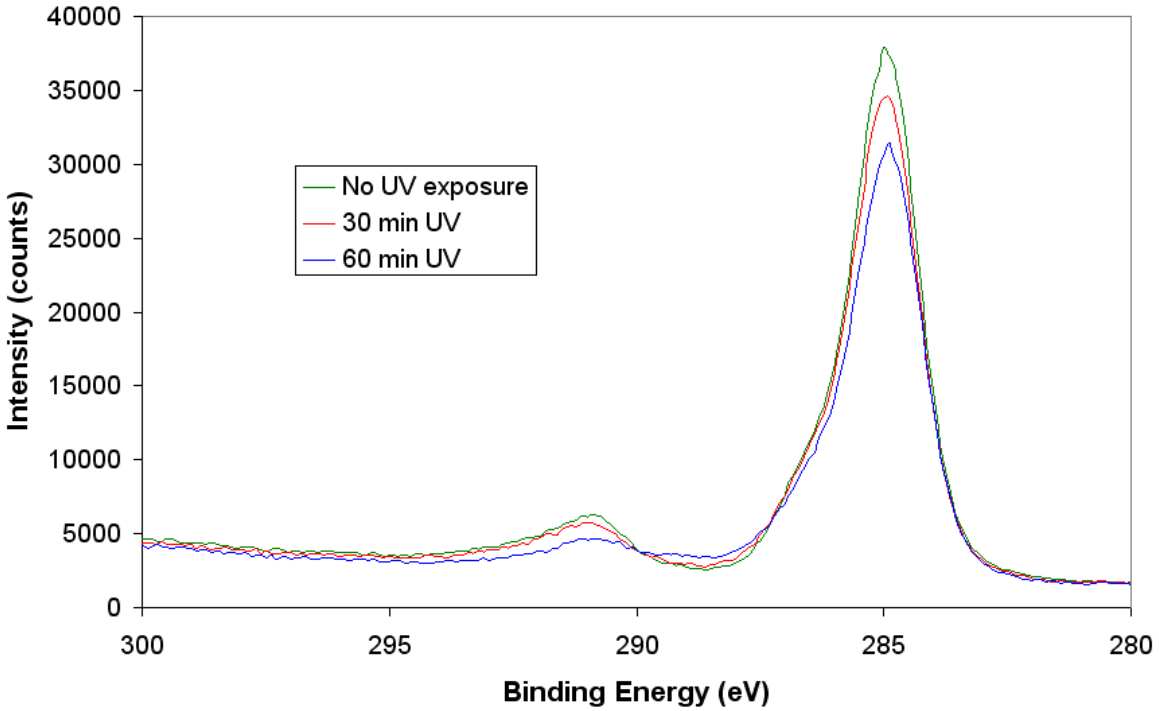

Figure 5.8 Energy profile for the C1s orbital of polycarbonate as a function of UV exposure on the surface.

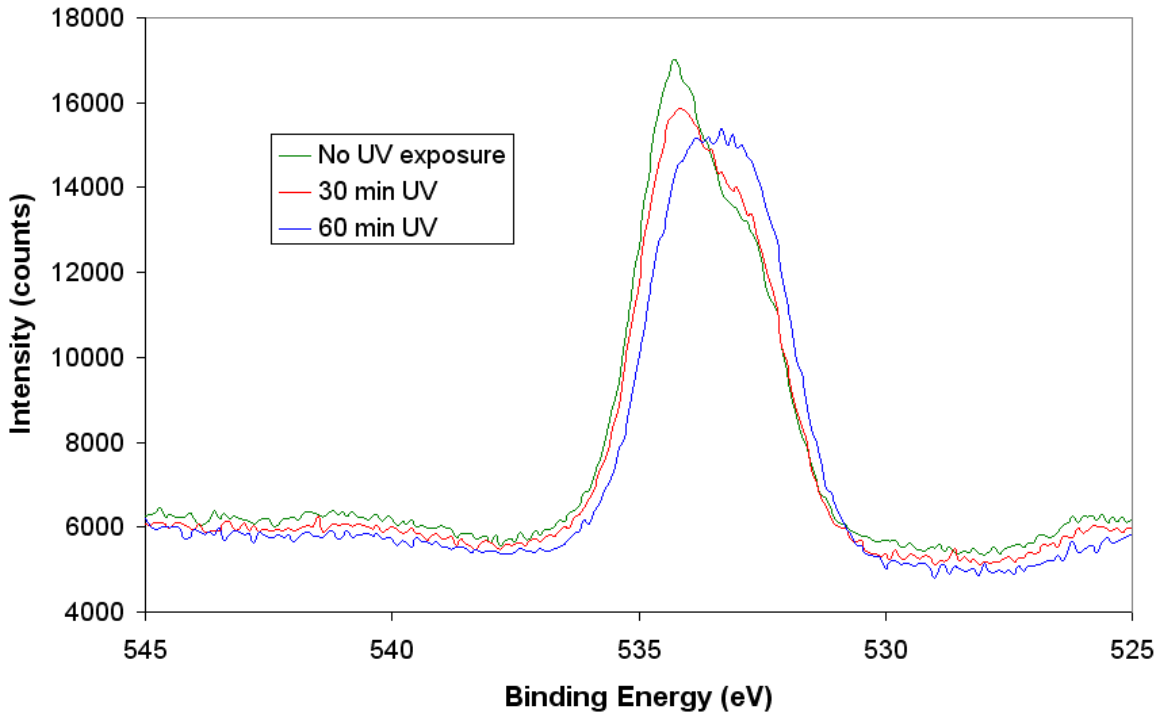

Figure 5.9 Energy profile for the O1s orbital of polycarbonate as a function of UV exposure on the surface.

Sample	Single-bonded oxygen peak area (%)	Double-bonded oxygen peak area (%)	Single-to-double bonded oxygen ratio
No UV exposure	63.7	36.3	1.75
30 minutes UV exposure	58.6	41.4	1.42
60 minutes UV exposure	50.9	49.1	1.04

Table 5.3 Comparison of how the peak area between single and double bonded oxygen changes as a function of UV exposure.

To conclude, I studied how the surface chemistry of polycarbonate was affected by UV irradiation using UV/VIS/IR spectroscopies and XPS for elemental analysis. I confirmed several findings by Geretovszky; namely that UV treatment resulted in photo-Fries rearrangement of the

structure and surface oxidation that created surface charged functional groups. These functional groups serve as a platform for the buildup of ISAM films containing SiO_2 NPs.

5.4 Optical properties and adsorption characteristics of PAH/SiO_2 NP ISAM films on UV-treated polycarbonate

In this section I show how the UV treatment of polycarbonate facilitates uniform ISAM deposition of PAH and silica nanoparticles per adsorption cycle. I also provide data that shows how the optical clarity can be improved by increasing the duration of UV exposure. Lastly, the impact of UV irradiation on the macro and microscopic film uniformity is discussed.

After verifying that deep UV treatment oxidized the polycarbonate surface with functional carboxylate species, I deposited PAH/SiO_2 NP ISAM coatings to see how the treatment affected the film growth, optical transmittance, and homogeneity. For all of the PAH/SiO_2 NP films, I prepared 150 mL of 10 mM PAH at pH = 7, and 150 mL of 3.76 M silica nanoparticle aqueous suspension at pH = 9. The substrates were exposed to UV and then placed in the automated dipper for layer-by-layer self-assembly. One of the first characteristics to be studied in ISAM systems is the uniform deposition of film constituents per adsorption cycle. Six PAH/SiO_2 NP ISAM films were deposited onto polycarbonate that was treated with one hour of deep UV. These films varied according to the number of adsorption cycles, which included 4, 5, 6, 7, 8, and 9 bilayers. **Figure 5.10** is a plot of the transmittance versus wavelength (300-1100 nm) for these samples. The transmission peak of the 4-bilayer sample is somewhere in the mid-to-far end of the visible spectrum. The peak for the 5-bilayer coating is at the far end of the visible, while the peaks of the 6-, 7-, 8-, and 9-bilayer films continue to shift into the near IR. It is important to note that polycarbonate has several absorption peaks in the VIS/IR range (600, 673, 865, and 903 nm) that can suppress transmission peaks arising from destructive interference of light at those respective wavelengths. The absorption peaks at 673 and 865 nm correspond to the 5^{th} and 4^{th} harmonic C-H stretching modes, respectively. The figure shows that PAH/SiO_2 NP films on UV-exposed PC follow the behavior of typical ISAM films, as the thickness appears to increase linearly with the number of deposited bilayers.

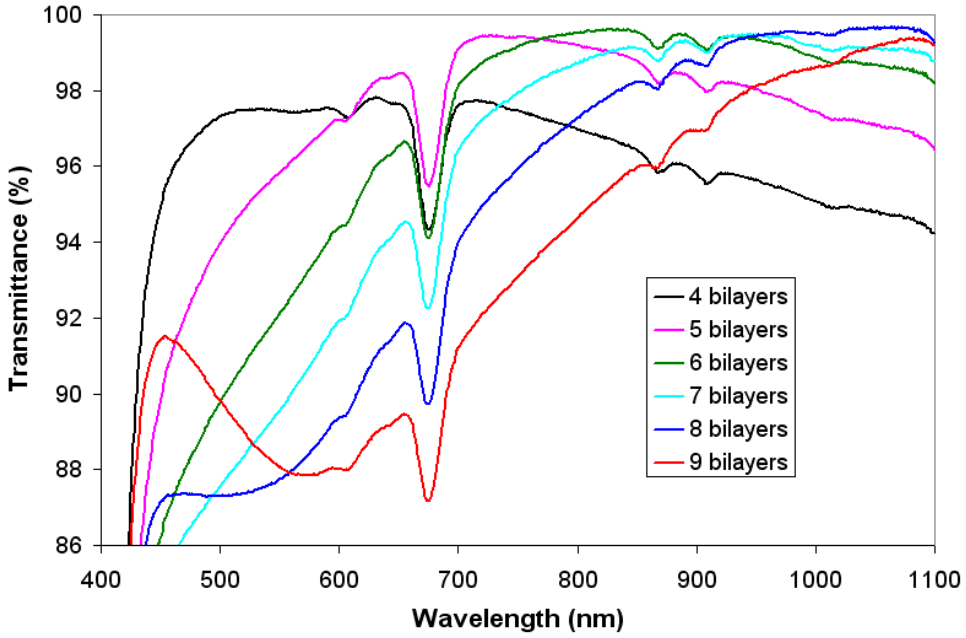

Figure 5.10 Transmittance spectra of PAH/SiO_2 NP films on polycarbonate irradiated by UV for one hour. The wavelength at which reflected light undergoes maximum destructive interference shifts from the mid-to-far visible and into the near IR as the number of adsorption cycles is increased.

Since the index of refraction of polycarbonate is higher than glass (1.585 vs. 1.5), the desired coating refractive index to achieve complete destructive interference of light for a given wavelength λ is 1.26 (as compared to ~ 1.23 for glass). Therefore the optical clarity of PAH/SiO_2 NP films on polycarbonate was expected to exceed those deposited on glass ($T \approx$ 99.6%). It was also postulated that increased dosage of UV on PC before ISAM deposition would improve the transmittance of these coatings. To test this hypothesis, I took four PC substrates and exposed them to UV for different times (0, 15, 30, and 60 minutes of UV on each side). After this the substrates were coated with 8 bilayers of PAH and silica nanoparticles, and finally measured in transmission mode with the UV/VIS spectrophotometer. **Figure 5.11** shows the resulting transmittance plot of the samples. The spectrum of an uncoated polycarbonate substrate was included for the sake of comparison. Without a coating the polycarbonate substrate, in general, permits nearly 91% of incident light to transmit. The transmittance improved dramatically, however, when an ISAM film was deposited onto the surface. The plot shows a general increase in transmittance across the spectral range with longer UV dosage times.

Transmission as high as 99.85% was achieved when the substrate was exposed to UV for one hour on each side. What is surprising, however, is the very high transmittance (99.3%) of the ISAM film on polycarbonate *without* UV exposure. In theory, the surface of an untreated polycarbonate sample should be inert, thus making film formation by ISAM deposition impossible. I address this concern in the next section (5.5).

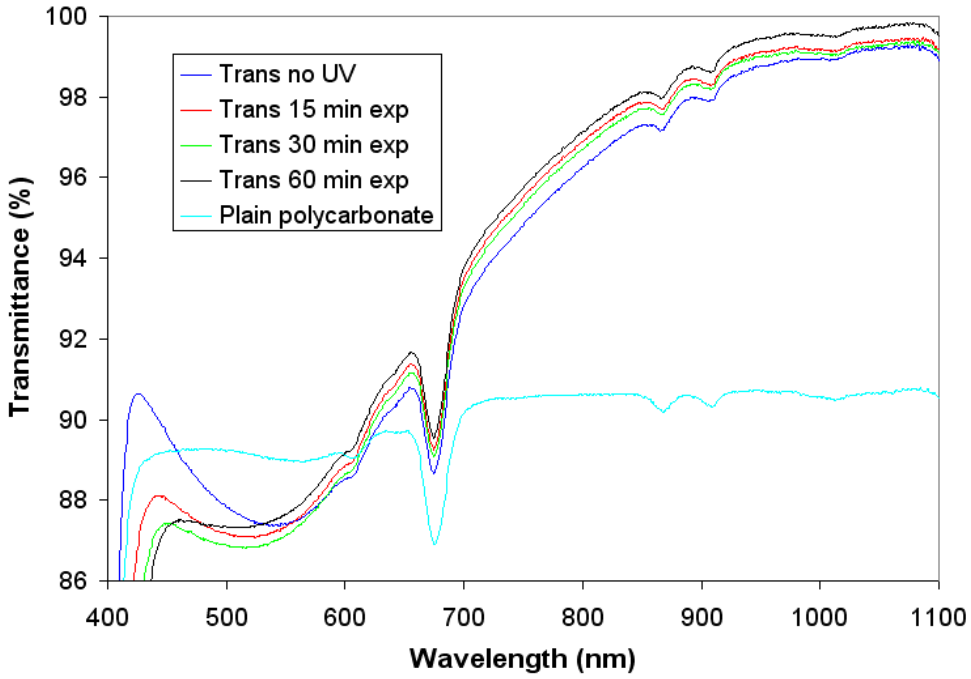

Figure 5.11 Transmittance spectra of 8 PAH/SiO_2 NP bilayers deposited onto polycarbonate. The plot shows that transmittance increases for samples that have undergone longer UV treatment prior to ISAM deposition.

Despite the fact that coatings were deposited on polycarbonate without any UV exposure, it was clear by visual inspection that the film uniformity was inferior compared to UV-treated substrates. I decided to study the macro and micro-scale homogeneity of PAH/SiO_2 NP films as a function of UV exposure using quantitative and qualitative methods. To study the macro-scale uniformity, I measured the transmittance at different locations on the substrate and calculated the standard deviation of transmittance across the sample's surface. The logic behind this method was that a film with inhomogeneities would have different properties (e.g. thickness, surface roughness) at different sample locations, which would consequently affect the transmittance profile. The extent of inhomogeneity of the film directly determines how different the

transmittance spectrum is from one position on the slide to the next. Hence, the standard deviation of the transmittance spectra for each film is an effective quantitative method to analyze the macro-scale uniformity. Four samples were exposed to UV for different times (0, 15, 30, and 60 minutes for each side) and coated with 4 bilayers of PAH/SiO_2 NPs. The transmittance was measured (from 300 – 850 nm) at nine selected locations on the sample; which essentially formed a 3 X 3 grid (**Figure 5.12**). The standard deviation of the transmittance spectra for each sample can be seen in **Figure 5.13**. Over the visible range there is very little difference in the standard deviation for the specimens irradiated by UV. The average standard deviation for PC with no UV, however, is nearly three times higher in the visible range. This is consistent with the visual observation that the films are less homogeneous without pre-treating the surface with UV.

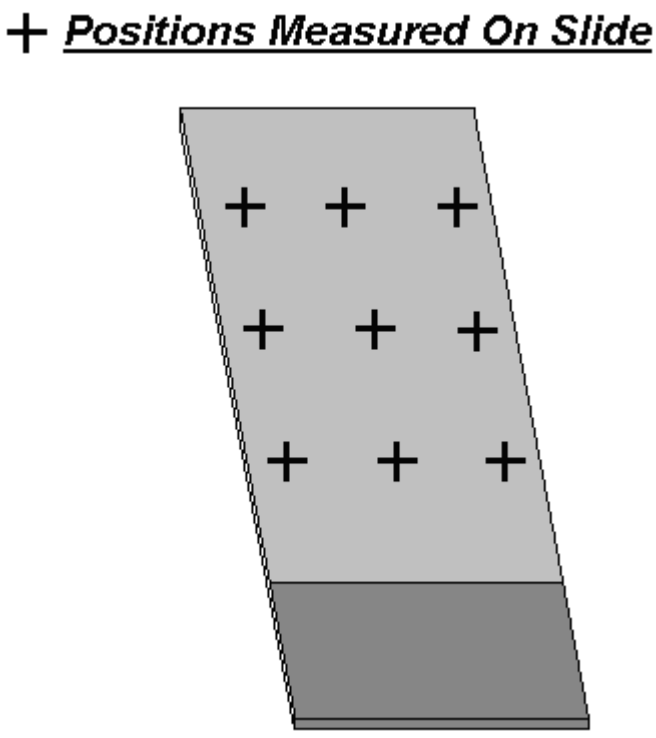

Figure 5.12 Locations on the substrate (represented by "+") where the transmittance was measured in order to quantify the macro-scale homogeneity as a function of UV irradiation.

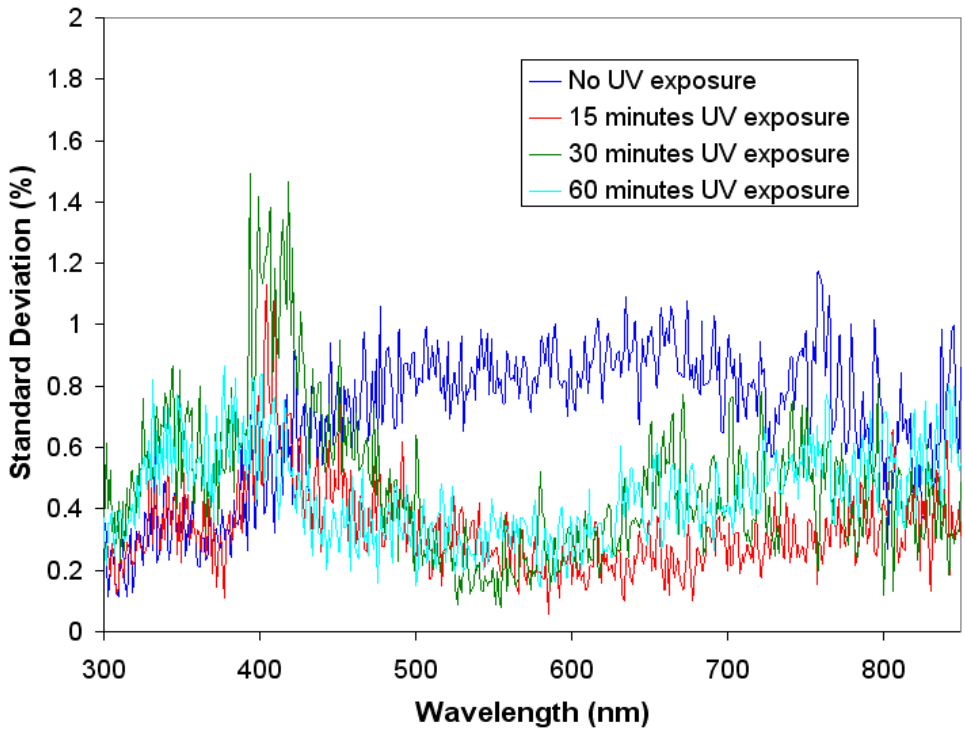

Figure 5.13 Standard deviation of nine transmission measurements plotted versus wavelength for films irradiated by 0, 15, 30, and 60 minutes of UV on each side.

To study the micro-scale uniformity and nanoparticle adsorption, I prepared eight polycarbonate samples; four with no UV irradiation and four with 60 minutes of UV on each side. Next, I made PAH/SiO_2 NP films with 1, 2, 3, and 4 bilayers, respectively, for each treatment group. After this, I took SEM images of each film at different magnifications. **Figure 5.14** compares the progression of deposited PAH/SiO_2 NP layers for treated and untreated PC at a magnification of 200,000X (200KX). The images in the left column (**Figure 5.14A**, **C**, **E**, and **G**) correspond to 1-, 2-, 3-, and 4-PAH/SiO_2 NP layers on untreated polycarbonate, while **B**, **D**, **F**, and **H** (right column) correspond to 1-, 2-, 3-, and 4-layers adsorbed onto UV-treated substrates. First consider the films adsorbed onto PC surfaces without UV irradiation. There appears to be very sparse adsorption after one PAH/SiO_2 NP layer (**5.14A**). The nanoparticles that did adsorb were not well dispersed, and instead tended to form small aggregate islands on the surface. The second layer of PAH and silica nanoparticles (**5.14C**) preferentially attached to the small clusters and increased the size of the islands. The rest of the available area was slowly filled but primarily due to the expanding islands rather than selective adsorption of nanoparticles onto the surface. After three bilayers (**5.14E**), the open areas continued to be filled, but there

appeared to be contour discrepancies in the film, which consisted of regions devoid of nanoparticles with neighboring mounds of appreciable thickness. After four bilayers (**5.14G**), the surface was finally covered, but the thickness profile along the surface still varied considerably. The adsorption of silica nanoparticles was dramatically improved on the PC substrates with UV exposure. After a single bilayer (**Figure 5.14B**), the nanoparticles were arranged in a well-dispersed manner, and with a relative density of nanoparticles that was far greater than the coating on PC with no UV. The sample with two deposited bilayers (**5.14D**) had a small degree of clustering, but the surface was filled much more uniformly compared to the untreated sample. The surface of the three bilayer sample (**5.14F**) was nearly (if not completely) filled, and appeared to have a more uniform thickness profile. Finally, the four-bilayer film (**5.14H**) was merely a result of nanoparticles stacking neatly on top of an already covered surface.

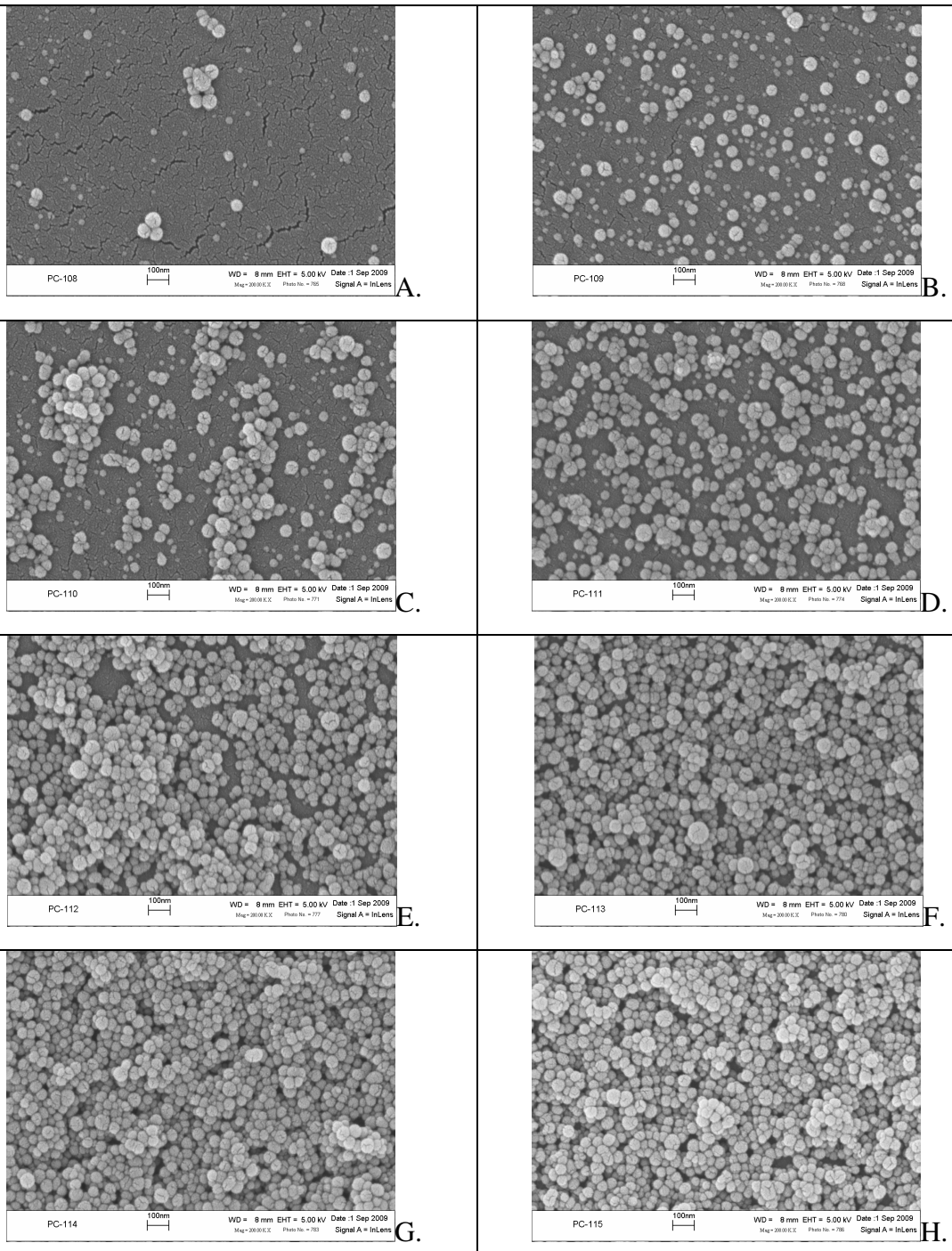

Figure 5.14 SEM images with 200,000X magnification acquired on polycarbonate substrates with (B, D, F, and H) and without (A, C, E, and G) UV treatment. The images were taken to see how the nanoparticle adsorption depends on UV. The number of deposited PAH/SiO_2 NP layers (from top to bottom) in each column are: 1, 2, 3, and 4. Scale bar = 100 nm.

SEM images of the same samples were also acquired with a magnification of 50,000X (**Figure 5.15**). This magnification better illustrates the nanoparticle distribution on the polycarbonate surface. The layout of **Figure 5.15** is similar to **Figure 5.14**; the images on the left-hand column (**A**, **C**, **E**, and **G**) correspond to 1-, 2-, 3-, and 4-bilayer films on polycarbonate that was not treated by UV, while the right-hand column (**B**, **D**, **F**, and **H**) correspond to 1-, 2-, 3-, and 4-bilayer films on polycarbonate with UV treatment. The observations made regarding **Figure 5.14** become clearer when looking at this figure. With no UV treatment, the nanoparticles formed sparse aggregate islands on the surface (**5.15A**) which increased in size with subsequent deposition (**5.15C**). The surface coverage improved after three bilayers (**5.15E**), but it is clear that some dendritic behavior was present with large nanoparticle mounds dominating the surface features. Finally the large voids began to fill in after four bilayers (**5.15G**). By contrast the evolution of film growth on the UV-treated PC substrate was far more uniform. The well-dispersed behavior after a single bilayer was clear from **5.15B**, and the surface continued to be uniformly filled with deposition of nanoparticles. While the adsorption of nanoparticles on untreated polycarbonate is somewhat of a mystery (addressed in section 5.5), it is clear from the SEM images that UV treatment of PC improved the deposition of nanoparticles in the early stages of film growth. This is due to the presence of acidic sites as a result of the photo-degradation by energetic photons. Furthermore, the large-scale nanoparticle aggregation observed in the first two or three bilayers on samples without UV treatment may explain why those samples are less uniform and less transparent. Despite the fact that the bare regions of the surface were eventually filled, the large irregular geometries may be responsible for interfacial scattering of light at the surface of the film and the substrate. Another possibility is that after mound formation, the nanoparticles uniformly fill the entire surface. Atomic Force Microscopy (AFM) can be used to compare the surface roughness between PAH/SiO_2 NP films on treated and untreated substrates. Regardless, the surface treatment improved the optical properties of films deposited onto PC.

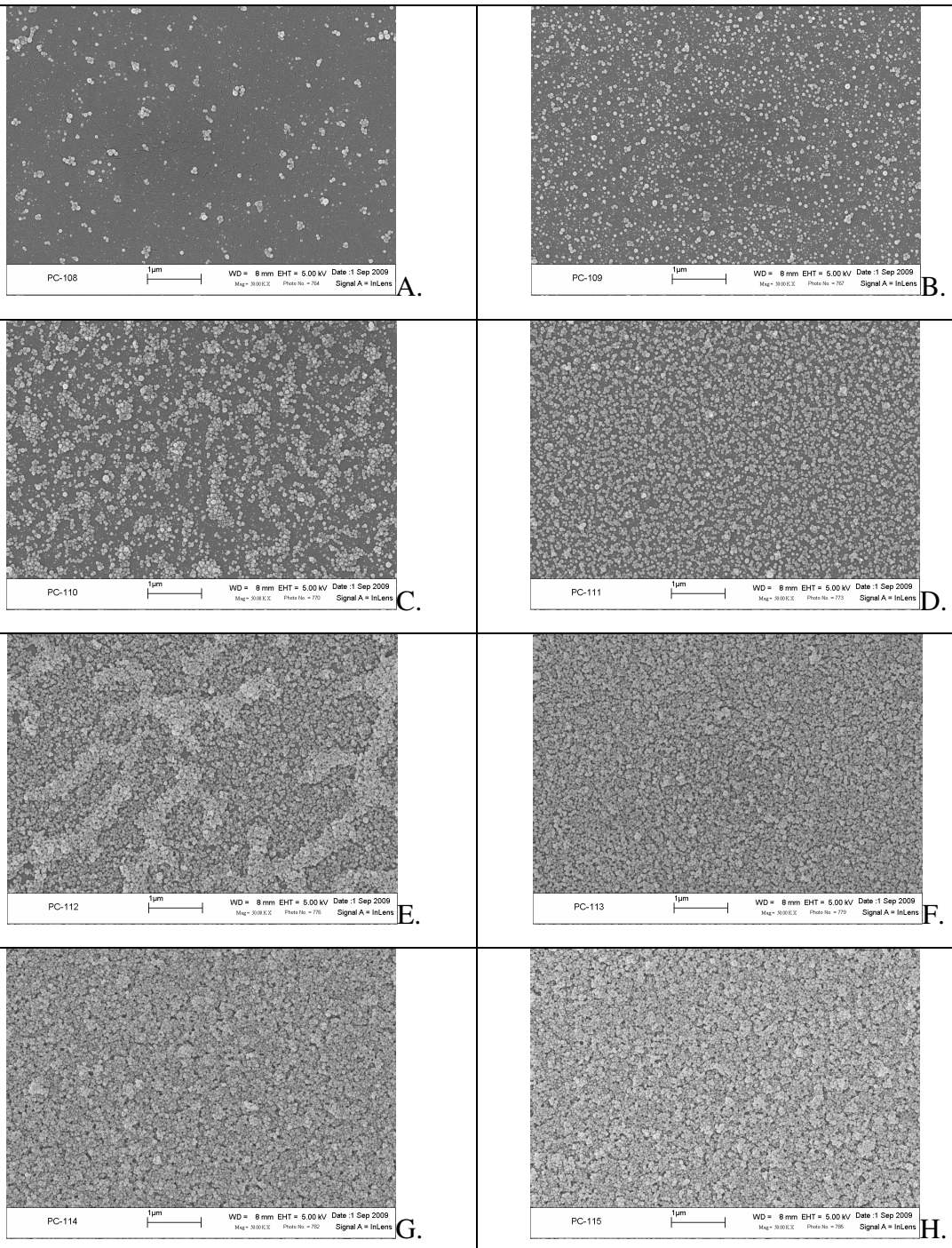

Figure 5.15 SEM images with 50,000X magnification acquired on polycarbonate substrates with (B, D, F, and H) and without (A, C, E, and G) UV treatment. The images were taken to see how the nanoparticle adsorption depends on UV. The number of deposited PAH/SiO_2 NP layers (from top to bottom) in each column are: 1, 2, 3, and 4. Scale bar = 1 μm.

In conclusion, I have shown that UV treatment of polycarbonate moderately improves the optical clarity and results in very high transmittance (99.85%). I found, much to my surprise, that nanoparticle adsorption was possible even without UV irradiation of the substrate. Despite this fact, UV/VIS spectroscopy showed that the macro-scale uniformity of films on the UV-exposed substrates was superior. Finally, SEM imaging showed that the nano-scale order of coatings was improved when utilizing deep UV to populate the surface with acidic functional species.

5.5 Understanding the Mechanism Behind Adsorption of Silica Nanoparticles on Polycarbonate without UV irradiation

In this section I discuss the experiments that were conducted in order to determine the nature of nanoparticle adsorption onto polycarbonate without UV treatment.

Despite the fact that UV irradiation of polycarbonate before ISAM deposition improved thin film optical clarity and homogeneity, it was still unclear how nanoparticles could be deposited without pre-treating the surface. This was important to understand since the mechanism behind adsorption of nanoparticles on untreated PC could also contribute to adsorption on irradiated samples. Hence, the adsorption of nanoparticles on UV-treated samples could be a combined effect of electrostatic attraction to the functional acidic species and the unknown mechanism. A number of theories were considered in an effort to identify the mechanism. They are as follows:

1. Many polymers can hydrogen bond to a surface. Hydrogen bonding occurs when a hydrogen atom is attracted to an electronegative atom on a different molecule. The bond is weaker than ionic or covalent bonds and it is common for intermolecular distances (and consequently the bond strength) to vary. Hydrogen bonding with polycarbonate is a strong possibility because of the oxygen atom protruding from the carbonate group (acceptor).
2. Cleaning the surface with isopropanol could change the molecular chemistry of the polycarbonate surface. It's possible that this solvent could functionalize the surface or create stress cracks that can trap incoming polymer chains.

3. Residual adhesive could still be on the surface even after cleaning. Perhaps the bulk of the adhesive has been removed by cleaning with isopropanol, but if some of it remains, then the first PAH layer would attach to those regions on the substrate. Furthermore, it is also possible that functional groups are created by removing the adhesive from the surface.

What follows is a discussion of the experiments conducted to try and target the most likely explanation for nanoparticle adsorption onto PC without UV treatment.

The possibility of hydrogen bonding between the polymer and substrate was tested. The goal of the experiment was to select a polymer that does not hydrogen bond, and deposit polymer/silica nanoparticles onto PC substrates with varying degrees of UV exposure, including a substrate with no UV. If a film could not be deposited onto the substrate without UV, then I could confirm that hydrogen bonding was one of the mechanisms responsible for adsorption. Dr. Harry Gibson recommended that I use polydiallyldimethylammonium chloride (PDDA) polycation (**Figure 5.16**); this polymer was less likely to hydrogen bond compared to polymers such as PAH. I prepared a 10 mM PDDA aqueous solution (pH = 4) and a 3.76 M silica nanoparticle solution (pH = 9) for ISAM deposition. Four polycarbonate substrates were irradiated by UV for different times (0, 15, 30, and 60 minutes on each side), and then dipped in the PDDA and silica nanoparticle solutions for 8 total cycles. **Figure 5.17** is a plot of the transmittance spectra for the 8 bilayer PDDA/SiO_2 NP samples. The spectra look strikingly similar to the ones from **Figure 5.11**, which consist of 8 PAH/SiO_2 NP bilayers. Once again the transmission improved with increased dosage of UV, but more importantly the spectral profile of the sample with no UV indicates that a thin film was deposited on the substrate. This was also confirmed by visual inspection. Therefore, provided the assumption that PDDA does not hydrogen bond, it is highly probable that it is not the mechanism responsible for adsorption without UV irradiation of the PC surface.

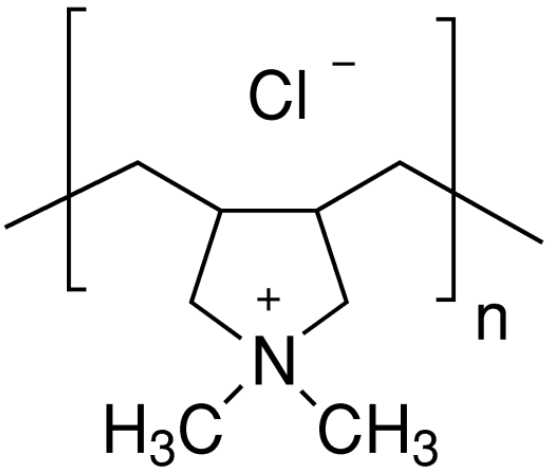

Figure 5.16 Molecular structure of polydiallyldimethylammonium chloride (PDDA). Permission granted from Sigma Aldrich for reuse and reproduced from: http://www.sigmaaldrich.com/catalog/ProductDetail.do?lang=en&N4=522376|ALDRICH&N5=SEARCH_CONCAT_PNO|BRAND_KEY&F=SPEC.

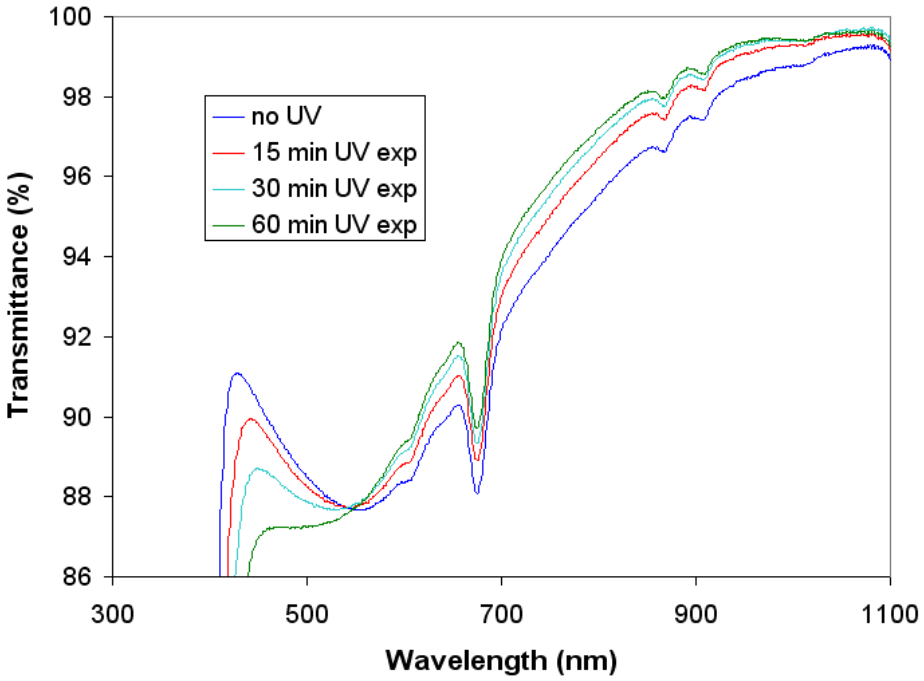

Figure 5.17 Transmittance spectra of 8 PDDA/SiO_2 NP bilayer films as a function of UV irradiation on the substrate.

I also conducted a test to determine if isopropanol created functional groups on the PC surface during the cleaning process. As a basis for comparison, I used hexane to clean the sample. Hexane is a hydrocarbon, which in principle should effectively remove the adhesive, but not alter the polycarbonate surface chemistry. It is likely that the hydrocarbon would preserve the inert state of the surface if the choice of solvent used in the cleaning process was the mechanism behind adsorption. After cleaning two PC surfaces with hexane, I irradiated one of them with UV (60 minutes each side) and did nothing to the other one. After this, I deposited one bilayer of PAH/SiO_2 NPs on both samples and took SEM images to see if material had adsorbed on the surface. The images can be seen below in **Figure 5.18**. The snapshots in the left column (**A.**, **C.**, and **E.**) are of the sample without UV, while the sample in the right column (**B.**, **D.**, and **F.**) was exposed to UV. The magnification was varied (**A.** & **B.** = 10 kX, **C.** & **D.** = 50 kX, and **E.** & **F.** = 200 kX) in order to view the nanoparticle system on different scales.

Looking first at the substrate without UV (**A.**, **C.**, and **E.**), it is clear that adsorption was successful. Not only was the surface coverage fairly low, one can also see that the nanoparticles aggregated into tiny islands. This is the same behavior I commented on in **Figure 5.14**; the only difference is the choice of solvent used to clean the surface. On the other hand, very uniform adsorption was observed on the surface with UV exposure (**B.**, **D.**, and **F.**). The fact that it was possible to deposit thin films on untreated substrates cleaned with hexane shows that isopropanol may not have functionalized the surface.

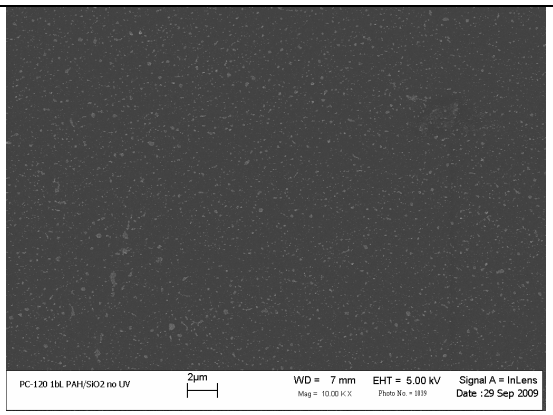

A.

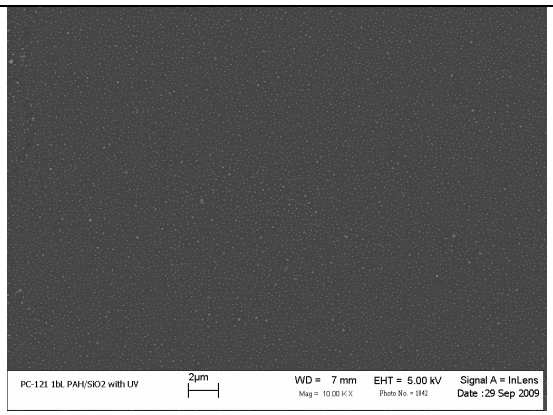

B.

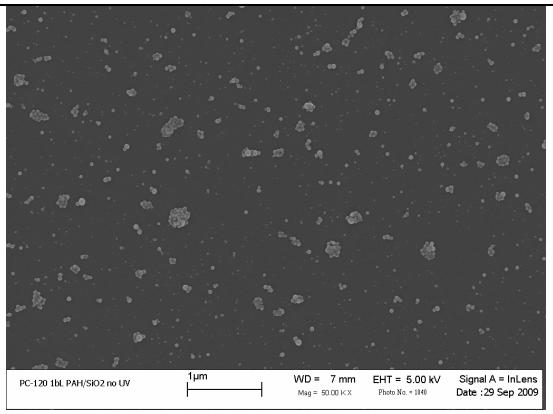

C.

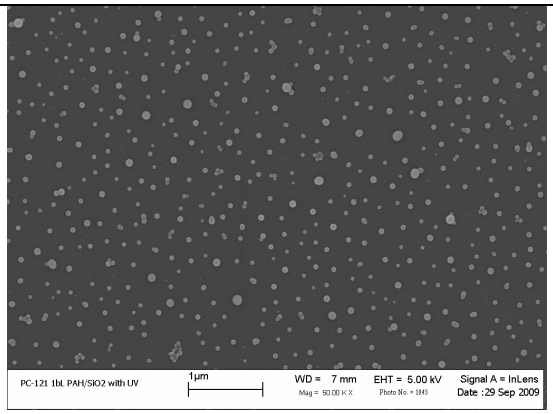

D.

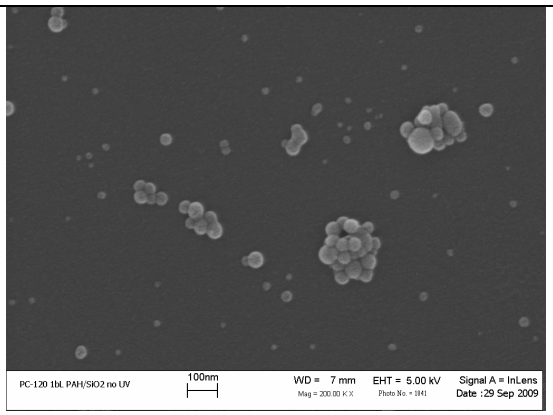

E.

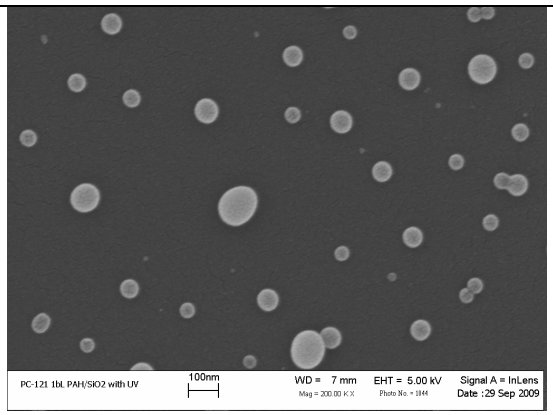

F.

Figure 5.18 SEM images of PC cleaned by hexane and coated with a single layer of PAH/SiO_2 NPs. Images in the left column are of a sample that was not exposed to UV, while the sample in the right column was exposed for 60 minutes on each side. The selected magnifications are: 10 kX (**A.** & **B.**, scale bar = 2 µm), 50 kX (**C.** & **D.**, scale bar = 1 µm), and 200 kX (**E.** & **F.**, scale bar = 100 nm).

To summarize, I used PDDA polycation for ISAM deposition with silica nanoparticles on an untreated surface to see if adsorption was possible. PDDA was selected because we were advised that it is less susceptible to hydrogen bonding than most polymers. I found that ISAM deposition was possible and thus claim that hydrogen bonding is not the primary adsorption mechanism. In support of this view, I argue that hydrogen bonding theoretically should occur uniformly over the entire surface, yet the SEM images (**Figure 5.18 A.**, **C.**, and **E.**) indicate that the nanoparticles are selectively binding. In the second experiment, I cleaned PC with hexane instead of isopropanol to determine if the choice of solvent significantly affected the surface chemistry. Hexane was selected for this experiment because it was unlikely to interact with the polycarbonate. The SEM images in **Figure 5.18** show that PAH and silica nanoparticles still deposited onto the surface without UV, so I conclude that cleaning the substrate with isopropanol was not the cause for thin film adsorption. This leaves the following possible reasons:

- Stress cracks created as a result of cleaning with a solvent.
- Residual adhesive on the surface.
- Creation of functional species after adhesive is removed from the surface.

The SEM images (**Figures 5.14**, **5.15**, and **5.18**) offer the most insight for understanding the reason for adsorption onto PC without UV treatment. During the deposition of the first two bilayers, the nanoparticles appear to aggregate at locations that are non-uniformly distributed over the substrate. With this in mind, it is less likely that functional groups are created as a result of adhesive removal. If this was the case, and the adhesive was completely removed, one would expect to see uniform coverage on the surface because a functional group would replace the site vacated by the adhesive. The seemingly selective nature of nanoparticle adsorption to the substrate indicates a non-uniform process occurs at the surface. Therefore it is more likely that residual adhesive is still on the surface and/or stress cracks are formed. In both cases, nanoparticles would tend to accumulate at locations with adhesive and/or stress cracks. Regardless, it is ill-advised to make such assumptions without data to support them. Additional experimentation will be necessary to conclusively identify the true mechanism(s) behind adsorption of ISAM constituents onto untreated polycarbonate.

5.6 Summary

In this chapter I have introduced the reader to a novel application of deep UV irradiation (λ =185, 254 nm), which is to create functional carboxylate species on the surface of polycarbonate for improved deposition of PAH and silica nanoparticles. XPS and UV/VIS/IR spectroscopies show that the PC surface underwent molecular reorganization and surface oxidation after exposure to UV.

The optical properties of PAH/SiO_2 NP ISAM films on polycarbonate were explored. Rapid deposition of the films was possible with a roughly linear increase in thickness for each adsorption bilayer. The films also demonstrate superb optical clarity (max T = 99.85%). Surprisingly, ISAM films were also deposited onto polycarbonate that had not received the UV treatment. Visual inspection showed that these samples were not as uniform as coatings on substrates with the UV treatment. As a result, I devised both qualitative and quantitative methods to compare the homogeneity of films on PC samples with and without UV irradiation. The quantitative comparison was accomplished by calculating the standard deviation of the transmittance measured at nine different substrate locations. For the qualitative study, SEM images were acquired for 1-, 2-, 3-, and 4-bilayer PAH/SiO_2 NP samples on treated and untreated PC substrates. These images allowed me to compare the nanoparticle adsorption for both cases. Both quantitative and qualitative studies support the claim by visual inspection that the film homogeneity was improved by the UV irradiation.

Finally, theories were presented to explain the adsorption of ISAM constituents on untreated polycarbonate. I conducted experiments to see if hydrogen bonding and/or functionalization by solvent cleaning were responsible for adsorption. Provided two key assumptions are correct (i.e. PDDA does not hydrogen bond, and hexane does not affect the surface chemistry of polycarbonate), it was shown that those mechanisms were not responsible for adsorption of PAH and silica nanoparticles onto polycarbonate without UV exposure.

[1] W. Kern and D. A. Puotinen, "Cleaning solutions based on hydrogen for use in silicon semiconductor technology," RCA Review **31** 187-206 (1970).

[2] S. Vallon, A. Hofrichter, L. Guyot et al., "Adhesion mechanisms of silica layers on plasma-treated polymers .1. Polycarbonate," J. Adhes. Sci. Technol. **10** (12), 1287-1311 (1996).

[3] T. N. Chen, D. S. Wuu, C. C. Wu et al., "Effects of plasma pretreatment on silicon nitride barrier films on polycarbonate substrates," Thin Solid Films **514** (1-2), 188-192 (2006).

[4] S. Vallon, B. Drevillon, F. PoncinEpaillard et al., "Argon plasma treatment of polycarbonate: In situ spectroellipsometry study and polymer characterizations," J. Vac. Sci. Technol. A-Vac. Surf. Films **14** (6), 3194-3201 (1996).

[5] L. Zajickova, D. P. Subedi, V. Bursikova et al., "Study of argon plasma treatment of polycarbonate substrate and its effect on film deposition," Acta Phys. Slovaca **53** (6), 489-504 (2003).

[6] S. Dahl, D. Rats, J. von Stebut et al., "Micromechanical characterisation of plasma treated polymer surfaces," Thin Solid Films **355-356**, 290-294 (1999).

[7] John R. Hollahan and Alexis T. Bell, *Techniques and applications of plasma chemistry*. (Wiley, New York,, 1974), pp.viii, 403 p.

[8] A. Rivaton, D. Sallet, and J. Lemaire, "The photochemistry of bisphenol-A polycarbonate reconsidered," Polymer Photochemistry **3** (6), 463-481 (1983).

[9] A. Rivaton, "Recent advances in bisphenol-A polycarbonate photodegradation," Polymer Degradation and Stability **49** 163-179 (1995).

[10] Z. Geretovszky, B. Hopp, I. Bertoti et al., "Photodegradation of polycarbonate under narrow band irradiation at 172 nm," Applied Surface Science **186** 85-90 (2002).

[11] A. Welle and E. Gottwald, "UV-based patterning of polymeric substrates for cell culture applications," Biomed. Microdevices **4** (1), 33-41 (2002).

[12] K. M. K. Srivatsa, M. Bera, A. Basu et al., "Antireflection coatings on plastics deposited by plasma polymerization process," Bull. Mat. Sci. **31** (4), 673-680 (2008).

[13] N. Yamaguchi, K. Tadanaga, A. Matsuda et al., "Formation of anti-reflective alumina films on polymer substrates by the sol-gel process with hot water treatment," Surf. Coat. Technol. **201** (6), 3653-3657 (2006).

[14] Z. Gemici, H. Shimomura, R. E. Cohen et al., "Hydrothermal treatment of nanoparticle thin films for enhanced mechanical durability," Langmuir **24** (5), 2168-2177 (2008).

CHAPTER SIX

ISAM Deposition of PAH/Silica Nanoparticles on Glass Fibers to Reduce Thermo-Optic Losses in Reinforced Polymer Composites

This work was funded by a Director's Research Initiative at the Army Research Lab. Dr. Daniel O.' Brien, one of our collaborators at ARL, was the principal investigator. Sample fabrication was completed at Virginia Tech, and the rest of the research was conducted at the Army Research Labs where I spent 10 weeks as an intern.

6.1 Introduction and Review

Creating optically transparent materials that have high impact resistance is a topic of particular interest to the U.S. Army. Furthermore, the increasing need for unit mobility in the presence of a threat necessitates that these materials be lightweight. Polymer composites with glass fiber reinforcement meet these requirements, and hence are an attractive option for implementation in armored structures. Appropriate polymers can be selected that have a refractive index that closely matches the glass fiber reinforcement at some temperature T, resulting in an optically transparent media. Changes in temperature, however, lead to changes in the refractive index (dn/dT) for most materials. When dn/dT (thermo-optic coefficient) is not the same for the constituents of a given medium the transmittance is reduced due to increased scattering of light passing through numerous mismatched interfaces.[1] To address this problem, a passive solution was proposed to buffer the refractive index mismatch of constituents in polymer composite materials:

Proposed solution: Introduction of a nanocomposite interphase region into the matrix material. The glass fiber reinforcement is coated with silica nanoparticles by ISAM deposition. The coating around each fiber consists of nanoparticles closely resembling a random closed-packed (RCP) structure. The interstitial voids are sufficiently large to permit infiltration of the polymer matrix. Thus, the nanocomposite interphase consists of silica nanoparticles and the polymer. **Figure 6.1** illustrates the architecture of the nanocomposite interphase, and the impact this region has on the transparency of the composite material. **Figure 6.1(a)** shows the simple

polymer matrix with fiber reinforcement, while **6.1(b)** shows the complex system with the nanocomposite interphase. Beneath each illustration are plots of the refractive index versus the constituent of the polymer composite when the temperature is at the R.I. matching point and above said temperature. Clearly, the refractive index is the same for each constituent at the matching temperature. As T increases, however [**6.1(a)**], the refractive indices become mismatched. Since the nanocomposite interphase is a combination of polymer and silica with particle size (45 nm silica nanoparticles) much smaller than the wavelength of incident light, its refractive index will be the volume-averaged refractive index of the primary constituents[2] and can be determined by the following relation:

$$n_i(T) = v_g n_g + (1 - v_g) n_p(T),$$

where n_i, n_g, and n_p are the refractive indices of the interphase, silica nanoparticles, and polymer respectively, and v_g is the volume fraction of the silica nanoparticles in the interphase. Therefore, the role of the nanocomposite interphase is to provide a refractive index step between glass fiber and polymer matrix and should theoretically reduce the interfacial scattering of light and loss in transmission with changes in temperature.

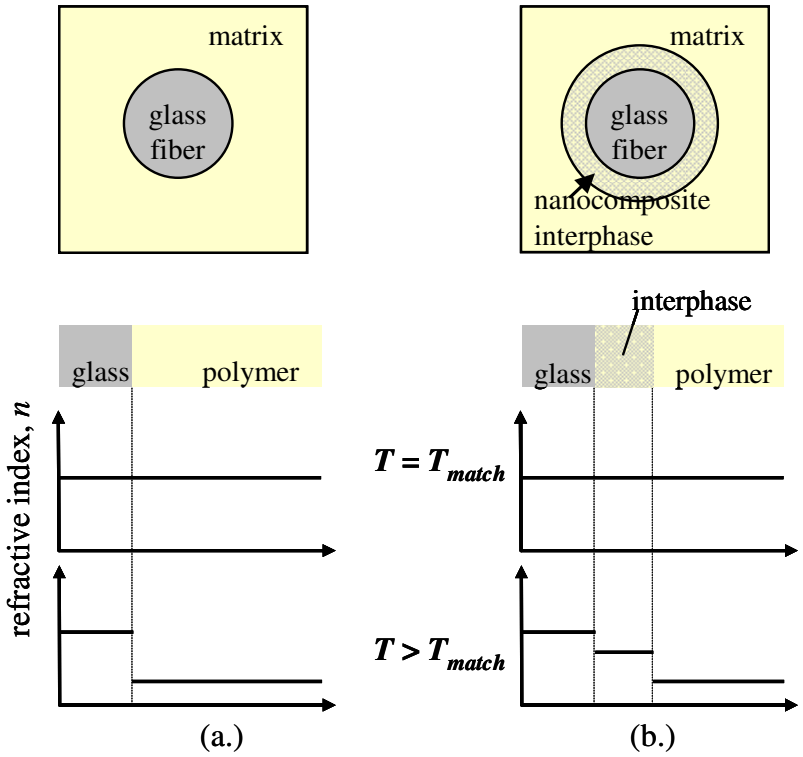

Figure 6.1 Schematic of (a) a simple reinforced polymer composite and (b) complex reinforced polymer composite with a nanocomposite interphase.

6.2 Model Design for Proof of Concept

A proof of concept experiment was designed to show that the addition of a nanocomposite interphase can improve the transmittance of light passing through adjacent regions with mismatched refractive indices. A large cuvette was purchased from Starna Cells Inc. to hold liquids that would serve as the model polymer matrix. Several liquids were selected to simulate the polymer matrix in the experiment including water (n = 1.333), glycerol (n = 1.473), and a 50/50 mixture of water and glycerol (n ≈ 1.403) in order to obtain a range of refractive index mismatches with glass. What follows are the results for a polymer matrix consisting of water. The transmittance was measured using a Perkin Elmer Lambda 25 UV/Vis spectrophotometer. Measurements for several different configurations were taken (**Figure 6.2**). In the first measurement, the cuvette contained only water. In this configuration there were only two air/glass and water/glass interfaces. As a result, the transmittance was reduced to approximately 90% in the visible. Next, five uncoated glass slides were placed in the water-

filled cuvette with equal spacing in between and at normal incidence to the beam. This increased the total number of water/glass interfaces from 2 to 12. This decreased the transmittance in the visible from 90% to nearly 86%. Next, five glass substrates coated with 10 bilayers of PAH/SiO_2 were placed in the cuvette. Since the refractive index of the PAH/SiO_2 coating is simply the weighted average of the silica and external media (which in this case is water), it is going to be some value between glass and water. The corresponding refractive index gradient reduced the reflection/scattering of incident light, and as seen in **Figure 6.2**, increased the transmittance to a peak value of 88.6%. However, the thick 10 bilayer coatings on the glass substrates produced a couple of interference fringes in the visible and as a result the transmittance for this configuration was not always better than the one with the uncoated glass substrates. Therefore, 5 PAH/SiO_2 coatings consisting of 5 bilayers were made on a second set of glass slides. These films had broader transmission peaks and as a result the transmittance in this configuration was higher throughout the visible spectrum compared to uncoated glass slides. Similar transmittance spectra were acquired for the described configurations above in model polymer matrix systems consisting of water/glycerol (**Figure 6.3**) and glycerol (**Figure 6.4**). The figures clearly show that a smaller change in transmittance occured as the indices of refraction between the polymer matrix and the glass substrate were more closely matched. In addition to this, the effect of the nanocomposite interphase on the transmittance, while still present, was less dramatic. Also, the matrices containing substrates coated with 5 bilayers of PAH/SiO_2 generally had higher transmittance values throughout the visible range compared to the substrates with 10 bilayers of PAH/SiO_2. In conclusion, this experiment confirmed that a nanocomposite interphase effectively acts as a refractive index step between the polymer matrix (water) and the glass substrate(s) and can be used to reduce thermo-optic losses in polymer composites with glass fiber reinforcement.

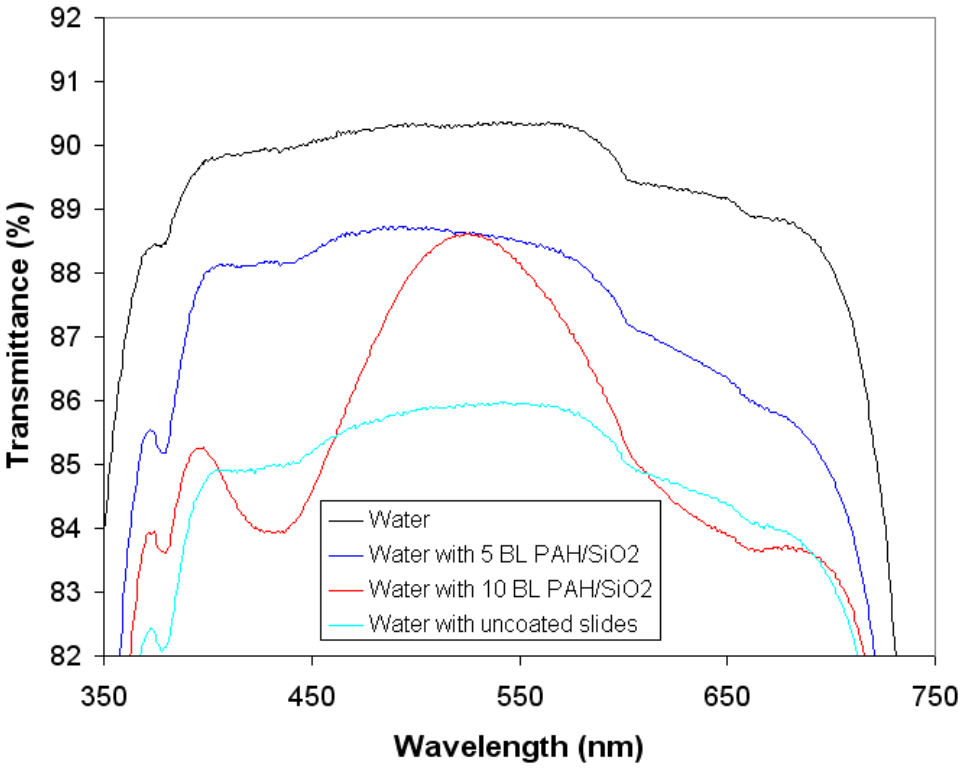

Figure 6.2 Transmittance spectra for a water-filled cuvette containing five glass substrates. The substrates were coated with the following: nothing, 5 bilayers of PAH/SiO_2, or 10 bilayers of PAH/SiO_2.

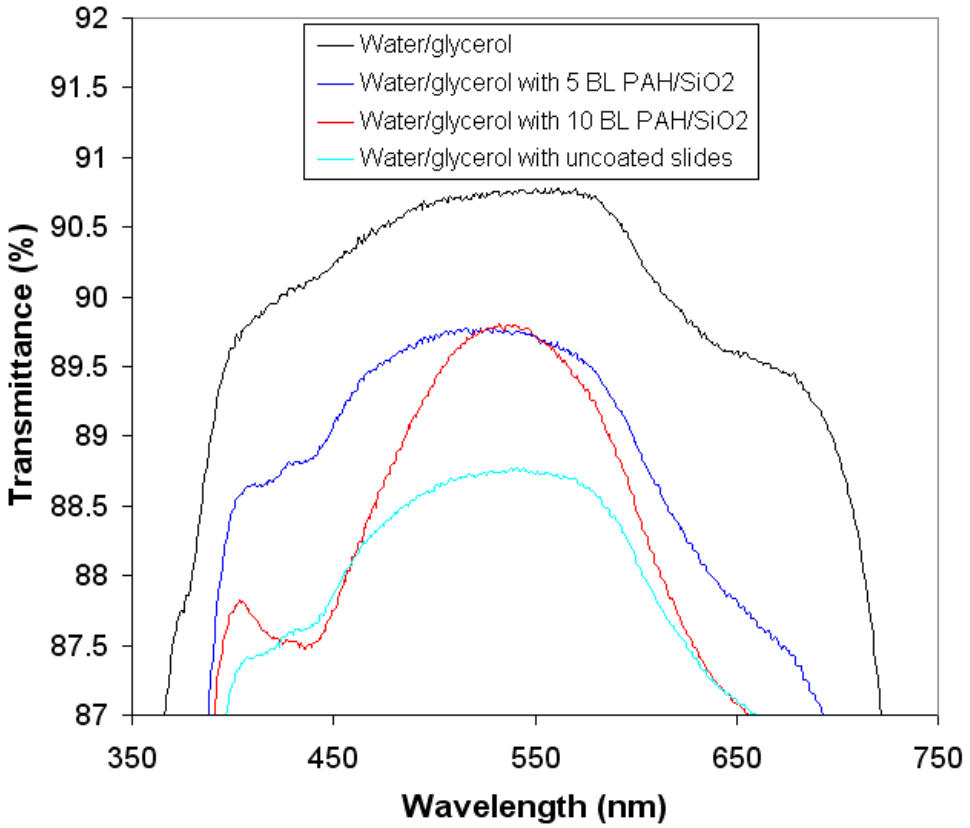

Figure 6.3 Transmittance spectra for a water/glycerol-filled cuvette containing five glass substrates. The substrates were coated with the following: nothing, 5 bilayers of PAH/SiO_2, or 10 bilayers of PAH/SiO_2.

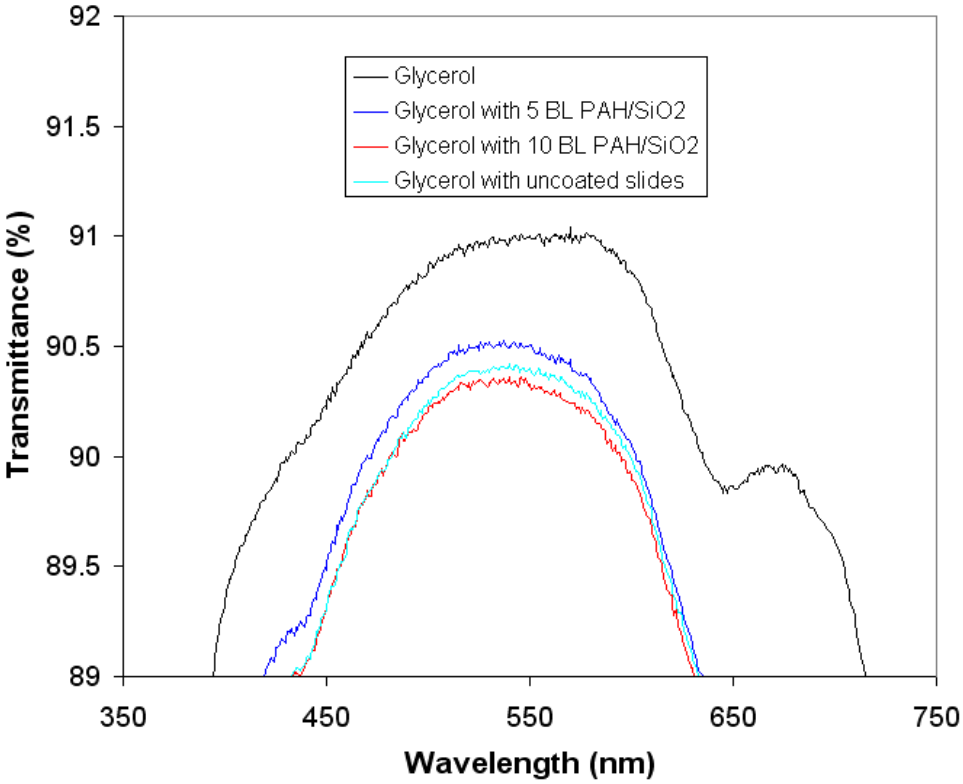

Figure 6.4 Transmittance spectra for a glycerol-filled cuvette containing five glass substrates. The substrates were coated with the following: nothing, 5 bilayers of PAH/SiO_2, or 10 bilayers of PAH/SiO_2.

6.3 Results and Discussion

Demonstrating the somewhat intuitive phenomenon of improved transparency with a nanocomposite interphase proved to be a challenge. Fiber bundles (called "tows") were cut and aligned into the cavity of a rubber gasket, which was sandwiched between two glass slides. The cavity was filled with a liquid of known refractive index to simulate the polymer matrix. Metal plates with attached heaters were clamped to the glass slides to heat the liquid and tows (**Figure 6.5**). The assembly was mounted into a spectrophotometer (Perkin Elmer Lambda 950 UV/VIS spectrometer) for measurements of transmittance.

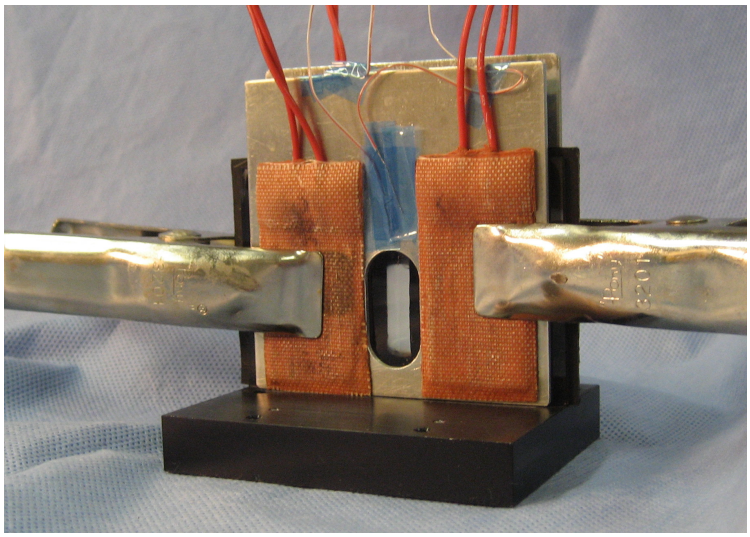

Figure 6.5 Mounting unit for temperature-dependent measurements of transmission.

The first, and perhaps most critical challenge, was to ensure that the effects of the nanocomposite interphase on transmission measurements would not be drowned out by noise associated with tow realignment in the cavity from one sample run to the next. The transmission varies with respect to a number of factors, particularly the fiber volume fraction,[3] as well as the degree of infiltration by the polymer matrix into the fiber network. The effect of tow alignment was also studied by creating cavity templates that support either an in-line single tow or side-by-side in-line configuration. The tows were also immersed in several different liquids, specifically dimethyl sulfoxide (DMSO, n = 1.476), and two immersion liquids from Cargille (refractive indices n = 1.4587 and 1.4590, respectively) to see if the liquid type created additional variability. The relative fractional difference (in wavelength space, $\lambda = 400 \rightarrow 800$nm) was used to quantify configuration variability. The fractional difference at wavelength λ was calculated as follows:

$$\text{Relative fractional difference } (\lambda) = \frac{\left|Tn(\lambda) - Tavg(\lambda)\right|}{Tavg(\lambda)},$$

where *Tn* and *Tavg* are the transmission values for a specific run and for the average, respectively.

In general, the variability was quite low for most cases (between 2-6%) in the visible regime. Furthermore, filling the cavity with more tows was preferred because it packed the fibers into a more orderly configuration and consequently reduced scattering, particularly at shorter wavelengths. Too many bundles, however, inflated the fractional difference calculation due to small average transmission quantities. Nevertheless, it was clear that more tows improved the repeatability of the measurements (**Figure 6.6**). There was no discernable difference between measurements conducted using the different cavity templates (i.e. in-line or side-by-side tow configurations). The type of liquid used also did not significantly affect the fractional difference, though it was important to note if any strong absorption modes attributed to the liquid were present that could bias the measurements.

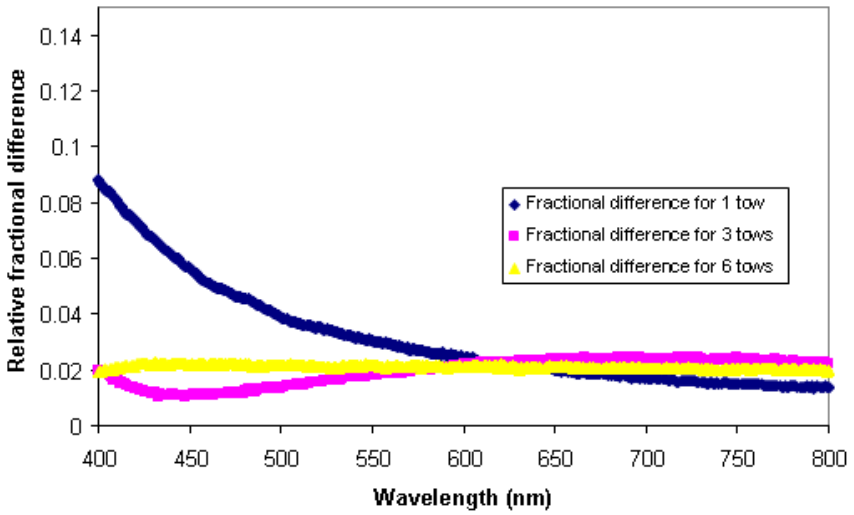

Figure 6.6 Relative fractional difference versus wavelength with respect to the number of tows aligned in the cavity (single tow width template).

Lastly, I took temperature-dependent transmission measurements for the composite media. Tows were assembled as shown in **Figure 6.5**, and placed in the spectrophotometer. Thermocouples were placed both inside the cavity and on the metal plates to record the cavity temperature. The samples were heated by a Digitrol II heat source (Glas-Col) from room temperature at a rate of 0.5 °C/min. A Fluke 54II thermometer recorded the temperature every 60 seconds. A typical transmission versus temperature plot can be seen in **Figure 6.7**. The plot in **6.7(a)** is a temperature sweep of 8 uncoated tows immersed in a Cargille liquid with refractive

index n = 1.4590, while **6.7(b)** shows the results for tows immersed in DMSO, which was used because it has a high thermo-optic coefficient.[4] The refractive index of a fused silica fiber is 1.4587. Thus at room temperature, the fibers were well matched with the Cargille liquid **6.7(a)**. As the temperature increased, however, the refractive index of the liquid changed steadily while remaining relatively constant for the glass fibers. The refractive index of DMSO at room temperature is fairly different than fused silica, and hence the transmittance was initially quite low (<20 %). As the temperature was increased, however, the refractive index of DMSO decreased until it matched the glass (at ≈ 61 °C). As the temperature proceeded above 61 °C, the transmittance began to decrease once again.

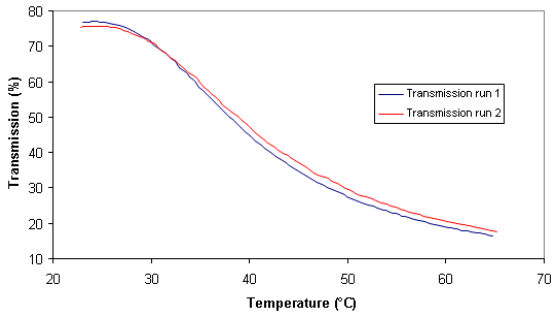

A.

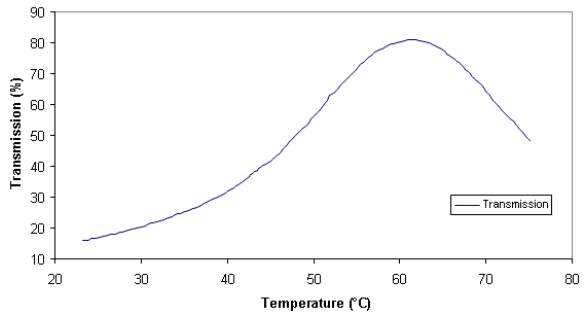

B.

Figure 6.7 Plot of transmission versus sample temperature for 8 uncoated tows immersed in: **a)** Cargille immersion fluid with refractive index n = 1.4590, and **b)** dimethyl sulfoxide (n = 1.476).

Temperature-dependent measurements of transmission were taken on a set of 8 uncoated tows and 8 tows coated with silica nanoparticles (25 bilayers of PAH/SiO_2 NPs). The results can be seen in **Figure 6.8**. The maximum transmission was drastically better for the uncoated tows than for those coated with nanoparticles. This is because the coated fibers agglomerate during ISAM deposition and conform to a cylindrical geometry, while the uncoated tows were ribbon-shaped (**Figure 6.9**). Therefore, incident light passing through a coated tow will interact with more fibers, encounter more polymer matrix/glass interfaces, and as a consequence scatter more light. It's also possible that there may be nanoparticle aggregation present, which would also cause light to scatter. It is surprising to note, however, that the transmittance of light passing through

both uncoated and coated bundles was the same at room temperature despite the fact that the coated fibers appear "whiter" (i.e. scatter more light) than the uncoated tows outside of the liquid. Clearly, the aggregation of fibers and nanoparticles reduced the peak transmittance of the coated samples around 61 °C, but it's unlikely that the scattering attributed to aggregation alone would be different at room temperature. Therefore, because the transmittance of both uncoated and coated samples were the same at room temperature, it is probable that the nanocomposite interphase is mitigating some of the temperature-dependent scattering, and is in effect offsetting the scattering due to fiber/nanoparticle aggregation. If the aggregation can be limited, it may be possible to match the transmission peaks at the optimal temperature (~ 61 °C), with the potential to significantly improve the transmittance at temperatures away from the peak.

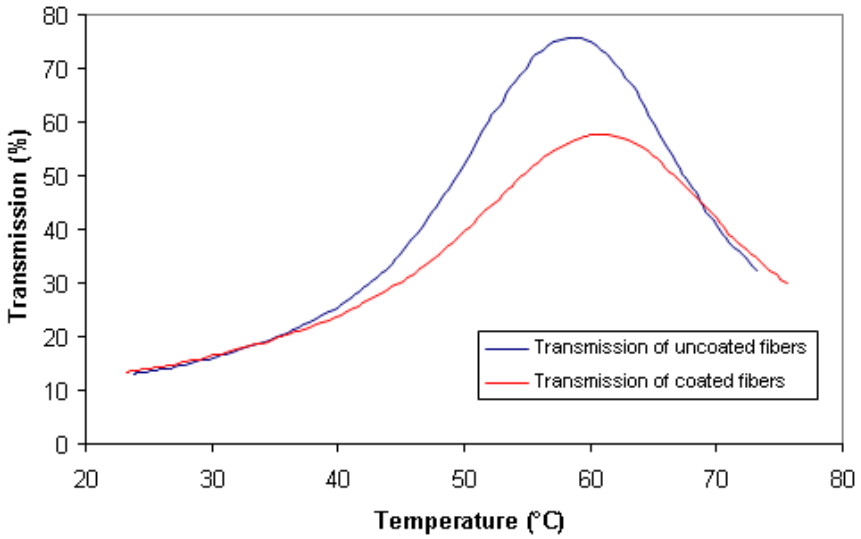

Figure 6.8 Transmission versus temperature for coated/uncoated specimens consisting of 8 tows immersed in DMSO.

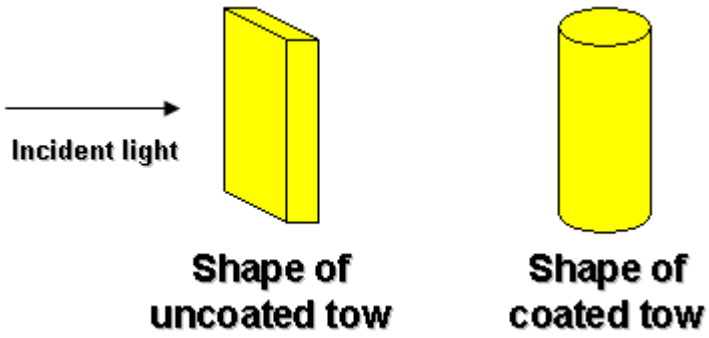

Figure 6.9 Fiber bundle conformation before and after being coated with PAH and silica nanoparticles. The bundles are initially ribbon-shaped, but conform to a cylindrical geometry after ISAM deposition due in part to fiber aggregation.

The aggregation of glass fibers during the ISAM process clearly had an adverse affect on the optical properties of the reinforced polymer composite system. One way to try to minimize this was to immerse the glass fibers in PAH and silica nanoparticle solutions under sonication with the hopes that this could prevent the fibers from coupling during adsorption. The fibers were coated with 25 PAH/SiO_2 NP bilayers. After completing ISAM deposition on the glass fibers, I took SEM images for analysis. **Figures 6.10** and **6.11** are images (mag. 8.57 and 30 kX, respectively) of a fiber with nanoparticles on its surface. Glaring evidence of fiber agglomeration is presented in the images. Several bands of thick, uniform layers of silica nanoparticles run along the length of the fiber. These regions however, are adjacent to bands without nanoparticles. There are no conditions present to suggest preferential adsorption in the manner observed. Thus, the logical explanation is that the fiber in the image was part of a larger aggregate of fibers. At some point between completion of ISAM deposition and the time the SEM images were taken, the neighboring fibers were ripped from this one leaving behind the bare surface. Sufficient nanoparticle adsorption was successfully realized on the remaining surface. While it is still unclear whether sonication reduces the total aggregation of glass fibers, it is clear that it does not completely solve the problem.

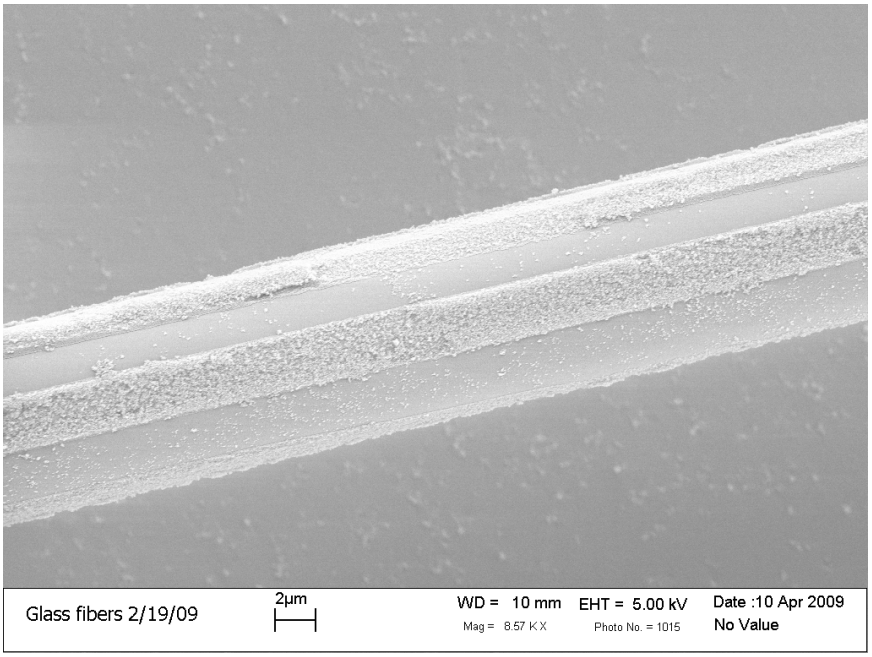

Figure 6.10 SEM micrograph (mag. 8.57 kX) of a glass fiber coated with 25 bilayers of PAH and silica nanoparticles. During ISAM deposition this fiber aggregated with adjacent fibers. At some point, the neighboring fibers were separated from the specimen, leaving bare regions on the surface. Scale bar = 2 µm.

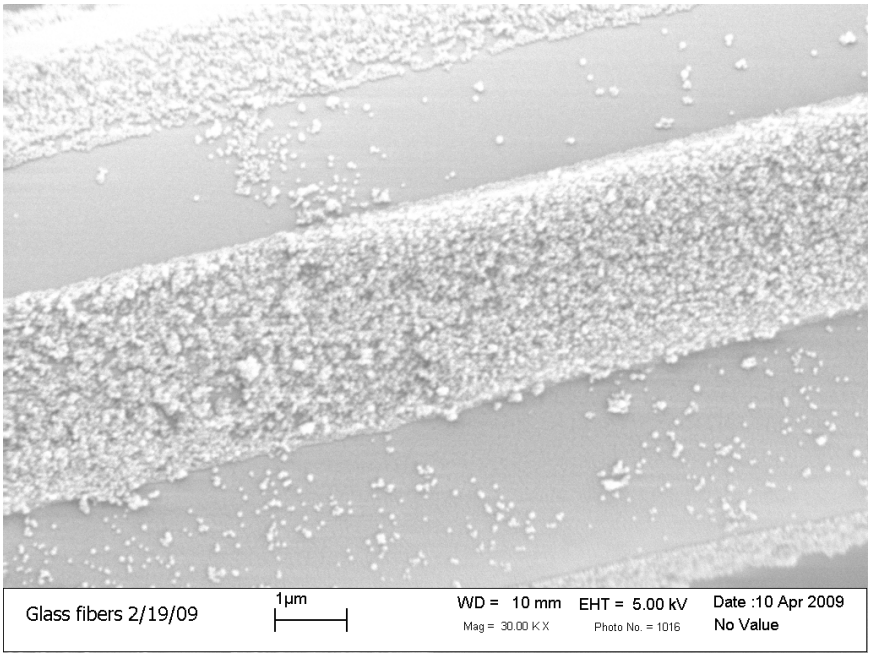

Figure 6.11 SEM micrograph (mag. 30 kX) of a glass fiber coated with 25 bilayers of PAH and silica nanoparticles. Scale bar = 1 µm.

6.4 Summary

Polymer composites with glass fiber reinforcement are an attractive prospect for high impact resistance media. The refractive index of the polymer composite is tuned to match the glass fibers, thus making them optically transparent. Unfortunately, the thermo-optic coefficients of the fibers and the surrounding polymer matrix are generally not the same, and as a result their refractive indices become mismatched with changes in temperature. As the difference in the refractive index values of the constituents in the media increases, so do optical losses via scattering. In principle, it is possible to buffer these losses by coating the glass fibers with silica nanoparticles and in the process creating a nanocomposite interphase. I was able to successfully coat the micron-scale glass fibers with ISAM layers of PAH and silica nanoparticles. The thermo-optic performance of the coated fibers was compared with uncoated fibers in DMSO. Unfortunately, the peak transmittance of the media containing the coated fibers was not as high. The scattering observed for this sample was attributed to severe fiber/nanoparticle aggregation during the ISAM process. On the other hand, I speculate that the nanocomposite interphase does buffer optical losses since the transmittance of both uncoated and coated samples was the same at room temperature, well away from the transmittance peak (~ 61 °C). Consequently, it appears that at room temperature, the nanocomposite interphase offsets the fiber aggregation that causes unwanted scattering. SEM images confirm fiber aggregation.

[1] H. Sato, H. Iba, T. Naganuma et al., "Effects of the difference between the refractive indices of constituent materials on the light transmittance of glass-particle-dispersed epoxy-matrix optical composites," Philosophical Magazine B-Physics of Condensed Matter Statistical Mechanics Electronic Optical and Magnetic Properties **82** (13), 1369-1386 (2002).

[2] M. Sandrock, M. Wiggins, J. S. Shirk et al., "A widely tunable refractive index in a nanolayered photonic material," Appl. Phys. Lett. **84** (18), 3621-3623 (2004).

[3] H. G. Lin, D. E. Day, and J. O. Stoffer, "Model for the temperature-dependent transmission of optically transparent poly(methyl methacrylate) composites," Journal of Materials Research **8** (2), 364-370 (1993).

[4] H. El-Kashef, "The necessary requirements imposed on polar dielectric laser dye solvents-II," Physica B-Condensed Matter **311** (3-4), 376-379 (2002).

CHAPTER SEVEN

Summary and Future Studies

This thesis has focused on the development of a variety of approaches for deposition of ionic self-assembled multilayers containing silica nanoparticles on glass, polycarbonate, and micron-scale glass fibers with the goals of increased transmittance and mechanical strength for the coating. This chapter summarizes the work presented and outlines research initiatives that build on the progress to date.

Methods to Improve Cohesion and Adhesion of ISAM Silica Nanoparticle Films

In this research I presented three methods to improve the cohesion of silica nanoparticles in ISAM films and the adhesion of the coating to the substrate. In the first approach, I used diazo-resin (DAR) polycation for ISAM deposition with silica nanoparticles. The photo-reactive property of DAR made it possible to convert the ionic bonds joining the nanoparticles into covalent ones by UV irradiation. The works of Sun and others, however, showed that this mechanism was successful when DAR was ionically attached to sulfonate and carboxylic functional groups. Therefore, I coated the substrate and silica nanoparticles with sulfonate groups. Glass substrates were silylated with MPTS, which is a silane containing a thiol that can be converted into a sulfonate after immersion in a heated CH_3COOH:H_2O_2 bath. The silica nanoparticles were surface-coated with PAH and PSS by performing ISAM deposition of the polymers in the colloidal suspension. The outermost polymer monolayer (PSS) contained sulfonate end groups which, if mixed in appropriate proportions, also stabilized the nanoparticles. Unfortunately, the ISAM deposition process on the particle surfaces caused the nanoparticles to aggregate. The aggregation was reduced somewhat by sonication after each adsorption step, but DLS confirmed that the average particle size was 196 nm. While I did successfully deposit ISAM coatings on the surfaces of the silica nanoparticles and incorporate the modified nanoparticles into ISAM films on glass substrates, the DAR/modified SiO_2 NP ISAM films scattered a significant amount of light. Not only did this severely affect the optical transparency, but it's likely that the scattering also minimized UV cross-linking.

In order to further develop this approach, it is imperative to minimize the average particle size of PAH/PSS ISAM-coated silica nanoparticles. There are a number of relatively simple approaches to try. The first is to reduce the silica nanoparticle concentration. In principle, the fewer nanoparticles in solution during ISAM deposition of PAH/PSS, the less likely they are to aggregate with each other due to the increased average separation distance. Since the nanoparticle concentration will be changed, the polymer concentrations will need to be adjusted as well. Therefore, ζ-potential measurements should be conducted over a suitable range of PAH and PSS concentrations. This will enable one to determine the new ζ saturation concentration for each polymer. The average particle size should be monitored simultaneously using DLS. Ideally, a silica nanoparticle concentration can be found that yields sufficient adsorption of coated particles with a mean size approaching 60 nm. Alternatively, one can centrifuge the ISAM-coated nanoparticles formed under the conditions reported in the thesis in order to remove the larger bodies from the solution.

The second approach to improve the mechanical strength was by thermally treating PAH/SiO_2 NP films. This effectively burned away the organic constituent and partially fused the silica nanoparticles throughout the film, including the layer of nanoparticles adjacent to the substrate. The thickness of the film decreased as a result of the calcination process, but according to transmittance and reflectance spectra the optical transparency was not compromised ($T > 99\%$, $R < 1\%$). This is because the PAH occupied some volume of space between the nanoparticles before calcination and after heating the polymer was removed. This increase in void space offset the decrease in thickness (decrease in void space). The calcined samples proved to be highly robust, and were not removed after tape peel and abrasion tests.

The calcined SiO_2 NP films have demonstrated excellent mechanical integrity. What may be of particular interest is to study the effect of calcination time and temperature on the film thickness and void fraction. In doing so, we may be able to target specific calcination conditions to optimize the optical properties while maintaining their excellent mechanical stability. These studies should correlate the transmittance/reflectance, adhesion/cohesion strength, and film structure as determined by electron microscopy with the calcination time and temperature.

The third approach involved the addition of PAH/PMA precursor and capping layers to surround the bulk PAH/SiO_2 NP ISAM film. The purpose of the precursor layer was to create a malleable ionic bed of material for the nanoparticles to diffuse into. The capping layer was

added with the hope that the smaller polymers would infiltrate the interstitial voids of the nanoparticles to increase the general connectivity of the bulk film. The strength of the precursor and capping layers were tested by a tape peel test that confirmed their positive effect on the mechanical strength. Unfortunately these coatings could still be removed after abrasion, so a new design to increase the interstitial polymer content was tested. This design incorporated a quadlayer system of PAH/SiO_2/PAH/PMA for the bulk structure. The precursor and capping layers were deposited before and after the bulk film as before. The mechanical strength was moderately improved with the addition of the quadlayers, but the optical transparency was also reduced. Furthermore, the pH conditions of the PAH/PMA interlayers appeared to affect the nanoparticle adsorption and film uniformity. Therefore, spectroscopic and QCM studies were conducted to find ideal pH values for PAH and PMA during interlayer deposition. There appeared to be some consistency between the two studies, but the reported QCM data is very preliminary, incomplete, and biased.

It's not easy to assess the direction of the SiO_2 NP films with polymer interlayers. The next logical course of action is to conduct new spectroscopic and QCM studies in which the set of interlayer polymer pH conditions are the same. A proper cleaning protocol for the quartz crystals is now in place, so many of the inconsistencies from my study can be avoided. Even if ideal pH conditions can be found, it's possible that the mechanical properties will not achieve an acceptable standard without significantly compromising the optical quality.

In addition to the above suggestions, it is imperative that new and more sophisticated methods to test the adhesive/cohesive strength be incorporated to better assess the mechanical quality of the films. An abrasion test with a constant and measurable applied force is preferred because the resultant haze can be determined in order to quantify the abrasive resistance of the film. Nanoindentation via AFM can be used to study a number of mechanical properties including the hardness and modulus of elasticity. Nanoscratch tests are another option to test the adhesive and cohesive failure of these films.

Improved Adsorption of Silica Nanoparticle Films on Polycarbonate by Deep UV Irradiation

In this work, I presented a novel and simple technique to functionalize polycarbonate substrates for ISAM deposition of PAH and silica nanoparticles. Deep UV (λ = 185, 254 nm)

irradiation of polycarbonate changes its molecular structure and creates charged carboxylate species on its surface. These changes were confirmed using XPS and UV/VIS/IR spectroscopic methods. Silica nanoparticle films were subsequently built on the prepared substrates. The optical transparency of the coatings was outstanding, with transmittance as high as 99.85 %. I discovered, however, that ISAM films could also adsorb onto polycarbonate without UV irradiation. In comparison to the UV-treated substrates, the uniformity of these films was not as good. This was verified at the macro-scale by UV/VIS spectroscopy and at the micro-scale by SEM. In response to this surprising result, I conducted several studies to determine the reason for adsorption of ISAM materials without UV irradiation of the PC substrate. The most probable reason for adsorption was that adhesive from the protective masking originally on the PC sheet was left behind despite earnest efforts to remove it.

This polycarbonate work was guided by our Materials Center of Excellence collaboration with the Army Research Labs. Our research team consists of faculty and students from several departments on campus. The overarching goal of the research team is to provide novel multi-functional thermoplastics that can be readily synthesized, processed, modeled, and coated. One promising thermoplastic synthesized in Dr. Turner's (Department of Chemistry) group is a modified polysulfone. Now that our group has successfully deposited highly uniform PAH/SiO_2 NP coatings on polycarbonate, the next logical step is to coat the modified polysulfone using the ISAM technique. Careful inspection of the polymer's molecular structure will help us determine how to functionalize the surface, whether it is by plasma etching or UV. Once the surface can be functionalized, we should focus our efforts on understanding how the treatment affects the molecular structure at the surface of the polysulfone and characterize the optical properties of PAH/SiO_2 NP ISAM coatings on the substrate.

Having already demonstrated deposition of films with exceptional clarity, another goal should be to improve their mechanical integrity. The calcination technique discussed previously (Chapter 4) cannot be used because the polysulfone would melt before reaching temperatures (500 °C) high enough to fuse the nanoparticles. Hence, an approach similar to the first one discussed in Chapter 4 is plausible. Since we can already attach sulfonate groups onto silica nanoparticles, we simply need to find a way to populate the polysulfone with them. If this is possible we can attempt to improve the mechanical strength by depositing ISAM films consisting

of diazo-resin (DAR) and sulfonate-containing silica nanoparticles, and exposing the film to UV to convert the ionic bonds into covalent ones.

ISAM Deposition of PAH/Silica Nanoparticles on Glass Fibers to Reduce Thermo-Optic Losses in Reinforced Polymer Composites

In this chapter, I discussed the ISAM deposition of PAH and silica nanoparticles onto glass fibers with micron-scale diameter. The motivation behind this research is due to the fact that glass fibers are an attractive option for reinforcing polymer composites. The refractive index of the composite can be tuned so that it matches the glass fibers and thus creates an optically transparent medium at a given temperature. However, the thermo-optic coefficients of glass and the polymer composite typically are different, which means that the change in refractive index with temperature is different for the two materials. As a result, extreme changes in temperature could potentially result in significant light scattering through the composite medium. By coating the fibers with silica nanoparticles, one can set up an intermediate region between the glass and polymer matrix that consists of both materials. This is possible because the silica nanoparticle film is nanoporous and allows the polymer to infiltrate the interstitial void space. In effect, the nanocomposite interphase is a buffer zone to reduce temperature-related optical losses. I deposited PAH/SiO_2 NP coatings on the glass fibers, immersed them in a "polymer matrix" (DMSO), and compared its transmittance as a function of temperature with uncoated fibers. I found that the ISAM process caused the fibers to aggregate, and as a result the peak transmittance of the coated fibers was not satisfactory. According to the data, it is possible that the nanocomposite interphase was mitigating temperature-dependent losses, but was competing with scatter attributed to fiber/nanoparticle aggregation. In an effort to minimize aggregation, the fibers were immersed in ionic solutions under sonication. I found that the fibers clumped together despite sonication. Regardless, if this problem can be avoided there is plenty of reason to believe that the nanocomposite interphase will improve the transmittance away from the refractive index matching temperature.

In considering future work, the major problem is the fiber/nanoparticle aggregation during ISAM deposition. Sonication during ISAM assembly is still advisable; in addition to that less aggregation may occur if the fibers are somehow separated for each immersion step. This is

not a trivial task however as the fibers can be easily fractured/broken. Another possibility is to lay the fibers in a channel through which the ISAM materials can flow. The premise of this idea is that the less the fibers are moved during the ISAM process, the less likely they are to interact with each other and aggregate. A final alternative would be to perform ISAM assembly on larger fibers. These fibers would be less susceptible to aggregation because of their comparatively larger mass, but may potentially scatter more light due to their shear size. The primary question to address is whether that particular tradeoff can improve the transparency of the polymer composite with significant changes in temperature.